The Development of Optical Biosensors for the Detection of Proteins in Solution

by

Nicola Jayne Toole

A thesis submitted to the

University of Birmingham

For the degree of

Doctor of Philosophy

School of Chemistry

College of Engineering and Physical Sciences

University of Birmingham

April 2023

Statement of Own Work

I declare that the results presented throughout this work are composed by myself. Some of the work is an extension of the work completed before me by previous group members, and in these instances the work has been referenced and acknowledged accordingly.

Abstract

Biosensors for use in point of care (POC) settings are highly sought after; yet, fabrication is often difficult due to costly materials. Hydrogels can be prepared using cheap and commercially available materials. Leaky waveguide (LW) biosensors have been developed previously using hydrogels, leading to the formation of label-free, real-time optical biosensors from readily available materials. If the instrumentation required for these devices was smaller and more user friendly, then LWs would be ideal for POC diagnostics.

In order to improve the portability of LWs for POC testing, the useability of a three-dimensional (3D) printed instrument for the testing of hydrogel-based LW devices was studied. This included comparing the refractive index sensitivity (RIS) and porosity of LWs tested on a traditional benchtop laboratory-based instrument to those tested using a 3D printed instrument. The 3D printed instrument was also then tested for the ability to detect biologically relevant analytes, in the form of immunoglobulin G (IgG).

The structure of the 3D printed instrument eliminated the ability to use a two-channel flow cell to incorporate an internal reference, which is a requirement for the user-friendly data analysis. The internal reference allows for the subtraction of signals caused by non-specific binding from the detection signal, giving an accurate representation of binding due

to the desired immobilisation strategy. In order to address this, LWs comprised of photocaged hydrogels were investigated. Following this, photolabile protecting groups (PPGs) were designed and used to photocage monomers.

LWs were then created using these photocaged monomers, prior to selective photodeprotection of the PPGs to release protein reactive functional groups. This incorporated a reference internally within the LW device through the production of protein reactive and protein inert regions. These internally referenced LW biosensors were then tested for their ability to act as biosensors.

Acknowledgements

Initially I would like to thank those who are no longer here to celebrate with me, my dad, Norman, and my grandmother, Elsie, who were always supportive of my studies and proud of me. I'd also like to thank my mum, Jill, for being there throughout the good and the bad times, all of my siblings and their children, and the rest of my very large family.

I suppose my greatest thanks have to go to Jake, without whom I never would have embarked upon this journey. Thank you for supporting me through all my complaining, listening to me while I reasoned my thoughts out to myself then pretending you were listening, and also for not killing me when we were locked up in a flat for 3 months with seemingly no end in sight.

I would like to thank my supervisor Dr Gupta, and the rest of the Gupta group for their knowledge and expertise in areas where mine was originally lacking and for their support. Thank you to the EPSRC and the School of Chemistry at the University of Birmingham for providing the funding for this project.

To Hazel, thank you for accepting that misery loves company, for helping me when ever my waveguide decided to misbehave, and for being quite the unintended source of comic relief. To Elisabetta, thank you for being the happiness that was required on a bad day, and the social butterfly of the group. To William, thank you for being the optimistic friend we all needed. Thank you to the Tucker group, in particular Charlotte and Francia for all of your help, and allowing me to intrude on your lab space when feeling overwhelmed.

I would like to extend my gratitude to Trevor Hardy, Katherine Webb and Richard Petford for helping the many times that things went wrong, especially when our office kept locking us out. Finally, I would like to thank the analytical team at the University of Birmingham, in particular Cécile Le Duff, Allen Bowden and Chris Williams for their aid.

Covid Impact Statement

As many students, postgraduate and undergraduate alike, would agree, to study throughout 2020 – 2021 was a task more complicated than anyone would have ever expected. As of March 2020, the University of Birmingham informed all students that campus would remain closed for at least 11 weeks. Personally, I lost closer to 21 weeks of practical study time due to the closure of the University, of this, 13 weeks were awarded to me as an extension at the end of my minimum registration period. Following the return to in person attendance and resuming practical laboratory work, social distancing rules were in effect. These rules required me to return to practical work part time, a schedule alternating weekly for a further 10 weeks. These weeks of forced work from home plus time of forced self isolation resulted in a total loss of approximately 15 weeks of practical experimental time.

In addition to the lost time from being forced to work from home, time was also lost due to the social distancing rules on campus. Completing analysis of samples took more time as only 1 person at a time was able to enter certain rooms, resulting in queues which slowed down the process. Another negative impact that COVID had on this project was that collaboration between different schools dwindled. In order to free up space for their own researchers, schools often denied access to their buildings for students from other schools. This prevented me from visualising the photopatterned gels via fluorescence microscopy as was originally planned.

Overall, COVID resulted in a decreased time frame to complete laboratory work, and inhibited access to facilities which would have improved the quality of data provided. Had COVID not occurred throughout the duration of these studies, I'd like to think that the final stages of study would be more thorough and have more data to rely on.

Contents

List of Figures

List of Tables

Abbreviations

2D-PAGE	Two-Dimensional Polyacrylamide Gel Electrophoresis
3D	Three-Dimensional
$\Delta\theta_R$	Shift in Resonance Angle
ε	Molar Extinction Coefficient
AAm	Acrylamide
AC	4-(chloromethyl)-7-(dimethylamino)-2*H*-chromen-2-one
Ac_2O	Acetic Anhydride
AP	Atmospheric Pressure
APMA	*N*-(3-aminopropyl) Methacrylamide
APS	Ammonium Persulfate
ASAP	Atmospheric Solids Analysis Probe
BAAm	*N*-*N*'-methylenebis(acrylamide)
BSA	Bovine Serum Albumin
Boc	*tert*-butoxycarbonyl
CDMVS	Chloro(dimethylvinyl)silane
CNC	Computer Numerical Control
CRP	C-Reactive Protein
d	Doublet
DBF	Dibenzofuran
DBF-1	Dibenzo[*b,d*]furan-2-carbaldehyde
DBF-2	3-nitrodibenzo[*b,d*]furan-2-carbaldehyde
DBF-3	(3-nitrodibenzo[*b,d*]furan-2-yl)methanol

DBF-4	2-(chloromethyl)-3-nitrodibenzo[*b,d*]furan
DBF-5	*N*-(3-(((3-nitrodibenzo[*b,d*]furan-2-yl)methyl)amino)propyl)methacrylamide
DCM	Dichloromethane
DDLW	Dye Doped Leaky Waveguide
DFU	Diabetic Foot Ulcer
DI	Deionised
DM	Diabetes Mellitus
DMEMA	2-(dimethylamino)ethyl Methacrylate
DMF	N,N-dimethylformamide
DMSO	Dimethylsulfoxide
DNA	Deoxyribonucleic Acid
ECM	Extracellular Matrix
EGF	Epidermal Growth Factor
EI	Electron Ionisation
ESI	Electron Spray Ionisation
EtOH	Ethanol
ELISA	Enzyme Linked Immunosorbent Assay
FITC	Fluorescein Isothiocyanate
FMOC	9-fluorenylmethoxycarbonyl
HAT	Hydrogen Atom Transfer
hCG	Human Chorionic Gonadotropin
HEPES	4-(2-hydroxyethyl)-1-piperazineethanesulfonic Acid
HIC	Hydrophobic Interaction Chromatography

HMDS	Hexamethyldisilazane
HPLC	High Performance Liquid Chromatography
IEF	Isoelectric Focusing
IgG	Immunoglobulin G
IL-1	Interleukin-1
IR	Infrared
LED	Light Emitting Diode
LW	Leaky Waveguide
m	Multiplet
MALDI	Matrix Assisted Laser Desorption/Ionisation
MC	4-(chloromethyl)-6,7-dimethoxy-2*H*-chromen-2-one
MC-1	*N*-(3-(((6,7-dimethoxy-2-oxo-2*H*-chromen-4-yl)methyl)amino)propyl) methacrylamide
MC-2	*N*-(3-(((6,7-dimethoxy-3-nitro-2-oxo-2*H*-chromen-4-yl)methyl)amino)propyl) methacrylamide
MC-2a	4-(chloromethyl)-6,7-dimethoxy-3-nitro-2*H*-chromen-2-one
MC-3	(6,7-dimethoxy-2-oxo-2*H*-chromen-4-yl)methyl (3-methacrylamidopropyl) carbamate
MC-3a	4-(hydroxymethyl)-6,7-dimethoxy-2*H*-chromen-2-one
MC-3b	(6,7-dimethoxy-2-oxo-2*H*-chromen-4-yl)methyl (4-nitrophenyl)carbonate
MCLW	Metal Clad Leaky Waveguide
MeOH	Methanol
mRNA	Messenger Ribonucleic Acid

MS	Mass Spectrometry
NaOAc	Sodium Acetate
NB-1	2-(2-(2-methoxyethoxy)ethoxy)ethyl-4-methylbenzenesulfonate
NB-2	3,4-bis(2-(2-(2-methoxyethoxy)ethoxy)ethoxy)benzaldehyde
NB-3	4,5-bis(2-(2-(2-methoxyethoxy)ethoxy)ethoxy)-2-nitrobenzaldehyde
NB-4	(4,5-bis(2-(2-(2-methoxyethoxy)ethoxy)ethoxy)-2-nitrophenyl)methanol
NB-5a	1-(chloromethyl)-4,5-bis(2-(2-(2-methoxyethoxy)ethoxy)ethoxy)-2-nitrobenzene
NB-5b	4,5-bis(2-(2-(2-methoxyethoxy)ethoxy)ethoxy)-2-nitrobenzyl carbonochloridate
NB-6a	N-(3-((4,5-bis(2-(2-(2-methoxyethoxy)ethoxy)ethoxy)-2-nitrobenzyl)amino)propyl)methacrylamide
NB-6b	4,5-bis(2-(2-(2-methoxyethoxy)ethoxy)ethoxy)-2-nitrobenzyl (methacrylamidopropyl) carbamate
NHS	N-hydroxysuccinimide
NHS	National Health Service
NMR	Nuclear Magnetic Resonance
NVOC-APMA	4,5-dimethoxy-2-nitrobenzyl (3-methacrylamidopropyl)carbamate
NVOC-Cl	4,5-dimethoxy-2-nitrobenzyl Chloroformate
PAAm	Polyacrylamide
PCR	Polymerase Chain Reaction
PEG	Polyethylene Glycol
PG	Protecting Group

POC	Point of Care
PPG	Photolabile Protecting Group
RB4	Reactive Blue 4
RI	Refractive Index
RIU	Refractive Index Units
RIS	Refractive Index Sensitivity
RNA	Ribonucleic Acid
RP-HPLC	Reversed Phase High Performance Liquid Chromatography
RT	Room temperature
s	Singlet
SDS-PAGE	Sodium Dodecylsulphate Polyacrylamide Gel Electrophoresis
SEC	Size Exclusion Chromatography
SMC	4-(chloromethyl)-6,7-dimethoxy-2*H*-chromene-2-thione
SMC-1	*N*-(3-(((6,7-dimethoxy-2-thioxo-2*H*-chromen-4-yl)methyl)amino)propyl) methacrylamide
SMC-2	*N*-(3-(((6,7-dimethoxy-3-nitro-2-thioxo-2*H*-chromen-4-yl)methyl)amino)propyl) methacrylamide
SMC-2a	4-(chloromethyl)-6,7-dimethoxy-3-nitro-2*H*-chromene-2-thione
SMC-3	(6,7-dimethoxy-2-thioxo-2*H*-chromen-4-yl)methyl (3-methacrylamidopropyl) carbamate
SMC-3a	4-(hydroxymethyl)-6,7-dimethoxy-2*H*-chromene-2-thione
SMC-3b	(6,7-dimethoxy-2-thioxo-2*H*-chromen-4-yl)methyl (4-nitrophenyl)carbonate
SPR	Surface Plasmon Resonance

t	Triplet
TE	Transverse Electric
TEA	Triethylamine
TEMED	*N,N,N',N'*-tetraethylmethylenediamine
THF	Tetrahydrofuran
TIR	Total Internal Reflection
TMTFS	Trimethoxy(trifluoropropyl)silane
TNF-a	Tumour Necrosis Factor Alpha
TOF	Time of Flight
tRNA	Transfer Ribonucleic Acid
UV	Ultraviolet
UV-Vis	Ultraviolet – Visible
VEGF	Vascular Endothelial Growth Factor

Chapter 1 - Introduction

1.1 *Wounds and Inflammation*

In accordance with the Oxford English Dictionary, the term wound is defined as "an injury to part of the body, especially one in which a hole is made in the skin using a weapon."[1] That is not to say however, that all wounds must be created through the use of a weapon, there are many possible causes of wounds.

In the UK a retrospective analysis of the years 2012/2013 showed that the National Health Service (NHS) managed an estimated 2.2 million wounds. Almost 170,000 (≈ 8%) of these were wounds associated with complications caused by diabetes mellitus (DM).[2,3] Additionally, it was found that of those accessing wound healthcare through medicare in the USA, 17% were DM related (Figure 1.1).[4] During a study period of one year, the cost to the NHS of treating diabetic foot ulcers (DFUs) ranged between £525 million and £730 million, evidently making these wounds a huge economic burden.[2,5]

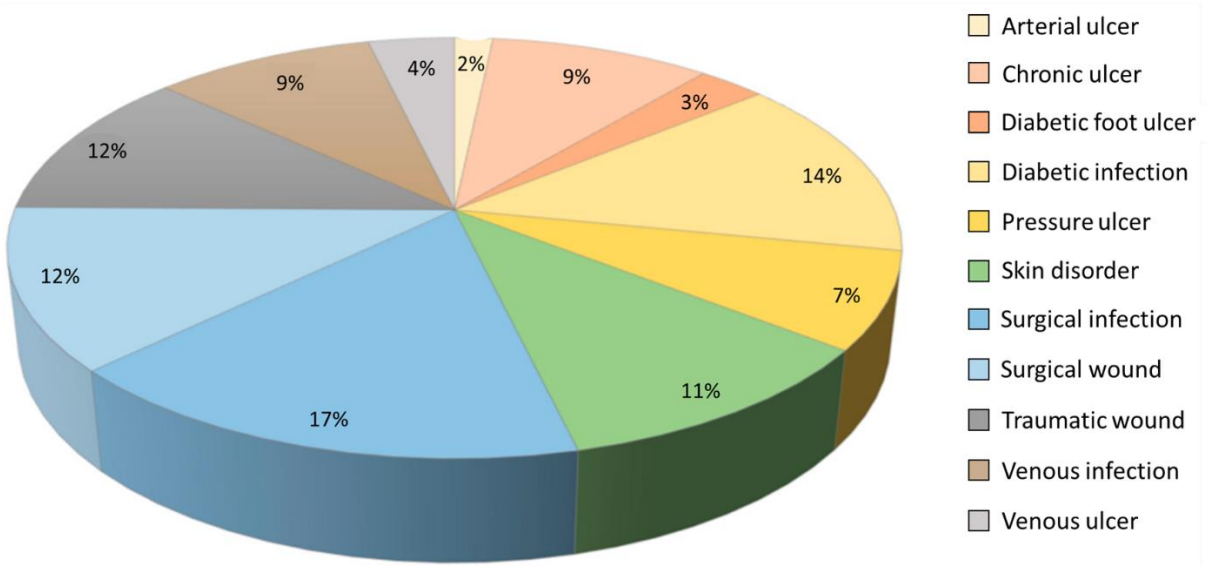

Figure 1.1: *A pie chart showing the distribution of wounds requiring care in the US in 2014; arterial ulcers, 2%; chronic ulcers, 9%; DFUs, 3%; diabetic infections, 14%; pressure ulcers, 7%; skin disorders, 11%; surgical infections, 17%; surgical wounds, 12%; traumatic wounds, 12%; venous infections, 9%; and venous ulcers, 4%. Image adapted from Pinto et al.*[4]

1.1.1 Wound Healing

Wounds can be separated into two categories, acute or chronic, depending on the time taken to heal or likelihood of recurrence.[5] Studies conducted into the healing of acute wounds have determined that recovery occurs in four phases; these phases are not autonomous and are known to overlap with one another. The four phases, briefly described in Figure 1.2 are as follows:

Hemostasis: The first phase is characterised by the reduction of blood flow *via* vasoconstriction and the formation of a fibrin/platelet plug, triggering blood clotting. Platelets result in the production of growth factors, which attract a variety of cells such as macrophages, neutrophils and fibroblasts, among others, which are necessary for the later phases of wound healing.[6]

Inflammation: The second phase of wound healing overlaps with hemostasis, with the two happening simultaneously for a short period. Following clot formation, neutrophils clear the extracellular space of contaminants such as bacteria and matrix proteins through phagocytosis. Macrophages aid with this phagocytosis; they also stimulate the formation of granulation tissue and angiogenesis. Various types of growth factors enter the wound at this point.[6]

Proliferation: Angiogenesis begins. Growth factors stimulate the migration and regeneration of healthy cells from nearby tissues. Structural proteins, such as collagen, elastin and extracellular matrix (ECM) proteins used in the formation of new tissue are produced by fibroblasts, which undergo a phenotypic change into myofibroblasts. These various components provide the strength and support required for the ECM. The formation of granulation tissue begins.[6]

Maturation/Remodelling: The wound begins to contract. Proteins such as matrix metalloproteinases initiate the remodelling of the foetal type III collagen into the stronger and more abundant type I variant. This results in the healed wound, which will achieve a maximum strength that is 80% of that of undamaged tissue.[6]

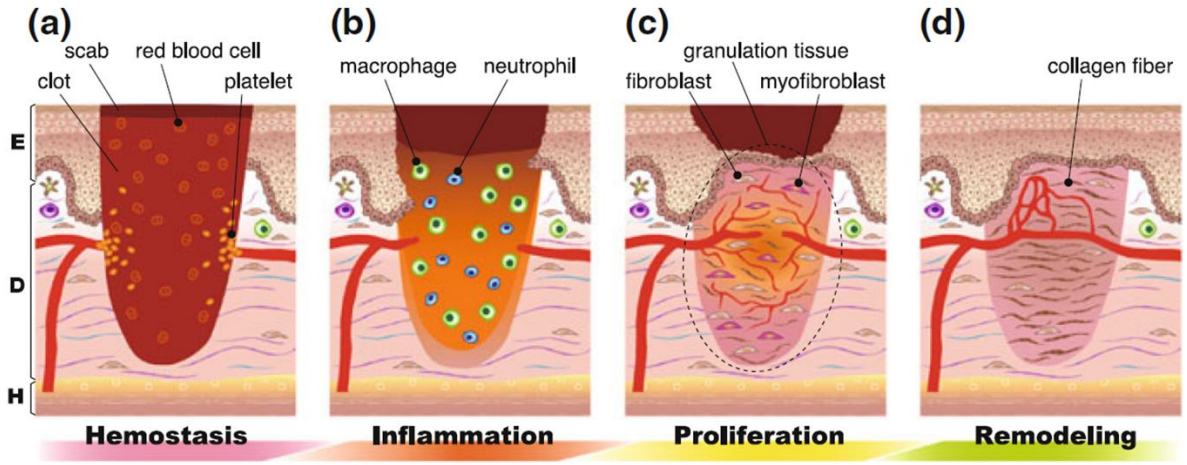

Figure 1.2: *An image depicting the four phases of healing in acute wounds and the important components of them.* ***a) Hemostasis,*** *platelets bind to the walls and initiate the clotting of red blood cells and extracellular matrix proteins.* ***b) Inflammation,*** *neutrophils and macrophages enter the wound site, the former resulting in the phagocytosis of external contaminants and the activation of the inflammatory response. Macrophages stimulate angiogenesis and tissue granulation.* ***c) Proliferation,*** *migration of healthy cells begins. Fibroblasts produce proteins, such as collagen and elastin, and are converted into myofibroblasts in the formation of a new extracellular matrix. Granulation tissue begins to be formed.* ***d) Remodelling,*** *the type III collagen matrix is converted into a type I collagen abundant tissue causing the maturation from granulation to scar tissue. Image adapted from Kawasumi et al.*[7]

With acute wound healing, it takes a matter of weeks to progress through these stages to complete wound healing.[8] For the majority of wounds, ranging from burns to surgical incisions this is often the case; however, there are some instances in which it takes much longer to progress through the phases of healing, which results in the formation of chronic wounds.

1.1.2 Bacterial Infections

Bacterial contamination of wounds is a common occurrence, much more common than any of us would like to believe; in fact, all wounds become contaminated with bacteria from the immediate environment and the skin encircling the wound.[9]

Initially, wound infections are colonised in very low volumes, making them simple to treat; however, in these stages, low bacterial loads do not illicit a strong immune response, limiting the possibility of diagnosis. While this sounds like it may be troublesome, this presence of bacteria has in fact been shown to encourage wound healing.[10] This is due to contamination of wounds inducing healing by promoting the inflammatory response, the second phase of healing.[3] Unfortunately, occasions occur where this inflammatory response is insufficient to impede further bacterial colonisation of the wound, and in these instances, the exponential replication of bacterial cells causes infection to develop.[10]

There are five classifications of bacterial infection based on bacterial loads; this is known as the wound infection continuum, and is described in detail below (Figure 1.3)[4]:

Contamination: The presence of bacteria on the surface of a wound. Low levels of bacteria enter the wound site from surrounding tissues and the immediate environment. Contamination is a common occurrence and does not elicit an immune response or impede the healing process. This remains undiagnosed.[11]

Colonisation: Bacteria slowly start to reproduce and proliferate, increasing the bacterial load. At this stage, the presence of bacteria may initiate a low-level immune response which aids with wound healing by promoting the inflammation phase. Infection remains undiagnosed.[11]

Local Infection: As bacteria continue to proliferate, reproduction increases exponentially. Bacteria begin to migrate from the surface of the wound, deeper into the tissue. The immune response begins to display symptoms of infection.[11]

Spreading Infection: Increasing bacteria numbers spread to nearby healthy tissues, no longer being localised in the wound tissue. The immune response is strong, symptoms of wound infection are clear.[11]

Systemic Infection: Bacteria have now spread throughout the body by various means. Symptoms of infection are no longer localised at the wound. Failure to treat at this stage may have dire consequences.[11]

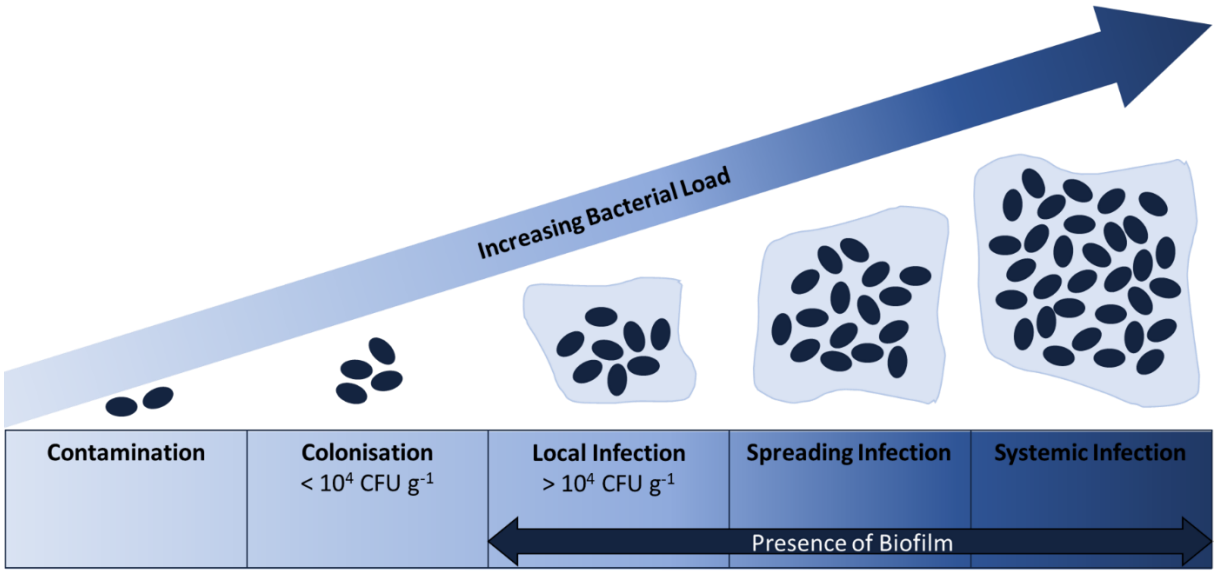

Figure 1.3: *An image depicting the progression of bacterial infections. First stage, contamination, low bacterial load. Second stage, colonisation, bacteria replicate but do not yet cause infection. Third stage, local infection, bacterial load surpasses the threshold of 10^4 CFU g^{-1} and infection is now present, biofilms form. Fourth stage, spreading infection, bacteria begin to inhabit nearby healthy cells. Fifth stage, systemic infection, the bacterial cells have multiplied and spread throughout the body. Image adapted from Pinto et al and Farhan et al.*[4,11]

High bacterial loads can result in non-healing wounds, thus being a cause of chronic wound formation. This is frequently observed in clinical settings, in fact at the point of hospital admission up to 60% of DFUs display signs of infection, with analysis of chronic wound fluids

often containing bacteria and endotoxins.[3,6,12] If wound tissue infections remain untreated, the non-healing state is exacerbated, leading to further, more serious consequences.[13]

Unfortunately, due to the presence of low-level bacteria promoting wound healing, it is ill-advised to immediately resort to antibiotic use for wounds. Due to this, treatments for bacterial infections are often only administered when there are physical factors suggesting infection, such as malodorous discharge, redness, heat, pain and swelling.[10] All of these factors can be affected by a patients age, health, and current medication, causing complications for infection diagnosis and treatment.[3] Not only this, but other than malodorous discharge, these symptoms are also indicative of the human inflammatory response, which is vital to healing.[14] Additionally, these symptoms may not be typical in chronic wounds, as supported by a study conducted by Serena *et al* who, following biopsies, found that 14 patients out of 49 had infected wounds, despite being cleared by a physical examination.[13,15]

In an attempt to combat problematic diagnostic techniques, a clinical swab is taken of the surface for bacterial culturing in approximately 70% of cases.[16,3,15] Due to the requirement for infection to proliferate, and then awaiting culture results after that, the time taken to diagnose a bacterial infection in a wound can be quite long, resulting in limited treatment options.[16] This results in bacterial infections being a common cause of chronic, non-healing wounds.

1.1.3 Chronic Non-Healing Wounds

The state of wound healing is currently determined by a physical examination from a medical professional.[17] To monitor wound healing, physicians commonly measure the wound

width and depth at regular intervals as prevention of wound healing would cause minimal change in wound size over time (Figure 1.4).[17] The phases of acute wound healing (Figure 1.2) can be influenced by a variety of factors, ranging specifically from the wound size, depth and location, to more general factors such as the patients age and underlying health conditions such as DM.[6]

It is believed that a disruption to these phases of healing is the cause of chronic wounds such as DFUs and pressure ulcers. This is due to chronic wounds possessing an enhanced inflammatory state in comparison to acute wounds.[12] This prevents the wound from moving into the proliferation stage, thus healthy cells cannot migrate into the wound matrix and continue the healing process. Numerous factors may result in disruption to the phases of wound healing such as protein levels, pH of the wound environment, the presence of reactive oxygen species and finally, high levels of bacterial contamination.[18]

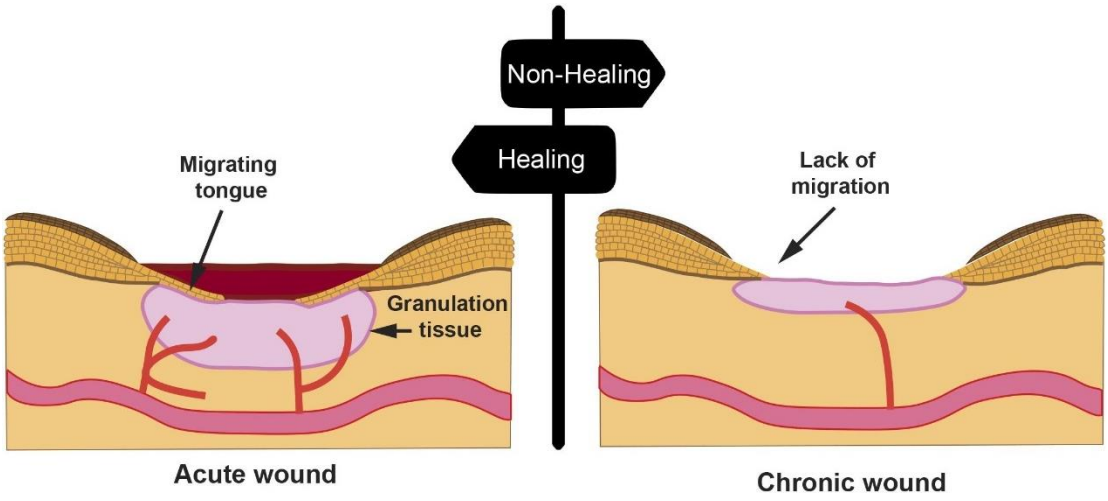

Figure 1.4: *An image depicting the migration of skin cells in an acute wound, and a lack of migration in a chronic wound, thus the prevention of wound healing. Image adapted from Ruiz-Cañada et al.* [19]

Due to there being no universally agreed definition of chronic wounds, diagnosis can be difficult and time consuming, often taking between four and twelve weeks.[3] Chronic

wounds are a drain on the economy, but the physical effects they have on people can be far worse, as DFUs are often the cause of major health issues in DM patients.[5] DFUs affect between 4 and 10% of DM patients annually, and these patients tend to have higher mortality rates than average.[6,20] Not only this, but, in those who do survive, DFUs are the main cause for hospitalisation of DM patients, and result in more than half of all non-traumatic lower limb amputations.[6,21] Chronic wounds are prevalent in DM patients for a myriad of reasons, lack of mobility, loss of sensation, degradation of muscle and structural changes in the foot have all been found to contribute to DFUs.[21] Scientific studies have shown that the fluids of DFUs are vastly different to those of acute wounds in terms of inflammatory mediators and growth factors. As a result of this discovery, biopsies of wounds would go a long way to reducing the effect of DFUs, however they are deemed to be impractical in the clinical environment.[12,15]

Visual monitoring is how physicians are inherently taught to diagnose wounds; as can be seen with students who approach wounds with the recitation of the Latin phrase “dolor, rubor, calor and tumor”, referring to the common symptoms described earlier (Chapter 1.1.2).[15] Physicians are not at fault for the issues regarding chronic wound detection, as the problem is larger than a single cause. Despite academia conducting much research into the bacteriology of chronic wounds, the clinic is a much more hectic setting with limited funding and resources.[15] The final, and most important reason for this antiquated diagnosis method, is the simple lack of user-friendly and high-speed tests which can be completed by the physician. Despite quantitative biopsies being available, and superior for accurate diagnosis, they are not implemented in clinics because they are impractical.[15]

1.1.4 Wound Observation and Treatment

Throughout the healing process, wounds require care and protection; there are multiple ways to do this, from the removal of tissue to promote the growth of healthy cells, to the protection of the wound environment with dressings. These are generic methods which can be applied to any wound, and while they promote healing, they rarely treat any underlying problems. In the late 1970's, it was determined that to be effective, a wound dressing must fit certain criteria, shown in Table 1.1, and these are still valid today, however they have since been expanded upon.[22,23]

Table 1.1: *A table showing the desired characteristics of wound dressings.*[22,23]

Parameters of Ideal Wound Dressings	
General Characteristics	Biocompatible, non-toxic Removeable without causing excess trauma Simple application, minimal maintenance Aesthetically pleasing Cost effective Simple storage conditions Hypoallergenic
Healing Facilitation	Maintain humid atmosphere Heat preservation Permeable to gaseous exchange Minimise trauma or maceration to wound edges
Minimise Infection Risks	Absorb wound exudates Impermeable to contaminants Debride necrotic tissue

Any necrotic tissue surrounding the wound opening must be removed immediately as this hinders the healing process; this removal is known more commonly as wound debridement. Once a wound is deemed to be clean and free of unviable tissue, it can then be dressed and frequently monitored. Wound dressings can be designed to promote wound healing (Figure 1.5) and there are many different types of dressing in circulation today (Table 1.2). Through collating this information, the optimum dressing to promote wound healing can be used.

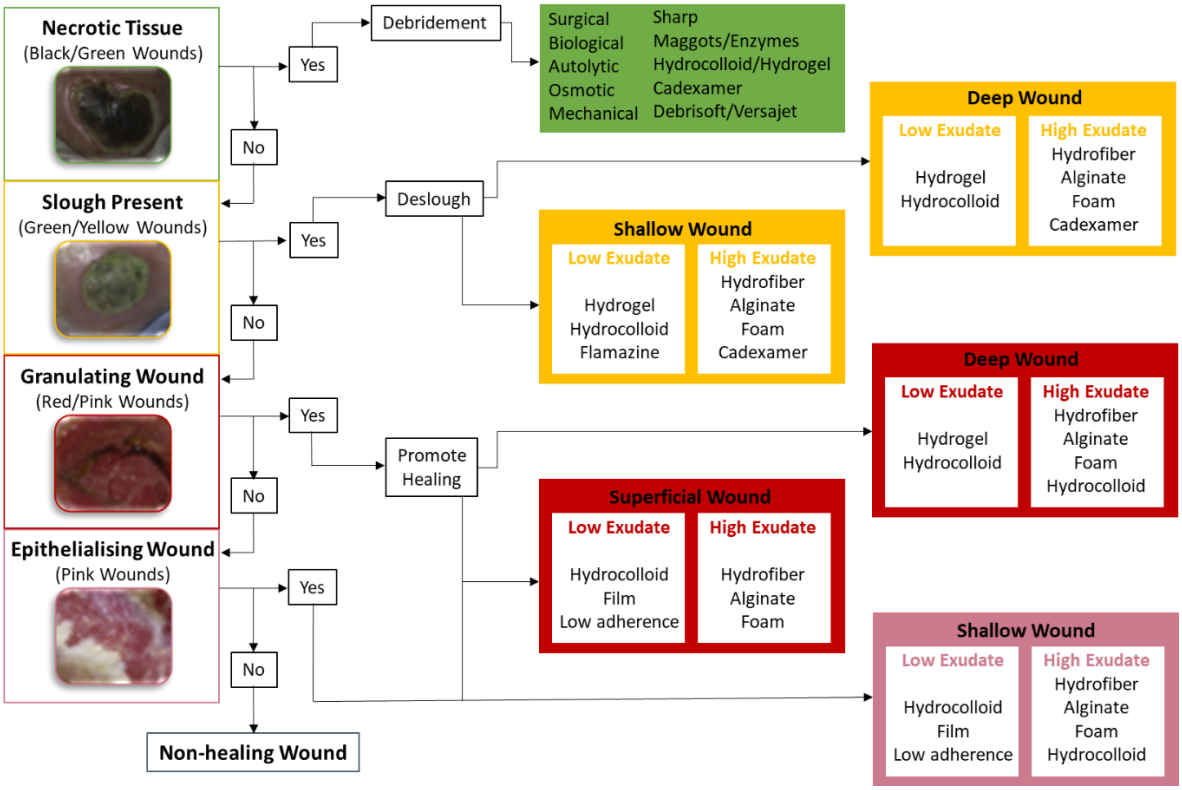

***Figure 1.5**: A flow chart to aid in the choice of wound care for a variety of wounds. For necrotic wounds (black/green appearance), debridement is the method of choice. Wounds with slough present (green/yellow appearance) require wound dressings which can deslough the wound, the dressings of choice are consistent for both shallow and deep wounds. Granulating wounds (red/pink in appearance) are on the way to becoming healed, therefore only need dressings to promote healing. There is little difference in dressings for superficial and deeps wounds. Epithelialising wounds (appearing pale pink) are almost fully healed, only occur as shallow wounds and need dressings to protect from reinjury. If the wounds do not fit into one of these categories, they are likely to be in a state of non-healing. Image adapted from Vowden et al.[24]*

Table 1.2: *A table displaying the various forms of wound dressings and their respective advantages and disadvantages.*[25]

Dressing Type	Advantages	Disadvantages
Gauze	Low cost, absorbent.	May dry the wound, may adhere to the wound.
Semipermeable Film	Allows for gaseous exchange, watertight, flexible.	Low exudate absorption, unsuitable for high exudative wounds.
Semipermeable Foam	Allows for gaseous exchange, flexible, absorbs exudate.	Not suitable for low exudative wounds.
Hydrogels	Suitable throughout healing process, hydrating, easy removal/changing.	Weak structure, exudate accumulation, over-hydration.
Hydrocolloid	Permeable to $H_2O(g)$, impermeable to bacteria, absorbs exudate, long lasting.	Unsuitable for high exudate, infected and neuropathic wounds.
Alginate	Limits exudate, minimises bacterial contamination, aids healing process.	Hinders skin cell migration, unsuitable for dry wounds.
Bioactive	Assists proliferation phase, biocompatible.	Weak structure, exudate accumulation.
Engineered Skin Substitutes	Assists proliferation phase, biocompatible, alters protein levels.	Low exudate absorption, infection and immune response risk, costly.
Medicated	Targeted therapy.	May encourage resistant microorganisms.

For many years wound dressings have been developed with therapeutic abilities. For example, in the USA over 2 decades ago a technique known as negative pressure wound therapy was developed, which is now a common staple in hospital burns units due to a correlation with low wound infection rates. Negative pressure wound therapy is comprised of a foam dressing, which needs to be changed every two days, and an evacuation tube. As Figure 1.5 describes, foam dressings are flexible, allowing for full contact with the wound, and readily absorb wound exudates, they also maintain a moist environment which is ideal for wound healing. The evacuation tube applies pressure to the wound, which optimises blood flow and promotes wound closure.[26]

1.1.5 Hydrogel Wound Dressings

Hydrogel wound dressings occur in two forms. In the first instance, a hydrogel is pre-formed on the surface of a solid substrate; in the second instance, the dressing is aerosolised and sprayed onto the wound, where polymerisation occurs resulting in hydrogel formation.

A hydrogel is commonly described as being a three-dimensional (3D) network of hydrophilic polymers (Figure 1.6).[27] The range of polymers suitable to make hydrogels is vast, encompassing almost any existing hydrophilic polymer, both synthetic and natural.[28] Due to the hydrophilicity of these polymers, they are able to absorb up to 1000 × their dry mass of water into their structure.[27] Despite their hydrophilic nature, hydrogels themselves are insoluble in water due to the many cross-links between the polymer chains. These cross-links can be both physical, such as hydrogen bonding, and chemical, such as covalent bonding.[29,30]

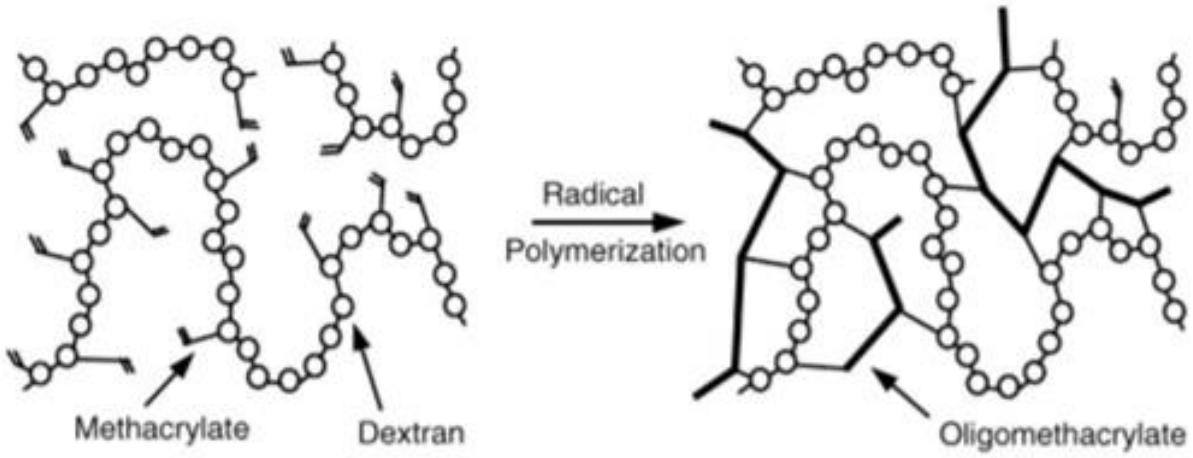

Figure 1.6: *A diagram to show the formation of cross-links across a polymer to create 3D structures. Image adapted from Hennink.*[31]

Due to their biocompatibility, hydrogels have many applications in the medical industry, such as, but not limited to, drug delivery, biosensors, electrophoretic media for the separation of DNA, and wound dressings. Hydrogel-based wound dressings are efficient at maintaining a moist environment for dry wounds and aiding with autolytic debridement of necrotic wounds, however they also have the ability to absorb low volumes of wound exudates.[32]

The porous nature of hydrogels allows for the simple diffusion of oxygen into the wound environment, promoting wound healing.[33] Not only this, but, due to the biocompatibility of hydrogels, they can also act as the perfect media to introduce substances to the wound environment to promote wound healing. Hydrogel wound dressings have been used to supply wounds with antibacterial agents and various proteins to treat wounds while protecting them from the external environment.[33]

One hydrogel which is already readily used in the formation of hydrogel based wound dressings is chitosan. Through the deacetylation of chitin, we can produce the polymer

chitosan.[34,35] This is advantageous as chitin is highly abundant, naturally occurring polymer, being a major component of crustacean and insect shells.[34,35] The natural abundance of chitin results in a low cost for the material, which is beneficial for large scale production using the material.[36] Multiple wound dressings designed from the chitosan structure are already commercially available [36] and this is due to the innate characteristics of chitosan. Chitosan, being derived from a biological source, is inherently biocompatible and biodegradeable, not only that, the material has been determined to have antimicrobial properties, and adheres well to the skin, while also possessing properties which aid in the healing of inflammation.[37] The low cost for materials and high biocompatibility make chitosan an ideal candidate for hydrogel based wound dressings.

1.2 Proteins

There are 20 amino acids which are made in nature that are vital to human life; some of these we produce ourselves, some of which we must obtain through our diet. All of these amino acids are crucial for proper bodily function, as they are the building blocks of the proteins which make the majority of our dry mass. These proteins make up to 20% of our total body mass, which when the 60% of water weight is taken into account, is a large volume.

The human body is currently known to have the ability to synthesise between 200,000 and 500,000 different proteins; however, it is theorised that this number may be as high as 1,000,000.[17,38] Making such a large number of different proteins from a combination of only 20 different amino acids seems to be an impossible feat; however, proteins can range from being as small as 51 amino acids long, as is the case with insulin, to 27,000 amino acids long as is seen in titin.[39,40] Different chain lengths add variety into the number of proteins which can be formed, however, even without this, if all proteins were 51 amino acids long, as is the case with insulin, this allows for the formation of over 20^{51} different iterations, which is equal to over 2×10^{66} protein chains. This means that while the human proteome currently creates up to an estimated 500,000 different proteins, this number is negligible in comparison to the potential number of proteins possible.

1.2.1 Protein Synthesis

The sequence of proteins is imperative to function, and highly specific; the specificity of protein structure is determined by deoxyribonucleic acid (DNA).

In-vivo, the first step of protein synthesis is transcription which is the formation of messenger ribonucleic acid (mRNA) from a DNA sequence. Following the formation of this

mRNA strand, transfer ribonucleic acid (tRNA) carries an amino acid to the ribosome. The tRNA molecule contains an anticodon arm, a section of three nucleotide bases; these bases are bound to complementary codons present in the mRNA chain.[41] The amino acid carried by tRNA is specific to the anticodon arm, as can be seen in Figure 1.7, however, a single amino acid can be coded for by multiple codons, such as alanine which is coded for by 4 different codons.[41,42] This amino acid then binds to another present on the adjacent tRNA molecule and is released from the tRNA when another binds to it. This process continues throughout the entire mRNA strand until a stop codon is reached, at which point the protein synthesis terminates, resulting in a fully formed protein chain.[41]

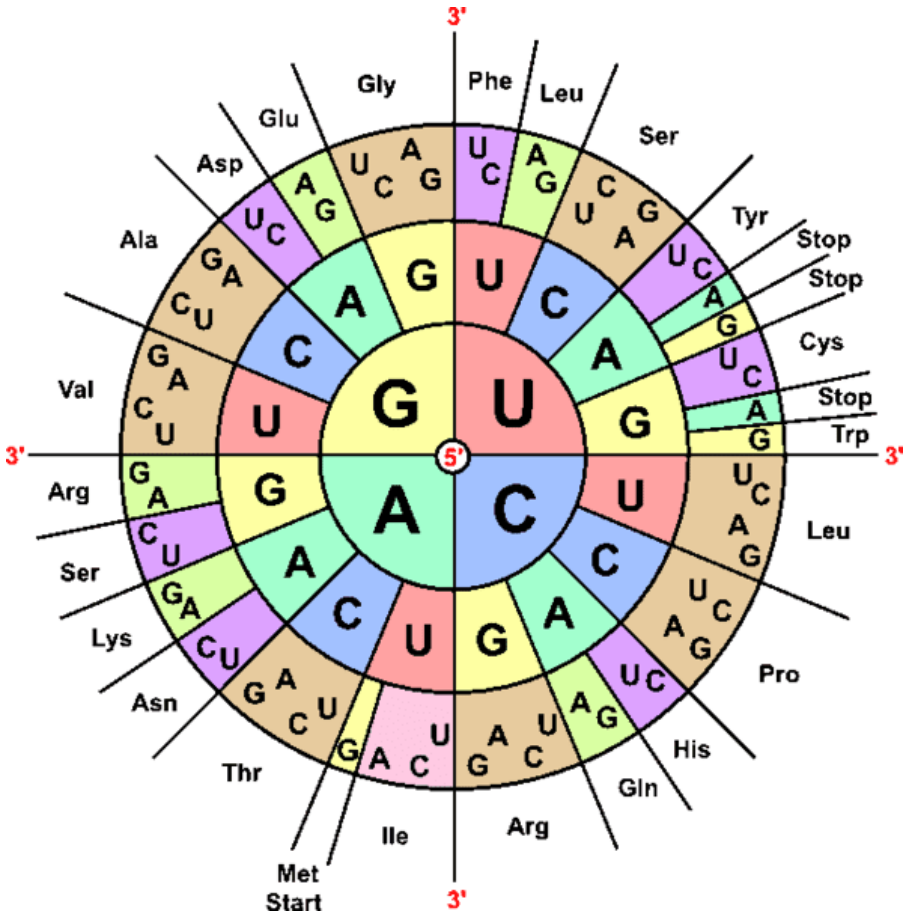

Figure 1.7: *An image displaying the different nitrogenous base combinations to form codons and which amino acids they code for, or it they code for the start/stop of transcription. Image adapted from Biology Online.*[42]

This is the basis for the highly specific order of amino acids within a protein, which is required for correct functionality. This forms the primary structure of proteins; however, proteins do not simply exist as long straight chains. The proteins fold into secondary structures thanks to hydrogen bonds between hydrogen atoms and oxygen and nitrogen atoms present in amide bonds and other functional groups.[43] This secondary structure yet again folds to form a tertiary structure. The complex tertiary structure is caused by the protein folding to exist in the lowest energy state possible. These folds are caused by favourable bond formations through a variety of interactions such as hydrogen bonding, electrostatic interactions, van der Waals forces, covalent bonds and hydrophobic clustering forces.[44] For a number of proteins, such as haemoglobin and insulin, their protein structure, known as a quaternary structure, is more complex and comprises of multiple protein chains held together through intermolecular bonds (Figure 1.8).[45] As structure is based on amino acid interactions, and these bonds are required for the final structure, the order of amino acids present in a protein chain is specific.

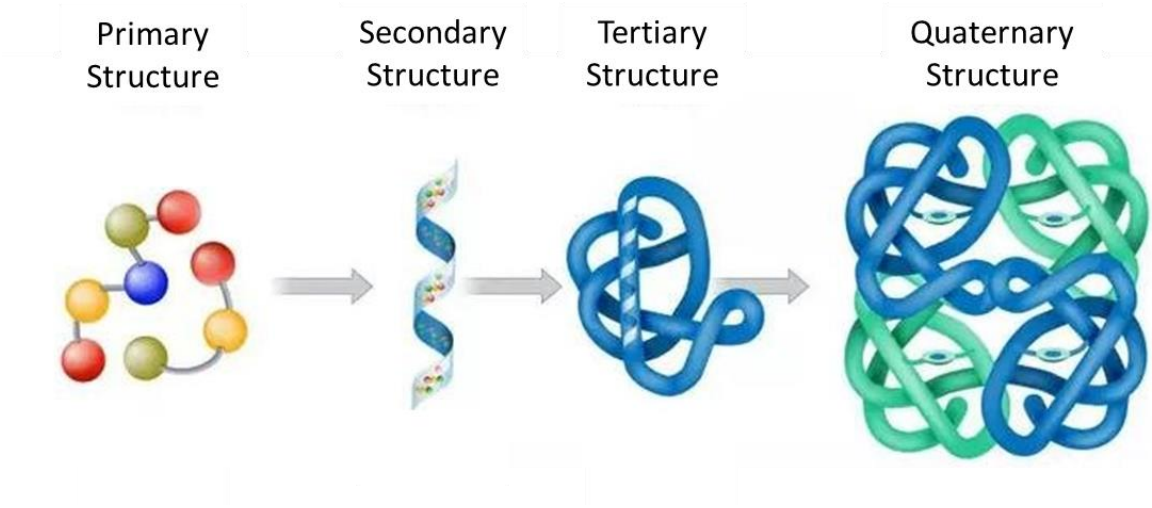

Figure 1.8: *An image depicting the differences between primary, secondary, tertiary and quaternary structures of proteins. Image adapted from Mandal et al.*[46]

1.2.2 Binding Selectivity and Activity

Along with the structure, the strength of binding interactions, known as binding affinities, are another characteristic of proteins which is determined by amino acid sequencing. As the functional side chains contain a variety of functional groups, ranging in characteristics from hydrophobic to charged to hydrogen bond donors and acceptors, their positioning determines how well a protein binds with an analyte. Due to most interactions with proteins being weak intermolecular interactions, with the exception of disulfide covalent bonds formed between two different cysteine residues, the binding affinities of proteins with any analyte can be quite low.

In some cases, strong binding between protein and analyte is of great importance, as a result binding sites are often created to fit complementary to one another. This is commonly described as the lock and key model of binding; however, we now lean towards the induced fit model, or flexible docking theory. This theory suggests that a protein binding site will alter slightly around an analyte, however it must fit the general shape of the original target analyte.[47] We see examples of flexible docking frequently in everyday life, for example, the contraceptive pill contains a compound known as desogestrel to mimic that of the natural human hormone progesterone (Figure 1.9).[48] It does this with high efficiency due to the similarity between the two structures.

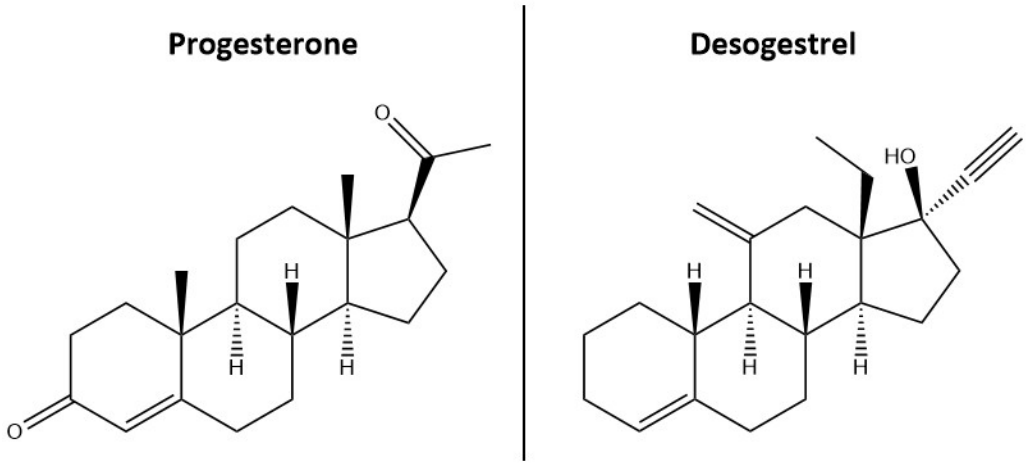

Figure 1.9: *An image depicting the structure of progesterone compared to that of desogestrel.*

This highly selective binding is important, and an example of binding sites being specially designed in nature is seen with antibodies. Antibodies are a protein created within the body; they are designed to bind perfectly with a single antigen which the body is exposed to. This specific design allows for the antibody to have a high affinity for selectively binding with the desired antigen, with minimal instances of unwanted binding.[49] It is based on this information, that for the detection of proteins within a test sample, complementary antibodies are an ideal detection element.

1.3 Determining the Composition of Bodily Fluids

Proteins made by the human body are secreted in various bodily fluids, such as bile, saliva and most commonly blood.[17] Due to this, samples of these fluids are often submitted for testing, to measure the protein levels as indicators for a variety of medical conditions.[17] Before tests can be designed and implemented, the average levels of proteins in various fluids needs to be determined, followed by how these levels are affected by a variety of events such as illnesses or physical trauma. Therefore, the composition of bodily fluids had to be determined. This is achieved by extracting proteins from the sample media, then separating the various proteins prior to identification.[50]

1.3.1 Sample Separation

Separation of proteins is required before identification can occur. Proteins can be separated based on a number of characteristics, such as size, charge and polarity.[51] There are a plethora of methods to achieve this, many of which are based on the technique known as gel electrophoresis, of which there are multiple types.

One method of gel electrophoresis is sodium dodecyl sulphate polyacrylamide gel electrophoresis (SDS-PAGE). In this method, cell membranes are dissolved in SDS detergent, this denatures and solubilises cell proteins while giving them an overall negative charge. The proteins are then loaded onto a polyacrylamide (PAAm) gel, while a direct current field is applied; the negatively charged proteins move towards the positive anode, and the distance travelled is based on the mass to charge ratio of the protein. This results in the formation of protein bands along the gel, each correlating to different molecular weights.[17]

Another commonly used electrophoretic method is two-dimensional polyacrylamide gel electrophoresis (2D-PAGE). Initially, proteins are loaded onto a PAAm gel with a pH gradient then a voltage is applied. The proteins migrate until the surrounding pH is equal to the proteins isoelectric point, this is known as isoelectric focusing (IEF). The gel is then softened in a denaturing solution and a detergent, causing the proteins to unfold and bind with a negative charge respectively. An electric current is applied perpendicular to the previous, causing the proteins to again migrate. The smaller the mass the further the protein travels (Figure 1.10). These gels are then stained to allow for protein visualisation.[17]

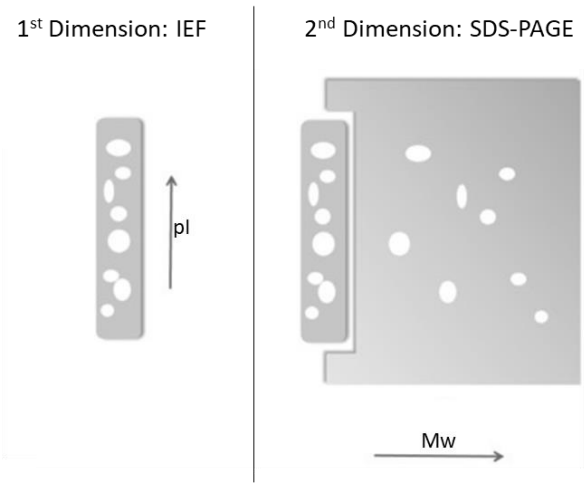

Figure 1.10*: An image depicting 2D-PAGE. First, IEF separates the proteins based on their isoelectric points. Following this, the first gel is added to the second, and separated in terms of relative size, with the smaller proteins travelling further. Image adapted from Lee et al.*[52]

Electrophoresis is not the only separation method for proteins; chromatographic techniques are also frequently used for the separation of water soluble compounds such as proteins.[51]

Hydrophobic interaction chromatography (HIC) is one chromatographic method commonly used for the purification of proteins; separation is caused by variations in polarity of proteins and their hydrophobic interactions. Samples are applied to a HIC column in a high

concentration salt buffer. Following this, the solvent system has a decreasing salt gradient; this causes samples to elute in order of increasing hydrophobicity, meaning the most hydrophilic proteins are the first to elute (Figure 1.11).[51,53]-

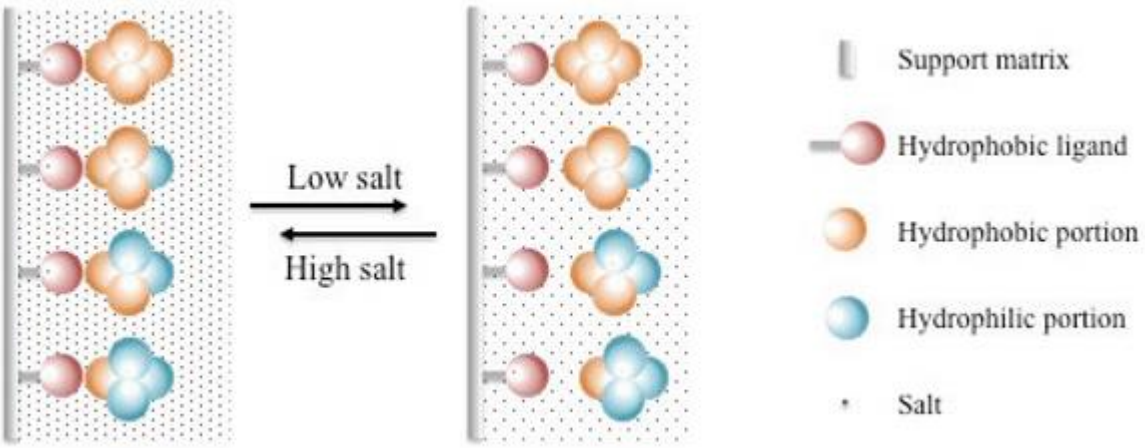

Figure 1.11: *An image depicting the principles of HIC. In a high salt buffer, all compounds bind to the hydrophobic functionalised column. As the salt content decreases, the more polar compounds are solvated and elute. Image adapted from American Pharmaceutical Review.*[54]

A simple method to separate proteins is through the use of size exclusion chromatography (SEC). This method involves the introduction of the sample to a SEC column, which is comprised of a gel containing spherical beads. The beads alter the path which proteins can take through the column; small proteins enter many pores, increasing time taken to elute, whereas large proteins take a more direct route through the column causing them to elute first (Figure 1.12).[51,53]

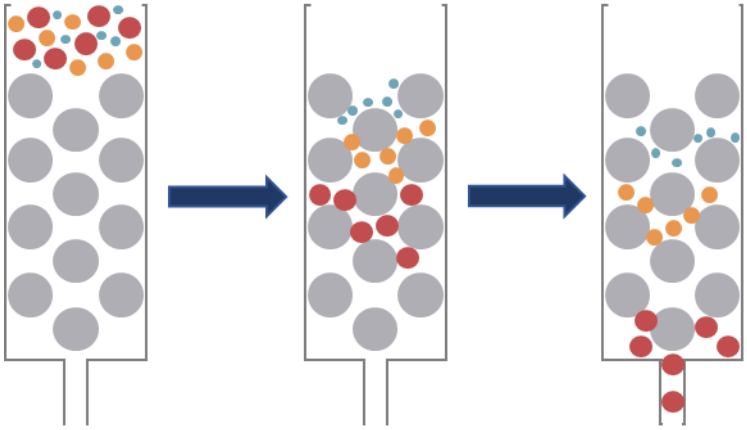

Figure 1.12: *An image depicting the principles of SEC. Larger compounds travel faster through the bead filled column as they cannot fit into channels between beads, causing them to elute faster. Image adapted from Majeed et al.*[55]

All of these methods separate the various proteins present in a sample, however at this point, the identity of the proteins themselves remain a mystery, all that is known is that there are a known number of compounds found within the sample.

1.3.2 Protein Identification

Following the separation of fluid mixtures, the components must then be analysed to determine the identity of the constituents. Without this, the separation of fluids is redundant as the only information gathered up until this point is merely knowing how many constituents there are in a fluid and their relative sizes. This is the step where we learn what biomarkers are present in a mixture. While there are numerous methods, the most common of these are detailed below.

One common method of protein identification is through the use of a technique commonly used throughout chemistry, mass spectrometry (MS). MS is a technique that determines molecular mass through the ionisation of compounds and observing how they

fragment, these fragments can be used to aid in the determination of structure. Matrix-assisted laser desorption/ionisation (MALDI) is the most commonly used ionisation technique for the MS of proteins; the ionisation process begins with the drying of a small volume of a protein sample combined with a light absorbing matrix molecule on a target plate. Pulses of laser light vaporise the sample mixture, releasing ionised proteins. An electric field is used to increase the velocity of the sample, the increase in velocity is inversely related to the protein mass to charge ratio. Due to this, the smaller proteins are often the first to reach the detector. This technique is often combined with time-of-flight (TOF) MS, which calculates the mass of ions based on the time taken for detection.[17,56] As the fragmentation pattern for each protein is unique, this is then compared to a database of known patterns and the proteins they stem from to identify the mystery protein, and this process is known as peptide mass fingerprinting (Figure 1.13).

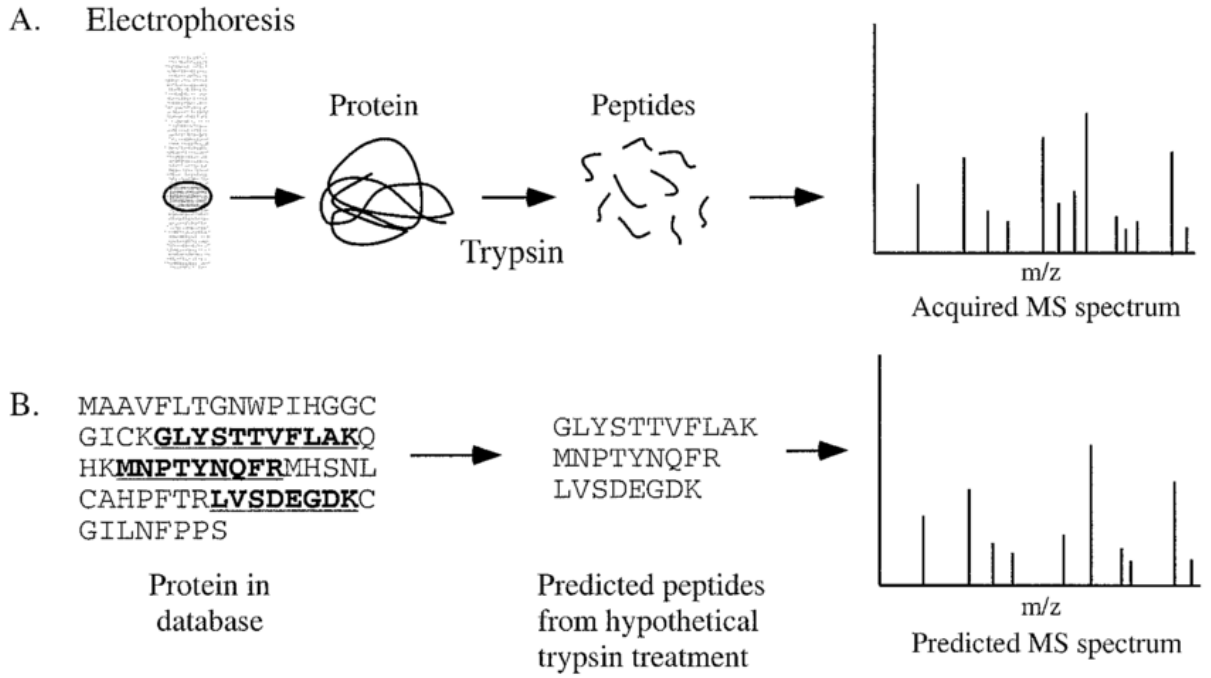

Figure 1.13: *An image depicting the process of PMF. A). Protein is collected following PAGE, treated with trypsin to split into smaller sequences and analysed by mass spectrometry. B). Database is used to find proteins which give matching predicted MS spectrum. Image adapted from Graves et al.*[57]

If the purpose of identifying proteins is to determine the presence of a particular protein, then the technique most frequently used is Western Blot. This technique is used for the identification of proteins which have been previously separated by PAGE and involves transferring the proteins from the PAGE to a nitrocellulose surface and blocking any remaining non-specific reactive binding sites with protein solutions such as bovine serum albumin (BSA). An antibody, specific to the target antigen, is linked with a reporter enzyme; when this is exposed to the substrate, an antigen-antibody complex forms. Following this binding, the reporter enzyme undergoes a colour change which is visible to the human eye (Figure 1.14). This is a qualitative identification method.[17]

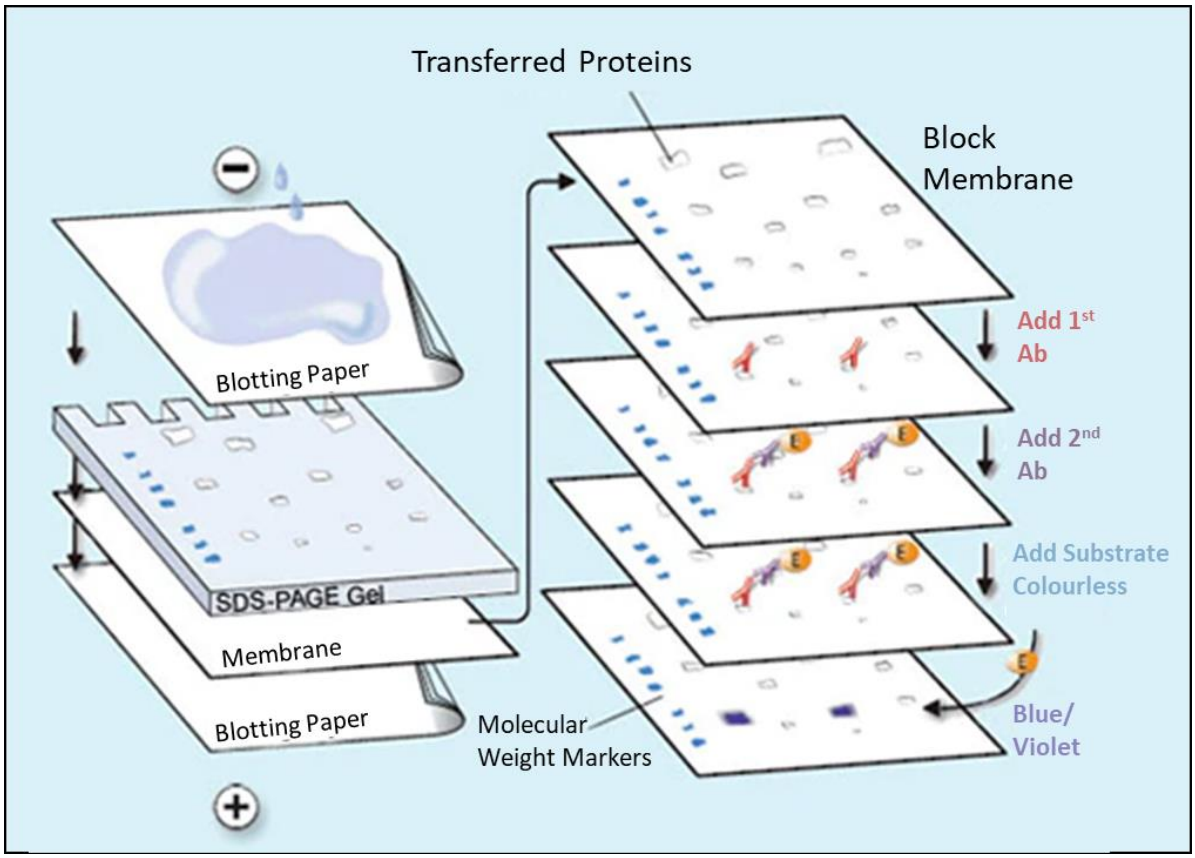

Figure 1.14: *An image depicting the steps of western blotting following SDS-PAGE including the transference of the proteins on a membrane, followed by the tagging of proteins with antibodies and colorimetric detecting groups. Image adapted from Merck Millipore.*[58]

1.3.3 Testing of Wound Exudates

Based on the secretion of proteins into bodily fluids, it was theorised that the wound fluid composition also contains proteins, which could accurately reflect what is happening in the wound environment.[59] Wound exudates would be the ideal sample medium as they can be collected non-invasively, therefore causing minimal discomfort to the patient.[5,12] Conversely, wound fluids could simply contain nutrients required for wound healing, the removal of which may be detrimental to wound health.[12] Due to the lack of knowledge surrounding wound fluid exudates, studies were conducted into the composition of wound fluids, *via* methods which have been previously described.[17]

Studies conducted determined that wound fluid exudates are often comprised of the same proteins, sugars and electrolytes that are found in serum, however in different ratios.[60] As was previously discussed in Chapter 1.1.1, a large number of proteins are important for wound healing such as interleukin-1 (IL-1), epidermal growth factor (EGF), vascular endothelial growth factor (VEGF) and tumour necrosis factor alpha (TNF-α).[61] Not only can these proteins be found in serum for wound patients, but they can also be found in collected wound fluids.[62] The current working theory regarding the cause of chronic non-healing wounds is the presence of a prolonged inflammatory phase. It therefore comes as no surprise that in chronic wounds those proteins which are expressed throughout the inflammatory phase of healing, such as IL-1 and TNF-α, are expressed in higher concentrations in chronic wounds when compared to their acute counterparts.[61] Conversely to this, those proteins which are expressed in the latter stages of wound healing, proliferation and maturation/remodelling such as EGF and VEGF are found to be in lower levels in chronic wound fluids than in acute wounds.[61]

Factors related to the phases of wound healing are not the only potential biomarkers however, the natural immune response also provides analytes which can be detected.

C-reactive protein (CRP) is a protein comprised of five subunits synthesised by liver cells during an immune response to inflammation, and are present in high concentrations not only in serum, but also in chronic wound exudates.[62,63] While CRP is also expressed in acute wounds, after 7 days, levels of CRP had significantly decreased in those with acute wounds, unlike chronic wounds; due to this disparity in CRP levels with time it is a sensitive and reliable biomarker with regards to detecting non-healing wounds.[64,65]

Another class of proteins elicited by the immune system in response to a wound are immunoglobulins such as immunoglobulin G (IgG).[66] IgG is an antibody, produced by the immune response to bind to cell surface proteins, tag foreign bodies and encourage phagocytosis.[67] IgG is found to be present in wound fluid exudates, likely as a result of the human immune response.[68]

These studies show that there are numerous potential biomarkers to be found within wound fluids which can be used to study the healing process of wounds. Some of these factors are released as a direct response to the state of the wound, while others are a secondary response to the non-healing wound. Through the immobilisation of these biomarkers with compounds with which they form strong analyte-substrate complexes, such as protein-A and IgG, these analytes can be used as the basis of biosensors for chronic wounds.[69] Following detection of these biomarkers, the concentration of their presence within the chosen sample media can be detected; the current concentration can then be compared against the concentration expected in a healthy sample, examples of which are listed below in ***Table 1.3***.

Table 1.3: *A table displaying the average concentrations of biomarkers of interest present in wound fluids, measured in either units per millilitre (U mL^{-1}) or nanograms per millilitre (ng mL^{-1}) and how these levels may change to indicate a non-healing chronic wound.*[65,70,71]

Biomarker	Average Healthy Concentration	Impact of Non-Healing on Concentration
IL-1	2700 U mL^{-1}	Expressed in increased concentrations.
EGF	20 U mL^{-1}	Expressed in lower concentrations.
VEGF	1.8 ± 1.2 ng mL^{-1}	Expressed in lower concentrations.
TNF-α	1639 U mL^{-1}	Expressed in increased concentrations.
CRP	0.1 – 3.0 ng mL^{-1}	Expressed for prolonged period of time.

1.4 Modern Biosensors

A biosensor is defined as an analytical device, measuring physico-chemical changes observed by a transducer, caused by interactions between a target analyte and a biological detection element, the main aspects of which are displayed in Figure 1.15.[72,73] Target analytes can be a variety of compounds, ranging from simple compounds like sugars, protons and salts to more complex structures such as proteins and DNA.[74]

There are many ways to classify biosensors, most commonly they are classified based on transducer type, such as optical and electrochemical.[75] Electrochemical biosensors convert the binding interactions of analyte and detection element into a readable, electrical signal whereas optical biosensors provide data based on the interactions of the sample with light.[76,77]

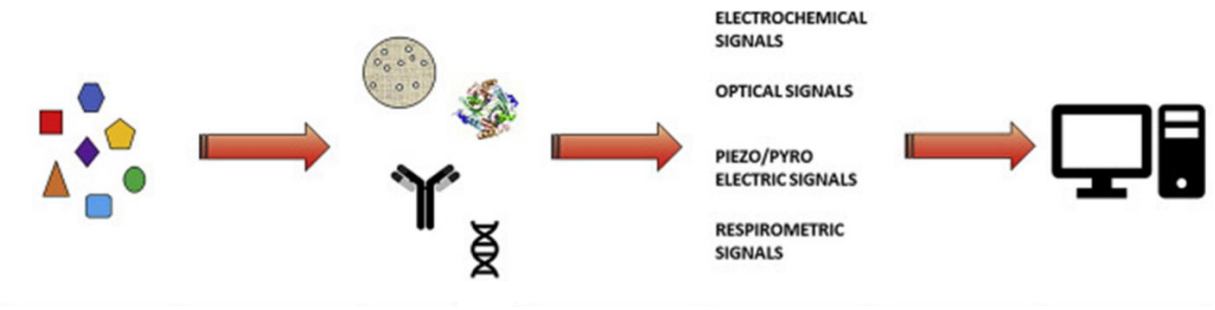

Figure 1.15: *A figure showing the composition of biosensors. This shows the sample analyte, which has a reaction with the biorecognition element. This reaction is detected by the transducer and converted into a readable output. Image adapted from Parkhey et al.*[78]

1.4.1 Laboratory-Based Biosensors

Optical biosensors can be classified as either label-based or label-free assays.[79] Label-based biosensors require the tagging of target analytes with detectable additives such as enzymes, dyes or radioactive isotopes. One such label-based optical biosensor is the Enzyme-Linked Immunosorbent Assay (ELISA) as it is a colorimetric biosensor (Figure 1.16).[80] This

method is based on antigen-antibody complex formation, and thus is a detection technique for proteins based on their selective, high binding affinities. A solid substrate is functionalised with antibodies, or antigens depending on the target of choice, to create immobilisation sites, the substrate is then washed before any remaining non-specific binding sites are blocked with small, neutral proteins. The target sample in solution is then added and binds selectively to the immobilisation sites. Enzyme tagged antibodies are then added to the assay, either complementary to the target antigen, or secondary antibodies which selectively bind to the target antibody, depending on the assay. After a wash, a substrate is then added, which when in contact with the enzyme undergoes a colour change, thus indicating the presence of the target analyte.[81]

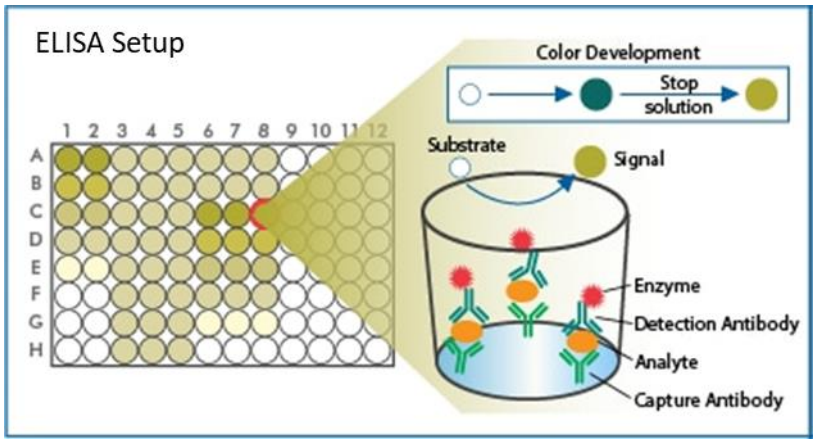

Figure 1.16: *An image depicting the setup of an ELISA, showing how detection occurs. Image adapted from Novusbio.*[82]

Label-free biosensors, as the name suggests, do not require the tagging of analytes with a label to allow for detection, an example of which is surface plasmon resonance (SPR), a frequently used optical biosensor which provides information in real-time.[83] The sensor is comprised of a light source, a prism, a sensor chip and a photodetector. The sensor chip is often coated in a metal film, usually a thin layer of gold, and the interactions between the

sample and electrons in the metallic surface form the signal, and this sensor chip is topped with a flow cell.[83]

For sensing, the light source is coupled into the sensor chip through use of the prism; light is then reflected by the sensor chip into the photodetector.[84] A sample solution is introduced to the sensing chip through the flow cell; when light is coupled into the sensing chip at the resonance angle, a small amount of the reflected light leaks. This light creates an evanescent field of energy, electrons in the metallic films absorb this energy, causing them to vibrate or resonate.[85] The detector registers reflected light and displays this evanescent energy as a dip in the SPR reflection intensity spectrum at the resonance angle.[86]

Biorecognition elements are immobilised to the metal surface; as the complementary target analyte in the sample binds, this alters the refractive index at the surface. The change in refractive index is caused by a build-up in concentration of target analyte due to the directly proportional relationship between the two.[87] As described in Snell's Law (Equation 1.1), this change in refractive index alters the resonance angle at the metal film – sample interface, thus, as the angle of incidence remains constant, altering the angle of refraction. This shows as a measurable signal by displaying movement in the dip in reflectivity detected (Figure 1.17).[86]

$$\frac{sin\theta_1}{sin\theta_2} = \frac{n_2}{n_1}$$

Equation 1.1: *Snell's Law of Refraction, where ϑ1 is the angle of incidence, n1 is the refractive index of one material, ϑ2 is the angle of refraction and n2 is the refractive index of the secondary material.*

As biorecognition elements can be varied, this technique can be modified to detect a range of analytes, with proteins, sugars and DNA being just a few of those reported in literature, making this a versatile technique.[85]

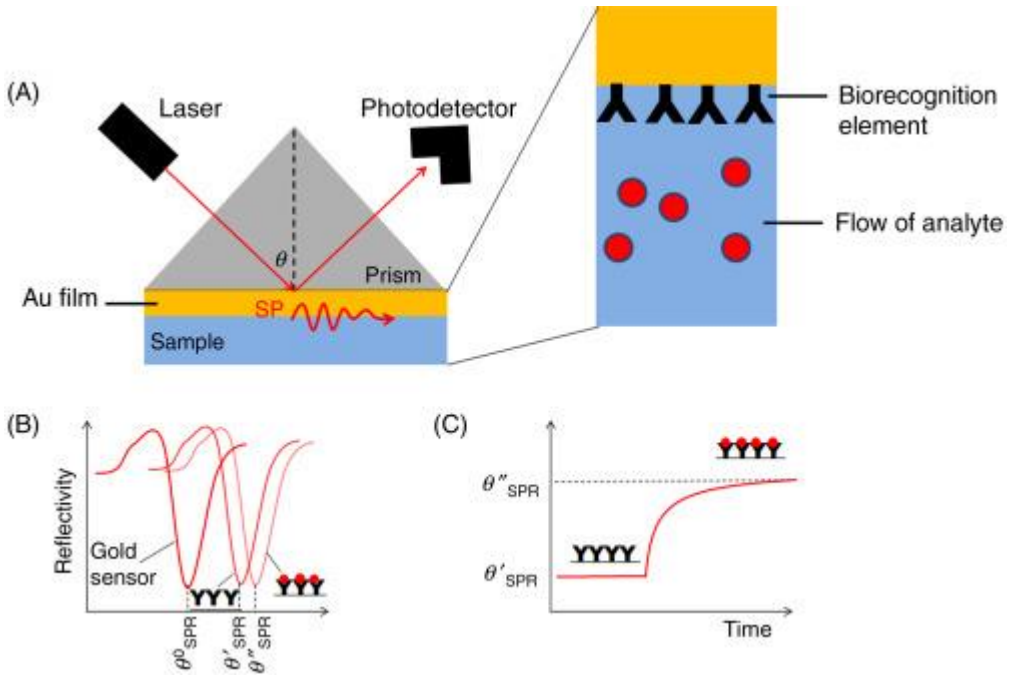

Figure 1.17: *A diagram showing the setup of an SPR biosensor. Light is coupled into a biorecognition element-functionalised gold film sensor chip through the use of a glass prism. Light is reflected into a detector, with the exception of light at the resonance angle which leaves a dip in reflectivity. As the sample is introduced to the biorecognition elements via a flow cell, binding occurs, permanently altering the resonance angle. Image adapted from Miyazaki et al.*[88]

The polymerase chain reaction (PCR) is described as being the "gold standard" for detection, being implemented in laboratories spanning the globe.[89] PCR is a technique for the amplification of DNA sequences; therefore the analytes it can detect are limited to DNA and in special circumstances, ribonucleic acid (RNA).[90] This is a highly sensitive method as amplification only occurs if the DNA strand is complementary to the biorecognition element, which in this case is a short single strand of DNA known as a primer.[91] Double stranded DNA is heated to separate into two separate single strands, which when cooled bind to the primers.

Enzymes such as DNA polymerase then extend these primers to match the complementary strand, resulting in amplification, which occurs at an exponential rate (Figure 1.18).[92]

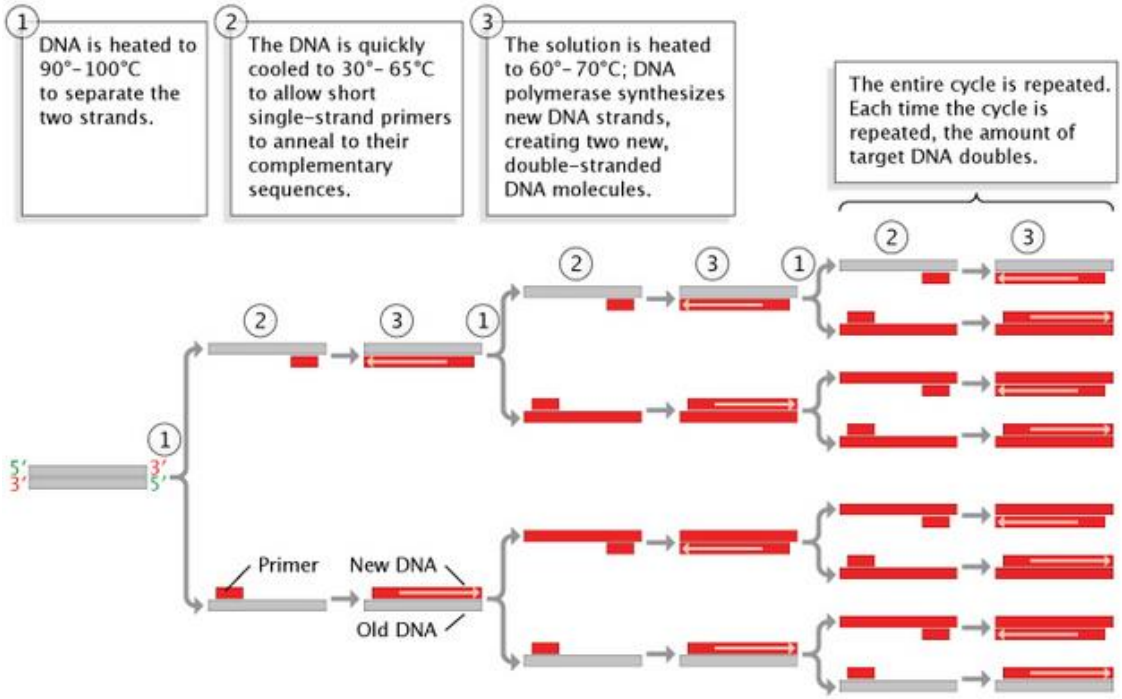

Figure 1.18: *A diagram to show the steps of PCR. In steps labelled 1. DNA is heated to split the double helix into two single strands. Steps labelled 2. DNA is rapidly cooled, short single strand primers bind to complementary nucleotide bases. In steps labelled 3, the solution is heated to the optimal temperature for DNA polymerase, which extends the primers and synthesises new double stranded DNA sequences. On the formation of double stranded DNA, the process repeats itself. Image adapted from Nature.*[93]

These are the fundamental steps in all PCR detection methods. The method of detection is however rather versatile. In many instances, a dye is incorporated into the PCR mixture; this dye provides a fluorescent signal when it intercalates with double stranded DNA, thus providing a visible signal.[94] Other methods involve the incorporation of PCR with another technique. PCR increases the concentration of sample, and this is then detected through a secondary technique, such as gel electrophoresis.[95]

While these techniques are highly sensitive and have been refined to give reliable results in clinical settings, the use and correct reading of results required trained professionals.

Not only that, but the procedures themselves can be quite time consuming, and in some cases energy intensive and expensive. In areas in which detection techniques are most important, for example third world countries where lack of access to hygienic products can cause infections to spread rapidly, these techniques are just not feasible. They have neither the personnel nor the infrastructure to monitor biomarkers *via* laboratory-based biosensors. It is due to this, that a new field of study within biomarkers is rapidly gaining traction.

1.4.2 Point of Care Testing

Point of care (POC) testing is a field of study based on the formation of biosensors which can be used instantly with minimal sample preparation and give rapid results on the detection of a particular biomarker. In some instances POC testing equipment is designed to be used by healthcare professionals with no training regarding that particular equipment, but, the more desirable situation results in devices which can be used by any person. Some characteristics required for the classification as POC tests include being small in stature, easy to move, using small sample sizes and having low production costs.[96]

Single use handheld devices can provide results within minutes while using a reasonable sample volume, a commonly used example of this is a pregnancy test. The lateral flow immunoassay is the basis of a pregnancy test and works in a similar way to ELISA biosensors.[97] Lateral flow immunoassays are label-based bioassays, most commonly relying on coloured or fluorescent labels, or enzymatic labels which cause a colour change to allow for ease of use in real world scenarios.[98] This is due to colour-based detection being simple to read without the use of external detectors.[99] A POC pregnancy test (Figure 1.19) is comprised of a test line and a control line.[100] A sample, in this case urine, containing the

target analyte human chorionic gonadotropin (hCG), is supplied. Capillary flow action then pulls the sample to a conjugation pad containing label-tagged hCG antibodies.[101] Once the analyte reaches the test line, antibodies specific to hCG immobilise the target, resulting in hCG-antibody conjugates. Meanwhile, free label-tagged hCG antibodies continue to be pulled by capillary action to the control line, where different antibodies such as anti-IgG then immobilise these compounds. If the test is negative, no hCG is present, thus no binding occurs at the test line, only the control line. This test relies on the selective antigen-antibody binding affinities discussed earlier (Chapter 1.2.2). The results of this test are binary, colour or no colour, yes or no, this makes lateral flow immunoassays a qualitative biosensor; while they can inform us of the presence of a target analyte, they cannot provide information as to the levels in which it is present.

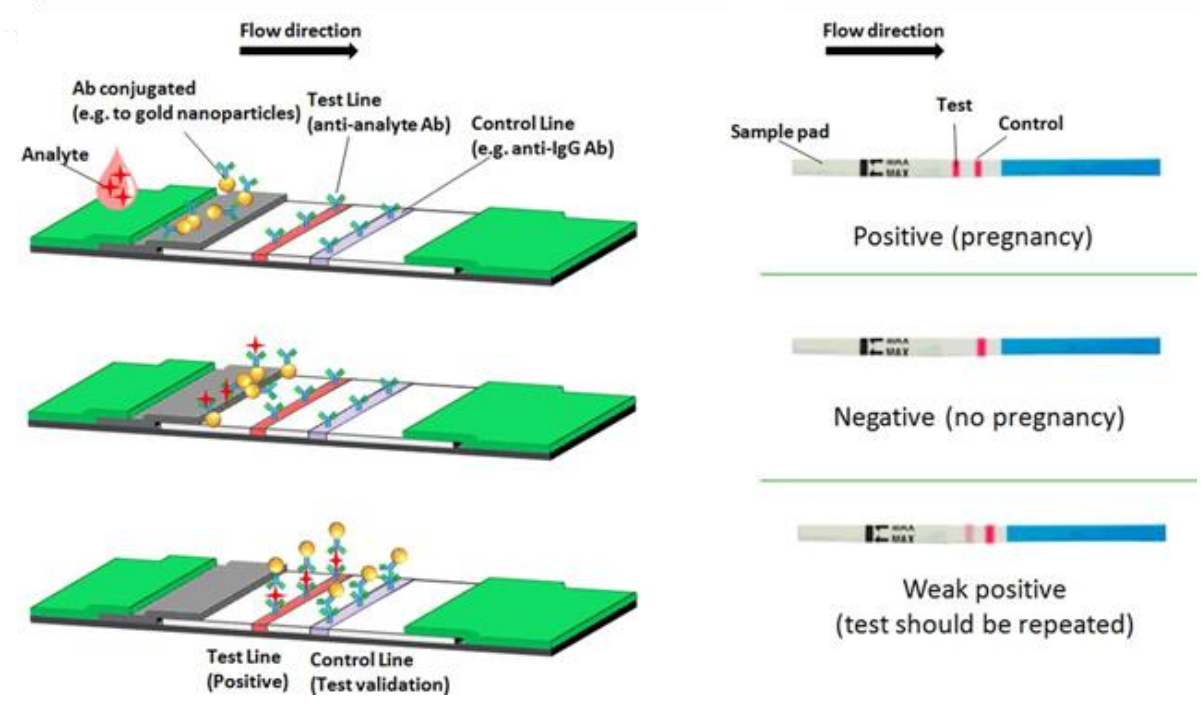

Figure 1.19: *A diagram to show how the lateral flow immunoassay in a pregnancy test works. The target analyte binds to tagged antibodies. These then flow through the assay via capillary action, the tagged analyte-antibody conjugates are then captured by bound antibodies at the test site. Tagged antibodies which do not conjugate to the analyte are then captured at the control site. Image adapted from Koczula et al.*[100]

While lateral flow immunoassays such as pregnancy tests are useful, and very effective, they are single use and result in high levels of waste. To keep POC tests simple to use, single use is an advantage as they can be disposed of easily, but this is neither cost effective nor environmentally friendly in the long run. A way to make single use biosensors more cost effective, is to have a dual purpose to them. Research has been conducted into the development of biosensors incorporated into wound dressings (Figure 1.20). Many of these bifunctional wound dressings have been based on electrochemical transducers. Electrochemical biosensors work by converting the binding interaction between an analyte and biorecognition element into an electronic signal.[102] As pH level is a good indicator of wound environment, many biosensor wound dressings (smart bandages) have been designed for the detection of pH, a simple biomarker for electrochemical detection.[103,104] Some smart bandages have also been designed with more complex, clinically relevant analytes however, such as TNF-α.[105] In this instance, electrodes were activated with either TNF-α antibody, or streptavidin. When TNF-α bound to the electrodes, a change in signal proportional to concentration of analyte was observed.[105]

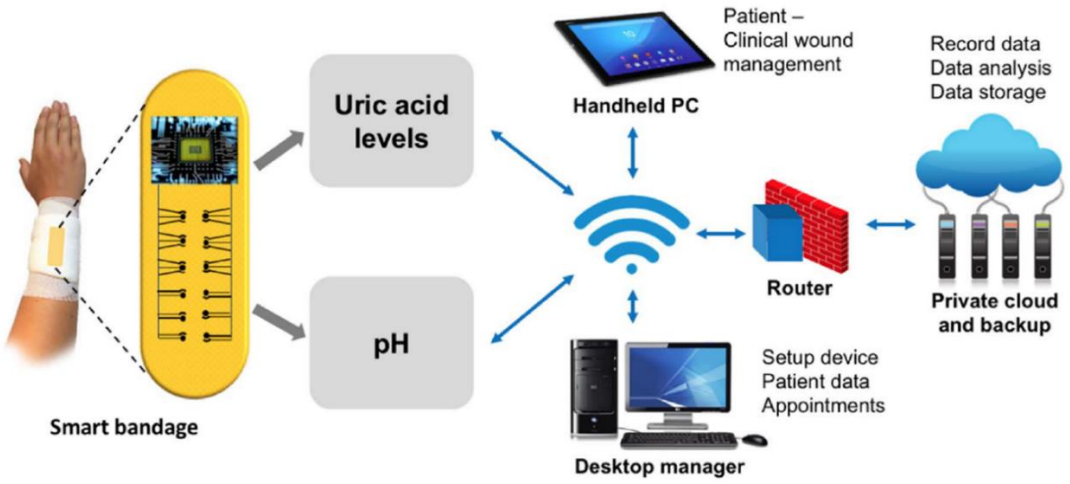

Figure 1.20: *A diagram showing a potential smart bandage, including methods of obtaining the data collected for analysis. Image adapted from RoyChoudhury et al.*[104]

POC tests allow for the continuous monitoring of wounds in any setting, unlike laboratory-based testing methods which require samples to be taken and tested by trained professionals. While lateral flow tests are useful, they simply indicate the presence of an analyte; as the target analytes for wounds are present still in low concentrations in acute wounds, lateral flow immunoassays would not be as effective in the monitoring of chronic wound formation as a quantitative analytical technique such as electrochemical sensing. Electrochemical biosensors incorporated into wound dressings address numerous issues:

- Sample collection: As the sample is applied directly from the wound to the sensor.
- Wastefulness: Dressings would be required nevertheless, by combining them with a sensor the level of waste is decreased.
- Quantitative detection: Electrochemical biosensors can accurately determine analyte concentration.

Based on all of this information, electrochemical smart bandages are the ideal solution, right? Well, in short, no. Electrochemical sensors require metal electrodes, making them an expensive addition to mass produced bandages, not only this, but computers are required for the analysis of the potentiometric data received. This, as with laboratory-based biosensors, requires the use of trained personnel. Research into the monitoring of wound fluid exudates is headed in the right direction, however, there is still much to be done to create a smart bandage which fits all the criteria for POC testing.

1.5 Summary

The diagnosis of chronic wounds as it is, is not an ideal system. It is a very subjective diagnosis, relying on the memory of possibly mentally impaired patients, and only occurs following weeks of pain and discomfort. Advances into protein detection are occurring more rapidly for use in the diagnosis of illnesses and diseases. Due to it having been determined that a number of proteins are expressed in varying levels when a wound is non-healing, these proteins can potentially act as biomarkers for monitoring the recovery of a wound and thus pinpoint when a prolonged state of inflammation begins. This would then increase the reliability of chronic wound diagnosis and, in theory decrease the time taken to achieve a diagnosis. Improving not only patient wellbeing but also the economic burden on various health services. Sample collection is not a hinderance in this scenario as following the diagnosis of non-healing wounds, it is common practice to obtain a wound fluid sample for a bacterial culture growth to determine if a bacterial infection may be at fault. All that would be required is that fluid samples are collected earlier, at regular intervals rather than weeks after the fact.

To combat these problems in diagnostics, it would be conducive to chronic wound diagnosis if inflammatory markers in wounds fluids could be continuously monitored. Many biosensing techniques have already been well established and implemented in other aspects of the health care system, however while they are all excellent techniques, as has been discussed, none of these are yet perfect. The advantages and disadvantages of these various techniques have been summarised below in ***Table 1.4***.

Table 1.4: *A table summarising the advantages and disadvantages of the biosensing techniques discussed throughout this chapter.*

Biosensor Type	Advantages	Disadvantages
ELISA	Simple colorimetric readout. High specificity and sensitivity. Possibility for multiplexing.	High possibility for false results. Storage is temperature sensitive. Costly to make.
SPR	Real-time, label-free analytical method. Small sample volumes. Possible to reuse chips.	Requires large instrument to read results. Costly to make. Use of non-renewable materials.
PCR	High specificity and sensitivity. Small sample volumes. Well implemented worldwide.	Costly reagents. Time and energy intensive. Requires highly trained staff.
Lateral flow device	Simple colorimetric readout. Inexpensive to produce. Long shelf life.	Single use devices. Qualitative detection. Limited in sample source.
Electrochemical diagnostics	High sensitivity. Small sample volumes. Biocompatible.	Sensitive to spoiling. Complex data analysis. Single use.

Wound dressings have been designed for the monitoring of wound exudate composition, however they are based on electrochemical biosensors. It is due to this that further research, into more sustainable materials and detection methods, and their suitability for their incorporation into wound dressings is imperative, such as looking into cheaper materials such as hydrogel wound dressings.

1.6 Aims

It is based on all of the information presented, that this thesis aims to contribute to the world of diagnostics for wounds. The initial way of doing this, is to take a currently developed biosensing technique, leaky waveguides (LWs), and miniaturising the equipment required for LW testing to a more portable size. This work will then display that the smaller instrument is equivalent to the currently established large benchtop instruments, while being just a fraction of the size and weight, and is simple to use in a clinical setting and store when not in use. This will improve diagnostics by making LWs a more POC friendly technique. Following from this, the project also aims to combine diagnostics with treatment to simplify chronic wound care. To do this, hydrogels which are suitable for wound dressings, but also capable to act as biosensors will be developed. These hydrogels will utilise photochemistry to incorporate sensing and non-sensing areas to allow the developed technique to be internally referenced. The biosensing will be dependent on antibody–antigen binding. Prior to development into wound dressings, the biosensing capability of the hydrogels must be determined first. Due to this, as a proof of concept, this work develops them into leaky waveguides, as they are a simple method of determining whether analyte immobilisation is occurring, resulting in the formation of biosensors, which have the possibility to be developed further to become more POC friendly.

1.7 Thesis Outline

This thesis is ordered in a way to discuss two projects carried out throughout the duration of this research, both of which are based on the development of waveguide biosensors for proteins. One project has been split into two sections discussing the synthesis and the biosensing respectively.

Chapter 2 is a discussion into the formation of a chitosan-based LW device for biosensing. Following that, this chapter will delve into the testing of a miniaturised structure capable of testing waveguide devices, comparing its sensitivity to that of a traditional benchtop laboratory-based instrument.

Chapter 3 discusses the protection of polymers with photocleavable protecting groups (PPGs). Alongside this, this chapter will then investigate the development of monomers protected with PPGs.

Chapter 4 explores the formation of photocaged hydrogels and the resultant photodeprotection of protecting groups. Following this, the ability for hydrogels formed from photo-protected monomers to detection of proteins as LW devices and their ability to internally reference is discussed.

Chapter 5 concludes the projects discussed within this thesis and discusses the future possibilities which stem from the work presented within this thesis.

Chapter 6 contains the details of the techniques, methods, instrumentation and chemicals used throughout the duration of this project.

Chapter 7 is the appendix and provides the complete versions of partial data which is included throughout the thesis.

1.8 References

1 wound1_1 noun - Definition, pictures, pronunciation and usage notes | Oxford Advanced Learner's Dictionary at OxfordLearnersDictionaries.com, https://www.oxfordlearnersdictionaries.com/definition/english/wound1_1?q=wound, (accessed 22 August 2022).
2 J. F. Guest, N. Ayoub, T. McIlwraith, I. Uchegbu, A. Gerrish, D. Weidlich, K. Vowden and P. Vowden, *Int. Wound J.*, 2017, **14**, 322–330.
3 A. R. Siddiqui and J. M. Bernstein, *Clin. Dermatol.*, 2010, **28**, 519–526.
4 A. M. Pinto, M. A. Cerqueira, M. Bañobre-Lópes, L. M. Pastrana and S. Sillankorva, *Viruses*, 2020, **12**, 235.
5 D. R. Yager, R. A. Kulina and L. A. Gilman, *Int. J. Low. Extrem. Wounds*, 2007, **6**, 262–272.
6 L. M. Morton and T. J. Phillips, *J. Am. Acad. Dermatol.*, 2016, **74**, 589–605.
7 A. Kawasumi, N. Sagawa, S. Hayashi, H. Yokoyama and K. Tamura, in *New Perspectives in Regeneration*, eds. E. Heber-Katz and D. L. Stocum, Springer Berlin Heidelberg, Berlin, Heidelberg, 2012, vol. 367, pp. 33–49.
8 S. Rajendran and S. C. Anand, in *Woven Textiles*, Elsevier, 2012, pp. 414–441.
9 S. J. Landis, *Adv. Skin Wound Care*, 2008, **21**, 531–540.
10 R. Edwards and K. G. Harding, 2004, **17**, 91–96.
11 N. Farhan and S. Jeffery, *Diagnostics*, 2021, **11**, 268.
12 M. W. Löffler, H. Schuster, S. Bühler and S. Beckert, *Int. J. Low. Extrem. Wounds*, 2013, **12**, 113–129.
13 S. E. Gardner, R. A. Frantz and B. N. Doebbeling, *Wound Repair Regen.*, 2001, **9**, 178–186.
14 *What is an inflammation?*, Institute for Quality and Efficiency in Health Care (IQWiG), 2018.
15 T. E. Serena, J. R. Hanft and R. Snyder, *Int. J. Low. Extrem. Wounds*, 2008, **7**, 32–35.
16 S. Li, P. Renick, J. Senkowsky, A. Nair and L. Tang, *Adv. Wound Care*, 2021, **10**, 317–327.
17 L. E. Edsberg, in *Bioengineering Research of Chronic Wounds*, ed. A. Gefen, Springer Berlin Heidelberg, Berlin, Heidelberg, 2009, vol. 1, pp. 343–362.
18 G. Tronci, in *Advanced Textiles for Wound Care*, Elsevier, 2019, pp. 363–389.
19 C. Ruiz-Cañada, Á. Bernabé-García, S. Liarte, M. Rodríguez-Valiente and F. J. Nicolás, *Front. Bioeng. Biotechnol.*, 2021, **9**, 689328.
20 A. Rastogi, G. Goyal, R. Kesavan, A. Bal, H. Kumar, Mangalanadanam, P. Kamath, E. B. Jude, D. G. Armstrong and A. Bhansali, *Diabetes Res. Clin. Pract.*, 2020, **162**, 108113.
21 C.-W. Lung, F.-L. Wu, F. Liao, F. Pu, Y. Fan and Y.-K. Jan, *J. Tissue Viability*, 2020, **29**, 61–68.
22 T. S. Stashak, E. Farstvedt and A. Othic, *Clin. Tech. Equine Pract.*, 2004, **3**, 148–163.
23 K. C. Broussard and J. G. Powers, *Am. J. Clin. Dermatol.*, 2013, **14**, 449–459.
24 K. Vowden and P. Vowden, *Surg. Oxf.*, 2017, **35**, 489–494.
25 B. Dalisson and J. Barralet, *Adv. Healthc. Mater.*, 2019, **8**, 1900764.
26 G. Han and R. Ceilley, *Adv. Ther.*, 2017, **34**, 599–610.
27 G. R. Mahdavinia, S. B. Mousavi, F. Karimi, G. B. Marandi, H. Garabaghi and S. Shahabvand, *Express Polym. Lett.*, 2009, **3**, 279–285.
28 T. R. Hoare and D. S. Kohane, *Polymer*, 2008, **49**, 1993–2007.
29 E. A. Kuru, N. Orakdogen and O. Okay, *Eur. Polym. J.*, 2007, **43**, 2913–2921.
30 K. Koumpouras and J. A. Larsson, *J. Phys. Condens. Matter*, 2020, **32**, 315502.
31 W. E. Hennink and C. F. van Nostrum, *Adv. Drug Deliv. Rev.*, 2012, **64**, 223–236.
32 N.-T. N. I. for H. and C. Excellence, BNF, https://bnf.nice.org.uk/wound-management/hydrogel-dressings.html, (accessed 11 May 2022).
33 S. Tavakoli and A. S. Klar, *Biomolecules*, 2020, **10**, E1169.
34 D. Elieh-Ali-Komi and M. R. Hamblin, *Int. J. Adv. Res.*, 2016, **4**, 411–427.

35 F. A. Vicente, M. Huš, B. Likozar and U. Novak, *ACS Sustain. Chem. Eng.*, 2021, **9**, 3874–3886.
36 H. Liu, C. Wang, C. Li, Y. Qin, Z. Wang, F. Yang, Z. Li and J. Wang, *RSC Adv.*, 2018, **8**, 7533–7549.
37 P. Feng, Y. Luo, C. Ke, H. Qiu, W. Wang, Y. Zhu, R. Hou, L. Xu and S. Wu, *Front. Bioeng. Biotechnol.*, 2021, **9**, 650598.
38 G. Walsh, *Proteins: biochemistry and biotechnology*, John Wiley & Sons Inc, Chichester, West Sussex, 2e edn., 2014.
39 P. K. Deb, O. H. A. Al-Attraqchi, J. Stanslas, A. Al-Aboudi, N. Al-Attraqchi and R. K. Tekade, in *Biomaterials and Bionanotechnology*, Elsevier, 2019, pp. 153–189.
40 B.-A. Sela, *Harefuah*, 2002, **141**, 631–635, 665.
41 Ribosomes, Transcription, Translation | Learn Science at Scitable, https://www.nature.com/scitable/topicpage/ribosomes-transcription-and-translation-14120660/, (accessed 10 May 2022).
42 Protein synthesis, https://www.biologyonline.com/dictionary/protein-synthesis, (accessed 10 May 2022).
43 M. Gromiha, *Protein bioinformatics: from sequence to function*, Elsevier, Amsterdam Boston Paris, 2010.
44 B. Alberts, *Molecular biology of the cell*, Garland Science, Taylor and Francis Group, New York, NY, Sixth edition., 2015.
45 R. J. Ouellette and J. D. Rawn, in *Principles of Organic Chemistry*, Elsevier, 2015, pp. 371–396.
46 S. Mandal and S. Bose, *ejpmr*, 2020, **7**, 648–656.
47 S. Singh, Q. Bani Baker and D. B. Singh, in *Bioinformatics*, Elsevier, 2022, pp. 291–304.
48 S. Mayor, *BMJ*, 2016, i4345.
49 Definition of antibody - NCI Dictionary of Cancer Terms - NCI, https://www.cancer.gov/publications/dictionaries/cancer-terms/def/antibody, (accessed 10 May 2022).
50 S. Liu, Z. Li, B. Yu, S. Wang, Y. Shen and H. Cong, *Adv. Colloid Interface Sci.*, 2020, **284**, 102254.
51 O. Coskun, *North. Clin. Istanb.*, , DOI:10.14744/nci.2016.32757.
52 P. Y. Lee, N. Saraygord-Afshari and T. Y. Low, *J. Chromatogr. A*, 2020, **1615**, 460763.
53 RP-HPLC, SEC, HIC and IEX Methods performed by BioPharmaSpec, https://biopharmaspec.com/protein-characterization-services/liquid-chromatography-hplc/, (accessed 13 May 2022).
54 Friday, July 31, and 2015, Hydrophobic Interaction Chromatography for Antibody Drug Conjugate Drug Distribution Analysis, http://www.americanpharmaceuticalreview.com/Featured-Articles/177927-Hydrophobic-Interaction-Chromatography-for-Antibody-Drug-Conjugate-Drug-Distribution-Analysis/, (accessed 20 May 2022).
55 S. A. Majeed, K. E. Sekhosana and A. Tuhl, *Arab. J. Chem.*, 2020, **13**, 8848–8887.
56 G. L. Hortin, *Clin. Chem.*, 2006, **52**, 1223–1237.
57 P. R. Graves and T. A. J. Haystead, *Microbiol. Mol. Biol. Rev.*, 2002, **66**, 39–63.
58 Western Blotting Protocols | Life Science Research | Merck, https://www.merckmillipore.com/GB/en/life-science-research/protein-detection-quantification/western-blotting/protocols/q9ib.qB.710AAAFBRP0RRkww,nav?ReferrerURL=https%3A%2F%2Fwww.google.com%2F, (accessed 18 May 2022).
59 M. B. Witte and A. Barbul, *Surg. Clin. North Am.*, 1997, **77**, 509–528.
60 N. J. Trengove, S. R. Langton and M. C. Stacey, *Wound Repair Regen.*, 1996, **4**, 234–239.
61 S. Barrientos, O. Stojadinovic, M. S. Golinko, H. Brem and M. Tomic-Canic, *Wound Repair Regen.*, 2008, **16**, 585–601.
62 J. Broadbent, T. Walsh and Z. Upton, *PROTEOMICS - Clin. Appl.*, 2010, **4**, 204–214.
63 S. M. Nehring, A. Goyal and B. C. Patel, in *StatPearls*, StatPearls Publishing, Treasure Island (FL), 2022.

64 E. H. Wright and U. Khan, *J. Plast. Reconstr. Aesthet. Surg.*, 2010, **63**, 1519–1522.
65 T. Liu, F. Yang, Z. Li, C. Yi and X. Bai, *Ostomy. Wound Manage.*, 2014, **60**, 30–37.
66 E. Seria, S. Samut Tagliaferro, D. Cutajar, R. Galdies and A. Felice, *BioMed Res. Int.*, 2021, **2021**, 4762657.
67 L. Thau, E. Asuka and K. Mahajan, in *StatPearls*, StatPearls Publishing, Treasure Island (FL), 2022.
68 C. Wade, S. E. Wolf, R. Salinas, J. A. Jones, R. Rivera, L. Hourigan, T. Baskin, J. Linfoot, E. A. Mann, K. Chung and M. Dubick, *Nutr. Clin. Pract.*, 2010, **25**, 510–516.
69 H. Miyao, Y. Ikeda, A. Shiraishi, Y. Kawakami and S. Sueda, *Anal. Biochem.*, 2015, **484**, 113–121.
70 N. J. Trengove, H. Bielefeldt-Ohmann and M. C. Stacey, *Wound Repair Regen.*, 2001, **8**, 13–25.
71 G. Lauer, S. Sollberg, M. Cole, T. Krieg, S. A. Eming, I. Flamme, J. Stürzebecher and K. Mann, *J. Invest. Dermatol.*, 2000, **115**, 12–18.
72 Varnakavi. Naresh and N. Lee, *Sensors*, 2021, **21**, 1109.
73 N. Bhalla, P. Jolly, N. Formisano and P. Estrela, *Essays Biochem.*, 2016, **60**, 1–8.
74 S. Qazi and K. Raza, in *Smart Biosensors in Medical Care*, Elsevier, 2020, pp. 65–85.
75 V. Velusamy, K. Arshak, O. Korostynska, K. Oliwa and C. Adley, *Biotechnol. Adv.*, 2010, **28**, 232–254.
76 *Advanced Biosensors for Health Care Applications*, Elsevier, 2019.
77 S. M. Borisov and O. S. Wolfbeis, *Chem. Rev.*, 2008, **108**, 423–461.
78 P. Parkhey and S. V. Mohan, in *Microbial Electrochemical Technology*, Elsevier, 2019, pp. 977–997.
79 S. Sang, Y. Wang, Q. Feng, Y. Wei, J. Ji and W. Zhang, *Crit. Rev. Biotechnol.*, 2015, 1–17.
80 S. N. Sawant, in *Biopolymer Composites in Electronics*, Elsevier, 2017, pp. 353–383.
81 J. R. Crowther, *The ELISA guidebook*, Humana Press, Totowa, NJ, 2001.
82 ELISA, https://www.novusbio.com/application/elisa, (accessed 20 May 2022).
83 X. Zhu and T. Gao, in *Nano-Inspired Biosensors for Protein Assay with Clinical Applications*, Elsevier, 2019, pp. 237–264.
84 R. Bakhtiar, *J. Chem. Educ.*, 2013, **90**, 203–209.
85 H. H. Nguyen, J. Park, S. Kang and M. Kim, *Sensors*, 2015, **15**, 10481–10510.
86 R. B. M. Schasfoort, in *Handbook of Surface Plasmon Resonance*, ed. R. B. M. Schasfoort, Royal Society of Chemistry, Cambridge, 2nd edn., 2017, pp. 1–26.
87 T. G. Mayerhöfer, A. Dabrowska, A. Schwaighofer, B. Lendl and J. Popp, *ChemPhysChem*, 2020, **21**, 707–711.
88 C. M. Miyazaki, F. M. Shimizu and M. Ferreira, in *Nanocharacterization Techniques*, Elsevier, 2017, pp. 183–200.
89 I. M. Mackay, *Nucleic Acids Res.*, 2002, **30**, 1292–1305.
90 C. J. Smith and A. M. Osborn, *FEMS Microbiol. Ecol.*, 2009, **67**, 6–20.
91 L. Garibyan and N. Avashia, *J. Invest. Dermatol.*, 2013, **133**, 1–4.
92 J. M. Wages, in *Encyclopedia of Analytical Science*, Elsevier, 2005, pp. 243–250.
93 The Biotechnology Revolution, http://www.nature.com/scitable/topicpage/the-biotechnology-revolution-pcr-and-the-use-553, (accessed 20 May 2022).
94 E. Navarro, G. Serrano-Heras, M. J. Castaño and J. Solera, *Clin. Chim. Acta*, 2015, **439**, 231–250.
95 F. J. Loge, D. E. Thompson and D. R. Call, *Environ. Sci. Technol.*, 2002, **36**, 2754–2759.
96 R. Sista, Z. Hua, P. Thwar, A. Sudarsan, V. Srinivasan, A. Eckhardt, M. Pollack and V. Pamula, *Lab. Chip*, 2008, **8**, 2091.
97 J. E. Childerhose and M. E. MacDonald, *Soc. Sci. Med.*, 2013, **86**, 1–8.
98 D. W. Chan and M. T. Perlstein, Eds., *Immunoassay: a practical guide*, Academic Press, Orlando, 1987.
99 R. Gupta and N. J. Goddard, *The Analyst*, 2013, **138**, 3209.
100 K. M. Koczula and A. Gallotta, *Essays Biochem.*, 2016, **60**, 111–120.
101 F. Lu, K. H. Wang and Y. Lin, *The Analyst*, 2005, **130**, 1513.
102 D. Grieshaber, R. MacKenzie, J. Vörös and E. Reimhult, *Sensors*, 2008, **8**, 1400–1458.

103 T. Guinovart, G. Valdés-Ramírez, J. R. Windmiller, F. J. Andrade and J. Wang, *Electroanalysis*, 2014, **26**, 1345–1353.
104 S. RoyChoudhury, Y. Umasankar, J. Jaller, I. Herskovitz, J. Mervis, E. Darwin, P. A. Hirt, L. J. Borda, H. A. Lev-Tov, R. Kirsner and S. Bhansali, *J. Electrochem. Soc.*, 2018, **165**, B3168–B3175.
105 B.-Y. Kim, H.-B. Lee and N.-E. Lee, *Sens. Actuators B Chem.*, 2019, **283**, 312–320.

Chapter 2 – Leaky Waveguides

2.1 Introduction

Diagnostics in medicine have advanced to a point where many illnesses can be detected simply through testing for the presence or absence of biomarkers such as proteins in bodily fluids.[1] However, these fluids often contain a plethora of other biomarkers, which can interfere with detection.[2] It is due to this, that biosensors, such as surface plasmon resonance (SPR), have been developed for the detection of target analytes. Unfortunately, as SPR is a surface-based detection technique, the results can be heavily impacted by imperfections in the detection site.[3]

This chapter will investigate the development of a non-surface-based detection method, a leaky waveguide (LW). Following this the performance of a miniaturised instrument will be compared to its laboratory-based counterpart to determine suitability for point of care (POC) testing.

2.2 Waveguides

2.2.1 Planar Optical Waveguide Biosensors

Optical waveguides were in use long before their applications into diagnostics. By definition, an optical waveguide is a device which allows for the transportation of energy within the infrared and visible regions of the electromagnetic spectrum.[4] Technology of this kind has been used in fibre optics, and operates through the use of total internal reflection (TIR) to confine the electromagnetic energy within a material, thus enabling the propagation of the light to the end point, as displayed in Figure 2.1.[5] TIR can only occur if the core is of a higher refractive index (RI) than that of the material surrounding it.[5]

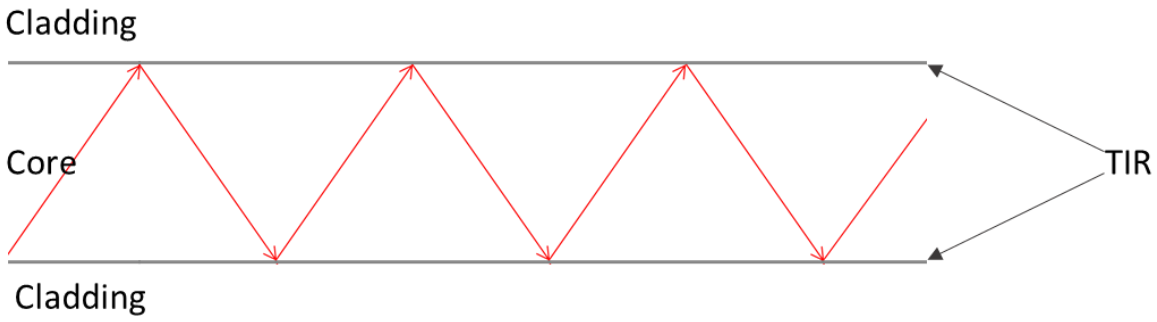

Figure 2.1: *An image depicting the setup of a waveguide, where the cladding is of a lower RI than the waveguide core. Image adapted from RP-Photonics.*[6]

Conventional planar optical waveguide biosensors operate in much the same way. Light is confined in the waveguide device *via* TIR due to the respective refractive indices of the waveguide device and the materials surrounding it. As a glass substrate is usually used to couple light into the waveguide device, the waveguide device must be made of a material of a higher RI than glass, which is noted in literature to be around 1.5.[7] Due to this, many planar

optical waveguide films are formed from metal containing substances such as tantalum pentoxide (RI = 2.1 to 2.3) or titanium dioxide (RI = 2.5 to 2.8).[8]

Despite the fabrication with different materials, conventional planar optical waveguide biosensors work much in the same way as SPR biosensors, discussed in Chapter 1.4.1 in more depth. Briefly, a film is functionalised with biorecognition elements and placed on a glass prism. Light is coupled into the conventional planar optical waveguide device through the glass prism, and TIR occurs; as TIR occurs, small levels of energy are released at the waveguide-sample interface, which is known as an evanescent field. The angle at which this evanescent field is produced is dependent on the RI difference between the waveguide device and the sample interfaces. All other light is reflected into a detector, with this evanescent field displaying as a dip in reflectivity. As analytes are immobilised by the biorecognition elements, the TIR angle, and therefore angle at which the evanescent wave is produced, alters; this being the signal which is converted by the transducer into real time results for the operator.[9]

Optical biosensors based on waveguide technology are already in development. The Epic™ developed by Corning is a waveguide based detection unit for the confirmation of the presence of aggregating compounds.[9]

Planar optical waveguides and SPR biosensors both have the advantage of being label-free, real-time biosensors; not only this, but the signals received from them are directly proportional to the level of target analytes within the sample, thus making them quantitative biosensors.[10] Both are excellent techniques operating on much the same fundamental principles, however, in this instance, waveguides are a more feasible option for wide spread diagnostics. This is simply due to the materials required for fabrication, SPR is requires the use

of inert precious metals such as gold and silver, which are too expensive to be of use globally, thus waveguides, being made of cheaper materials are the more cost-effective route. Waveguides are not the perfect replacement for SPR however, as both methods are based on surface sensing, this requires perfectly replicable and uniform fabrication methods which are difficult to achieve. To simplify the process, the ideal solution would be to develop a label-free biosensor which is not a surface-based technology.

2.2.2 Leaky Waveguide Biosensors

Stemming from the development of optical waveguides is a newer technique known as LWs. Unlike a conventional planar optical waveguide, in a LW, the setup is comprised of a waveguide material which has a lower RI than one of the adjacent materials.[11] In this instance, the glass is of a higher RI than the LW device, which in turn is of a higher RI than the sample. This results in TIR at the LW-sample interface as before, with an evanescent field formed, but also partial reflection, or Fresnel reflection, at the substrate-LW interface, leading to a loss of light, thus the name of leaky.[12,13]

Due to the confinement of light *via* Fresnel reflection, TIR at the substrate-LW interface is no longer a requirement, allowing the use of materials with a lower RI than glass for LW device formation.[13] As such, with a LW, the potential materials for device fabrication are more varied, this has led to the development of hydrogel based waveguide devices.[13,14] Hydrogels are an advantageous material as they are often porous to the many water-soluble analytes detected by biosensors, meaning that biorecognition elements can be dispersed throughout the entire structure of the hydrogel rather than just at the surface. As the analytes are absorbed and bound into the structure of the hydrogel waveguide, the RI of the waveguide

material is changed (Figure 2.2). The change in the RI alters other properties of the hydrogel, such as the velocity at which light travels through the material resulting in an altered resonance angle.[15] This change in resonance angle is the signal measured and converted to a readable output by the transducer.

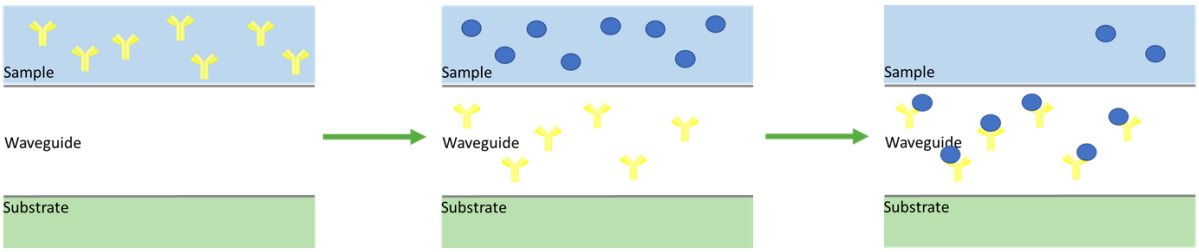

Figure 2.2: *An image displaying the immobilisation of biorecognition elements and target analytes within the structure of a hydrogel based LW device.*

The conventional set up of a LW is to have a glass slide bound to a transparent waveguide material with a low RI, the waveguide material is then covered with a microfluidic flow cell, which supplies the sample solution. [16,17] Light is coupled into the LW device by a glass prism, and reflected light is detected by a camera. Due to a loss of light, the resonance angle is depicted as a dip in reflectivity, known as a mode, a single waveguide device can have multiple modes as they are simply paths of reflection within the waveguide device.

The resonance angle of the hydrogel waveguide will alter as the RI of the sample solution changes.[18] Although the resonance angle will shift, so long as the structure of the hydrogel remains unchanged, once the waveguide is exposed to the initial sample solution, the resonance angle should return to its original position. This is how the waveguide can be used to detect biological compounds in a solution. If the biomolecules are bound and immobilised in the structure of the waveguide, the RI of the waveguide is permanently altered as the structure has irreversibly changed. This change in RI is evidence that the waveguide is

an effective optical biosensor.[19] The use of a hydrogel in this scenario is advantageous as the hydrogel can be synthesised to be as porous as is desired, leading to an increase in the number of biorecognition sites in comparison to non-porous waveguide materials.[20]

As biorecognition elements can be dispersed within the entire structure of the hydrogel based LW device, the technique is no longer surface based, and less impacted by imperfections in manufacturing.[21] This has improved upon the major drawbacks to both SPR and conventional planar optical waveguides.

2.2.3 Metal Clad Leaky Waveguides

The resonance angle of some hydrogels can be visualised without further enhancement, however, other hydrogels must be doped in order for this to be observed.[18] Metal films are commonly used as doping agents, these involve the use of glass slide substrates which are coated in a thin film of metal, these are commonly called metal clad leaky waveguides (MCLWs).[22] MCLWs are unique with their output, in that their resonance angle is visualised as a peak in reflectivity compared to the more commonly seen dip.[23] The presence of a metal film, usually titanium, on the substrate-LW interface acts to increase the sensitivity of the LW device by pushing the evanescent field further into the sensing layer, thus increasing the sensing area (Figure 2.3).[24]

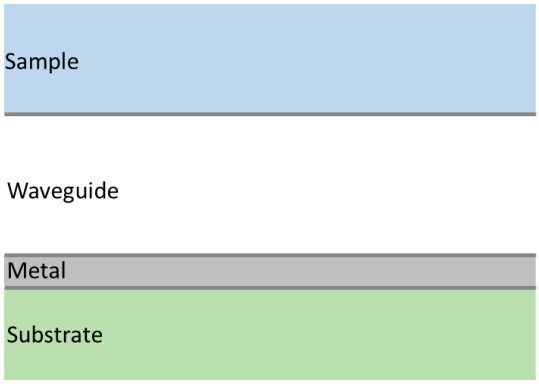

Figure 2.3: *An image displaying the set-up of a MCLW device. Image adapted from Gupta et al.*[25]

Many studies have been conducted into the preparation of these waveguide devices with gels of limited porosity such as silica gels with optimistic results.[26] A number of analytes have been detected using this technology, including bacterial cells and protein A; however, this method, while of increased sensitivity in comparison to SPR, does return to surface-based sensing techniques.[21,24,26] Not only that, this technique also reincorporates the need for inert metals such as gold and titanium to be deposited on glass films, thus increasing the cost of the procedure in comparison to other LW techniques.[27,28]

2.2.4 Dye Doped Leaky Waveguides

A second method of visualising the resonance angle of a hydrogel is through the use of a dye as a doping agent, resulting in the formation of a dye doped leaky waveguide (DDLW).[18] Following on from the development of MCLWs, DDLWs also improve the visualisation of the resonance angle within a hydrogel LW device.[29] This is achieved through the staining of the LW material surface with a compatible dye (Figure 2.4).[30] While some hydrogels can create a significant dip in reflectivity alone, others need a doping agent to do

so; this is the purpose of DDLWs as the dye interacts with light, thus enhancing the dip in reflectivity.[29]

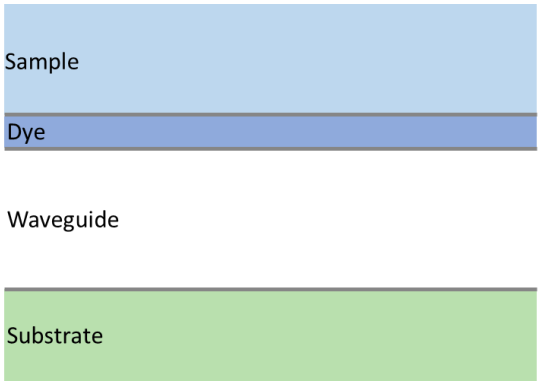

Figure 2.4: *An image displaying the set-up of a DDLW device.*

Biosensors of this type have been based on multiple LW materials, ranging from naturally obtained polymers such as chitosan and agarose, to synthetic polymers such as polymethyl methacrylate.[30–32] Some of the analytes of interest to be detected through the use of DDLWs are ferritin and bovine serum albumin (BSA), proving sensitivity to biomarkers, more specifically proteins.[16,31]

While both MCLWs and DDLWs have been used to detect changes in the RI of a sample solution, the DDLW is a more POC compatible device. This is due to the use of organic dyes as the visualisation material, which are simple to synthesise and can be produced on a large scale for low cost, in comparison to inert metals which are a finite substance and must be drilled from the earth's crust and processed. Not only this, but the method of forming DDLWs is based on fundamental chemistry, through choosing a hydrogel and a water-soluble dye which contain compatible functional groups, and allowing the dye solution to infuse into the structure of the hydrogel, strong covalent bonds can be formed. This is advantageous as it

does not require the use of complex, expensive instruments to deposit a thin film of metal onto the surface of a glass slide.[18,22]

2.3 Point of Care Testing

Many biochemical and microbiological tests in healthcare settings are performed in laboratories containing automated analytical processes; these are able to analyse a high volume of samples for a relatively low cost. The automated processes used in current laboratory testing methods require expensive machinery and highly trained staff to operate and maintain to high standards.[33] This results in an increase in the running cost for these analytical methods. Due to changing economic climates and the decrease in funding allocated to healthcare budgets, testing methods must be altered to be more cost effective.[34] POC testing is a method of diagnosing patients at their bedside, while in an operating theatre, in a general practitioner's office or even at home.[35] By definition POC tests must:

- give rapid results
- have little to no sample preparation
- be easy to use
- be of small size and easy to manoeuvre
- require small sample volumes
- be low cost to produce.[36]

One reason for the rapid results given by POC testing is that it requires fewer steps to obtain results in comparison to laboratory testing (Figure 2.5). In areas which are sparsely populated, or less economically developed, automated analytical processes are not a cost effective option and personnel trained in analytical techniques are often difficult to find, which further drives the need for research into POC testing.[34] Due to the success in the development of new scientific techniques, such as the creation of nanoparticles and the discoveries of new

biomarkers, research into POC testing has increased steadily since the 1970's.[34,35] Despite all of this, there are still disadvantages to POC testing such as:

- results are often of poor quality
- there is much room for error in self-administered tests
- tests are repeated multiple times, resulting in overuse and increased waste levels
- test production must be regulated
- as POC testing is usually single use, there is an increase in cost and waste product.[37]

Investigators into POC testing have mixed opinions on the notion that POC testing can replace automated analytical processes.[38] However, as technology continuously advances, it may be that there comes a time when POC testing is efficient and accurate enough to eliminate the need for healthcare laboratories entirely.[39]

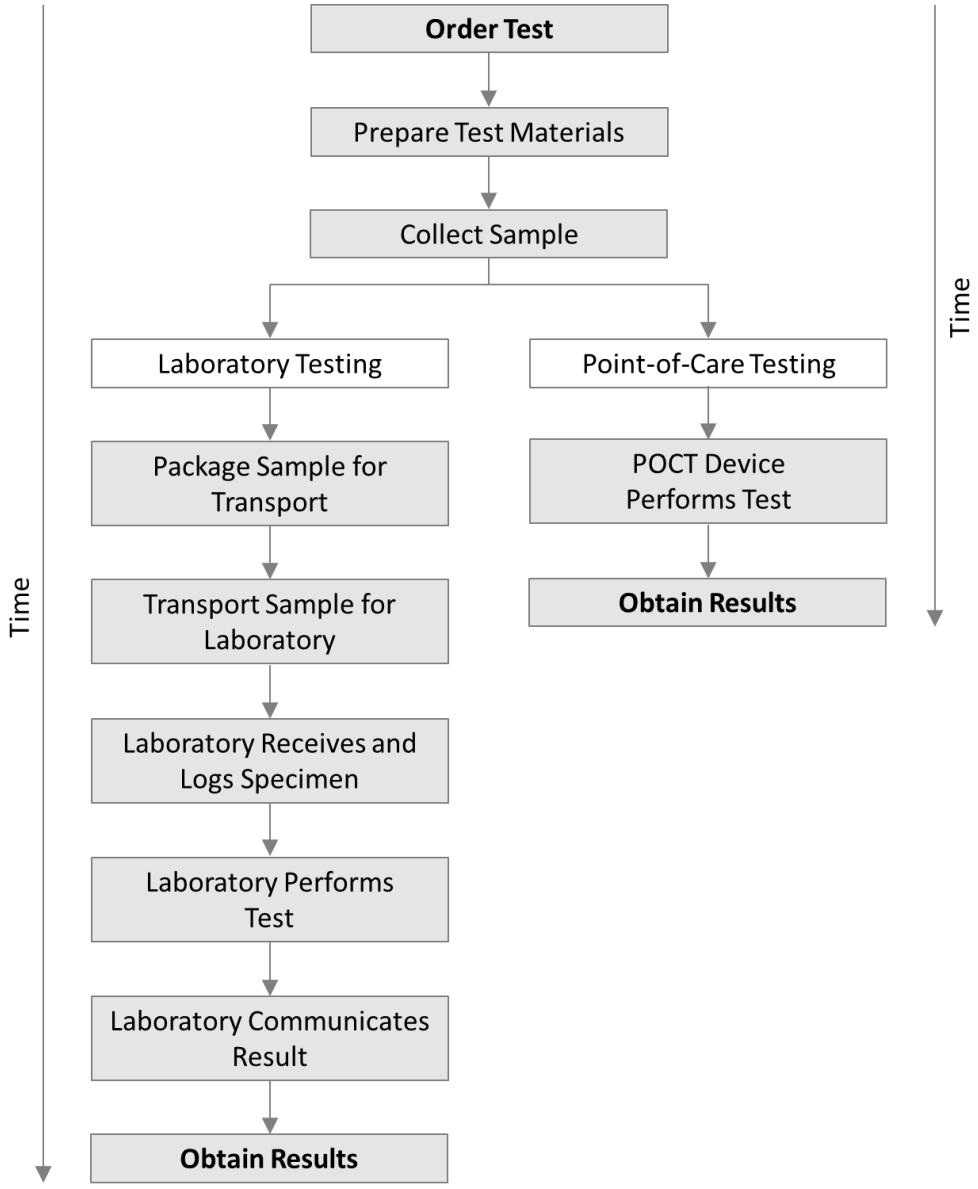

Figure 2.5: *A flow chart depicting the different stages of performing laboratory-based tests compared to POC testing.*[39]

POC testing has already been implemented for a number of common biological tests, such as testing blood chemistry, gas and electrolyte concentrations and for the detection of some proteins.[36] In fact, there are currently over 100 companies worldwide offering tests which provide rapid results.[37] This POC technology often takes on one of two forms: bench-top equipment or small, single use devices.[40]

Single use handheld devices can provide results within minutes while using a reasonable sample volume, a common example of this is a glucose test. Glucose tests are commonly produced in two forms, both requiring a small volume of sample (Figure 2.6). In the more common test, blood is applied to a test strip, which contains glucose oxidase and two electric terminals. When glucose in the sample reacts with glucose oxidase, gluconic acid is formed; a device, known as a blood glucose meter, is used to apply a current to the test strip. The blood glucose meter can then determine the current between the two terminals on the test strip, the value of this current is proportional to the volume of gluconic acid produced. The test strips are then disposed of, ready for a fresh test.[41] These single use tests require a transducer, however, there are some single use glucose tests in circulation which do not require specialist additional equipment. Examples of these are dipstick tests, these glucose tests provide a colorimetric response depending on the level of glucose present in the urine.[42] While less accurate than the blood glucose monitor, urine dipstick tests are a more convenient method for POC testing due to the simpler readout method.

Figure 2.6: *An image displaying a blood glucose test (left) and a glucose urine dipstick test (right). Images used from diabetes.co.uk and precision laboratories.*[43,44]

Alternatively, bench-top analysers are smaller versions of the processes used in laboratories and therefore still require trained personnel, however, these devices are being designed with a more simplistic user interface to allow for use by a wider variety of staff.[45,34] The advantage to these is that they are often more accurate and provide more quantitative results than single use devices. Also, as these instruments are multiuse, the waste produced per test is lower, as is the cost of preparation.[34] Additionally, these devices are ideal for small sample volumes, the disadvantage however is that these processes require more external energy than other proposed systems.[46] Bench-top POC testing systems are currently widely used for a number of bioassays, such as testing for c-reactive protein (CRP), troponin and glucose levels.[34] Many of these devices are designed to have their analysis completed *via* a computer, due to this, these systems can often be label-free.[34] These label-free biosensors often provide more accurate, quantitative results; live monitoring of samples and simplistic sample preparation making them ideal for POC testing.[16]

2.4 Project Aims

Previously within the group we have proven the ability to measure changes in RI of hydrogels through the use of LW devices.[19] Through the incorporation of biorecognition elements into the structure of a hydrogel, we alter the structure of the material and by extension, its RI. Based on these biorecognition elements we are able to detect the complementary analyte through binding, thus causing a permanent change in RI of the hydrogel material. Unfortunately, the equipment used to conduct these experiments are traditionally large in size. This large size is not desirable in a POC setting such as a doctor's office. Due to this, the desired outcomes of this project are:

1. To demonstrate the biosensing ability of chitosan-based LW devices.
2. To test the refractive index sensitivity (RIS) of these LW devices.
3. To miniaturise the equipment, to be suitable for POC testing.
4. To determine if the POC equipment data is comparable to that of a traditional benchtop laboratory-based instrument.

The work in this chapter was completed in collaboration with another student for the purpose of publication, however the data presented herein is the result of my own work. Data obtained by my peer for the publication has not been included in this thesis.

2.5 Results and Discussion

2.5.1 Chitosan Purification

As discussed earlier, chitin is a naturally occurring polymer, being a major component of crustacean shells; and through the deacetylation of chitin we can produce the polymer chitosan.[47,48] Chitosan has many advantageous properties which led to this being the material of choice in this work; firstly, it is non-toxic, so a safe media for protein encapsulation; secondly, depending on the degree of deacetylation, each repeating unit contains a free primary amine (Figure 2.7), which is necessary for the immobilisation route designed; third, the polymer has already been incorporated into the production of hydrogel based wound dressings; and finally, while some hydrogels are responsive to changes in pH and temperature, this one is not, minimising the risk of non-binding related signals. Unfortunately, as chitosan is obtained from natural sources, the polymer frequently contains impurities. To ensure the highest quality LW devices and help to ensure replicability, the polymer was purified prior to use with a method modified from literature.[49] To do this, the crude polymer was initially dissolved as a 1 mg mL^{-1} solution in acetic acid before being syringe filtered through 5 µm filters. Sodium hydroxide was then used to precipitate out the large molecular weight polymer, while the more soluble impurities remained within the solution. The precipitate was then purified through dialysis in deionised (DI) water to aid in the removal low molecular weight impurities. Finally, the polymer was further washed with DI water, before being freeze dried to collect the final, purified chitosan as a lyophilised powder. This resulted in a white, flaky solid, with a yield equal to 60% of the starting mass.

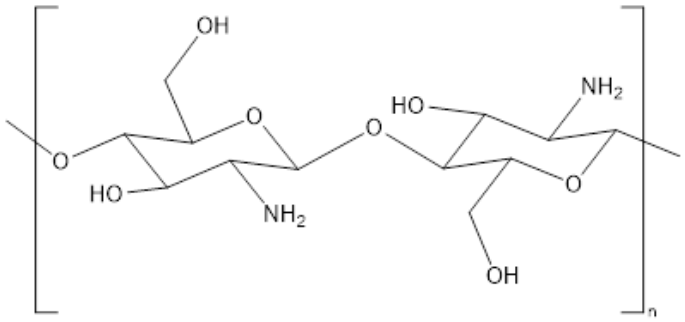

Figure 2.7: *An image depicting the structure of chitosan when 100% deacetylation occurs.*

2.5.2 Chitosan Leaky Waveguide Device Fabrication

As discussed earlier (Chapter 2.2.2), a substrate is required for the LW device, in this instance we chose to move forward with glass substrates; this decision was made as light would travel seamlessly through the glass prism and glass substrate into the hydrogel. To remove possible contaminants which could interfere with LW device formation and possibly alter later results, glass microscope slides, 2.5 cm by 2.5 cm, were cleaned by sonication in 5% decon 90, DI water and absolute ethanol for 30 minutes each prior to use as glass substrates. The purified chitosan was dissolved in 0.1 M acetic acid to a concentration of 1 mg mL^{-1}. To create a thin layer of chitosan on the surface of the glass substrate, this solution was spin coated at 900 rpm for 30 s with an acceleration of 100 rpm s^{-1} onto the surface of a glass substrate, creating a thin deposit of chitosan across the surface of the glass substrate. To promote the cross-linking of polymer chains required for hydrogel formation, the chitosan covered substrate was submerged in a 0.03% solution of glutaraldehyde in a 100 mM 4-(2-hydroxyethyl)-1-piperazineethanesulfonic acid (HEPES), pH 7.4 buffer solution for 10 minutes. Cross-linking occurs as the aldehyde functional groups in glutaraldehyde underwent a Schiff reaction (Figure 2.8) with the free primary amine groups present in chitosan, thus resulting in

the formation of imine bonds linking polymer chains to one another. The final step of fabrication was to stain the LW devices with a 0.1 mM solution of reactive blue 4 dye, which covalently binds to a small number of the free primary amines within the hydrogel film. This staining allows for better optical imaging of the resonance angles within the hydrogel film thus creating a DDLW. The newly fabricated DDLW devices were then stored in a 100 mM HEPES, pH 7.4 buffer solution out of direct light until use to preserve the dye.

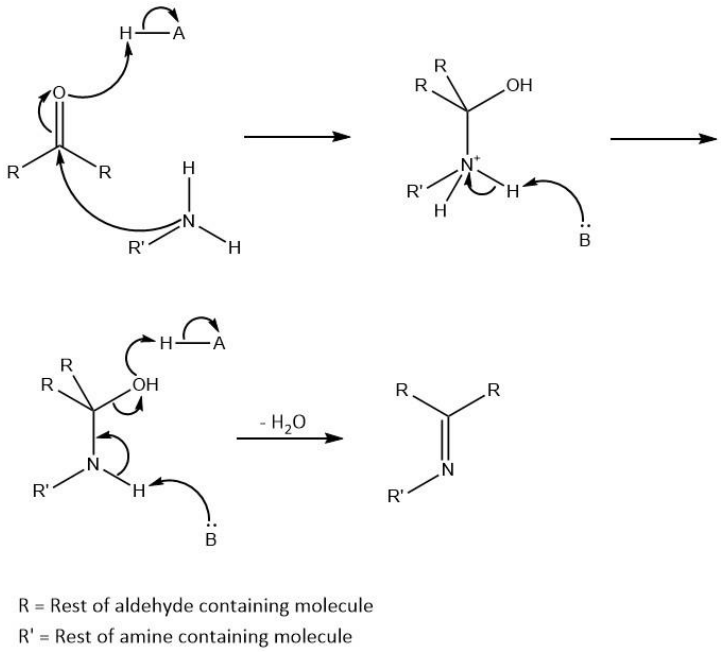

Figure 2.8: *A scheme depicting the Schiff reaction that occurs between aldehyde groups and primary amines where the rest of the molecules are undefined.*

2.5.3 Leaky Waveguide Instrumentation

Following the formation of chitosan DDLWs, studies were then conducted on a traditional benchtop laboratory-based instrument. This instrument was built in-house and consisted of a large metal container, with parts manufactured by milling aluminium and steel. The traditional benchtop laboratory-based instrument is bulky, approximately 60 × 60 × 35 cm in size and 25 kg in weight.

Once the characterisation of chitosan DDLWs on the traditional benchtop laboratory-based instrument was completed, studies were repeated on a smaller three-dimensional (3D) printed instrument. This was in order to miniaturise the instrument to a portable size, thus making it more suitable for POC testing. This was completed by collaborators who produced many parts of the instrument through 3D printing; this greatly decreased the size and mass to 16.2 × 13 × 10.7 cm and 825.05 g respectively. The results obtained from both instruments were then compared to determine whether miniaturisation had an effect on the useability of the chitosan DDLWs for biosensing.

Both instruments require the use of an external computer and a peristaltic pump, whereas in some instances, a water bath is also used with the traditional benchtop laboratory-based instrument (Figure 2.9).

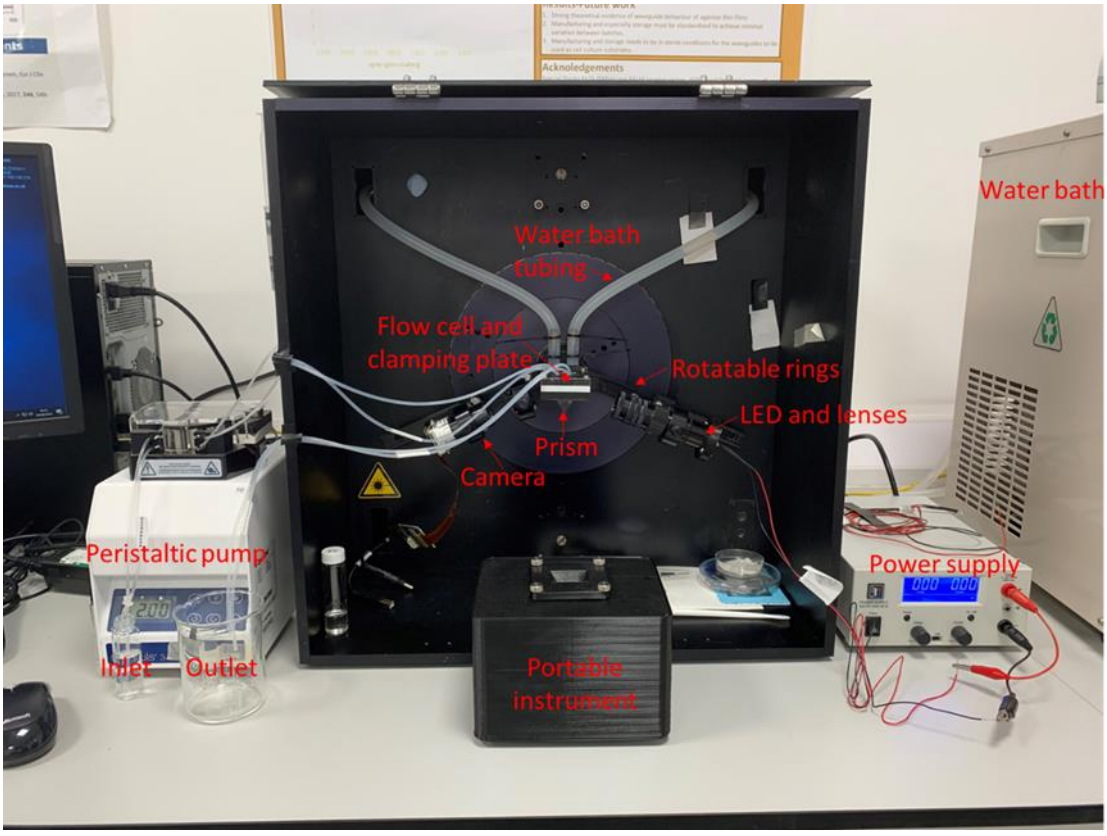

Figure 2.9: *A photograph of the traditional benchtop laboratory-based instrument (back) and the 3D printed instrument (front).*

2.5.4 Refractive Index Sensitivity Testing

One of the key properties of materials used for LW biosensing is the RIS, which is a measure of how sensitive the LW device is to changes in RI. The RIS is a measure of shift in resonance angle ($\Delta\theta_R$) versus RI of sample (Equation 2.1); a high RIS is desirable, as it suggests that even a minimal change in RI would result in an observable $\Delta\theta_R$.

$$\boldsymbol{RIS = \frac{\Delta\theta_R}{RI}}$$

Equation 2.1: *An equation displaying the relationship between RIS, $\Delta\vartheta_R$ and the RI of a solution.*

To measure this, a calibration curve was first made using solutions of known RI and measuring the response they created. The calibration curve in this instance consisted of glycerol solutions ranging in concentration from 0.125% glycerol to 2% (v/v). Glycerol was the compound of choice as it is of a similar structure to the polyethylene glycol (PEG) chains that were to be used later, it is inert to the hydrogel film, and it is a small compound that should be able to penetrate the hydrogel film completely. Prior to use for RIS testing, the RI of the glycerol solutions was measured in triplicate. A baseline signal was created with 100 mM HEPES, pH 7.4 buffer solution. Each solution was then added to the LW device sequentially (Figure 2.10).

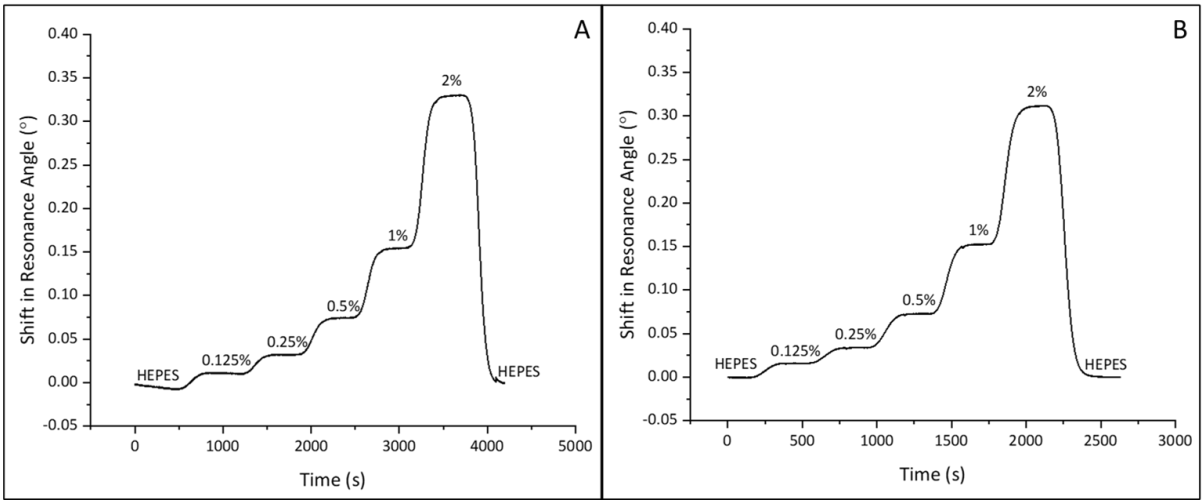

Figure 2.10: *A graph displaying the $\Delta\vartheta_R$ caused when glycerol solutions of concentrations equal to 0.125%, 0.25%, 0.5%, 1% and 2% (v/v) in a 100 mM HEPES, pH 7.4 buffer solution are introduced to a chitosan-based DDLW device on a traditional benchtop laboratory-based instrument (A) and on a 3D printed instrument (B). Data is an average of 3 repeats of each study.*

Through plotting the average $\Delta\theta_R$ against the RI of each solution, we obtained the calibration curve (Figure 2.11). Based on Equation 2.1, we determined that the gradient of this graph is equal to the RIS, thus making this an easy characteristic to determine.

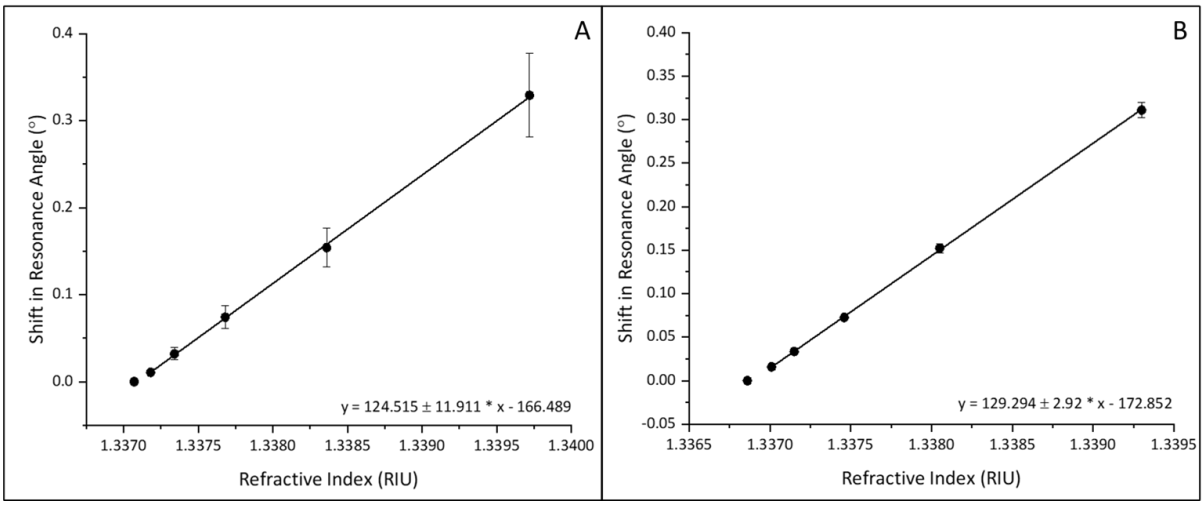

Figure 2.11: *A graph depicting the average $\Delta\vartheta_R$ in degrees caused by solutions of different refractive indices as obtained on (A) a traditional benchtop laboratory-based instrument and (B) a 3D printed instrument. Data is an average of 3 repeats of each study.*

From the above graphs, we can see that the RIS of the chitosan DDLW device is equal to 124.515 ± 11.911° RIU^{-1} when measured on the traditional benchtop laboratory-based instrument. Whereas identical DDLW devices result in a RIS equal to 129.294 ± 2.92° RIU^{-1} when tested on a 3D printed instrument. These measurements were completed in three-fold to test for variability across different LW devices, with the average measurement being plotted.

Through comparing the results, there is no significant difference between the RIS of the traditional benchtop laboratory-based instrument when compared with that of the 3D printed instrument. As can be seen, the RIS calculated from a traditional benchtop laboratory-based instrument had an error associated with it of ± 11.911° RIU^{-1}; we can see that the error associated with the 3D printed instrument, at ± 2.92° RIU^{-1}, is almost a quarter of this value. This informs us that while based on RIS, both instruments are comparable, the 3D printed instrument provides more consistent and therefore reliable results, thus being the superior instrument in this instance.

2.5.5 Porosity Testing

While sensitivity is one of the most important properties of LW devices when determining their suitability as biosensors, another vital property is porosity. While there are more conventional methods for the determination of pore sizes, such as scanning electron microscopy and transmission electron microscopy, these techniques can only be conducted on dry samples.[50] The pores in a dehydrated hydrogel are not comparable to those in a swollen hydrogel, making these techniques unsuitable for these studies.

Therefore, in order to test for porosity, we use the RIS value obtained through the calibration curve, as shown in Figure 2.11. Through rearranging the equation of the line of best fit obtained from a RIS testing graph (Equation 2.2), by multiplying the RI of the analyte solution by the RIS of the LW device with the addition of the intercept, we obtain a value for the expected $\Delta\theta_R$ if a film were to be 100% porous to the analytes.

$$\boldsymbol{\Delta\theta_{R\,(theoretical)} = (RIS \times RI) + c}$$

Equation 2.2: *An equation showing how we can rearrange the straight line equation given from RIS testing graphs to achieve the calculation of a theoretical $\Delta\vartheta_R$ ($\Delta\vartheta_{R(theoretical)}$) caused by 100% permeation of a solution of (RI) into a LW device of (RIS) where (c) is equal to the intercept on the RIS graph.*

The solutions used to test porosity were 1% (w/v) solutions of a range of PEG chains, ranging in size from 10 kDa to 300 kDa. The purpose of using a range of molecular weight compounds was to test how porosity changed with chain length as proteins can vary greatly in size from as small as 5.808 kDa, to up to 3,000 kDa; however, proteins within the human body tend to have an average mass of 46.4298 kDa.[51–53] In Figure 2.12 below, we see the trace observed from the input of these solutions and their subsequent washing out of the film for chitosan-based DDLW devices tested on both a traditional benchtop laboratory-based instrument and a 3D printed instrument.

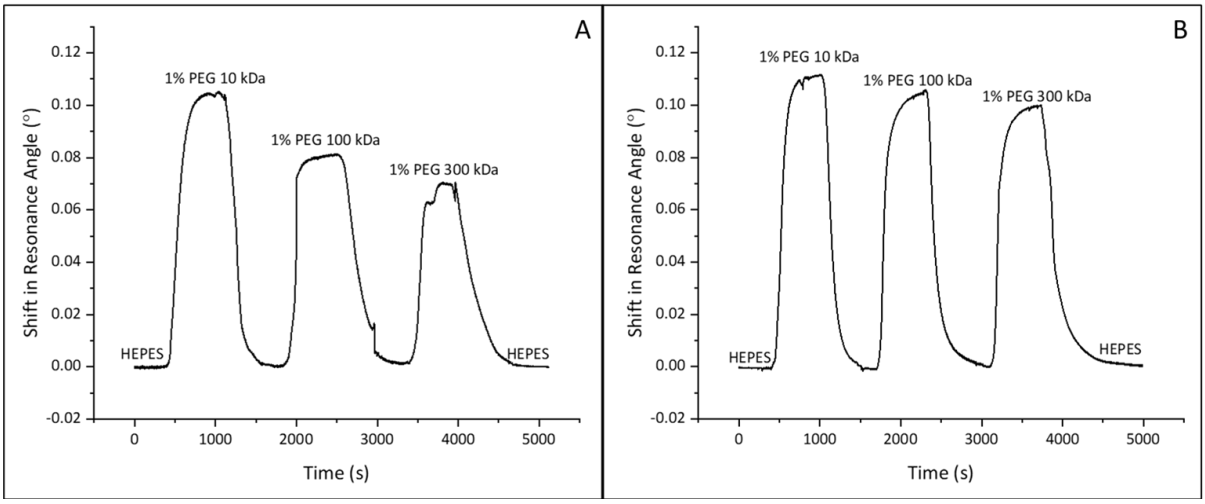

Figure 2.12: *A graph displaying the $\Delta\vartheta_R$ caused when 1% (w/v) polyethylene glycol solutions of sizes ranging from 10 kDa to 300 kDa in a 100 mM HEPES, pH 7.4 buffer solution are introduced to a chitosan-based LW device on (A) a traditional benchtop laboratory-based instrument and (B) a 3D printed instrument. Data is an average of 3 repeats of each study.*

Through comparing the average $\Delta\theta_R$ at the signal peak, to the expected values that have been calculated using Equation 2.2 and documented in Table 2.1, we can calculate the porosity of the film to different molecular weight compounds as a percentage of completely porous. As the hydrogel preparation was unchanged, we would expect porosity results from the 3D printed instrument to be comparable to those of the traditional benchtop laboratory-based instrument. We elected to repeat these tests as a control, and to ensure that the instruments are comparable.

Table 2.1: *A table listing the refractive index of 1% (w/v) PEG solutions used for porosity studies, the theoretical $\Delta\vartheta_R$, the obtained $\Delta\vartheta_R$, and the porosity of the film as a percentage of these values where the theoretical signal indicates 100% porosity when tested on both traditional benchtop laboratory-based instrument and a 3D printed instrument. Data is an average of 3 repeats of each study.*

Instrument	Solution	Refractive Index (RIU)	Theoretical $\Delta\theta_R$ (°)	Actual $\Delta\theta_R$ (°)	Porosity (%)
Laboratory-Based Instrument	1% PEG 10 kDa	1.33836	0.16138	0.10412	64.52
	1% PEG 100 kDa	1.33843	0.17008	0.08008	47.08
	1% PEG 300 kDa	1.33844	0.17132	0.06818	39.80
3D Printed Instrument	1% PEG 10 kDa	1.33824	0.17413	0.11062	63.53
	1% PEG 100 kDa	1.33821	0.17028	0.10227	60.06
	1% PEG 300 kDa	1.33823	0.17285	0.09851	56.99

Through comparing the results listed in Table 2.1, we can see that for a 1% solution of 10 kDa PEG in HEPES buffer solution, the porosity remains unchanged across the different instruments. The difference occurs with 1% solutions of PEG 100 kDa and 300 kDa in HEPES buffer solution; through using the 3D printed instrument, the LW devices appear to be more porous to these large molecular weight compounds. As the devices were created under identical conditions, it is more likely that as the 3D printed instrument actually afforded a more sensitive detection method, as displayed by the slightly higher RIS, it simply was more sensitive to detecting the larger molecular weight compounds. This suggests that the 3D printed instrument will be more effective in the detection of large proteins than the traditional benchtop laboratory counterpart, an ideal result for the adaptation of these devices for POC testing purposes.

2.5.6 Target Analyte Detection

Following the determination that chitosan-based LWs were sensitive to large molecular weight compounds, development into biosensors suitable for POC testing began. The intended target analyte for this work was immunoglobulin G (IgG) as it is a biologically relevant analyte that is cost effective for initial preliminary studies with the immobilisation method displayed in Figure 2.13.

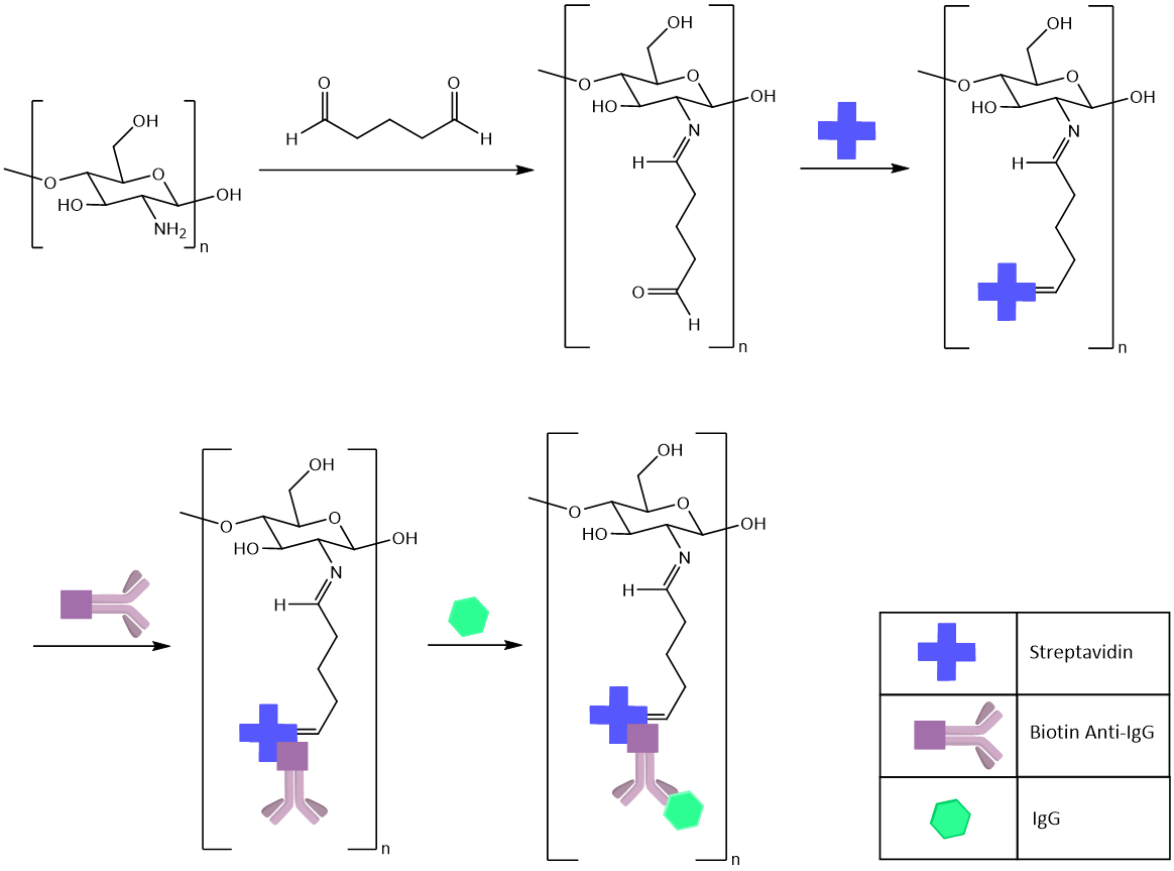

Figure 2.13: *An image depicting the biosensing of IgG completed in this work. Initially glutaraldehyde binds to a chitosan LW device, followed by the immobilisation of streptavidin. BSA is introduced to the system to block unreacted functional groups. Biotin anti-IgG binds selectively to form a streptavidin-biotin complex, functionalising the LW device with anti-IgG antibodies. The antibodies then form strong bonds with IgG.*

The first step for protein immobilisation was the introduction of glutaraldehyde to the system. The intention here was for one terminal aldehyde group to react with free primary

amine groups within the film *via* a Schiff base reaction resulting in imine formation. The result of this was the functionalisation of the hydrogel film with free aldehyde groups. Following this, streptavidin was added to the system, during which aldehyde functionalised hydrogel film reacted with the primary amine functional groups present in streptavidin, again through a Schiff base reaction. This resulted in the immobilisation of streptavidin into the hydrogel film *via* covalent imine bond formation. To prevent non-specific protein binding in later biosensing steps, BSA was introduced to the system. As BSA also contains lysine residues, it was expected to react with any remaining, non-specific protein reactive functional groups present in the LW device. The final step in the production of the biosensor was the incorporation of the biorecognition element itself, in this instance, biotin anti-IgG; this was immobilised through the strong binding affinity of streptavidin for biotin.[54] The other component of the conjugate, anti-IgG, is the antibody complementary to the target analyte, IgG. As streptavidin is a tetrameric protein, each molecule contains four possible binding sites for biotinylated compounds such as biotin anti-IgG.[55] At this stage, the biosensor was prepared, and ready for sensing to occur through the strong antibody-antigen binding which occurs with complementary proteins and antibodies. To sense for a relevant analyte, IgG was then introduced to the system to be immobilised into the LW device structure. Binding was measured in real time, with each step separated by buffer washes; the purpose of the buffer washes was to remove unbound analytes from the gel matrix. Through taking measurements following the washing with buffer, a more accurate representation of covalently immobilised compounds is achieved as the RI of the sample is returned to the baseline conditions, thus any changes must be caused by the permanent change of RI in the DDLW device.

As previous work within the group had determined the ability for traditional benchtop laboratory-based instruments to detect relevant analytes, and this study had proven that the 3D printed instrument provided comparable results in all other aspects, testing was only conducted on the small, portable 3D printed instrument.[19] The trace obtained from this study is shown in Figure 2.14. Due to the small size of the 3D printed instrument, the camera was closer to the prism, thus reducing the scope of the camera and it therefore covering a smaller area than a traditional benchtop laboratory-based instrument. Based on this information, the 3D printed instrument data had to be collected as multiple graphs and combined with the camera being moved between studies. By finishing and starting each graph with a buffer wash, this enabled a straightforward method of merging the results.

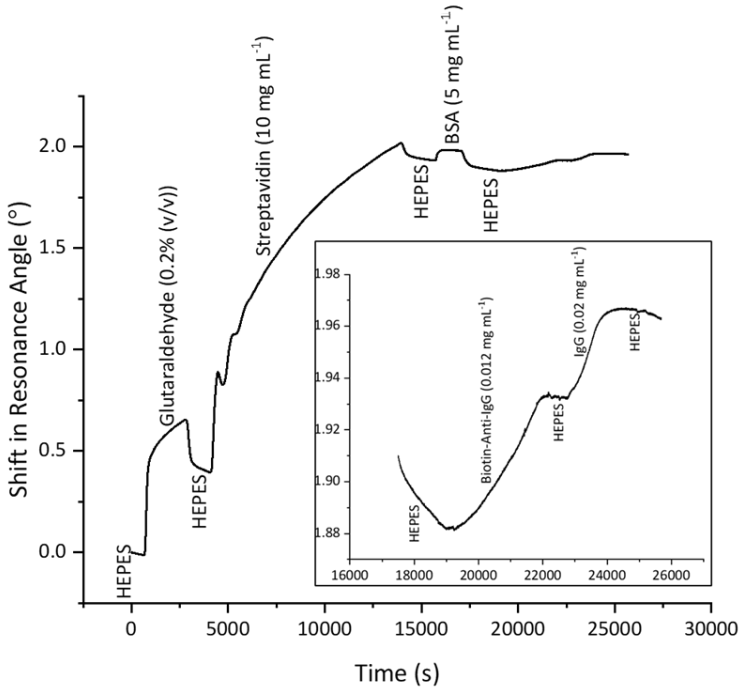

Figure 2.14: *A graph displaying the $\Delta\vartheta_R$ caused when detecting proteins on a chitosan-based LW device using a 3D printed instrument. Initially, a 100 mM HEPES buffer solution is introduced to the setup, this is normalised to 0 °. Following this, a 0.2% glutaraldehyde solution (v/v) is introduced, followed by a buffer wash. A 10 mg mL^{-1} solution of streptavidin is introduced followed by a buffer wash prior to the introduction of a 5 mg mL^{-1} solution of BSA. A buffer wash can be seen, which is continued into the inserted graph, a zoomed in view of 17,500 s until the finish. The zoomed in view shows more clearly the introduction of a 0.012 mg mL^{-1} solution of biotin-anti-IgG, followed by a buffer wash. This leads to the detection of the final target analyte, a 0.02 mg mL^{-1} solution of IgG, ending with a final buffer wash. Data is an average of 3 repeats of the study.*

The accurate $\Delta\theta_R$ caused by binding events can be determined by observing the signal given by the addition of buffer following the introduction of compounds and the average signal for each solution is displayed in Table 2.2. The reason for washing is that it removes unbound remnants of compounds and shows more accurately the $\Delta\theta_R$ caused by covalent binding.

Table 2.2: *A table comparing the $\Delta\vartheta_R$ caused by binding events in the development of a chitosan-based LW biosensor as observed from a portable 3D printed instrument. Data is an average of 3 repeats of the study.*

Analyte	$\Delta\theta_R$ (°) 3D Printed Instrument
Glutaraldehyde	+ 0.41
Streptavidin	+ 1.54
BSA	- 0.031
Biotin Anti-IgG	+ 0.05
IgG	+ 0.04

The signal observed by glutaraldehyde was high for a small molecular weight compound at a shift in resonance angle of 0.41°. There is an initial sharp increase in $\Delta\theta_R$ caused by the addition of glutaraldehyde, likely due to the change in refractive index of the sample from that of 100 mM HEPES, pH 7.4 buffer solution to that of glutaraldehyde. Following this, the increase in resonance angle is less steep, and likely caused by covalent immobilisation of glutaraldehyde into the structure of the hydrogel. Multiple scenarios can occur at this point, the desired outcome, is that a glutaraldehyde molecule would have a single reaction with the free primary amines present in the hydrogel, thus functionalising the film with free aldehydes. Other unwanted reactions can occur following the desired reaction including; the terminal

aldehyde could then react with another amine, thus increasing the level of cross-linking within the hydrogel; or, self-polymerisation of glutaraldehyde occurs *via* aldol condensation reactions (Figure 2.15). Due to the continuous increase in signal, it is suggested that the aldol condensation reaction was occurring, which while not ideal, still resulted in the functionalisation of the hydrogel film with free aldehyde groups for the next step.

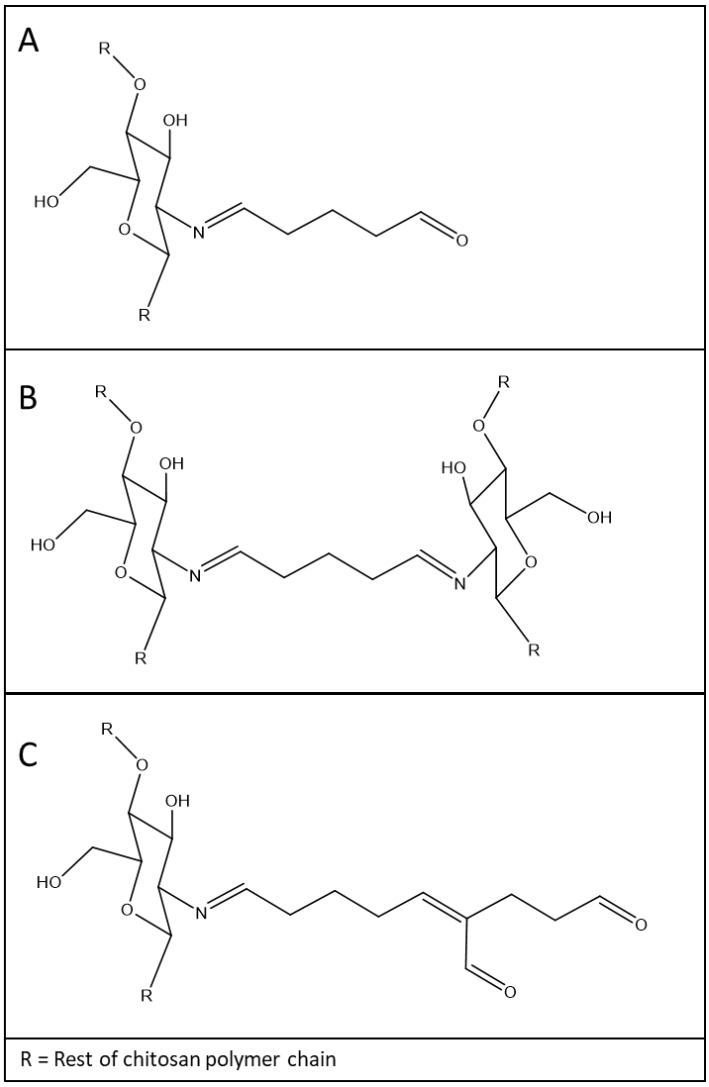

Figure 2.15: *Images depicting the possible reactions of chitosan with glutaraldehyde including (A) The desired single reaction. (B) the cross-linking of the hydrogel film. (C) The aldol reaction resulting in glutaraldehyde self-polymerisation. In all instances, R refers to the rest of the chitosan polymer chain.*

Streptavidin also produced a high $\Delta\theta_R$ with a change of 1.54°. Unlike the polymerisation explanation for glutaraldehyde, this is likely due to the sheer size of streptavidin, which has a molecular weight of approximately 60 kDa.[56] Due to the large molecular weight of the compound, the immobilisation of streptavidin into the structure of the hydrogel causes a larger change in refractive index than smaller compounds. The introduction of BSA was designed to react with any remaining free aldehyde groups, thus reducing the possibility of non-specific binding in the future. As discussed, the solution of BSA quickly plateaued, suggesting that non-specific protein reactive groups were no longer present, ultimately resulting in a signal of -0.031°. As can be seen throughout the HEPES buffer solution washes, the DDLW device was naturally inclined to drift in a negative direction, likely due to temperature effects on the device, thus from this we can say with certainty there was minimal binding of BSA to the DDLW device. Unfortunately, due to the structure of the 3D printed instrument, the temperature effects cannot be controlled to test if this is the case unlike the traditional benchtop laboratory-based instrument. Biotin anti-IgG and IgG were both introduced in low concentrations, thus providing low values for $\Delta\theta_R$ at 0.05° and 0.04° respectively. The purpose of using low concentrations for the biorecognition element and target analyte were to assess the sensitivity and useability of the instrument for real life samples which often contain very low levels of target analytes.

Unfortunately, as previously discussed, the signal had a general downward trend in $\Delta\theta_R$ likely due to temperature effects on the DDLW device; due to this, the signal as obtained from the graph may not be the correct absolute value, and these shifts in resonance angle may indeed be larger if the negative drift were to be accounted for.

2.6 Conclusion

Throughout this project, we have improved upon a literature method for the purification of chitosan. Due to chitosan being sourced from nature, the quality of material varies greatly with each batch, as such a purification method was required to removes small molecular weight impurities from the starting material. Through doing this, the uniformity of the material was increased, minimising the effect that batch to batch differences would have on results. Following on from that, we have deposited small volumes of purified chitosan solution onto clean glass substrates and evenly distributed the solution *via* spin coating. These polymer deposits were then cross-linked to form thin hydrogel films and doped with a solution of amine-reactive dye, thus leading to the development of a DDLW device. The RIS and porosity of these DDLW devices were then tested to ensure they are comparable with currently developed biosensors. Based on the results obtained from the traditional benchtop laboratory-based waveguide instrumentation, these procedures were then repeated with the use of a 3D printed waveguide instrument. Following this the DDLW devices were then utilised for the biosensing of clinically relevant analytes, in this instance IgG.

It was determined in this study that the small, portable, 3D printed waveguide instrument does produce RIS results comparable to that of its bulky traditional laboratory sized counterpart. Other than this, the 3D printed instrument enabled better detection of large molecules, and thus, should act as a more sensitive biosensor than its bulky counterpart. The final conclusion was the determination that not only was the 3D printed instrument in some instances superior to the bulky laboratory counterpart, but it is also comparable to current portable optical biosensors already in use.

2.7 Future Work

The work produced in this project has made great advancements in the potential use of LWs for POC testing, however there is still further to go. As one of the fundamental aspects of POC testing is fast readout time, the next step in this research must be to improve the protein immobilisation chemistry. While the immobilisation technique does indeed work and give results, the time taken to do so is approaching 7 hours, which is unfeasible at the POC site. Not only this, but as glutaraldehyde is used to cross-link the polymer chains in the first instance, a different linker would be advantageous for binding streptavidin to the hydrogel. This is because it will reduce the possibility of structural changes to the hydrogel itself during testing.

Following on from this, a range of hydrogels should be tested as potential LW devices. Through the use of synthetic polymers, we can control the number of available binding sites, thus potentially eliminating the need for BSA entirely. Not only this, but with synthetic polymers, the porosity of hydrogels can be more easily controlled. This would be advantageous as throughout the immobilisation process the LW becomes less porous to large molecules; starting with the highest possible porosity will improve porosity to the final target analyte. Some work within the group has already shown promising results with the use of functionalised agarose and polyacrylamide hydrogels in the formation of LW devices. Initial studies would be conducted to determine how suitable these polymers would be for use within this project. Following on from that, PEG polymers are an excellent opportunity to incorporate many functional groups into a single hydrogel, and would be more biocompatible than polyacrylamide so may be researched in the future.

The final direction for this research to progress in, would be to incorporate an internal reference into the LW device. While the traditional benchtop laboratory-based instrument can utilise a two-channel flow cell, with one channel being used for testing, and one being a reference, the 3D printed instrument cannot fit this flow cell into its design due to the small size. We have observed in this work that external effects can influence the signal, in this instance we observed a negative drift occurring throughout the study likely due to temperature changes throughout the day. The implementation of a reference would be extremely useful in determining any changes which are out of our control such as temperature and pKa of proteins. Therefore, for future work, this project would delve into the production of internal references in the LW device itself to allow for their use in the 3D printed instrument.

2.8 References

1 R. M. Califf, *Exp. Biol. Med. Maywood NJ*, 2018, **243**, 213–221.
2 Interference in immunoassays to support therapeutic antibody development in preclinical and clinical studies, https://www.future-science.com/doi/epub/10.4155/bio.14.127, (accessed 7 September 2022).
3 R. B. M. Schasfoort, Ed., *Handbook of surface plasmon resonance*, Royal Society of Chemistry, London, 2nd edition., 2017.
4 A. W. Snyder and J. D. Love, *Optical waveguide theory*, Chapman and Hall, London ; New York, 1983.
5 K. Okamoto, in *Fundamentals of Optical Waveguides*, Elsevier, 2006, pp. 1–12.
6 D. R. Paschotta, Numerical Aperture, https://www.rp-photonics.com/numerical_aperture.html, (accessed 22 September 2022).
7 D. Y. Smith and W. Karstens, *J. Phys. Conf. Ser.*, 2010, **249**, 012034.
8 H. Mukundan, A. Anderson, W. K. Grace, K. Grace, N. Hartman, J. Martinez and B. Swanson, *Sensors*, 2009, **9**, 5783–5809.
9 M. A. Cooper, *Drug Discov. Today*, 2006, **11**, 1061–1067.
10 K. Del Vecchio and R. V. Stahelin, *Methods Mol. Biol. Clifton NJ*, 2016, **1376**, 141–153.
11 R. Ulrich and W. Prettl, *Appl. Phys.*, 1973, **1**, 55–68.
12 B. Li and H. Ju, *BioChip J.*, 2013, **7**, 295–318.
13 R. Gupta and N. J. Goddard, *The Analyst*, 2013, **138**, 1803.
14 E. Benito-Peña, M. G. Valdés, B. Glahn-Martínez and M. C. Moreno-Bondi, *Anal. Chim. Acta*, 2016, **943**, 17–40.
15 J.-Q. Xi, M. F. Schubert, J. K. Kim, E. F. Schubert, M. Chen, S.-Y. Lin, W. Liu and J. A. Smart, *Nat. Photonics*, 2007, **1**, 176–179.
16 R. Gupta, N. A. Alamrani, G. M. Greenway, N. Pamme and N. J. Goddard, *Anal. Chem.*, 2019, **91**, 7366–7372.
17 R. Gupta and N. J. Goddard, *The Analyst*, 2013, **138**, 3209.
18 R. Gupta and N. J. Goddard, *Sens. Actuators B Chem.*, 2016, **237**, 1066–1075.
19 N. A. Alamrani, G. M. Greenway, N. Pamme, N. J. Goddard and R. Gupta, *The Analyst*, 2019, **144**, 6048–6054.
20 A. K. Pal, E. Labella, N. J. Goddard and R. Gupta, *Macromol. Chem. Phys.*, 2019, 1900228.
21 M. Zourob and N. J. Goddard, *Biosens. Bioelectron.*, 2005, **20**, 1718–1727.
22 R. Gupta, B. Bastani, N. J. Goddard and B. Grieve, *The Analyst*, 2013, **138**, 307–314.
23 M. Zourob, S. Mohr, P. R. Fielden and N. J. Goddard, *Sens. Actuators B Chem.*, 2003, **94**, 304–312.
24 M. Zourob, S. Mohr, B. J. T. Brown, P. R. Fielden, M. McDonnell and N. J. Goddard, *Sens. Actuators B Chem.*, 2003, **90**, 296–307.
25 R. Gupta and N. J. Goddard, *Sens. Actuators B Chem.*, 2020, **322**, 128628.
26 M. Zourob, S. Mohr, B. J. Treves Brown, P. R. Fielden, M. B. McDonnell and N. J. Goddard, *Anal. Chem.*, 2005, **77**, 232–242.
27 W. J. Im, B. B. Kim, J. Y. Byun, H. M. Kim, M.-G. Kim and Y.-B. Shin, *Sens. Actuators B Chem.*, 2012, **173**, 288–294.
28 N. J. Goddard and R. Gupta, *Sens. Actuators B Chem.*, 2020, **309**, 127776.
29 R. Gupta and N. J. Goddard, *Sens. Actuators B Chem.*, 2017, **244**, 549–558.
30 N. J. Goddard, H. J. Dixon, N. Toole and R. Gupta, *IEEE Trans. Instrum. Meas.*, 2020, 1–1.
31 N. J. Goddard and R. Gupta, *Sens. Actuators B Chem.*, 2019, **301**, 127063.
32 L. Cerdán, A. Costela, I. García-Moreno, O. García and R. Sastre, *Appl. Phys. B*, 2009, **97**, 73–83.
33 T. Songjaroen, W. Dungchai, O. Chailapakul, C. S. Henry and W. Laiwattanapaisal, *Lab. Chip*, 2012, **12**, 3392.

34 A. St John and C. P. Price, *Clin. Biochem. Rev.*, 2014, **35**, 155–167.
35 P. B. Luppa, C. Müller, A. Schlichtiger and H. Schlebusch, *TrAC Trends Anal. Chem.*, 2011, **30**, 887–898.
36 R. Sista, Z. Hua, P. Thwar, A. Sudarsan, V. Srinivasan, A. Eckhardt, M. Pollack and V. Pamula, *Lab. Chip*, 2008, **8**, 2091.
37 A. Warsinke, *Anal. Bioanal. Chem.*, 2009, **393**, 1393–1405.
38 B. McDonnell, S. Hearty, P. Leonard and R. O'Kennedy, *Clin. Biochem.*, 2009, **42**, 549–561.
39 A. Larsson, R. Greig-Pylypczuk and A. Huisman, *Ups. J. Med. Sci.*, 2015, **120**, 1–10.
40 C. P. Price, *BMJ*, 2001, **322**, 1285–1288.
41 C. Seery, Blood glucose test strips (diabetes test strips) are a key component of blood glucose testing., https://www.diabetes.co.uk/diabetes_care/diabetes-test-strips.html, (accessed 12 September 2022).
42 Glucose - Urine, https://www.ucsfhealth.org/Medical Tests/003581, (accessed 22 September 2022).
43 C. Seery, Keeping an accurate idea of your blood glucose levels is an integral part of successful diabetes management. Blood glucose meters allow you to do this., https://www.diabetes.co.uk/diabetes_care/blood_glucose_monitor_guide.html, (accessed 17 October 2022).
44 Glucose Test Strip - Precision Laboratories Test Strips, https://www.preclaboratories.com/product/glucose-test-strip/, (accessed 17 October 2022).
45 W. Jung, J. Han, J.-W. Choi and C. H. Ahn, *Microelectron. Eng.*, 2015, **132**, 46–57.
46 X. Qiu, M. G. Mauk, D. Chen, C. Liu and H. H. Bau, *Lab. Chip*, 2010, **10**, 3170.
47 D. Elieh-Ali-Komi and M. R. Hamblin, *Int. J. Adv. Res.*, 2016, **4**, 411–427.
48 F. A. Vicente, M. Huš, B. Likozar and U. Novak, *ACS Sustain. Chem. Eng.*, 2021, **9**, 3874–3886.
49 R. Signini and S. P. Campana Filho, *Polym. Bull.*, 1999, **42**, 159–166.
50 H. F. EL Sharif, F. Giosia and S. M. Reddy, *J. Mol. Recognit.*, , DOI:10.1002/jmr.2942.
51 PubChem, Insulin human, https://pubchem.ncbi.nlm.nih.gov/compound/118984375, (accessed 30 September 2022).
52 B.-A. Sela, *Harefuah*, 2002, **141**, 631–635, 665.
53 T. Maier, A. Schmidt, M. Güell, S. Kühner, A. Gavin, R. Aebersold and L. Serrano, *Mol. Syst. Biol.*, 2011, **7**, 511.
54 C. E. Chivers, A. L. Koner, E. D. Lowe and M. Howarth, *Biochem. J.*, 2011, **435**, 55–63.
55 Avidin-Biotin Interaction - UK, https://www.thermofisher.com/uk/en/home/life-science/protein-biology/protein-biology-learning-center/protein-biology-resource-library/pierce-protein-methods/avidin-biotin-interaction.html, (accessed 30 September 2022).
56 R. Modanloo Jouybari, A. Sadeghi, B. Khansarinejad, S. Sadoogh Abbasian and H. Abtahi, *Rep. Biochem. Mol. Biol.*, 2018, **6**, 178–185.

Chapter 3 – Photofunctionalisable Hydrogels

3.1 Introduction

Protecting groups (PGs) have been used for decades to help maintain control within reactions in which there are multiple potential reactive sites.[1] Many of these reactions occur within solution, therefore, to promote selective functional group deprotection, PGs with different cleavage conditions are implemented.[2] This is commonly observed in peptide synthesis, where the terminal amine functional group is protected with a 9-fluorenylmethoxycarbonyl (FMOC) PG which is cleaved under basic conditions, whereas the amino acid side chains are protected with a *tert*-butyl PG, which undergoes cleavage in acidic conditions.[3] Methods such as this are the most widely used techniques to maintain control of deprotections within solution, however, for samples in the solid state, photolabile PGs (PPGs) add an increased level of control in deprotection which is not possible in liquid phase reactions. As hydrogels are a solid three-dimensional (3D) structure, protected functional groups in this structure are immobilised; thus, by targeting a specific region for deprotection, selective uncaging can occur with the use of a single PG.

This chapter will discuss the development of photofunctionalisable hydrogels; from the reaction of hydrogels with PPGs to the development and synthesis of new photocaged monomers based on a variety of PPG structures.

3.2 Hydrogels

A hydrogel is commonly described as being a 3D network of hydrophilic polymers.[4] The range of polymers suitable to make hydrogels is vast, encompassing almost any existing hydrophilic polymer, both synthetic and natural.[5] Due to the hydrophilicity of these polymers, they are able to absorb up to 1000 × their dry mass of water into their structure.[4]

Despite their hydrophilic nature, hydrogels themselves are not water soluble due to the many cross-links between the polymer chains. These cross-links can be caused by both physical interactions, such as hydrogen bonding; and chemical bonds, such as covalent bonding.

Single component hydrogels are, as the name suggests, hydrogels formed from a single polymer. For hydrogel formation to occur, cross-links are formed *via* physical interactions within the polymer chains themselves.[6] An example of this is agarose, a polymer formed from alternating disaccharide units. The heating of agarose in solution allows for the hydrogen bonding to drive the formation of double helix structures which result in the formation of a hydrogel.[7] Another example is collagen, which self-assembles into triple helical structures, which then self-assemble into collagen fibres and ultimately, assemble into a 3D hydrogel structure (Figure 3.1). It is suggested that the zwitterionic nature of collagen proteins is the driving force behind this self-assembly procedure.[8]

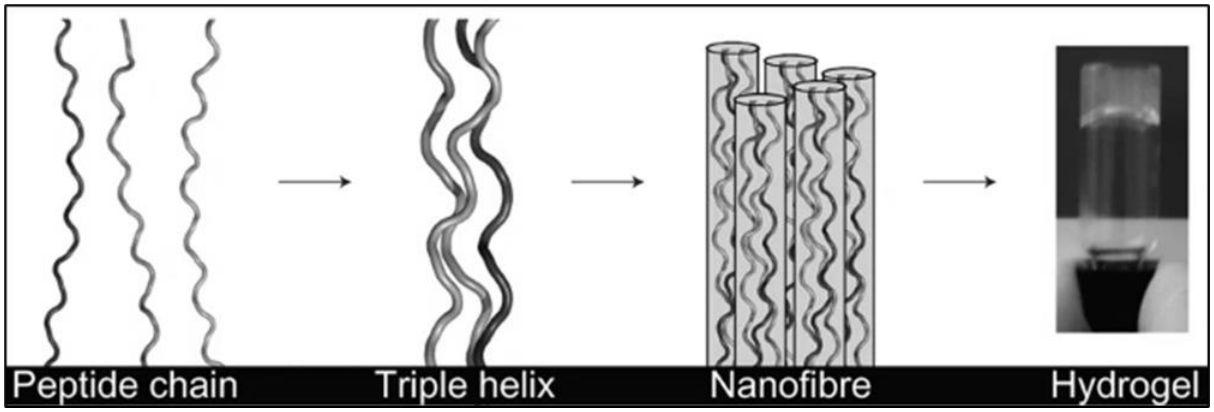

Figure 3.1: *An image displaying the formation of single composite collagen hydrogels. Image adapted from O'Leary et al.*[8]

Conversely to single component hydrogels, we have the more common multicomponent hydrogels. Broadly speaking, multicomponent hydrogels are structures comprised of more than one compound. This can be in the form of hybrid hydrogels, containing at least two different polymeric chains such as collagen-agarose hydrogels.[9] The use of a single polymer in collaboration with a chemical cross-linker also constitutes a multicomponent hydrogel.[10] A well-known example of this is the polyacrylamide (PAAm) gel used in gel electrophoresis. The PAAm hydrogel contains *N,N'*-methylenebis(acrylamide) (BAAm) monomer units for cross-linking (Figure 3.2).[11] It is under this category that most hydrogels in use fall.

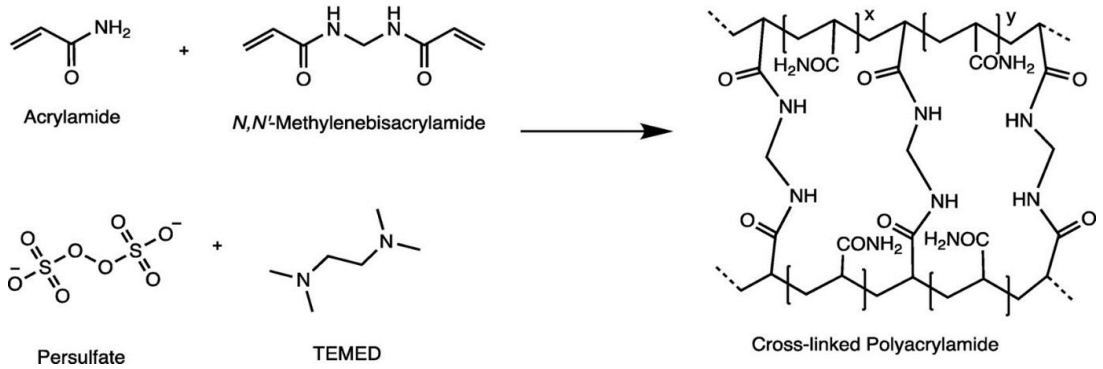

Figure 3.2*: An image of the formation of a PAAm hydrogel using BAAm as a cross-linking agent. Image used from Ferrag et al.*[12]

It was previously discussed how hydrogen bonding is the basis for hydrogel formation within agarose gels. This is not the only method of physical cross-linking however, other methods include hydrophobic interactions and ionic interactions.[6] Polymers such as alginate which contain many anionic carboxylate groups undergo cross-linking *via* ionic interactions. The addition of metal cations such as Ca^{2+}, Mg^{2+} and Zn^{2+} form ionic bonds with two different carboxylate groups, thus cross-linking the polymer chains.[13]

The most widely used form of cross-linking hydrogels is through the use of covalent bonds, known as chemical cross-linking. Chemical cross-linking can be used for polymers which do not form hydrogels alone. Chitosan can form hydrogels upon addition of glutaraldehyde *via* a dehydration reaction, in which primary amines react with aldehydes to produce imine functional groups.[14] Chemical cross-linking is also used to increase the mechanical strength of hydrogels which can form *via* physical cross-linking. For example, the formation of collagen hydrogels, as previously discussed, can be due to physical interactions, however, the additional cross-linking of these hydrogels with glutaraldehyde has been known to improve the hydrogel physicochemical properties.[15]

As can be seen, the number of different characteristics of hydrogels are astounding. It is due to this that the classification of hydrogels is not a simple process, with categories sometimes overlapping. Hydrogels can be classified based on a plethora of characteristics such as polymer source, cross-linking method, physical properties, charge etc. (Figure 3.3).[6]

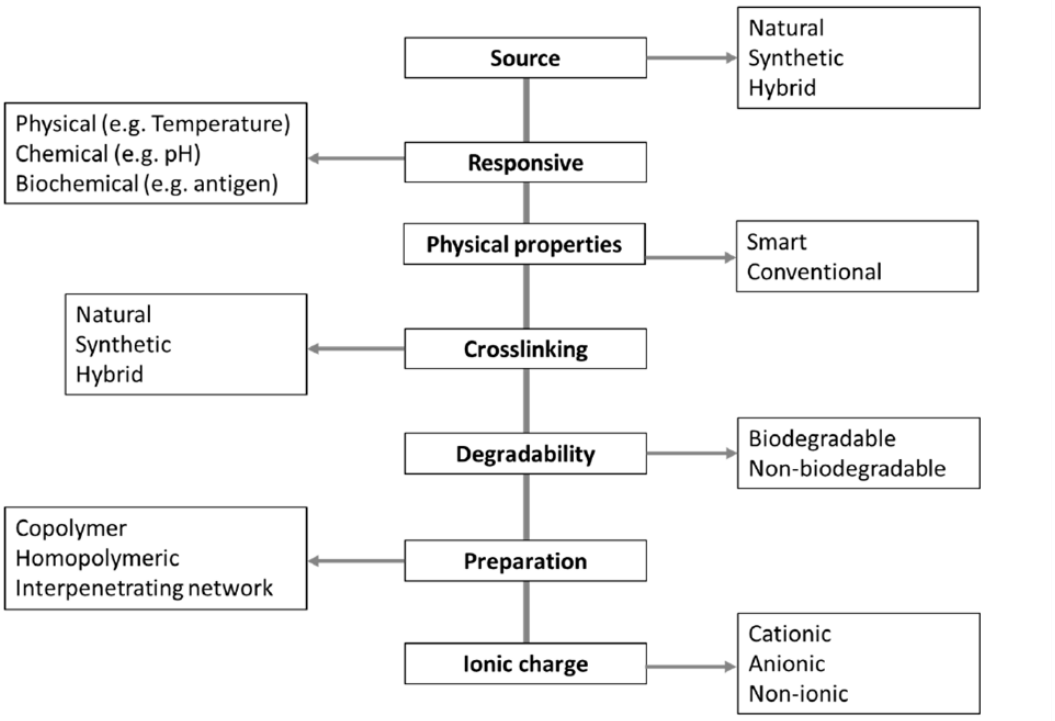

Figure 3.3: *An image displaying the many possible classification methods of hydrogels. Image adapted from Karoyo et al.*[6]

The uses for hydrogels are vast. Due to their biocompatibility they have many medical applications, including but not limited to, drug delivery, biosensors, and electrophoretic media for the separation of DNA.[16,17] Not only are hydrogels frequently used in the medicinal industry, they also have uses elsewhere, such as the removal of metal ion water pollutants, baby diapers, absorbent pads, agriculture and horticulture.[4,18] One reason for the many applications of hydrogels is that they can be created in a number of forms such as micro and nano-sized particles, as thin films or large blocks.[5]

3.2.1 Natural Polymers

Naturally occurring polymers such as proteins, polysaccharides and DNA are often used for the production of biopolymer-derived hydrogels; these biologically sourced materials

are advantageous as due to their nature, they are inherently highly biocompatible.[19] It is due to this that these hydrogels are often implemented for the development of artificial extracellular matrices (ECMs), as the hydrogels can be created from polymers common to those found in the natural ECM.[20] Furthermore, biopolymer-based hydrogels are desirable for *in-vivo* use as the degradation products are those which will naturally be found within the body, therefore will cause minimal unwanted side effects.[19]

This biocompatibility of degradation products has allowed for the use of biopolymer-derived hydrogels as drug delivery systems (Figure 3.4). The porous nature of hydrogels allows for the loading of drugs into their structures, then the drugs can be released *in-vivo* by one of two methods, either the slow diffusion of the drug out of the 3D structure, or to be released by the degradation of the polymeric structure.[21]

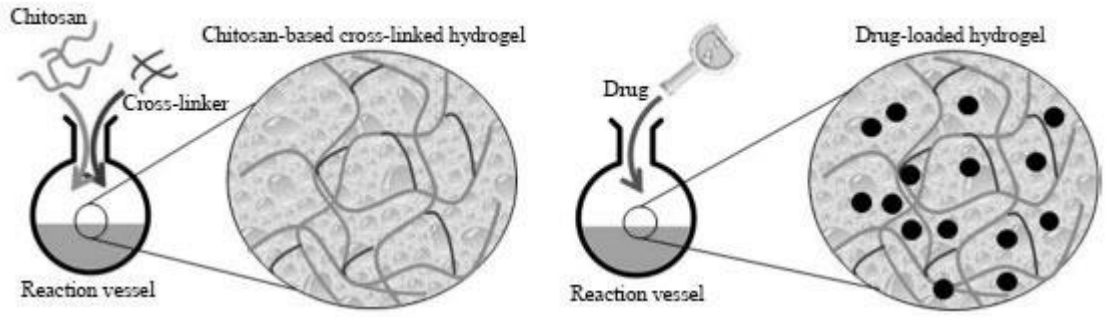

Figure 3.4: *An image displaying the loading of drugs into a natural polymer-based chitosan hydrogel. Image used from Villalba-Rodriguez et al.*[22]

As many of nature's polymers are based on proteins or polysaccharides, this results in the presence of many free functional groups such as alcohols, amines, carboxylic acids and amides.[23,24] These groups allow for the incorporation of analyte-reactive groups into the structure of the hydrogel, enabling their use as a medium for biosensors.

Unfortunately, biopolymer-derived hydrogels are often comprised of structurally weak polymers, limiting their usability.[25] It is due to this that many biopolymer-derived hydrogels are in-fact multicomponent hydrogels, containing either chemical cross-linkers to form strong bonds, or synthetic co-polymers to add rigidity to the structures.

3.2.2 Synthetic Polymers

Research into the development of synthetic hydrogels has been ongoing for over 60 years.[26] This is due to synthetic hydrogels having the potential for larger volumes of water absorption, long shelf-lives and an increased mechanical strength in comparison to their biopolymer-derived analogues.[6]

Hydrogels formed through the use of synthetic polymers can be either homopolymers, co-polymers or interpenetrating networks.[23] As suggested by the name, homopolymers are comprised of a single repeating monomer unit.[27] Slightly more complex is the co-polymer, which is formed through the co-polymerisation of two of more different monomer units.[28] Interpenetrating networks are the most complex of the three. These hydrogels are formed through the cross-linking of different types of polymer chains together (Figure 3.5).[29]

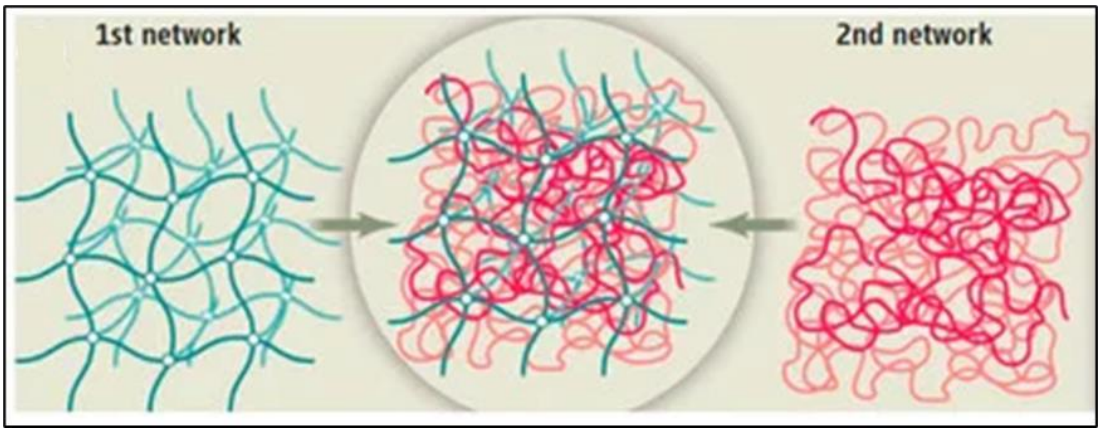

Figure 3.5: *An image displaying the complex structure of interpenetrating networks. Image adapted from Panteli et al.*[30]

Before a synthetic hydrogel can be created however, polymer chains must first be produced. There are numerous methods for the polymerisation of monomers to form long polymeric chains, the method most notably seen throughout nature is condensation polymerisation. In this instance, monomers have functional groups which react together and result in the release of water as a by-product, notable examples are the formation of proteins and polyesters.[31]

Despite the simplicity of condensation polymerisation, addition polymerisation methods are most commonly used for the production of synthetic polymers; these methods require the presence of functional groups on the monomers, such as unsaturated bonds. An initiator compound creates a reactive site on the functional group of the monomer, this forms a covalent bond with another monomer, and chain propagation occurs.[32] Examples of addition polymerisation techniques are free radical polymerisation, the use of free radical groups to initiate chain propagation; and ionic polymerisation, the formation of a charged group within a monomer, other monomers covalently bind in an attempt to stabilise the charge.[32]

Synthetic hydrogel properties can be altered easily by introducing new components which respond to external stimuli (Figure 3.6). For example, the addition of *N*-isopropylacrylamide monomers into a co-polymer acrylamide hydrogel is known to incorporate temperature sensitive swelling abilities.[33] To introduce pH responsive swelling abilities into a hydrogel, often acidic groups such as itaconic acid are integrated into the hydrogel structure.[34] Responses to external stimuli such as pH and temperature can make for ideal biosensing materials, however, these are not the only methods of detecting biomarkers.[35] The immobilisation of bioreceptors into the structure of a hydrogel is another

way to introduce a biosensing capability. This can be achieved through the polymerisation with biorecognition element reactive monomers such as those containing free primary amines, thiols or carboxylic acid functional groups.[36]

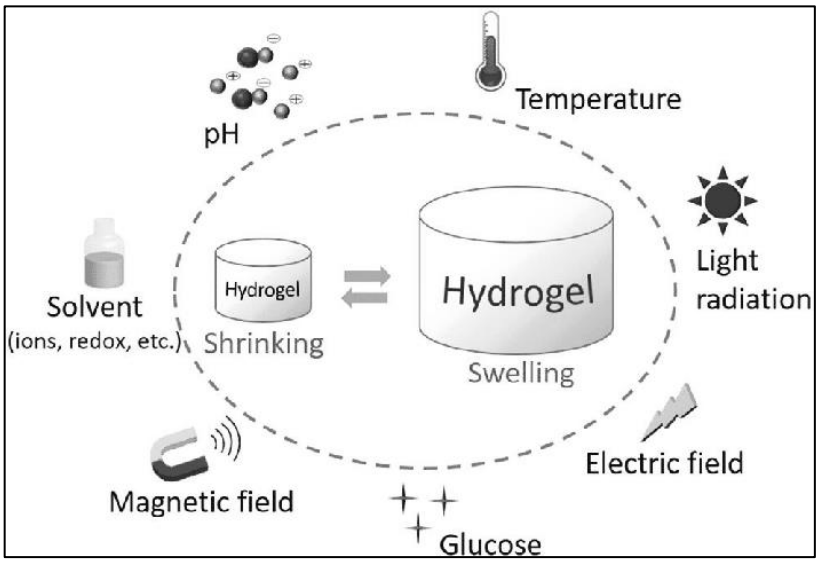

Figure 3.6: *An image displaying the various stimuli which can trigger an observable response by a hydrogel. Image used from Fu et al.*[37]

The mechanical strength of hydrogels and their ability to absorb analytes into their 3D structure increases the number of available binding sites compared to non-porous substrates.[38] Covalent immobilisation in biosensors often makes use of functional groups such as primary amines, thiols and carboxylic acids.[38] In biopolymer-derived hydrogels, these functional groups are often highly prevalent, for instance, chitosan can contain up to one primary amine per repeating unit, depending on the level of deacetylation, leading to many potential immobilisation sites.[39] Too many immobilisation sites may result in non-specific analyte binding, resulting in false signals, therefore this is not a desirable outcome. Due to the versatility of synthetic polymers, the number of biorecognition element binding sites can be

easily controlled through molar ratios; this is advantageous as it provides more control and uniformity within the hydrogel-based biosensors.

3.3 Protecting Groups

The formation of covalent bonds within chemistry is reliant on the use of functional groups. In some instances, the presence of multiple functional groups with similar reactivities within a compound can result in undesirable bond formations; in an attempt to regulate this, PGs have entered development to temporarily conceal functional groups.[40]

In some cases, multiple functional groups require protecting, for instance in solid-phase protein synthesis (Figure 3.7). The monomeric components of proteins, amino acids, contain both primary amine and carboxylic acid functional groups; these two functional groups react together to form amide bonds.[41] To prevent self-polymerisation of amino acids, the amine terminal is frequently blocked with a PG. The starting amino acid is loaded onto the solid support resin *via* the carboxylic acid terminal, followed by the removal of the amine PG. The chain then propagates through the addition of monomers which bind to the peptide chain *via* the carboxylic acid followed by amine release.[42] Unfortunately, this PG alone is not enough to control the protein synthesis technique. Many amino acids contain side chains which are also functionalised with carboxylic acids, amines and other reactive groups such as alcohols which can interrupt chain propagation. To minimise the effects of these side chains, they also require PGs.[43] Initial methods to deprotect amines while maintaining the protection of reactive side chains employed the use of *tert*-butoxycarbonyl (Boc) and benzyl PGs. Boc was used to protect the *N*-terminal of the peptide chain and was rapidly released in the presence of weak acid; conversely the benzyl side chain PG had slow deprotection kinetics in the

presence of weak acid, thus was cleaved at the end of the synthesis with a strong acid. Unfortunately, while the benzyl PG was slow to deprotect in the presence of weak acid, deprotection did still occur.[3] In an attempt to allow for the more selective removal of PGs, procedures moved on to using two different PGs which cleave *via* different mechanisms, known as an orthogonal protection scheme. In this instance, the amine is protected with FMOC groups which are cleaved under basic conditions, whereas the side-chains are protected with *tert*-butyl PGs that undergo acid catalysed cleavage.[3]

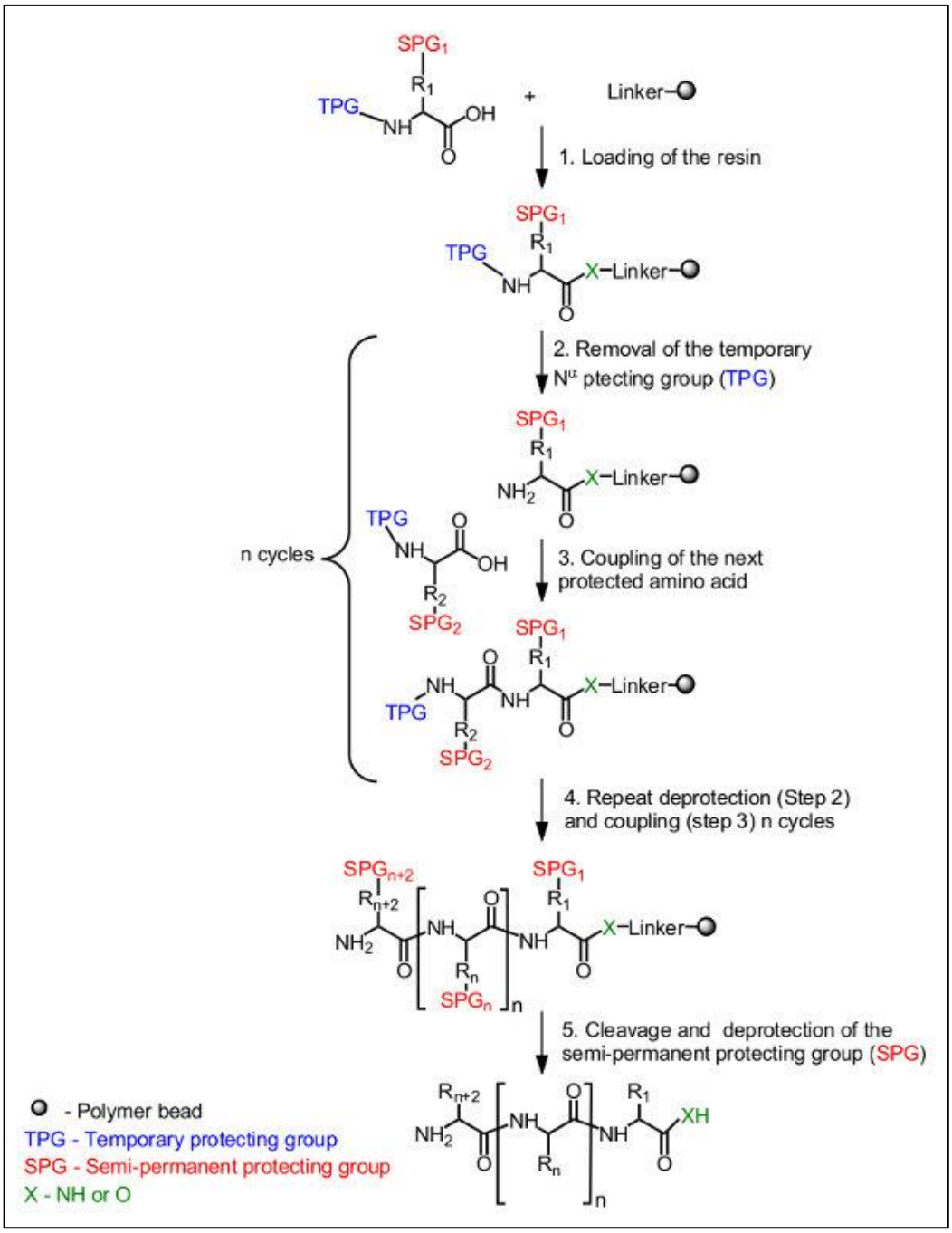

Figure 3.7: *A flow chart depicting solid-phase protein synthesis, where R refers to undefined amino acid side chains. Image used from Qvit et al.*[42]

As described, orthogonal methods allow for the chemo-selective PG cleavage, through the use of different cleavage methods such as acid and base catalysis, however, there are other methods which can initiate cleavage. PPGs are cleaved not with chemicals, but with

light.[44] Light is an ideal reagent in chemical reactions as it is low cost and does not add to chemical waste, not only this, but photochemical reactions allow for the increased spatio-temporal control of reactions.[45,46]

PGs of this class have been studied with increasing interest since the development of the first, an *o*-nitrobenzyl ester (Figure 3.8), in the 1960's.[47,48] Nitrobenzyl-based PPGs are known to be effective for polar groups such as alcohols and primary amines.[49]-

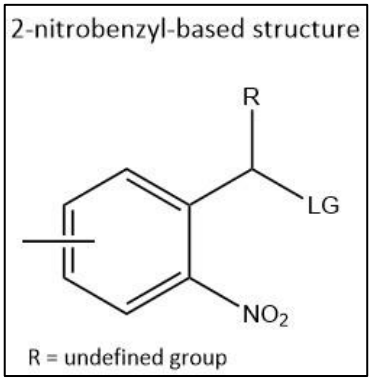

Figure 3.8: *An image of the ortho-nitrobenzyl structure that is the basis for many PPGs, R is a variable functional group. Image adapted from Wang.*[50]

Another common structure found among PPGs is the coumarin structure. The discovery of the photoactivity of coumarin derivatives dates back almost 40 years.[51] Coumarin derived PPGs for functional groups such as alcohols and amines are often utilised by forming carbonate, carbamate, phosphate or carboxy bonds as they produce good leaving groups.[46] Research has recently been conducted into the photocaging of thiols with a coumarin PPG *via* sulfide bond formation, resulting in a more complex deprotection mechanism.[52]

Much research has been conducted into the development of longer wavelength absorbing PPGs, to red-shift the deprotection wavelength to a less harmful region.[48] One

potential way of increasing the absorption wavelength of PPGs is through the creation of a more highly conjugated system.[46] The use of this method has led to the development of PPGs based on BODIPY dye structures leading to groups which can cleave with 680 nm light.[53] Coumarin and coumarin derivatives can absorb light at a variety of wavelengths, ranging from 200 nm to 500 nm, dependant on structural components (Figure 3.9), providing a wide range of PPGs.[54] Their system can become more conjugated through the incorporation of an electron withdrawing group at position 3, usually a functional group containing unsaturated bonds such as a nitro or cyano group. Other ways of increasing the absorbance maxima of a coumarin derivative are through thionation of the carbonyl or the incorporation of a highly electron donating group at position 7.[54,55]

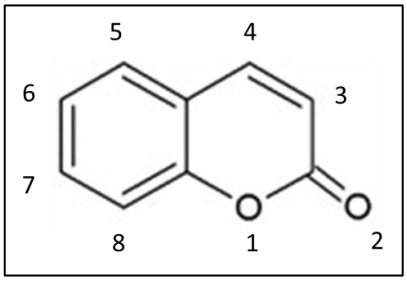

Figure 3.9: *An image showing the structure of a simple coumarin with labelling of the positions.*

The development of PPGs has led to a wide variety of structures with differing absorption wavelengths. Nitrobenzyl PPGs are by far the most widely used groups, due to the vast levels of research conducted into them, unfortunately, they only absorb at high energy wavelengths of light, towards the ultraviolet (UV) region. Coumarin PPGs are a simple, versatile structure which can be fine-tuned to absorb at different wavelengths of light, making them safer for biological specimens. Both of these groups can be cleaved from polar functional groups through the use of light selectively.

3.4 Project Aims

Previous work within the group has proven the ability to use a commercially available PPG, 4,5-dimethoxy-2-nitrobenzyl chloroformate (NVOC-Cl), to photocage monomers such as allylamine and 2-(dimethylamino)ethyl methacrylate (DMEMA).[56] Following this, the monomer has been incorporated into the structure of hydrogels. The purpose of this was to allow for the selective release of PPGs within a hydrogel to produce free primary amines, which can be used as the basis for immobilisation chemistry within sensors. The photocaged hydrogel, NVOC-EA-DMEMA, contains a charged quaternary amine, which may cause unwanted electrostatic interactions with proteins when sensing. Due to this, the desired outcomes of this project are two-fold, firstly:

1. To determine if hydrogels are compatible with polar organic solvents.
2. To photocage pre-formed hydrogels with commercially available PPGs.

Secondly:

3. To design and synthesise amine-reactive PPGs which are otherwise inert.
4. To photocage an amine-containing monomeric unit with the PPGs, to allow for future polymerisation.
5. To assess the ability of the monomer to absorb light at a particular wavelength, thus assessing the ability to photodeprotect.

3.5 Results and Discussion

3.5.1 Photocaging of Hydrogels

3.5.1.1 The Effect of Organic Solvents on Hydrogel Structure

As it was determined that chitosan, as a naturally occurring polymer, contains too many protein-reactive binding sites, this work moved on to study synthetic polymers. Hydrogels formed of PAAm were decided upon as gel electrophoretic methods have already proven PAAm to be compatible with proteins.[57] A major requirement for these hydrogels to be suitable for biosensing purposes is the presence of a primary amine, therefore, the monomer *N*-(3-aminopropyl) methacrylamide (APMA) was incorporated into the structure as a co-monomer.

To test hydrogels for suitability as waveguide devices, they were first supported onto a glass substrate. To do this glass slides were cleaned with 5% decon 90, deionised (DI) water and ethanol, followed by functionalisation with chloro(dimethylvinyl)silane (CDMVS), this was to ensure strong interactions between the glass substrate and the hydrogel film. To create a thin spacer, another glass slide was again cleaned and this time functionalised with trimethoxy(trifluoropropyl)silane (TMTFS), this functionalisation was to create a hydrophobic layer on the top glass slide to minimise interactions between the hydrogel and the spacers. A solution of 1.1 µm latex bead solution (1 µL) was deposited at 8 equal distances around the edge of the glass slide. Through sandwiching a hydrogel mixture containing AAm, APMA, BAAm, 10% ammonium persulfate (APS) solution and *N,N,N',N'*-tetraethylmethylenediamine (TEMED) between these glass slides and compressing the two together with a 500 g weight, ≈ 1.1 µm thick AAm/APMA co-monomer hydrogel films were produced.

These films were tested for their refractive index sensitivity (RIS) and porosity to various sized polyethylene glycol (PEG) chains. As discussed in Chapter 2.5.4 the RIS of a leaky waveguide (LW) device is a measure of shift in resonance angle ($\Delta\theta_R$) versus the refractive index (RI) of the sample solution (Equation 3.1).

$$\boldsymbol{RIS = \frac{\Delta\theta_R}{RI}}$$

Equation 3.1: *An equation displaying the relationship between RIS, $\Delta\vartheta_R$ and the RI of a solution.*

To measure RIS, a calibration curve was first made, using glycerol solutions of known refractive index and measuring the response they created. The calibration curve consisted of glycerol solutions of concentrations equal to 0.125%, 0.25%, 0.5%, 1% and 2% (v/v) in a 100 mM 4-(2-hydroxyethyl)-1-piperazineethanesulfonic acid (HEPES), pH 7.4 buffer solution. Glycerol was the compound of choice as it is of a similar structure to the PEG chains that were used later, it is inert to the hydrogel film, and it is a small compound that should be able to penetrate the hydrogel film completely. Prior to RIS testing, the RI of these solutions was measured in triplicate. A baseline signal was created with buffer solution, following that, each solution was then added to the leaky waveguide device sequentially, then finally washed out back to the baseline with HEPES buffer solution (Figure 3.10).

Through plotting the average $\Delta\theta_R$ for each refractive index solution, we obtained the calibration curve. Based on Equation 3.1, we see that the gradient of this graph is equal to the RIS, thus making the calculation of RIS simple (Figure 3.10).

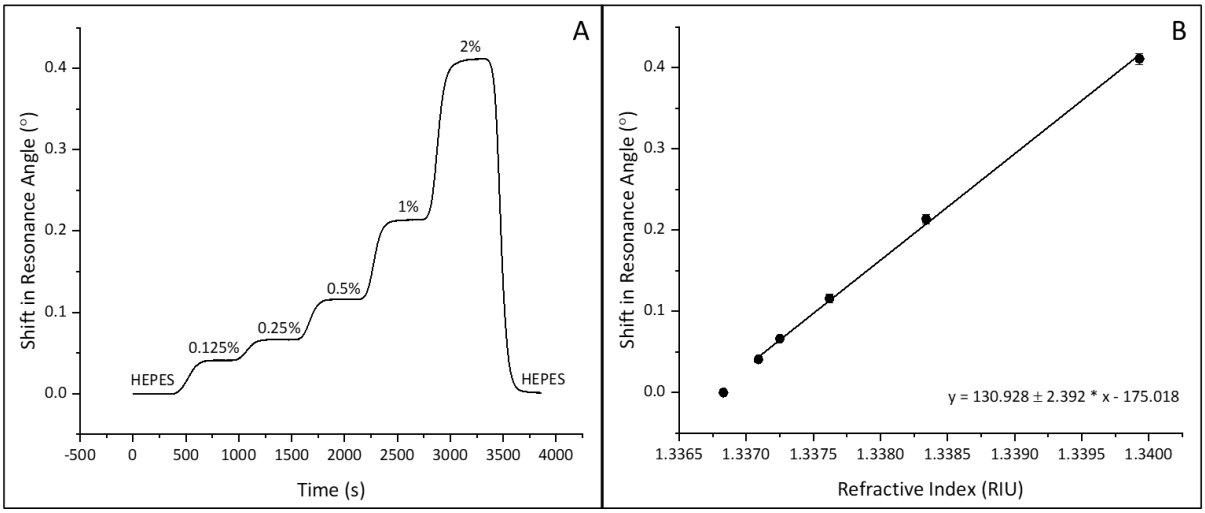

Figure 3.10: *(A) A graph displaying the $\Delta\vartheta_R$ caused when glycerol solutions of concentrations equal to 0.125%, 0.25%, 0.5%, 1% and 2% in a 100 mM HEPES, pH 7.4 buffer solution are introduced to an AAm/APMA co-polymer based LW device and (B) A graph depicting the average $\Delta\vartheta_R$ in degrees caused by solutions of different refractive indices on an AAm/APMA co-polymer based LW device. Data is an average of 3 repeats of each study.*

From the above graph (Figure 3.10), we can see that the RIS of this device is equal to 130.928 ± 2.392° RIU^{-1}. These measurements were completed in three-fold to test for variability across different leaky waveguide devices. In Chapter 2.5.4, we observed that chitosan-based dye doped LW devices had a RIS of 124.515 ± 11.911° RIU^{-1}. We can therefore determine that AAm/APMA co-polymer hydrogel-based LW devices are more sensitive, and based on the associated error, more consistent than chitosan-based dye doped LW devices. Based on this experimental data, the ease of control in terms of number of reactive functional groups and the elimination of the dye, AAm/APMA hydrogels are an improvement for LW device materials when compared to chitosan.

A sensitive LW device is required for usability, however, as biomarkers can often be large in size, another important characteristic in a LW biosensor is porosity. As discussed earlier (Chapter 2.5.5) conventional methods for the determination of porosity are unsuitable for these studies; therefore, in order to test for porosity, we utilise the RIS value obtained

through the calibration curve. Through rearranging the equation of the line of best fit obtained from a RIS testing graph (Equation 3.2), by multiplying the RI of the analyte solution by the RIS of the LW device with the addition of the intercept, we obtain a value for the expected $\Delta\theta_R$ if a film were to be 100% porous to the analytes.

$$\boldsymbol{\Delta\theta_{R\,(theoretical)} = (RIS \times RI) + c}$$

***Equation 3.2**: An equation showing how we can rearrange the straight line equation given from RIS testing graphs to achieve the calculation of a theoretical $\Delta\vartheta_R$ ($\Delta\vartheta_{R(theoretical)}$) caused by 100% permeation of a solution of (RI) into a LW device of (RIS) where (c) is equal to the intercept on the RIS graph.*

As proteins within the human body tend to have an average mass of 46.4298 kDa, it was important to test how porous the LW devices were to large molecules.[58–60] To test the porosity of LW devices around this range of mass, 1% (w/v) solutions of PEG chains were used as different molecular weight templates. The different masses of PEG used were 10 kDa, 100 kDa and 300 kDa, this was the achieve a range of masses encompassing and exceeding the average mass of human proteins. In Figure 3.11 below, we see the trace given to us from the input of these solutions and their subsequent washing out of the film for AAm/APMA co-polymer hydrogel-based LW devices.

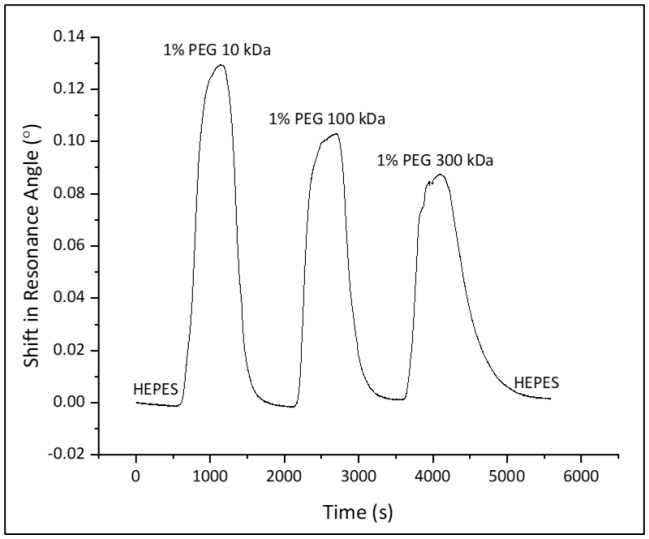

Figure 3.11: *A graph displaying the $\Delta\vartheta_R$ caused when 1% polyethylene glycol solutions of sizes ranging from 10 kDa to 300 kDa in a 100 mM HEPES, pH 7.4 buffer solution are introduced to an AAm/APMA co-polymer based LW device. Data is an average of 3 repeats of the study.*

Through comparing the average $\Delta\theta_R$ at the signal peak, to the expected values that have been calculated using Equation 3.2 and documented in Table 3.1, we can calculate the porosity of the film to different molecular weight compounds as a percentage of completely porous. If we refer back to Chapter 2.5.5, Table 2.1, we can observe that the porosity of these LW devices is comparable to those formed using chitosan.

Table 3.1: *A table listing the refractive index of 1% PEG solutions used for porosity studies, the theoretical $\Delta\vartheta_R$, the obtained $\Delta\vartheta_R$, and the porosity of the film as a percentage of these values where the theoretical signal indicates 100%. Data is an average of 3 repeats of the study.*

Solution	Refractive Index (RIU)	Theoretical $\Delta\theta_R$ (°)	Actual $\Delta\theta_R$ (°)	Porosity (%)
1% PEG 10 kDa	1.33817	0.18592	0.12781	68.74
1% PEG 100 kDa	1.33826	0.19771	0.10110	51.14
1% PEG 300 kDa	1.33821	0.19116	0.08561	44.78

These slides were exchanged out of water and into the organic solvents methanol, 1,4-dioxane and dimethylsulfoxide (DMSO) by changing the composition of the solution they were submerged in by 10% every 90 minutes. Following this process, the hydrogel films were then returned to water, and RIS and porosity tests were repeated (Figure 3.12) to determine if the organic solvent had resulted in structural changes to the hydrogel. The reason for this was that the PPG used previously within the group, NVOC-Cl, is water reactive, thus was unable to photocage hydrogels in an aqueous media. Due to this, the determination of a suitable organic solvent for this reaction was necessary.

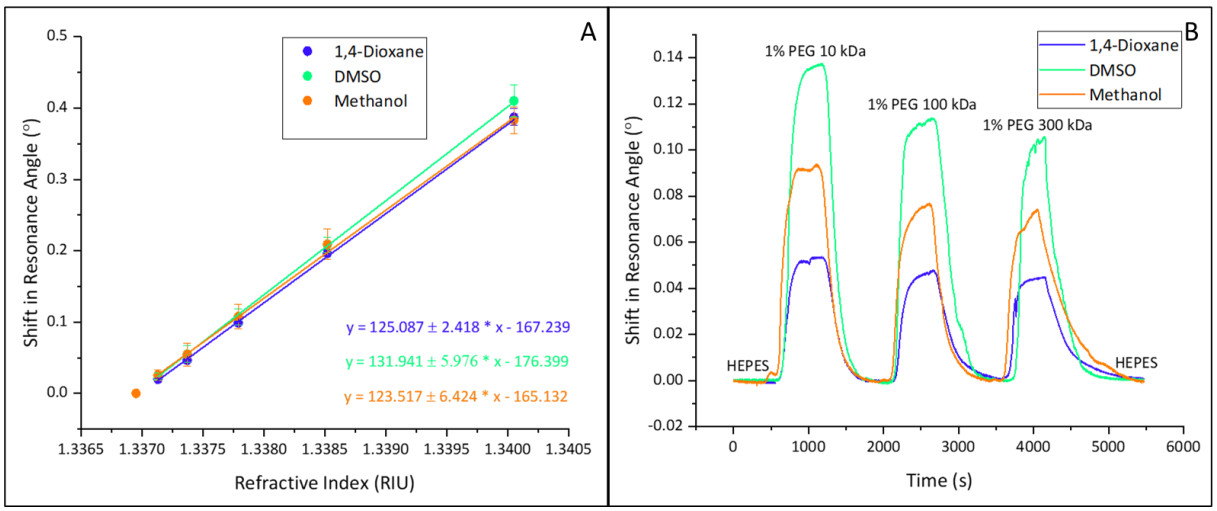

***Figure 3.12**: Graphs depicting the effect of methanol, DMSO and 1,4-dioxane on the (A) RIS of an AAm/APMA co-polymer based LW device and (B) the porosity of an AAm/APMA co-polymer based LW device. Data is an average of 3 repeats of each study.*

Following the repeated functionality testing of the hydrogel films, the solvent which had the largest effect on RIS was methanol, decreasing the RIS from 130.928 ± 2.392° RIU^{-1} to 123.517 ± 6.424° RIU^{-1}. It can be observed that DMSO caused a slight improvement in RIS, with a value of 131.941 ± 5.976° RIU^{-1}. As shown by the subsequent porosities of the hydrogels to large PEG compounds (Table 3.2), DMSO had minimal effect, whereas films treated with 1,4-

dioxane and methanol caused a decrease in porosity, indicating that these solvents had an adverse effect on the hydrogel structure. This led to these solvents being eliminated from use. On the other hand, as DMSO repeatedly caused minimal damage to, and in fact appeared to improve the properties of the LW device, further photocaging reactions were completed in DMSO.

Table 3.2: *A table displaying the $\Delta\vartheta_R$ observed when 1% solutions of PEG 10 kDa, PEG 100 kDa and PEG 300 kDa are introduced to an AAm/APMA co-polymer based LW device before the solvent exchanges (water) and after (1,4-dioxane, DMSO and methanol). Data is an average of 3 repeats of each study.*

Solution	Water $\Delta\theta_R$ (°)	1,4-Dioxane $\Delta\theta_R$ (°)	DMSO $\Delta\theta_R$ (°)	Methanol $\Delta\theta_R$ (°)
1% PEG 10 kDa	0.127805	0.05294	0.13621	0.09183
1% PEG 100 kDa	0.101101	0.04683	0.11169	0.07460
1% PEG 300 kDa	0.085608	0.04439	0.10363	0.07055

3.5.1.2 The Photocaging of Hydrogels in DMSO

As DMSO was the only organic solution tested which did not cause irreversible damage to the LW devices, this was the solvent of choice for studies on 100 µm thick hydrogel films. To make these films, a CDMVS functionalised glass slide, as described in Chapter 3.5.1.1, was placed into a custom-made plastic mould; this is a more replicable method of film formation than the use of spacer beads which is unfortunately unfeasible for 1.1 µm thick films. The hydrogel mixture, comprising of AAm, APMA, BAAm, APS, TEMED and DI H_2O, was vortexed in an Eppendorf tube and, using a syringe, injected through a hole in the mould onto the glass slide. The centre of the mould contained a 100 µm thick plastic spacer to control the thickness

of the film formed. The solution was then left to gel before dismantling to obtain the hydrogel covered glass substrate. The newly formed 100 µm thick films were slowly transitioned into DMSO. Once fully immersed in a solution of 100% DMSO, NVOC-Cl and triethylamine were added to the hydrogel film. The reagents were then left to undergo the base-catalysed photocaging of the hydrogel prior to the gradual return to an aqueous media.

The ultraviolet-visible (UV-Vis) spectra of the glass substrate supported film were collected: prior to solvent exchange; following the reaction, whilst still containing DMSO; and finally following the reaction, whilst the film had been returned into aqueous media. While in DMSO, a large peak at 350 – 400 nm was observed which indicated the presence of NVOC-Cl in the film (Figure 3.13). Once returned to the aqueous environment, a weak, broad peak was retained across 350 – 450 nm. The difference in spectra suggested that the photocaging of the AAm/APMA co-polymer hydrogel was successful as some NVOC-Cl was retained within the structure.

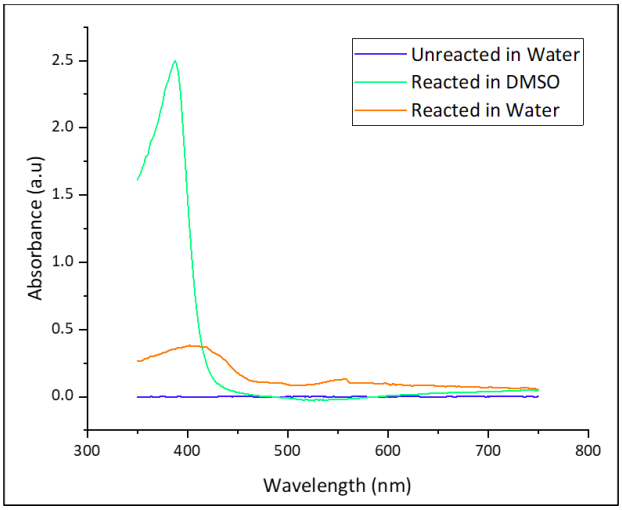

Figure 3.13: *A graph showing the UV-Vis absorbance spectra of an AAm/APMA co-polymer hydrogel (unreacted in water), following the hydrogel being photocaged while in DMSO (reacted in DMSO) before being returned to an aqueous media (reacted in water). Data is an average of 3 repeats of the study.*

The photocaged hydrogel was introduced to a solution of semicarbazide hydrochloride in 100 mM HEPES, pH 7.4 buffer solution prior to photodeprotection. As the deprotection mechanism results in the production of aldehyde functional groups, semicarbazide was introduced as a scavenger molecule, the purpose of this was to react with the aldehyde groups thus preventing imine formation between the aldehyde by-product and the freshly deprotected primary amine functional groups.

Based on the light sources available, the NVOC-Cl photocaged hydrogel was irradiated at 365 nm through a photomask (Figure 3.14), the intent was for the photomask to direct light in an identifiable pattern, and only the regions where light passed through the photomask (the pattern) should experience photodeprotection. The hydrogel was then stained with a solution of fluorescein isothiocyanate (FITC) in water; FITC contains the amine reactive isothiocyanate functional group, therefore, covalent binding of FITC was expected only where the primary amines had been released. Thus, a fluorescent pattern matching that of the photomask was expected to form, however, the observed was result was that the entire gel was stained (Figure 3.14).

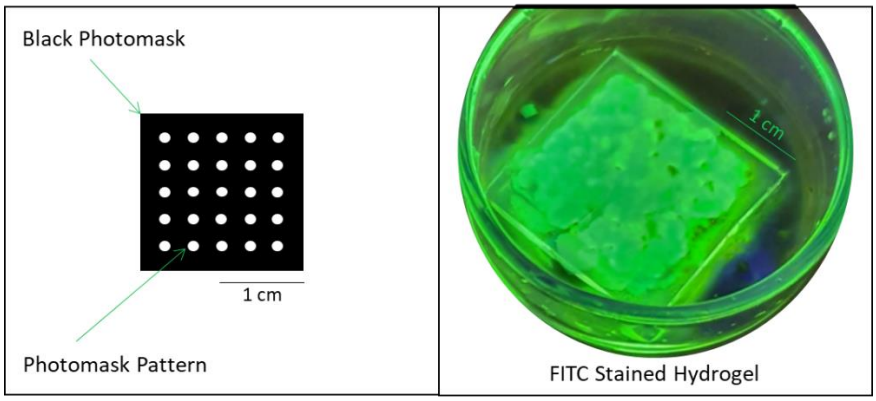

Figure 3.14: *An image depicting the photomask used, thus the photopattern expected to form (left) and the stained hydrogel film showing no photopattern (right).*

The UV-Vis absorption spectra clearly show that NVOC-Cl was absorbed into the structure of the hydrogel; however, FITC stained the whole of the hydrogel film. This led to the question of why carbamate bond formation did not occur between APMA and NVOC-Cl, resulting in the presence of free primary amines throughout the entire structure of the hydrogel.

3.5.1.3 The Effect of DMSO on PPGs

In an attempt to discover possible side reactions, research was conducted into the chemistry of chloroformate functional groups. This research culminated in the theory that a potential unwanted reaction may have occurred between NVOC-Cl and the solvent, DMSO (Scheme 3.1), thus eliminating the photocaging capability of the PPG. This theory was supported by literature, as the reagents are similar to those used in a Barton Modification.[61]

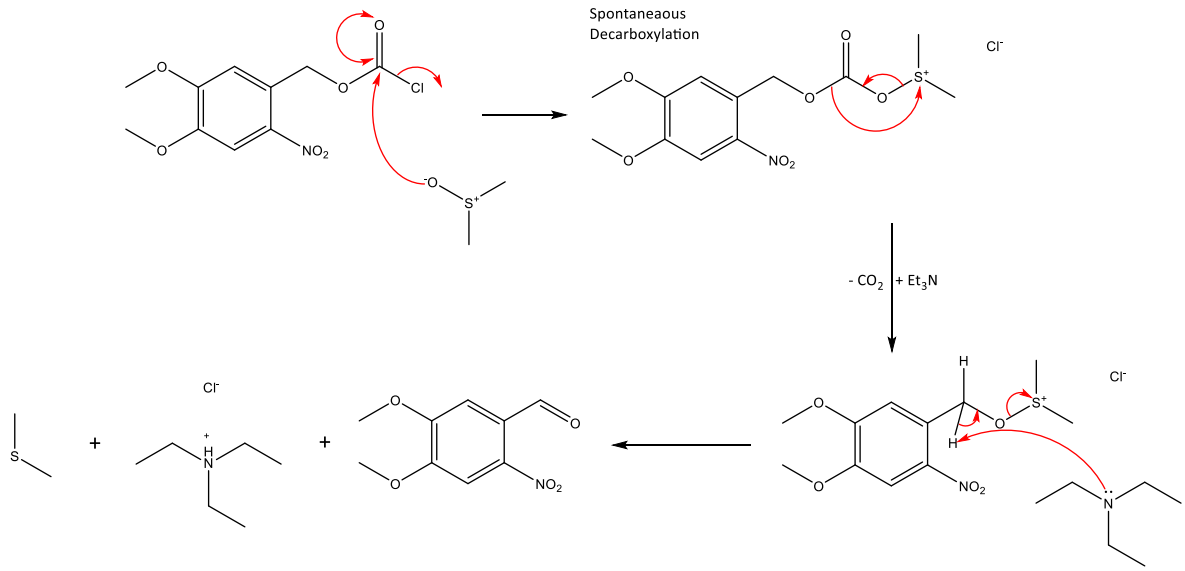

Scheme 3.1: *The theoretical base initiated side reaction between NVOC-Cl and DMSO.*

In response to the literature search, nuclear magnetic resonance (NMR) studies were conducted to determine if this side reaction was occurring. NMR was the analytical method of

choice as the development of an aldehyde functional group results in the formation of a signal at approximately 10 ppm, and no bonds in the reagents, nor in the desired product, would have provided a signal in this region. A sample of the reaction mixture which was analysed *via* NMR spectroscopy after 12 hours displayed a peak at approximately 10.22 ppm (Figure 3.15). Over the course of 48 hours the peak grew in intensity, lending support to the theory that an unwanted side reaction was taking place, thus resulting in aldehyde formation.

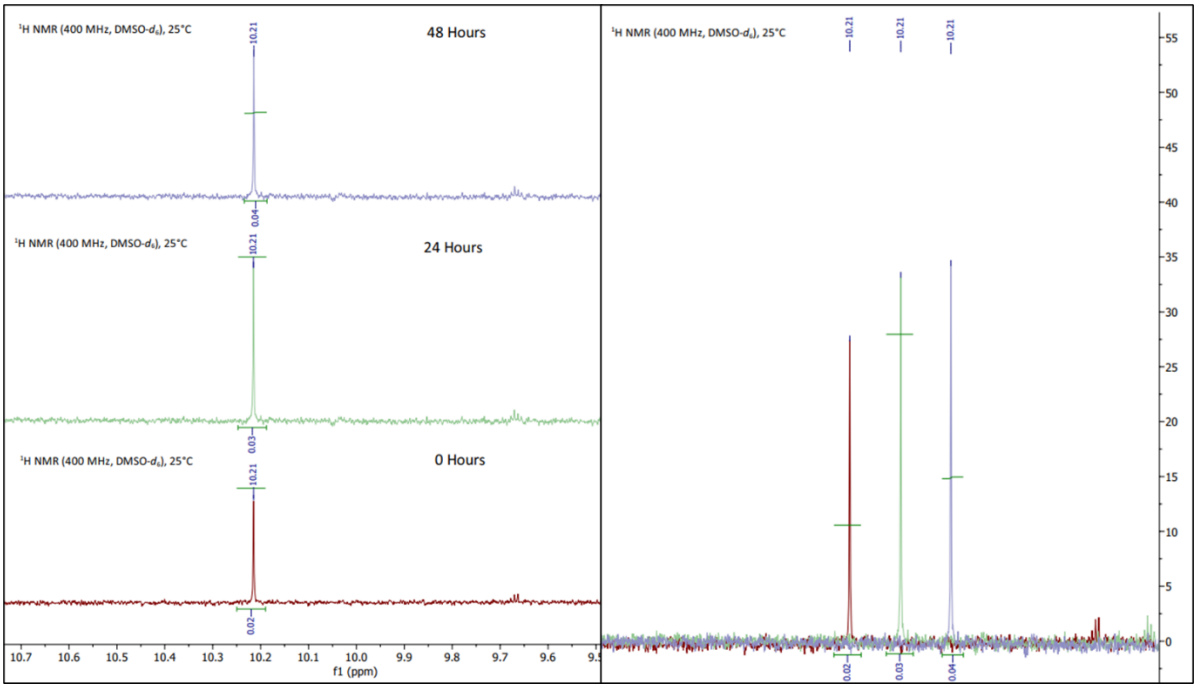

Figure 3.15: *NMR spectra displaying the position of the aldehyde peak at various time intervals (left) and the intensity of the aldehyde peak at various times relative to one another (right).*

3.5.2 Photocaging of Monomers

3.5.2.1 4,5-dimethoxy-2-nitrobenzyl (3-methacrylamidopropyl)carbamate (NVOC-APMA)

As some organic solvents were found to be destructive to the structure of hydrogel films, and others, such as water and DMSO, were incompatible due to reactivity with the PPG,

the photocaging of hydrogels with NVOC-Cl at this stage did not appear to be plausible. Due to this, we performed the photocaging of the APMA monomers prior to hydrogel formation. Previous work within the group had a mixed success rate with the incorporation of photocaged monomers into hydrogel structures, therefore a different monomer would be the basis of this work.[56] Based on this, the first monomer synthesised in this work was **NVOC-APMA** (Scheme 3.2). The reaction was conducted in methanol at room temperature.

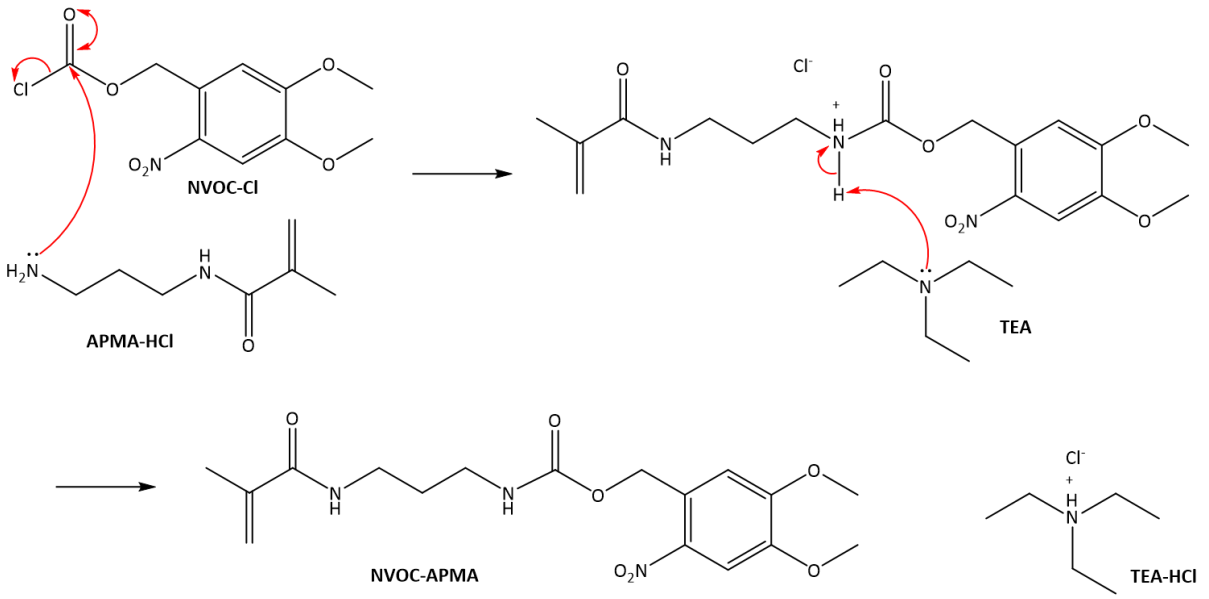

Scheme 3.2: *Mechanism of the base initiated carbamate formation between a primary amine and a chloroformate group to form NVOC-APMA.*

Carbamate formation through the reaction of a primary amine with a chloroformate group is base catalysed. The lone pair of electrons present in the free primary amine of APMA acts as a nucleophile, attacking the partially positive carbonyl carbon. Following this, the carbonyl double bond then kicks out to the oxygen, before reforming and eliminating the chlorine group, resulting in a positively charged quaternary amine. Finally, to revert the nitrogen atom back to a neutral charge, a proton is removed, either by the free chloride ion or by the triethylamine base, the exact method is unknown, however both methods result in

the formation of triethylamine hydrochloride salt as a by-product. This yields the final product **NVOC-APMA** (yield = 65.6%), as confirmed by infrared (IR) spectroscopy, proton and carbon NMR, and mass spectrometry (MS), which is a low yield for a single step reaction. Unfortunately, the resultant product was not water soluble.

The product **NVOC-APMA** was soluble in DMSO, however as it was unknown how this solvent would affect polymerisation, it was diluted in DI water to minimise any adverse effects. Therefore, the polymerisation was conducted in a DMSO/DI water solution with AAm as a co-monomer and BAAm as a cross-linker, using APS and TEMED to initiate free-radical polymerisation. This gel was submerged in a solution of semicarbazide hydrochloride and sodium hydroxide in pH 7.4 HEPES buffer to react with and aid in the removal of photocleavage products. As previously described the gel was then irradiated with 365 nm light over a photomask (Figure 3.14) for 20 minutes and subsequently stained with a FITC solution (Figure 3.16). FITC was used as it would selectively bind to the amines freed during photodeprotection, forming a pattern within the gel that corresponds to the mask used.

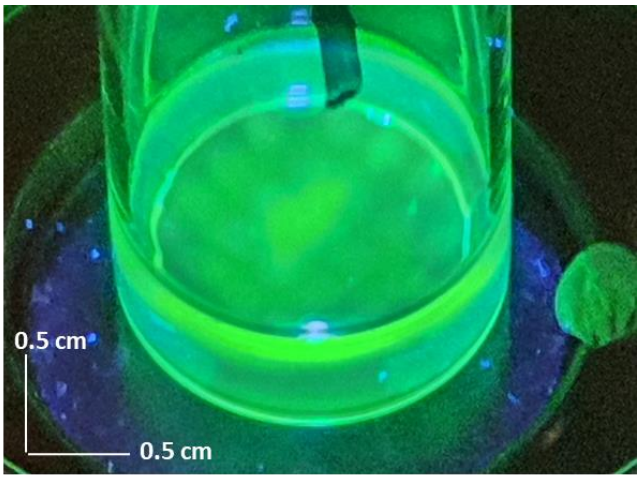

Figure 3.16: *An image showing a photodeprotected hydrogel made with* ***NVOC-APMA****, photodeprotected areas have been stained with FITC to allow visualisation.*

While gels were able to form using this monomer, and a photopattern matching that of the mask was observed, the concentration of **NVOC-APMA** present in the hydrogel was low. For adequate sensing levels achieving a sensible limit of detection, it was previously determined that a photocaged monomer needs to be present as 4% of the total monomer concentration.[56,62] In this scenario, the highest achievable concentration was 0.2%, any increase of monomer concentration prevented hydrogel formation, this led to the decision to synthesise photocaged monomers with increased water solubility.

3.5.2.2 4,5-bis(2-(2-methoxyethoxy)ethoxy)-2-nitrobenzyl (3-methacrylamidopropyl) carbamate (NB-6a)

Following on from **NVOC-APMA**, a water-soluble derivative based on commercially available monomers was synthesised. Synthesis of a similar compounds to **NB-1**, **NB-2** and **NB-3** (Scheme 3.3) had been reported in the literature.[63,64] Methods were modified for this particular synthesis as those stated in literature used a smaller polyethylene glycol chain which limited their water solubility.

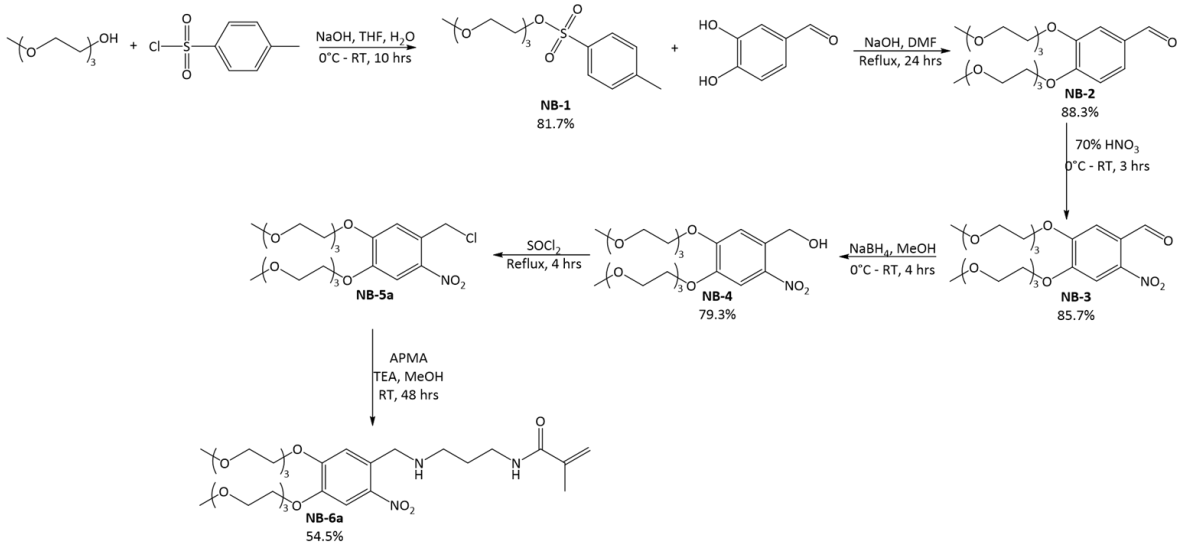

Scheme 3.3: *A schematic showing the synthesis of a nitrobenzyl-based PPG and the reaction with APMA to form the water soluble photocaged monomer* ***NB-6a****.*

As seen in literature, **NB-1** was formed by the tosylation of a free alcohol group (yield = 81.7%). The purpose of this was to increase the rate of reaction between triethylene glycol monomethyl ether and the phenolic groups of 1,4-dihydroxybenzaldehyde. A Williamson ether synthesis between **NB-1** and 3,4-dihydroxybenzaldehyde yielded product **NB-2**. Sodium hydroxide was substituted for potassium carbonate to increase the yield of **NB-2** as it allowed for the more favourable formation of the alkoxy ion intermediate required for etherification, thus increasing the yield of the product (yield = 88.3%). Nitration of **NB-2** with 70% nitric acid under atmospheric conditions yielded the product **NB-3** (yield = 85.7%). Following this, compound **NB-3** was dissolved in anhydrous methanol and cooled to 0 °C. Sodium borohydride was added slowly to selectively reduce the aldehyde group to a primary alcohol, compound **NB-4** (yield = 79.3%). The primary alcohol was treated with thionyl chloride at reflux for a chlorination reaction resulting in the photocaging compound, **NB-5a** which was used as collected in the next reaction. The photocaging of APMA occurred in a single step, **NB-5a** and APMA were dissolved in methanol and allowed to react at room temperature in the presence of triethylamine to produce the novel compound **NB-6a** (yield = 54.5%) *via* a substitution reaction, as proven by IR, proton NMR, carbon NMR and MS.

The final product was collected in a poor yield of 27% with respect to the initial reagents. While compounds **NB-1** to **NB-4** were collected in high yields, the final compound was a low yielding reaction. Much of this is due to the water solubility of the compounds resulting in some loss during compound extractions. In an attempt to rectify this in future reactions the synthetic procedure would be modified to allow for the incorporation of the ethylene glycol chains towards the end of the method, thus reducing losses to the aqueous washes in earlier stages.

An UV-Vis calibration study was conducted on **NB-6a** in DI water to determine the optimum wavelength for photodeprotection (Figure 3.17), as light sources of 365 nm and 405 nm were available for use. The calibration graph led to the determination of the molar extinction coefficient (ε) through the use of the Beer-Lambert Law, which is important in determining how well the compound absorbs light.

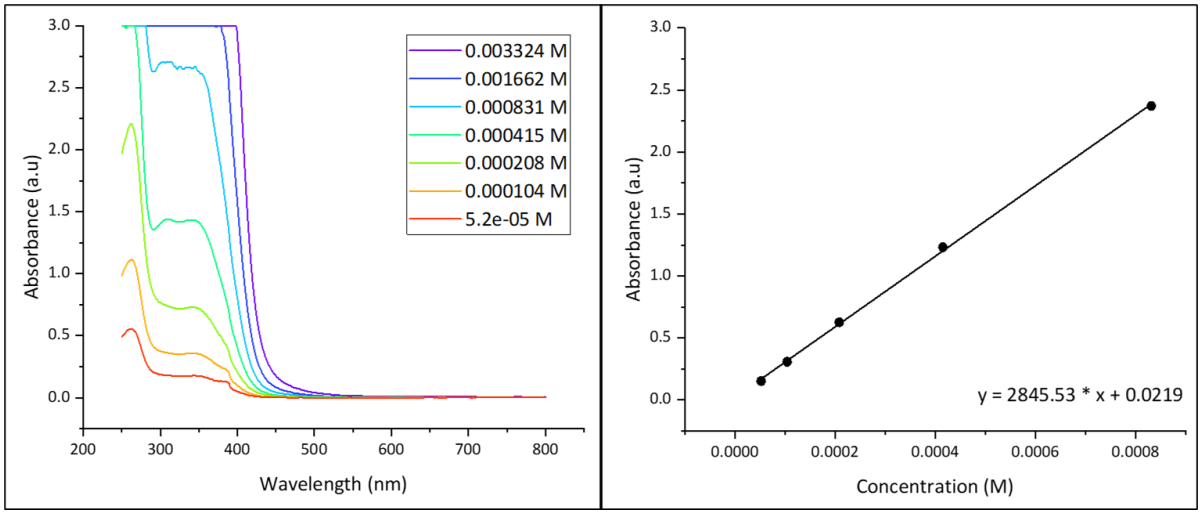

Figure 3.17: *Graphs depicting the absorbance spectra of **NB-6a** at a variety of concentrations in DI water (left) and the absorbance of various concentrations of **NB-6a** at 365 nm (right). Data is an average of 3 repeats of the study.*

NB-6a had an absorbance maxima of 266 nm, with a secondary peak at 345 nm. As the 365 nm light source was closest in wavelength to these values, this was the chosen wavelength for deprotection. As observed through the above graphs, the ε of **NB-6a** in DI water at 365 nm was found to be 2845.53 M^{-1} cm^{-1}. While 365 nm is not the absorbance maxima, it is the region being observed for this work due to the light sources available. As the ε of NVOC-Cl at 350 nm is 5000 M^{-1} cm^{-1} this means that the monomer produced absorbs light of 365 nm at approximately half the efficiency of NVOC-Cl.[65] However this is not an accurate comparison

as NVOC-Cl is just the chromatophore, and does not contain the APMA monomer which may have an effect on the absorbance.

3.5.2.3 4,5-bis(2-(2-methoxyethoxy)ethoxy)-2-nitrobenzyl (2-acrylamidopropyl) carbamate (NB-6b)

Compound **NB-6a** was designed as a secondary amine containing group based on the 4,5-dimethoxy-2-nitrobenzyl bromide photocaging group, the other possibility was to design a compound more similar to NVOC-Cl, which cages *via* carbamate formation.[66] To do this following the formation of **NB-4** in Chapter 3.5.2.2, an alternative pathway was devised to synthesise the novel compound **NB-6b** (Scheme 3.4).

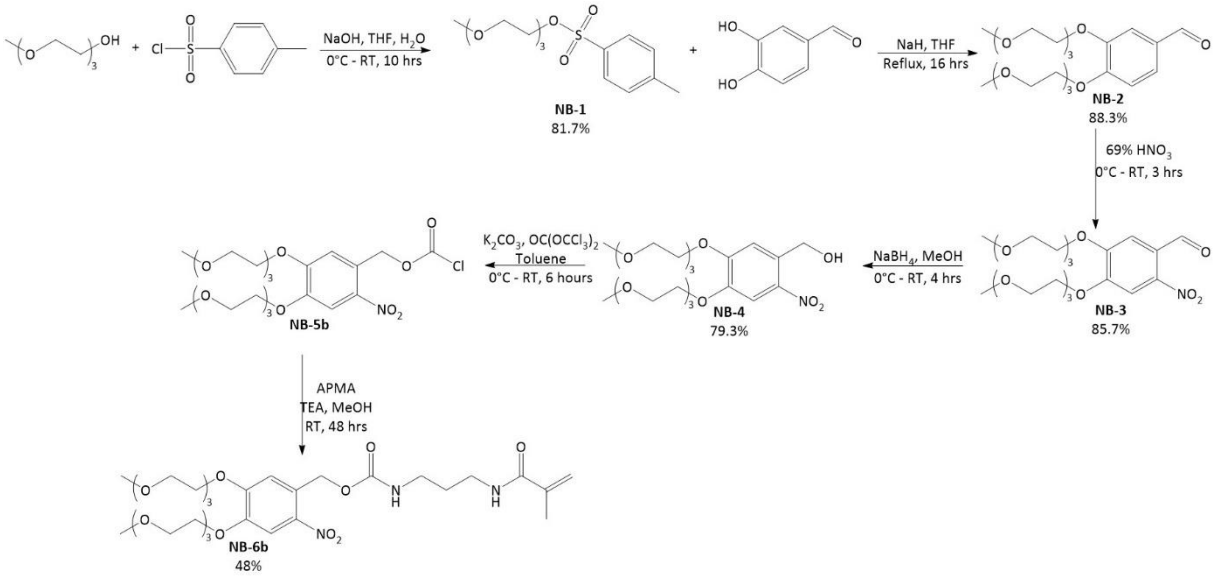

Scheme 3.4: *A schematic showing the synthesis of a nitrobenzyl-based PPG and the reaction with APMA to form the water soluble photocaged monomer* ***NB-6b****.*

Following the reduction of the aldehyde to form **NB-4** (Chapter 3.5.2.2), this compound was then reacted with triphosgene in the presence of potassium carbonate in anhydrous toluene. Triphosgene was used as due to its liquid state, it is a safer alternative to phosgene.

This resulted in the formation of a chloroformate functional group, forming compound **NB-5b**. This compound was then reacted immediately without purification with APMA in the presence of triethylamine in methanol to form the final compound **NB-6b** (yield = 48%), as confirmed by IR, proton NMR and carbon NMR. The final product was collected in a poor yield of 23.5% with respect to the initial reagents. As discussed earlier, compounds **NB-1** to **NB-4** were collected in high yields, the final compound was again a low yielding reaction. While the water solubility was again an issue here, the yield was further impacted due to the use of triphosgene. The chloroformate compound was susceptible to forming symmetrical compounds by over-reacting with **NB-4** instead of forming the desired hetero-reacted compound. This complicated the purification and decreased the yield of the desired product.

An UV-Vis calibration study was conducted on **NB-6b** in DI water to determine which light source is to be used, 365 nm or 405 nm, and the ε at the corresponding wavelength (Figure 3.18).

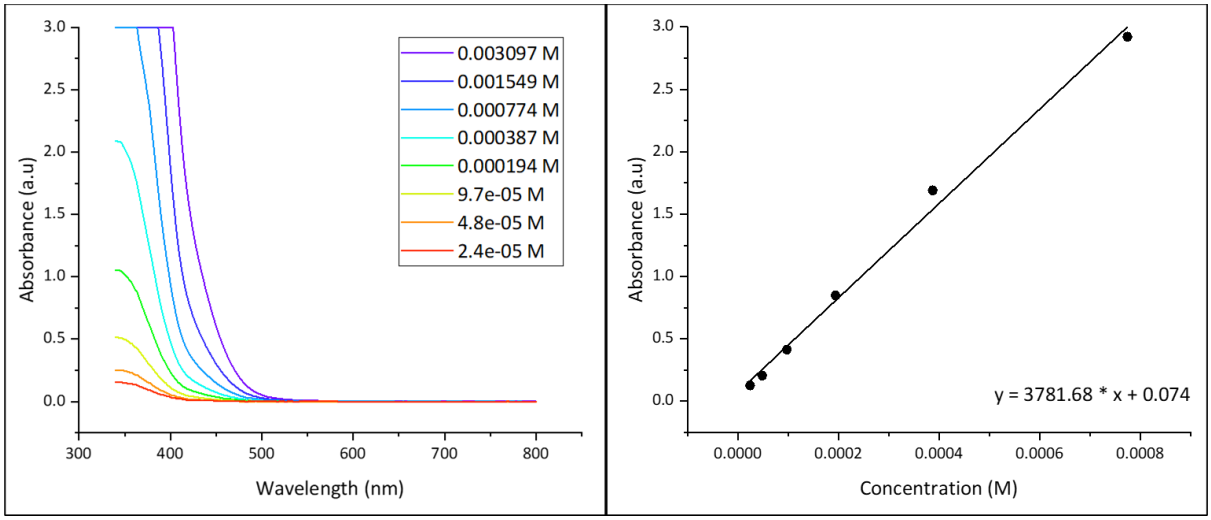

Figure 3.18: *Graphs depicting the absorbance spectra of **NB-6b** at a variety of concentrations in DI water (left) and the absorbance of various concentrations of **NB-6b** at 365 nm (right). Data is an average of 3 repeats of the study.*

NB-6b had an absorbance maxima of 344 nm which is closer to the 365 nm light source than 405 nm, hence further photoactive properties were determined with respect to 365 nm. As observed through the above graphs, the ε of **NB-6b** in DI water at 365 nm was found to be 3781.68 M^{-1} cm^{-1}. As the ε of **NB-6a** at 365 nm was found to be 2845.53 M^{-1} cm^{-1} this suggests that the compound **NB-6b** absorbs light more efficiently than the previous compound.

3.5.2.4 N-(3-(((3-nitrodibenzo[b,d]furan-2-yl)methyl)amino)propyl) methacrylamide (DBF-5)

The previous compounds synthesised all had a tendency to have absorbance maxima of less than 400 nm. As this is close to the UV region of light, a compound which absorbs at a higher wavelength was more desirable, as visible light is inherently safer and cheaper than UV. Due to this, a system with more conjugated double bonds was designed. This is due to highly conjugated systems being known to absorb at higher wavelengths.[67] The highly conjugated dibenzofuran (DBF) system was proposed as the building block for the PPG.[68] A similar compound to the dibenzofuran PPG, **DBF-4**, has been previously reported in literature. The final product was yielded after a 5-step synthetic procedure (Scheme 3.5), following a greener procedure than that reported in the literature.[69] The first step was modified from the literature method, which utilised a Friedel-Crafts acylation, to a Reiche Formylation reaction, this was to add an aldehyde functional group rather than a ketone. Throughout the literature method, this ketone functional group was then converted to an alkane through a Wolff-Kishner reduction. The Wolff-Kishner reduction employs the use of hydrazine, which is a carcinogenic compound. To incorporate a halogen functional group, this alkane was then treated with *N*-bromosuccinimide, benzoyl peroxide and carbon tetrachloride for

bromination; these chemicals are a suspected carcinogen, suspected mutagen and highly damaging to the ozone layer. Carbon tetrachloride itself is now banned from use in consumer products within the UK, highlighting its unpleasant nature.[70] While this new synthetic procedure is not without its safety hazards, it is greener than that discussed in literature as it uses chemicals which are inherently safer for the environment and for the user.[70]

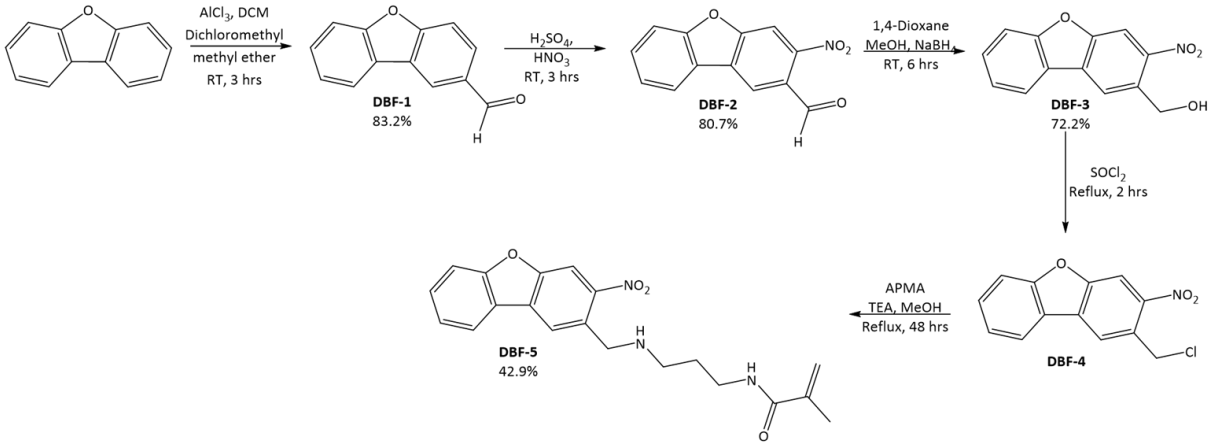

Scheme 3.5: *A schematic showing the five-step synthesis to create a dibenzofuran photocaged APMA monomer (**DBF-5**).*

The synthetic procedure began with the formation of an aldehyde group through a Rieche formylation of DBF to form **DBF-1** (yield = 83.2%). Following this, **DBF-2** was formed through a simple nitration reaction, by mixing **DBF-1** in nitric acid and sulfuric acid. The nitration was directed almost exclusively *ortho* to the aldehyde producing **DBF-2** (yield = 80.7%), this formed the basic structure similar to that of the *ortho*-nitrobenzyl PPGs previously discussed (Chapter 3.3). Following the nitration, the formation of an amine reactive group was necessary, therefore the aldehyde group was selectively reduced to a primary alcohol through the use of sodium borohydride in a mixture of 1,4-dioxane and anhydrous methanol. This produced compound **DBF-3** (yield = 72.2%). The primary alcohol was then treated with thionyl chloride at reflux for a chlorination reaction resulting in the PPG, **DBF-4** which was used as

collected in the next reaction. The photocaging of APMA occurred in a single step, **DBF-4** and APMA were dissolved in methanol and allowed to react at room temperature in the presence of triethylamine to produce the novel compound **DBF-5** (yield = 42.9%) *via* a substitution reaction, as proven by IR, proton NMR, carbon NMR and MS.

The final product was collected in a very poor yield of 20.1% with respect to the initial reagents. While compounds **DBF-1** to **DBF-3** were collected in good to high yields, the final compound was a low yielding reaction. As this was also observed in previous compounds, Chapter 3.5.2.2 and Chapter 3.5.2.3, it is possible that this is in fact just a low yielding reaction.

An UV-Vis calibration study was conducted on **DBF-5** in DI water (Figure 3.19). This was to determine which of the light sources available would be most efficient for photodeprotection of the PPG.

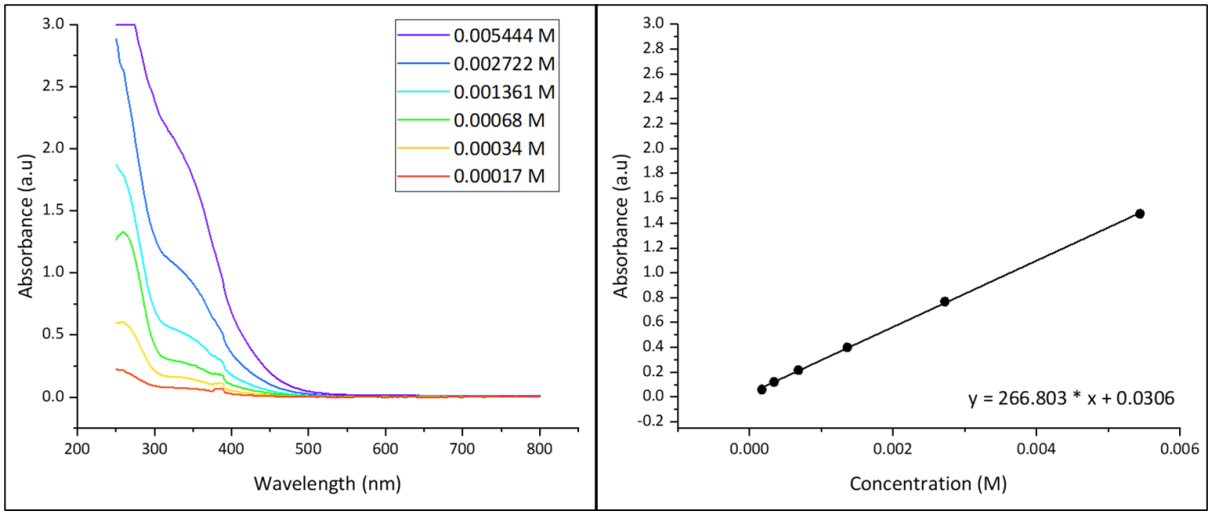

Figure 3.19: *Graphs depicting the absorbance spectra of **DBF-5** at a variety of concentrations in DI water (left) and the absorbance of various concentrations of **DBF-5** at 365 nm (right). Data is an average of 3 repeats of the study.*

The absorbance maxima of **DBF-5** was found to be at 258 nm, with a secondary shoulder peak at approximately 340 nm. This causes minimal absorbance to occur with 405

nm light, therefore further data was collected at 365 nm. As observed through the above graphs, the ε of **DBF-5** in DI water at 365 nm was found to be 266.803 M^{-1} cm^{-1}. This is much lower than anticipated, a factor of 10 times smaller than those observed for compounds **NB-6a** and **NB-6b** which was unexpected, as **DBF-5** is a more conjugated system, it was expected that it would act as a better chromatophore and therefore absorb light more efficiently.

3.5.2.5 N-(3-(((6,7-dimethoxy-2-oxo-2H-chromen-4-yl)methyl)amino)propyl) methacrylamide (MC-1)

As the more conjugated DBF system had minimal effect on moving from the 365 nm light source to the 405 nm light source, a coumarin-based PPG was designed. This was due to a literature search finding that coumarin structures commonly absorb between 300 and 500 nm, resulting in the formation of the novel compound **MC-1** (Scheme 3.6).[54]

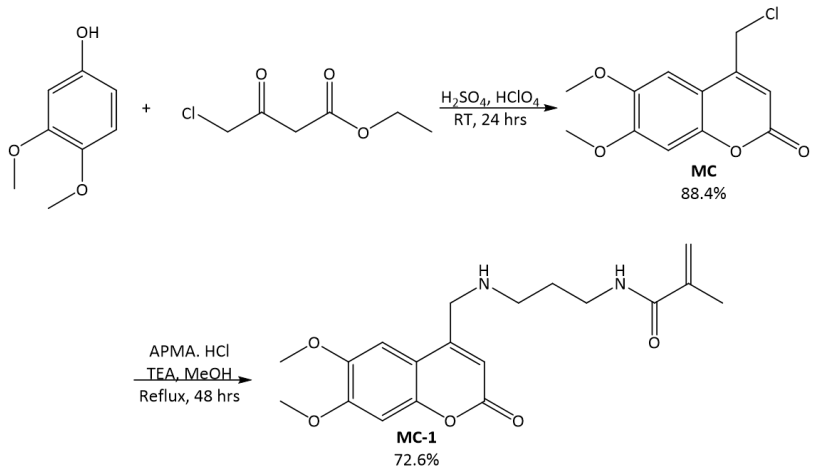

Scheme 3.6: *A schematic showing the synthesis of a coumarin PPG,* ***MC****, and the reaction with APMA to form the water soluble photocaged monomer* ***MC-1****.*

The coumarin, **MC**, was synthesised as is reported in literature *via* a Pechmann condensation reaction (yield = 88.4%), the exact mechanism of which is unknown. The acid of

choice to catalyse this reaction was a mixture of sulphuric acid and perchloric acid. Following this, **MC-1** was formed *via* a nucleophilic substitution reaction between **MC** and APMA (Scheme 3.6). As **MC** is only soluble in refluxing methanol, purification of this compound was simplified by having **MC** in excess which, once the reaction was cooled, was filtered out of the reaction mixture leaving **MC-1** in solution. **MC-1**, as proven by IR, proton NMR, carbon NMR and MS, was then extracted (yield = 72.6%).

As both reactions had yields upwards of 70%, this final product was collected in very good yield, with the entire synthetic procedure resulting in a good yield of 64.2% with respect to the original reagents.

An UV-Vis calibration study was conducted on **MC-1** in DI water to determine if the coumarin structure had increased absorbance at 405 nm in comparison to the previous compounds (Figure 3.20).

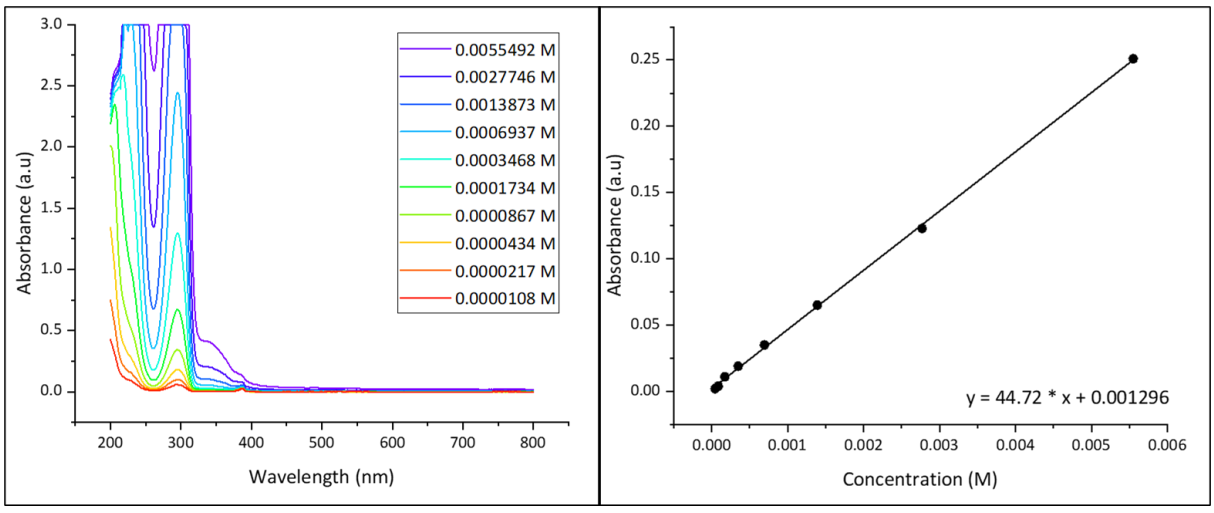

***Figure 3.20**: Graphs depicting the absorbance spectra of **MC-1** at a variety of concentrations in DI water (left) and the absorbance of various concentrations of **MC-1** at 365 nm (right). Data is an average of 3 repeats of the study.*

It can be seen that **MC-1** had two different absorbance maxima, the first at 205 nm, and the second at 299 nm, as the 365 nm light source is closest to these values, this was the

wavelength that was studied. As observed through the above graphs, the ε of **MC-1** in DI water at 365 nm was found to be 44.72 M^{-1} cm^{-1}. This is much lower than anticipated, even lower than that of **DBF-5**. Not only this, the compound does not absorb at greater than 400 nm, the optimum wavelengths for absorption are at approximately 200 nm and 300 nm, which is much lower than is desired.

3.5.2.6 N-(3-(((6,7-dimethoxy-3-nitro-2-oxo-2H-chromen-4-yl)methyl)amino)propyl) methacrylamide (MC-2)

As the coumarin derivative appeared to be an efficient synthetic procedure, steps were taken in an attempt to improve the photophysical properties of the compound. As a literature search suggested that the extension of the conjugated *pi* system through position 3 would increase the absorbance maxima, the compound was modified to incorporate a nitro functional group at position 3, forming the novel compound **MC-2** (Scheme 3.7).[71] This modification may also have another added advantage; as the nitro functional group will be positioned *ortho* to the leaving group, deprotection may occur in a similar way to that seen in the frequently used *ortho*-nitrobenzyl PPGs.

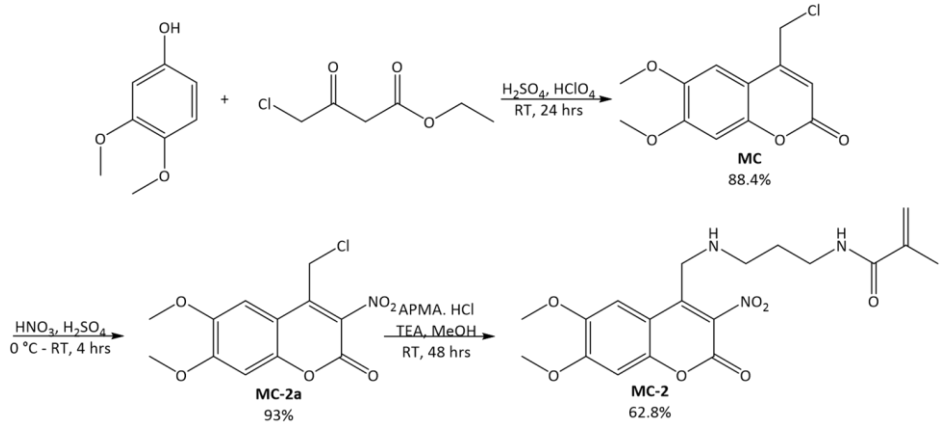

Scheme 3.7: *A schematic showing the synthesis of a coumarin PPG,* ***MC-2a****, and the reaction with APMA to form the water soluble photocaged monomer* ***MC-2****.*

The nitro group was substituted at position 3 of the coumarin compound through the nitration of **MC** (Chapter 3.5.2.5) with concentrated nitric acid and sulfuric acid under atmospheric conditions, resulting in compound **MC-2a** (yield = 93%). Ordinarily, under these conditions, it would be possible for nitration to occur on the benzene ring. That was not the case here, as shown by proton NMR analysis (Figure 3.21). Following nitration, the peak at 6.50 ppm, corresponding to the proton at position 3, is lost, meanwhile both aromatic peaks are retained. A potential reasoning for this is that the methoxy groups make the benzene ring too sterically hindered for the substitution of the large nitro functional group. The photocaging of APMA with **MC-2a** to form **MC-2** was performed in methanol with triethylamine (yield = 62.8%). The product was confirmed by IR, proton NMR and MS.

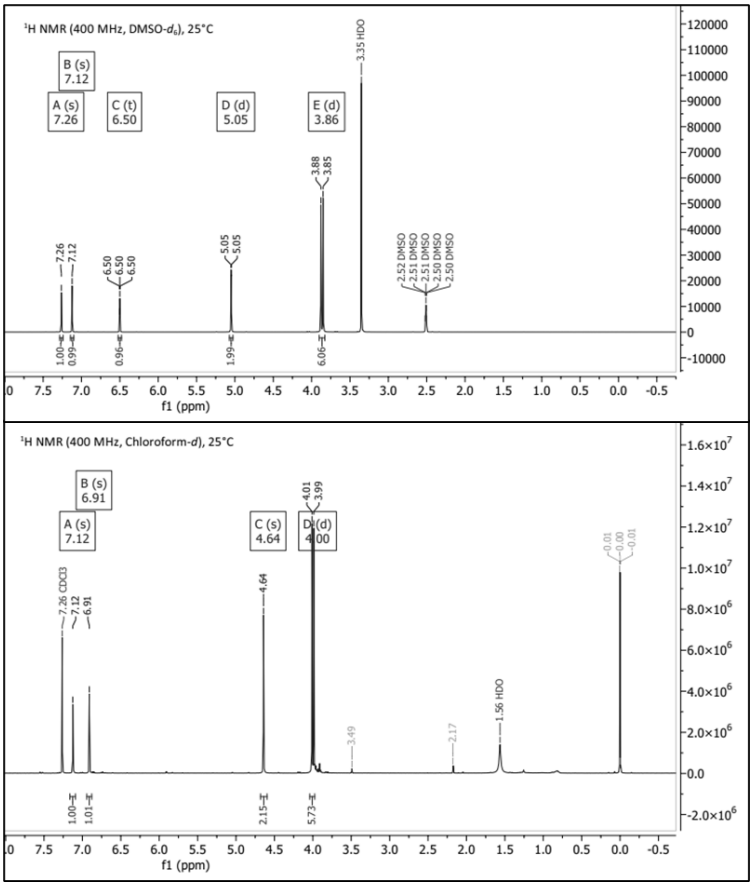

Figure 3.21: *NMR spectra of **MC** (top) and **MC-2a** (bottom), displaying the loss of the proton at 6.6 ppm, which refers to position 3 as labelled in Figure 3.9.Slightly different chemical shifts due to different solvents.*

As the reactions to form **MC** and **MC-2a** both were high yielding reactions, the limiting step here was the formation of **MC-2**. The yield of the product with respect to the original reagents was a fair yield of 51.6%.

UV-Vis studies of **MC-2** in DI water were used to determine that the light source of 365 nm would be more effective than that of 405 nm (Figure 3.22).

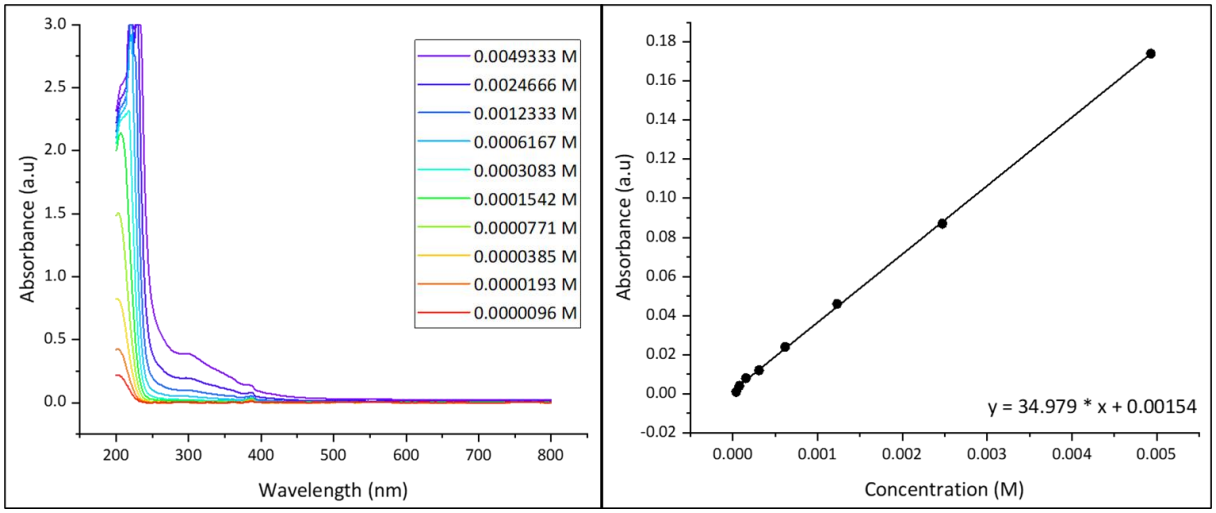

Figure 3.22: *Graphs depicting the absorbance spectra of **MC-2** at a variety of concentrations in DI water (left) and the absorbance of various concentrations of **MC-2** at 365 nm (right). Data is an average of 3 repeats of the study.*

MC-2 had an absorbance maxima of 206 nm, with a very small secondary peak at 302 nm. Due to there being minimal absorbance of this compound at 405 nm, photoactivity studies were conducted at 365 nm. As observed through the above graphs, the ε of **MC-2** in DI water at 365 nm was found to be 34.979 M^{-1} cm^{-1}. This was expected to be higher than that of **MC-1**, but is in fact slightly lower. Despite this, the compound will still be tested as it will hopefully be an efficient PPG.

3.5.2.7 (6,7-dimethoxy-2-oxo-2H-chromen-4-yl)methyl (3-methacrylamidopropyl) carbamate (MC-3)

As observed through the synthesis of compounds **NB-6a** and **NB-6b**, by the photocaging of the APMA monomer *via* a carbamate bond rather than an amine, the ε can be increased. It is based on this observation that a derivative of **MC-1** was designed with this in mind, resulting in the formation of **MC-3** (Scheme 3.8).

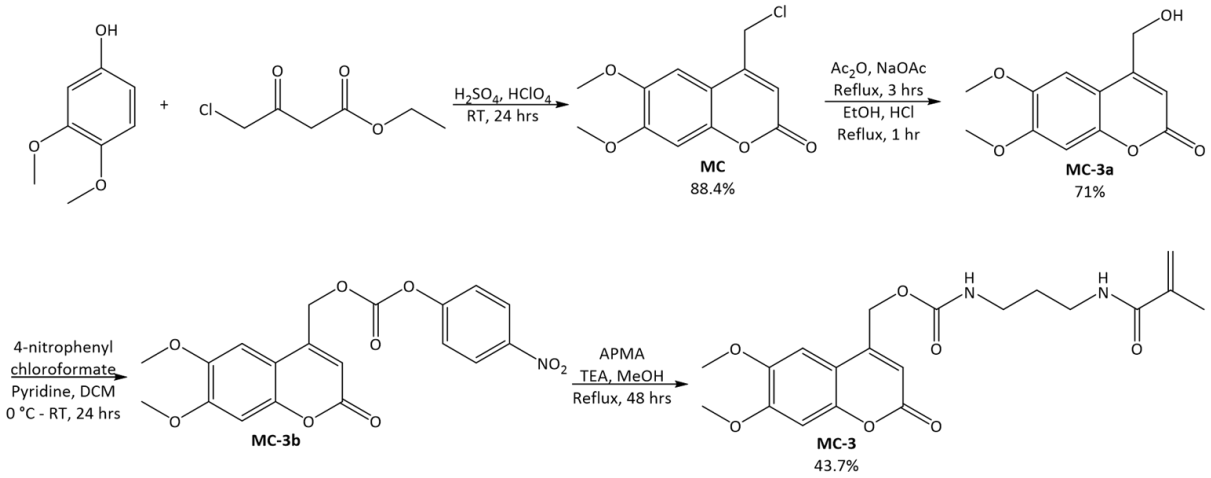

Scheme 3.8: *A schematic showing the synthesis of a coumarin PPG,* ***MC-3b****, and the reaction with APMA to form the water soluble photocaged monomer* ***MC-3****.*

In order to form a carbamate, **MC**, which was synthesised as previously described (Chapter 3.5.2.5) required hydroxylation. To do this, **MC** was heated to reflux in acetic anhydride in the presence of sodium acetate to form an ester. This reaction is driven through salt formation. Following this, the ester was cleaved, in the presence of a hydrochloric acid/ethanol mixture. This yielded **MC-3a** in high enough purity to be used as is (yield = 71%). Previously within this work, triphosgene was used for carbamate formation; however, reagents such as phosgene, triphosgene and 1,1'-carbonyldiimidazole which are commonly implemented for carbamate formation, are symmetrical compounds. This increases the risk

of unwanted by-products, as discussed in Chapter 3.5.2.3. Due to this, to increase the potential yield, **MC-3a** was reacted with 4-nitrophenyl chloroformate, in the presence of pyridine. This resulted in the formation of **MC-3b**, which in the presence of a weak base can only react at the chloroformate position. The photocaging of APMA with **MC-3a** to form **MC-3** was performed in methanol with triethylamine. Triethylamine was a sufficiently strong enough base to activate the nitrophenyl group to the point where APMA could undergo nucleophilic substitution, causing the release of nitrophenol as a by-product, and the formation of the carbamate compound **MC-3**, as proven by IR, proton NMR and MS (yield = 43.7%).

Despite the formation of **MC** and **MC-3a** being high yielding reactions, this synthetic procedure was low yielding with regards to the final product, achieving a yield of 27.4%. This is much lower than the previous coumarin derivatives, however it is expected as there is an increased number of steps in this method.

Two light sources were available for use for the deprotection of PPGs, these sources used wavelengths of 365 nm or 405 nm. Due to this, an UV-Vis calibration study was conducted on **MC-3** in DI water to determine the optimum wavelength for photodeprotection (Figure 3.23).

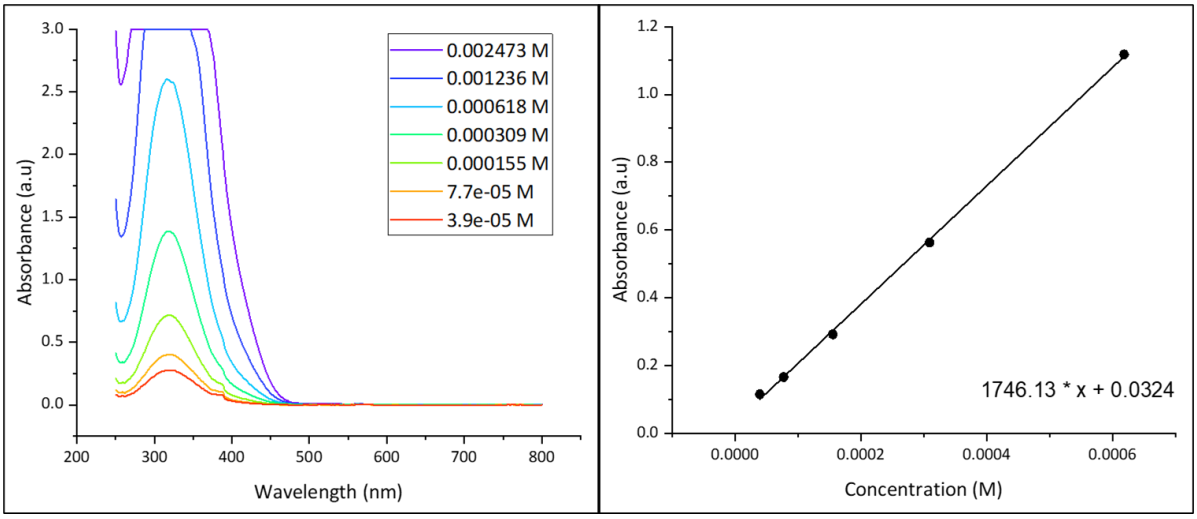

Figure 3.23: *Graphs depicting the absorbance spectra of* ***MC-3*** *at a variety of concentrations in DI water (left) and the absorbance of various concentrations of* ***MC-3*** *at 365 nm (right). Data is an average of 3 repeats of the study.*

The absorbance maxima of **MC-3** was found to be 317 nm, as the 365 nm light source was closer in wavelength to this value, this was the chosen wavelength for deprotection. As observed through the above graphs, the ε of **MC-3** in DI water at 365 nm was found to be 1746.13 M^{-1} cm^{-1}. This is much higher than the values observed for the other coumarin derivatives **MC-1** and **MC-2**, this means that the incorporation of the carbamate photocaging bond had the desired effect.

3.5.2.8 N-(3-(((6,7-dimethoxy-2-thioxo-2H-chromen-4-yl)methyl)amino)propyl) methacrylamide (SMC-1)

Despite the aim in using coumarin-based compounds as PPGs being to increase the absorbance maxima, those observed for compounds **MC-1**, **MC-2** and **MC-3** remained around the 200 – 300 nm range. As research indicated that a thiocarbonyl present at position 2 would increase the absorption wavelength of coumarin compounds, this was the next modification

attempted.[55] Based on this information, the novel compound **SMC-1** was synthesised (Scheme 3.9).

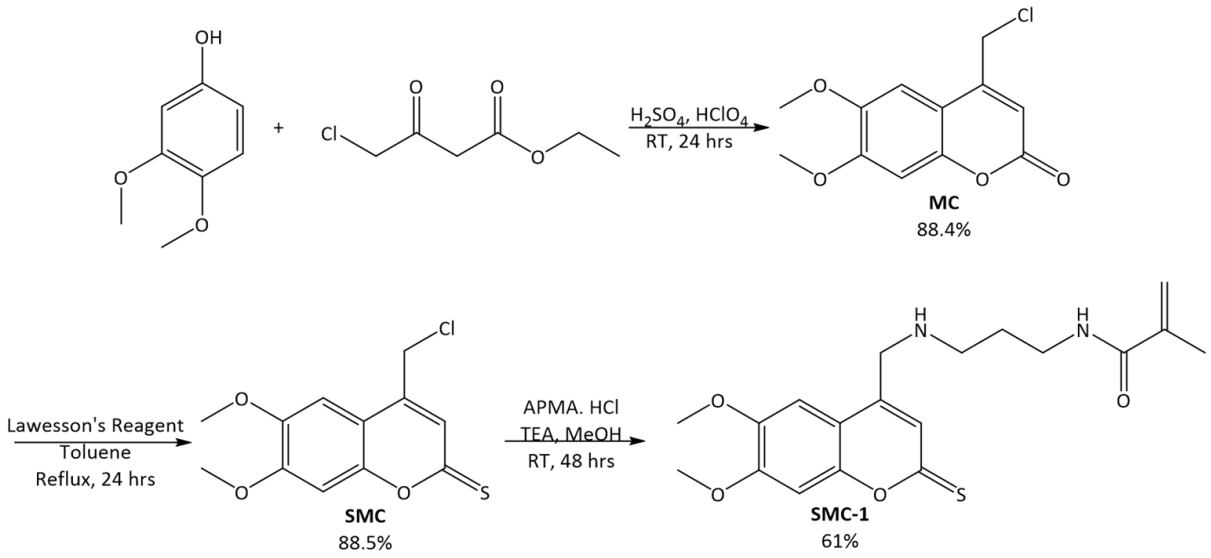

Scheme 3.9: *A schematic showing the synthesis of a coumarin PPG,* ***SMC****, and the reaction with APMA to form the water soluble photocaged monomer* ***SMC-1****.*

In order to form **SMC-1**, **MC**, synthesised as previously described (Chapter 3.5.2.5), was treated with Lawesson's reagent. The purpose of this was to convert the carbonyl into a thiocarbonyl functional group to form the product **SMC** (yield = 88.5%). As with **MC-1** formation, a nucleophilic substitution reaction between **SMC** and APMA was performed in basic conditions. As **SMC** is more highly soluble in methanol than **MC**, this reaction was conducted at room temperature. This resulted in the formation of the photocaged monomer **SMC-1** (yield = 61%). The structure of which was confirmed *via* IR, proton NMR, carbon NMR and MS.

As the initial two steps of the reaction had yields upwards of 80%, and the final was a yield of 61%. The final product was collected in a fair yield of 57.7% with respect to the original reagents.

In an attempt to determine the optimal deprotection wavelength, 365 nm or 405 nm, an UV-Vis calibration study was conducted on **SMC-1** in DI water (Figure 3.24).

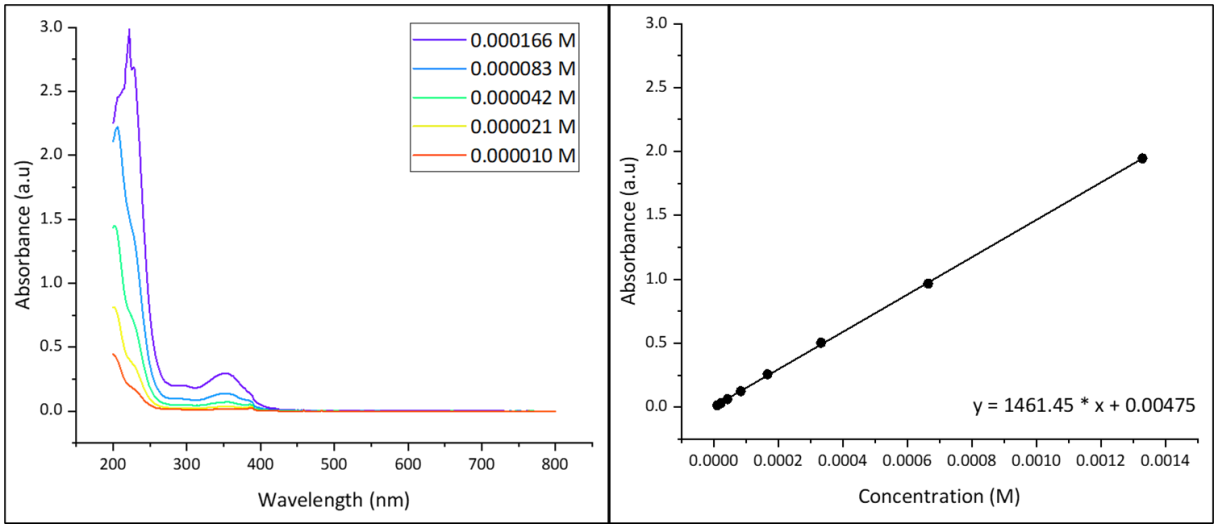

Figure 3.24: *Graphs depicting the absorbance spectra of **SMC-1** at a variety of concentrations in DI water (left) and the absorbance of various concentrations of **SMC-1** at 365 nm (right). Data is an average of 3 repeats of the study.*

Compound **SMC-1** displayed two absorbance peaks, the maxima at 207 nm, and also a secondary peak appearing at 353 nm. Due to 353 nm being very close to that of 365 nm, this is the wavelength of choice for further studies. As observed through the above graphs, the ε of **SMC-1** in DI water at 365 nm was found to be 1461.45 M^{-1} cm^{-1}. This is a vast improvement compared to the ε of **MC-1** which was found to be 44.72 M^{-1} cm^{-1}. This suggests that the thionation of the coumarin compound is beneficial for photochemical reactions.

3.5.2.9 N-(3-(((6,7-dimethoxy-3-nitro-2-thioxo-2H-chromen-4-yl)methyl)amino)propyl) methacrylamide (SMC-2)

As **SMC-1** led to improved photophysical properties in comparison to those of **MC-1**, the thionation of **MC-2** was also attempted to form the novel compound **SMC-2** (Scheme 3.10).

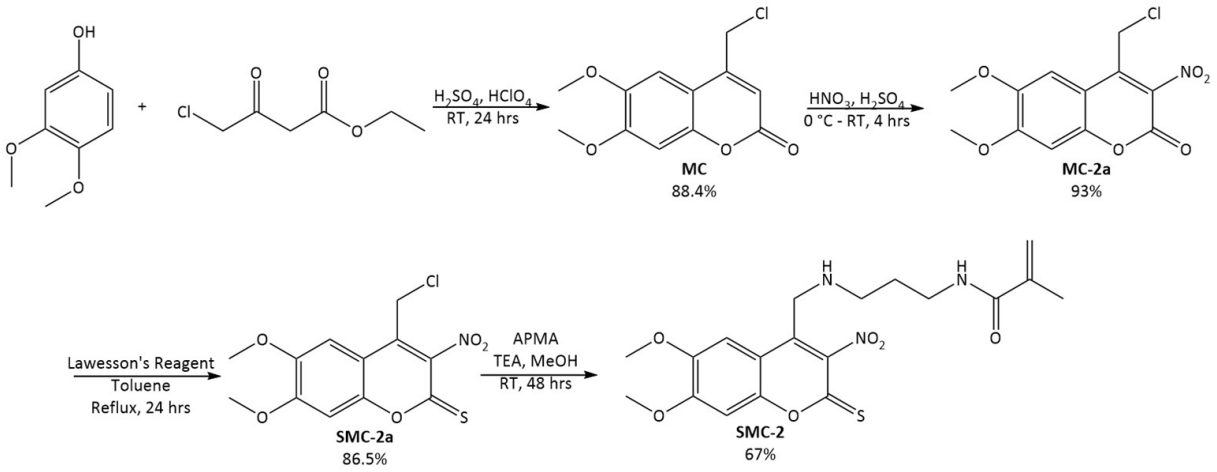

Scheme 3.10: *A schematic showing the synthesis of a coumarin PPG,* ***SMC-2a****, and the reaction with APMA to form the water soluble photocaged monomer* ***SMC-2****.*

Despite much research into the oxidation of the thiocarbonyl functional group, little evidence was found to show the stability of these groups in the presence of nitric acid, a known oxidising agent. To eliminate the possibility of **SMC** reverting to **MC** during nitration, **MC-2a** was synthesised as previously described (Chapter 3.5.2.6). This was then reacted with Lawesson's reagent while heated to reflux in order to form **SMC-2a** (yield = 86.5%). The photocaging of APMA with **SMC-2a** was performed in methanol with triethylamine to form **SMC-2** (yield = 67%). The structure of this compound was confirmed through the use of IR, proton NMR and MS.

As the reactions to form **MC**, **MC-2a** and **SMC-2a** were all high yielding reactions, the limiting step here was the formation of **SMC-2**. The final yield of the product was 46.6% with respect to the reagents. This is a fair yield for a 4-step synthetic procedure.

UV-Vis calibration studies were conducted on **SMC-2** in DI water to determine which wavelength, 365 nm or 405 nm, would be most efficient for photodeprotection (Figure 3.25).

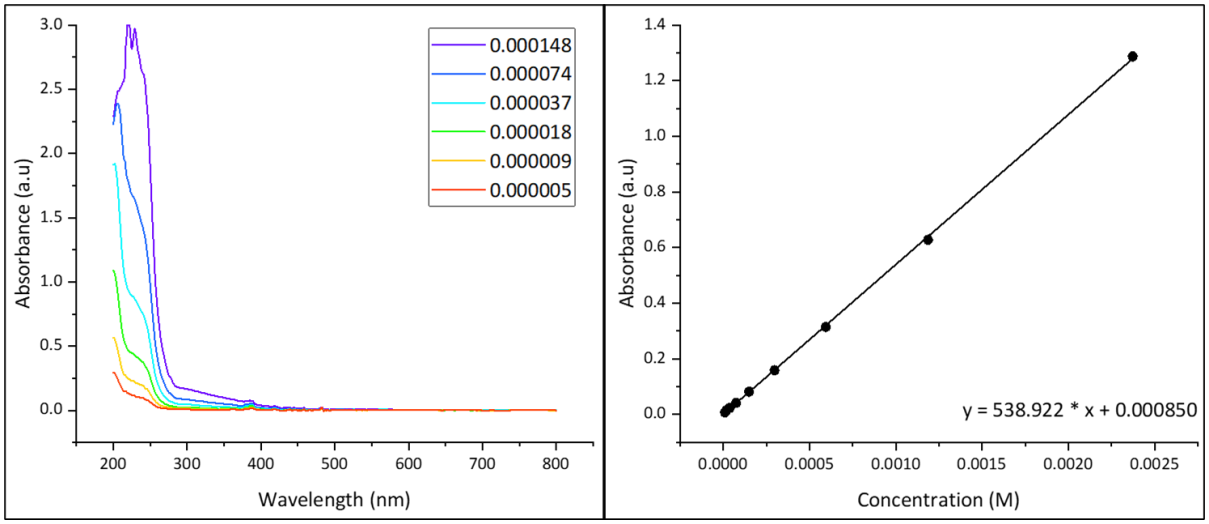

Figure 3.25: *Graphs depicting the absorbance spectra of **SMC-2** at a variety of concentrations in DI water (left) and the absorbance of various concentrations of **SMC-2** at 365 nm (right). Data is an average of 3 repeats of the study.*

SMC-2 had an absorbance maxima of 205 nm, with a smaller, secondary peak at approximately 240 nm. Due to the 365 nm light source being the closest in wavelength to these values, this was the chosen wavelength for deprotection. As observed through the above graphs, the ε of **SMC-2** in DI water at 365 nm was found to be 538.922 M^{-1} cm^{-1}. This is as expected, higher than that observed for **MC-2**, which was 34.979 M^{-1} cm^{-1}, however it is still much lower than that observed for **SMC-1**, 1461.45 M^{-1} cm^{-1}.

3.5.2.10 (6,7-dimethoxy-2-thioxo-2H-chromen-4-yl)methyl (3-methacrylamidopropyl) carbamate (SMC-3)

As **MC-3** had the highest ε of the coumarin derivatives, it was also thionated to further enhance this value to form the novel compound **SMC-3** (Scheme 3.11).

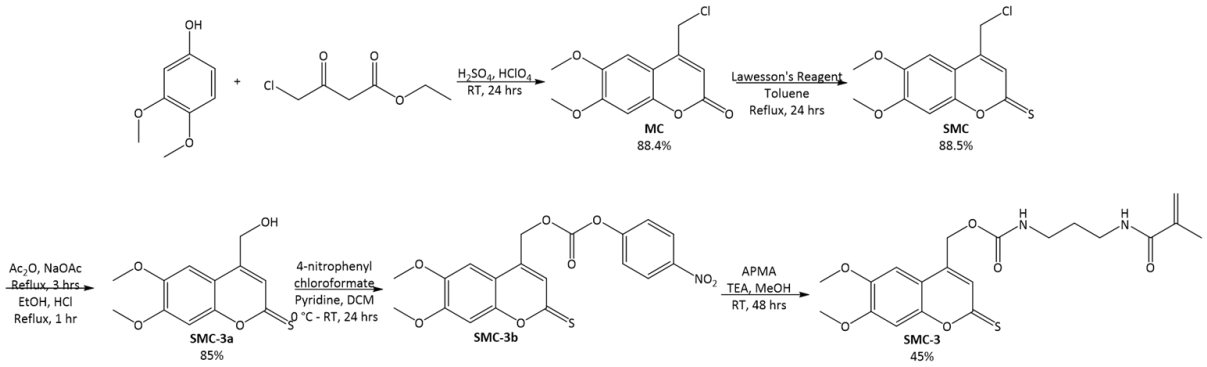

Scheme 3.11: *A schematic showing the synthesis of a coumarin PPG,* ***SMC-3b****, and the reaction with APMA to form the water soluble photocaged monomer* ***SMC-3****.*

Initially, **SMC** was formed as previously described (Chapter 3.5.2.8). This product was then hydroxylated by heating to reflux in acetic anhydride in the presence of sodium acetate to form an ester, immediately followed by acid catalysed ester cleavage with hydrochloric acid/ethanol. This produced the compound **SMC-3a** (yield = 85%). Following this, **SMC-3a** was then reacted with 4-nitrophenyl chloroformate in the presence of a weak base, resulting in the formation of the intermediate compound **SMC-3b**. The final carbamate protected amine was produced through the base catalysed nucleophilic substitution of APMA to form **SMC-3** (yield = 45%), as confirmed by IR, proton NMR and MS.

Despite the formation of **MC**, **SMC** and **SMC-3a** being high yielding reactions, all yielding in excess of 80%, this synthetic procedure was low yielding with regards to the final product, achieving a final yield of 30%. This is much lower than the previous coumarin

derivatives, however it Is expected as there is an increased number of steps in this method, and is in fact higher than that of **MC-3**.

In order to determine which light source would be optimal for photodeprotection, UV-Vis calibration studies were conducted on **SMC-3** in DI water (Figure 3.26).

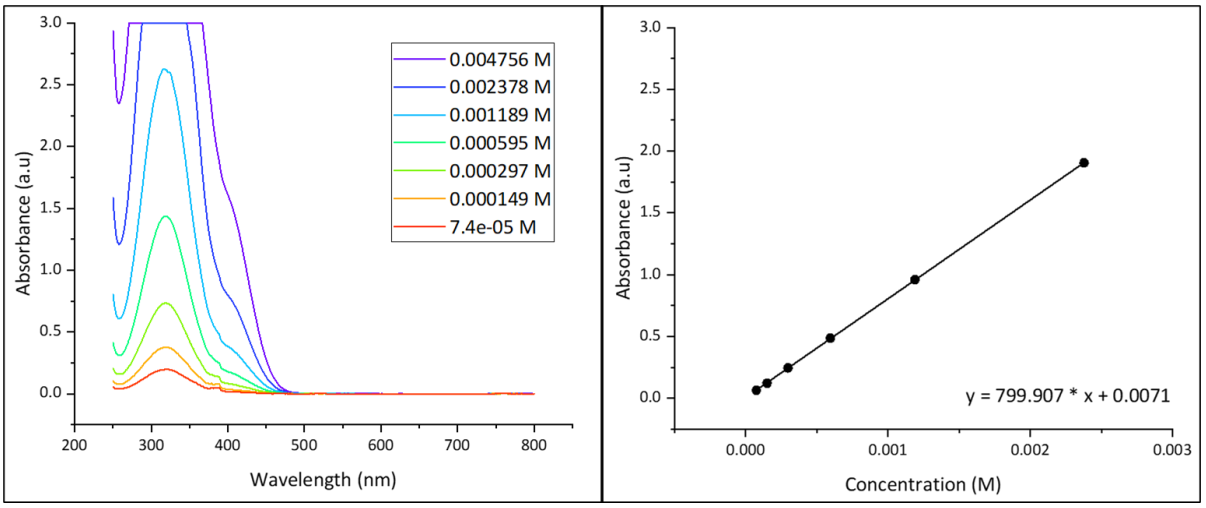

Figure 3.26: *Graphs depicting the absorbance spectra of **SMC-3** at a variety of concentrations in DI water (left) and the absorbance of various concentrations of **SMC-3** at 365 nm (right). Data is an average of 3 repeats of the study.*

Compound **SMC-3** had an absorbance maxima of 322 nm, there was also a secondary shoulder peak emerging at 411 nm. These wavelengths cover both of the potential irradiation wavelengths, therefore the wavelength with highest absorbance was used for further studies, which in this case was 365 nm. As observed through the above graphs, the ε of **SMC-3** in DI water at 365 nm was found to be 799.907 M^{-1} cm^{-1}. This is surprisingly lower than that of **MC-3**, which was found to be 1746.13 M^{-1} cm^{-1}, which appears to go against the trend as observed for other coumarin derivatives. This suggests that increasing the absorbance wavelength of a coumarin compound is not as simple as the conversion of a carbonyl group into a thiocarbonyl

group, the structure as a whole plays a much more complex role and cannot be merely broken down into its constituents.

3.5.2.11 (chloromethyl)-7-(dimethylamino)-2H-chromen-2-one (AC).

The methoxy coumarin derivatives proved to be simple to synthesise, however with low absorbance wavelengths. It is through the use of this knowledge that PPGs based on amino coumarins were designed (Scheme 3.12), as the more electron withdrawing group at position 7 is known to increase the absorption wavelength.[72]

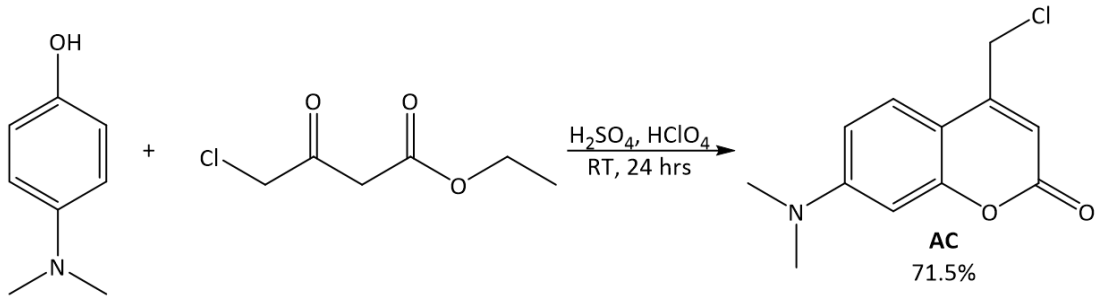

Scheme 3.12: *A schematic showing the synthesis of a coumarin PPG,* ***AC****.*

The coumarin, **AC**, was synthesised *via* a Pechmann condensation reaction (yield = 71.5%). The acid of choice to catalyse this reaction was a mixture of sulphuric acid and perchloric acid. Unfortunately, due to a delay in chemical deliveries and limited time, this is as far as the developments into amino coumarin derivatives reached.

As the UV-Vis spectra of APMA photocaged with **AC** could not be obtained, at this stage it was deemed more accurate to compare the ε of **AC** to that of **MC** at different wavelengths (Figure 3.27). The reason for this was to determine if the amino functional group at position 7 increased the absorbance wavelength in comparison to the presence of a methoxy functional group.

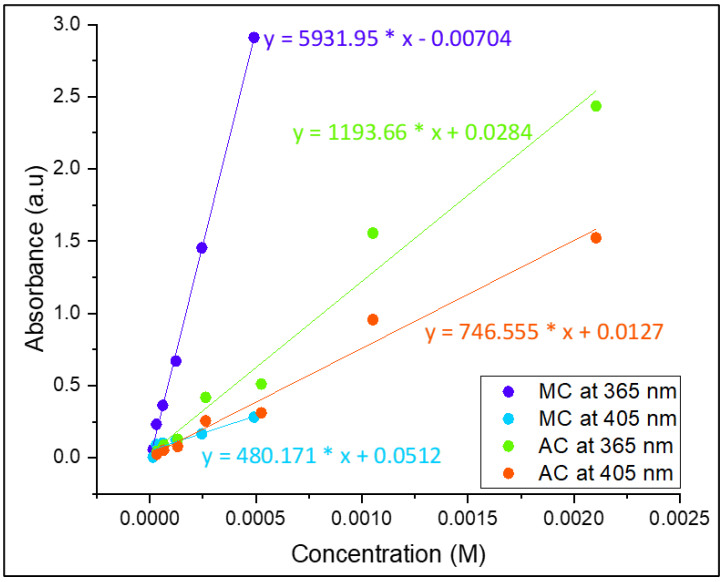

Figure 3.27: *A graph depicting the different ε values for* ***MC*** *and* ***AC*** *at 365 nm and 405 nm in DCM. Data is an average of 2 repeats of the study.*

For these studies, spectra were collected with dichloromethane as the solvent rather than DI water due to compound solubility. As can be seen, the ε of **MC** at 365 nm was found to be 5931.95 M^{-1} cm^{-1}, much higher than that observed for **AC** at the same wavelength which was 1193.66 M^{-1} cm^{-1}. This suggests that **MC** absorbs light of 365 nm more strongly that **AC**. Conversely, the ε of **MC** at 405 nm was 480.171 M^{-1} cm^{-1}, which is lower than that of 746.555 M^{-1} cm^{-1} which was observed for compound **AC**. This suggests that the amino functionalised coumarin does in fact absorb light more efficiently at higher wavelengths than the methoxy counterpart. This is a promising indication that the development of these PPGs was headed in the correct direction.

3.6 Conclusion

In conclusion, this work has set out to form photofunctionalisable hydrogels. Initially, based on previous work within the group, the photocaging of synthetic hydrogels with readily available PPGs was attempted; however, commercially available PPGs were found to be water reactive and therefore unsuitable for this purpose. Therefore, the project developed into testing the effect of polar organic solvents on the structure of hydrogels. To do this, we tested the RIS and porosity of LW devices, formed from a synthetic polymer hydrogel, before and after a gradual exchange of the solvent into organic media, and back into aqueous conditions. These tests showed that DMSO has minimal effect on the structure of hydrogels, thus DMSO was the solvent of choice for the photocaging of hydrogels. Unfortunately, while the hydrogels were found to be compatible with DMSO, the PPG NVOC-Cl was not, resulting in unwanted side reactions. These side reactions altered the functionality of the PPG, ultimately preventing the photocaging of primary amines.

It is due to this that the work in this chapter proceeded in a different direction. Following the discovery that commercially available PPGs are reactive with DMSO, the project progressed instead into the development of photocaged monomers. The initial PPGs designed were based on the widely used *ortho*-nitrobenzyl photocaging groups, followed by the coumarin structure. The ε of these compounds in DI water at the deprotection wavelength of 365 nm were studied to aid in the determination of how well deprotection will occur. Finally, the synthesis of a new coumarin photocaging agent was begun, to achieve a greater ε at 365 nm, or even to allow for the deprotection at the safer wavelength of 405 nm. However, due to time constraints this synthesis could not be completed, and is included to show that the project is advancing in the correct direction.

3.7 Future Work

The work discussed in this chapter leads to two different future paths. The first is to continue with the synthesis of three amino-coumarin based photocaging agents which have been designed, and to complete studies into their characteristics. As **AC** displayed improved absorbance at 405 nm in comparison to the analogous **MC**, this seems to be a promising direction to go in. As with the methoxy-coumarin derivatives, future work would involve the development of a family of PPGs with differing deprotection methods. Following this, as the thiocarbonyl derivatives were found to have increase ε values when compared to the carbonyl analogues, the thionation of amino-coumarin would also be studied in the future. This would lead to a large number of potential PPGs to choose from, of which there would hopefully be variety in the deprotection wavelengths.

The second path would be to determine the suitability of these monomers in the formation of hydrogel-based LW devices. Initially studies would have to be conducted to obtain the correct molar ratios of monomers and initiators to promote gel formation. Following that, studies into the deprotection of the monomers using 365 nm light are required to decide on irradiation time periods. Ascertaining if any hydrogels produced from these substances could support a waveguide mode without the need for doping in one way or another is required. Following that, if the compounds were suitable for the development of waveguide devices, then their hydrogel characteristics would need to be tested, such as their RIS and porosity to large compounds. Finally, tests to verify the biosensing ability of these potential LW devices could be conducted.

3.8 References

1 R. A. Fernandes, Ed., *Protecting-group-free organic synthesis: improving economy and efficiency*, Wiley, Hoboken, NJ, 2018.
2 Protective Groups, https://www.organic-chemistry.org/protectivegroups/, (accessed 30 September 2022).
3 F. Albericio, *Biopolymers*, 2000, **55**, 123–139.
4 G. R. Mahdavinia, S. B. Mousavi, F. Karimi, G. B. Marandi, H. Garabaghi and S. Shahabvand, *Express Polym. Lett.*, 2009, **3**, 279–285.
5 T. R. Hoare and D. S. Kohane, *Polymer*, 2008, **49**, 1993–2007.
6 A. H. Karoyo and L. D. Wilson, *Materials*, 2021, **14**, 1095.
7 Y. Zhang and Y. Huang, *Front. Chem.*, 2021, **8**, 615665.
8 L. E. R. O'Leary, J. A. Fallas, E. L. Bakota, M. K. Kang and J. D. Hartgerink, *Nat. Chem.*, 2011, **3**, 821–828.
9 T. A. Ulrich, T. G. Lee, H. K. Shon, D. W. Moon and S. Kumar, *Biomaterials*, 2011, **32**, 5633–5642.
10 H. K. Lau and K. L. Kiick, *Biomacromolecules*, 2015, **16**, 28–42.
11 M. Funaki and P. A. Janmey, in *Biology and Engineering of Stem Cell Niches*, Elsevier, 2017, pp. 363–373.
12 C. Ferrag, M. Abdinejad and K. Kerman, *Can. J. Chem.*, 2020, **98**, 66–73.
13 M. C. Catoira, L. Fusaro, D. Di Francesco, M. Ramella and F. Boccafoschi, *J. Mater. Sci. Mater. Med.*, 2019, **30**, 115.
14 G. Martínez-Mejía, N. A. Vázquez-Torres, A. Castell-Rodríguez, J. M. del Río, M. Corea and R. Jiménez-Juárez, *Colloids Surf. Physicochem. Eng. Asp.*, 2019, **579**, 123658.
15 Z. Tian, W. Liu and G. Li, *Polym. Degrad. Stab.*, 2016, **130**, 264–270.
16 E. Turan, S. Demirci and T. Caykara, *J. Appl. Polym. Sci.*, 2009, **111**, 108–113.
17 S.-C. Han, W.-D. He, J. Li, L.-Y. Li, X.-L. Sun, B.-Y. Zhang and T.-T. Pan, *J. Polym. Sci. Part Polym. Chem.*, 2009, **47**, 4074–4082.
18 J. Liu, D. Su, J. Yao, Y. Huang, Z. Shao and X. Chen, *J. Mater. Chem. A*, 2017, **5**, 4163–4171.
19 M. R. Singh, S. Patel and D. Singh, in *Nanobiomaterials in Soft Tissue Engineering*, Elsevier, 2016, pp. 231–260.
20 J. Zhu, J. Hu and R. E. Marchant, in *Biomimetic Biomaterials*, Elsevier, 2013, pp. 238–275.
21 J. Liao and H. Huang, *Biomacromolecules*, 2020, **21**, 2574–2594.
22 A. M. Villalba-R, K. Dhama and H. M. N. Iqbal, *Int. J. Pharmacol.*, 2017, **13**, 864–873.
23 U. S. K. Madduma-Bandarage and S. V. Madihally, *J. Appl. Polym. Sci.*, 2021, **138**, 50376.
24 E. M. Ahmed, *J. Adv. Res.*, 2015, **6**, 105–121.
25 J. Zhu and R. E. Marchant, *Expert Rev. Med. Devices*, 2011, **8**, 607–626.
26 E. Caló and V. V. Khutoryanskiy, *Eur. Polym. J.*, 2015, **65**, 252–267.
27 W. T. Godbey, in *Biotechnology and its Applications*, Elsevier, 2022, pp. 389–409.
28 A. J. Scott and A. Penlidis, in *Reference Module in Chemistry, Molecular Sciences and Chemical Engineering*, Elsevier, 2017, p. B9780124095472139010.
29 S. Maity, A. Chatterjee and J. Ganguly, in *Green Approaches in Medicinal Chemistry for Sustainable Drug Design*, Elsevier, 2020, pp. 617–649.
30 P. A. Panteli and C. S. Patrickios, *Gels*, 2019, **5**, 36.
31 K. Fukukawa and M. Ueda, in *Polymer Science: A Comprehensive Reference*, Elsevier, 2012, pp. 71–93.
32 A. Shrivastava, in *Introduction to Plastics Engineering*, Elsevier, 2018, pp. 17–48.
33 S. Bashir, M. Hina, J. Iqbal, A. H. Rajpar, M. A. Mujtaba, N. A. Alghamdi, S. Wageh, K. Ramesh and S. Ramesh, *Polymers*, 2020, **12**, 2702.
34 S. Dan, S. Banivaheb, H. Hashemipour and M. kalantari, *Polym. Bull.*, 2021, **78**, 1887–1907.

35 A. Herrmann, R. Haag and U. Schedler, *Adv. Healthc. Mater.*, 2021, **10**, 2100062.
36 J. Tavakoli and Y. Tang, *Polymers*, 2017, **9**, E364.
37 L.-H. Fu, C. Qi, M.-G. Ma and P. Wan, *J. Mater. Chem. B*, 2019, **7**, 1541–1562.
38 N. R. Mohamad, N. H. C. Marzuki, N. A. Buang, F. Huyop and R. A. Wahab, *Biotechnol. Biotechnol. Equip.*, 2015, **29**, 205–220.
39 D. I. Sánchez-Machado, J. López-Cervantes, Ma. A. Correa-Murrieta, R. G. Sánchez-Duarte, P. Cruz-Flores and G. S. de la Mora-López, in *Nonvitamin and Nonmineral Nutritional Supplements*, Elsevier, 2019, pp. 485–493.
40 A. Isidro-Llobet, M. Álvarez and F. Albericio, *Chem. Rev.*, 2009, **109**, 2455–2504.
41 16.4, https://chem.libretexts.org/Bookshelves/Introductory_Chemistry/Chemistry_for_Changing_Times_(Hill_and_McCreary)/16%3A_Biochemistry/16.04%3A_Proteins-_Polymers_of_Amino_Acids, (accessed 17 October 2022).
42 N. Qvit and O. S. Kornfeld, *J. Vis. Exp.*, 2016, 53589.
43 G. B. Fields, *Curr. Protoc. Protein Sci.*, 2002, **Chapter 18**, Unit 18.1.
44 *J. Chem. Soc. Perkin 1*, 2002, 125–142.
45 C. G. Bochet, *Tetrahedron Lett.*, 2000, **41**, 6341–6346.
46 A. Bardhan and A. Deiters, *Curr. Opin. Struct. Biol.*, 2019, **57**, 164–175.
47 C.-H. Park and R. S. Givens, *J. Am. Chem. Soc.*, 1997, **119**, 2453–2463.
48 R. Weinstain, T. Slanina, D. Kand and P. Klán, *Chem. Rev.*, 2020, **120**, 13135–13272.
49 A. Patchornik, B. Amit and R. B. Woodward, *J. Am. Chem. Soc.*, 1970, **92**, 6333–6335.
50 P. Wang, *Asian J. Org. Chem.*, 2013, **2**, 452–464.
51 A. P. Pelliccioli and J. Wirz, *Photochem. Photobiol. Sci.*, 2002, **1**, 441–458.
52 D. Abate-Pella, N. A. Zeliadt, J. D. Ochocki, J. K. Warmka, T. M. Dore, D. A. Blank, E. V. Wattenberg and M. D. Distefano, *ChemBioChem*, 2012, **13**, 1009–1016.
53 A. Yu. Vorobev and A. E. Moskalensky, *Comput. Struct. Biotechnol. J.*, 2020, **18**, 27–34.
54 M. J. Hansen, W. A. Velema, M. M. Lerch, W. Szymanski and B. L. Feringa, *Chem. Soc. Rev.*, 2015, **44**, 3358–3377.
55 A. S. C. Fonseca, A. M. S. Soares, M. S. T. Gonçalves and S. P. G. Costa, *Tetrahedron*, 2012, **68**, 7892–7900.
56 A. K. Pal, E. Labella, N. J. Goddard and R. Gupta, *Macromol. Chem. Phys.*, 2019, 1900228.
57 L. E. Edsberg, in *Bioengineering Research of Chronic Wounds*, ed. A. Gefen, Springer Berlin Heidelberg, Berlin, Heidelberg, 2009, vol. 1, pp. 343–362.
58 PubChem, Insulin human, https://pubchem.ncbi.nlm.nih.gov/compound/118984375, (accessed 30 September 2022).
59 B.-A. Sela, *Harefuah*, 2002, **141**, 631–635, 665.
60 T. Maier, A. Schmidt, M. Güell, S. Kühner, A. Gavin, R. Aebersold and L. Serrano, *Mol. Syst. Biol.*, 2011, **7**, 511.
61 DMSO Oxidation, http://ursula.chem.yale.edu/~chem220/chem220js/STUDYAIDS/oxidation/DMSOoxidation.html, (accessed 24 February 2020).
62 A. K. Pal, N. J. Goddard, H. J. Dixon and R. Gupta, *Biosensors*, 2020, **10**, 134.
63 C. Maity, F. Trausel and R. Eelkema, *Chem. Sci.*, 2018, **9**, 5999–6005.
64 M. T. Stone and J. S. Moore, *Org. Lett.*, 2004, **6**, 469–472.
65 G. Marriott, Ed., *Biophotonics. Pt. A: ...*, Acad. Press, Amsterdam, 2003.
66 4,5-Dimethoxy-2-nitrobenzyl bromide 97 53413-67-5, http://www.sigmaaldrich.com/, (accessed 13 October 2022).
67 1.10, https://chem.libretexts.org/Courses/Purdue/Purdue%3A_Chem_26505%3A_Organic_Chemistry

_I_(Lipton)/Chapter_1._Electronic_Structure_and_Chemical_Bonding/1.10%3A_Pi_Conjugation, (accessed 4 December 2020).
68 K. L. Woon, A. Ariffin, K. W. Ho and S.-A. Chen, *RSC Adv.*, 2018, **8**, 9850–9857.
69 M. M. Mahmoodi, D. Abate-Pella, T. J. Pundsack, C. C. Palsuledesai, P. C. Goff, D. A. Blank and M. D. Distefano, *J. Am. Chem. Soc.*, 2016, **138**, 5848–5859.
70 Carbon tetrachloride, https://www.gov.uk/government/publications/carbon-tetrachloride-properties-incident-management-and-toxicology/carbon-tetrachloride-general-information, (accessed 24 October 2023).
71 12 Principles of Green Chemistry, https://www.acs.org/content/acs/en/greenchemistry/principles/12-principles-of-green-chemistry.html, (accessed 31 October 2022).
72 Y. Chitose, M. Abe, K. Furukawa and C. Katan, *Chem. Lett.*, 2016, **45**, 1186–1188.
73 J. Donovalová, M. Cigáň, H. Stankovičová, J. Gašpar, M. Danko, A. Gáplovský and P. Hrdlovič, *Molecules*, 2012, **17**, 3259–3276.

Chapter 4 – Internally Referenced Biosensors

4.1 Introduction

The need for a reference is an important factor in any biosensor; without a reference, there is no way to determine if results are true or false. Obtaining a false positive result or a false negative can have serious repercussions on the patient.

Lateral flow tests such as pregnancy tests are equipped with a control line, to ensure the capillary flow action of the paper-based device is sufficient at pulling analytes along the length of the test strip.[1] If this were not present, a failed test, giving rise to a negative response which should in fact read positive, could potentially lead to harmful effects to the growing foetus.

Polymerase Chain Reaction (PCR) test wells can contain a blank sample (negative control), this ensures that there is no accidental, non-specific amplification. The absence of this solution could lead to a result being incorrectly analysed as a positive, thus giving rise to a false positive. While a false positive could lead to the minor inconvenience of an unnecessary forced isolation, in the case of SARS-COV-2 tests, this could lead to dire consequences in the case of other tests, such as the false diagnosis of cancer.[2]

A false result arising from biosensors can lead to any number of harmful consequences, for the patient or others around them. It is due to this that it is important for biosensors to include a control test, or an internal reference to ensure that they are in correct working order.

4.2 Photoresponsive Hydrogels

Since the development of mechanically strong hydrogels as biocompatible materials, much research has been conducted into the development of responsive hydrogels, such as those responsive to pH or temperature changes.[3] In comparison to other stimuli responsive hydrogels, the published research into hydrogels which react to light is not as extensive.[4] Photoresponsive hydrogels are ideal as their reactions are fast, clean and easy to control; as there is much spatio-temporal control with photochemical reactions, well defined structures can be formed through the use of a photoresponsive hydrogel.[3,5] Photoresponsive hydrogels currently developed are often patterned based on one of three methods: photoisomerization, click chemistry, or photolabile protecting groups (PPGs).[3]

Hydrogels which isomerise in response to light often reversibly transition from the solution to gel phase and back depending on the light source they are irradiated with (Figure 4.1). For example, an azobenzene functionalised peptide was found to transition from hydrogel to solution in the presence of UV light, this was reversible with visible light.[6] One potential use of these hydrogels which undergo photoisomerization is targeted drug delivery.[7] The drug can be encapsulated in the structure of the hydrogel, and subsequentially released in the solution phase initiated by light.

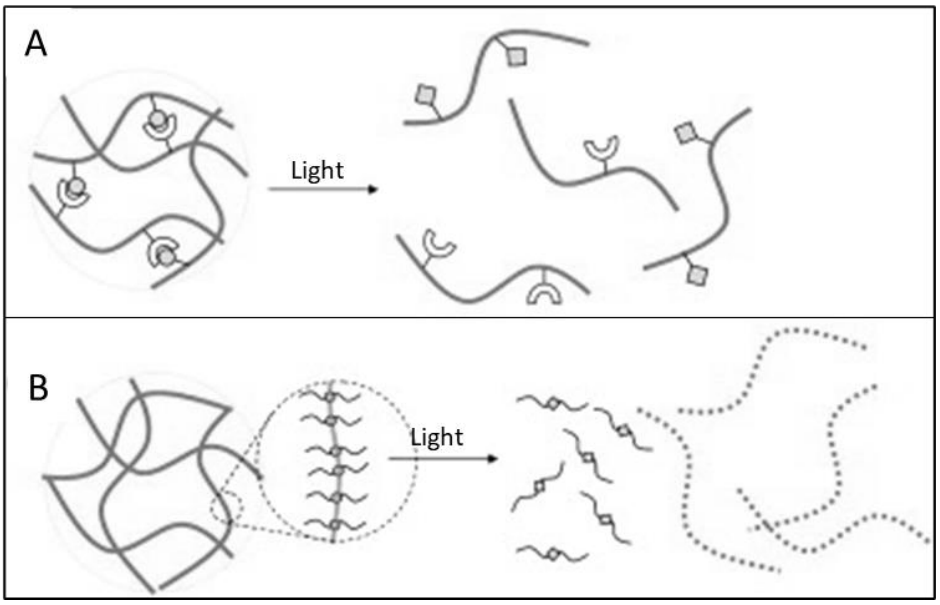

Figure 4.1: *An image depicting the transition of a gel to the solution phase through irradiation with light. (A) Cleavage of the cross-linking bonds results in the formation of a solution. (B) Light results in the breakdown of the polymer structure, thus resulting in the formation of a solution. Image adapted from Tomatsu et al.*[8]

Photoresponsive hydrogels can also be based on the principles of click chemistry. This has been achieved in a multitude of ways. The functionalisation of a dibenzocyclooctyne group with a cyclopropenone group neutralises its ability to form click chemistry reactions with azides, resulting in the formation of triazoles. This cyclopropenone-caged dibenzocyclooctyne can undergo a light-initiated decarbonylation reaction, resulting in the re-emergence of the carbon-carbon triple bond, thus enabling azide-alkyne cycloaddition (Figure 4.2).[9] The maleimide functionalisation of hydrogels provides an ideal surface for click thiol reactions. In this instance, a pattern was formed in the hydrogel structure of thiol-reactive and thiol-inert regions through the use of UV light. The UV light directed at maleimide groups initiates radical polymerisation of the maleimide, causing them to no longer be thiol reactive.[10] Both methods enable the formation of structures within the hydrogel structure itself.

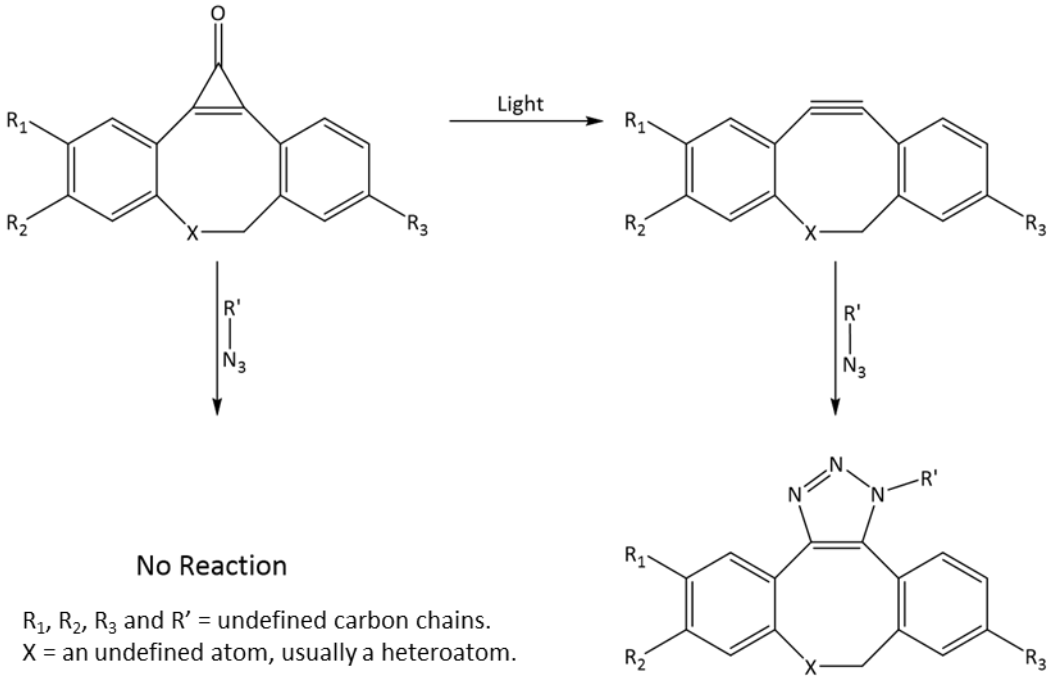

Figure 4.2: *An image depicting the lack of reaction between cyclopropenone-caged dibenzocyclooctone and azide functional groups, compared to the deprotection of the cyclopropenone group to result in a click chemistry compatible alkyne group formation. Image adapted from McNitt et al.*[9]

Research into PPGs is present in high abundance, slowly expanding into research for their use in the formation of photoresponsive hydrogels. Vast quantities of PPGs have now been developed for a variety of different functional groups; it is due to this that photoresponsive hydrogels based on photolabile chemistry have the widest range of characteristics. Light can be used to destroy the structure of hydrogels which are formed using PPGs (Figure 4.3). In the work of Griffin *et al*, through incorporating the protecting group, in this case an *ortho*-nitrobenzyl derivative, into the structure of the hydrogel, irradiation with light was able to cause structural destruction.[11] This method is similar to hydrogels which undergo photoisomerization as discussed earlier; thus these hydrogels can be used for similar purposes, such as delivery systems. In this study, the hydrogels were tested for the ability to safely release human stem cells.[11]

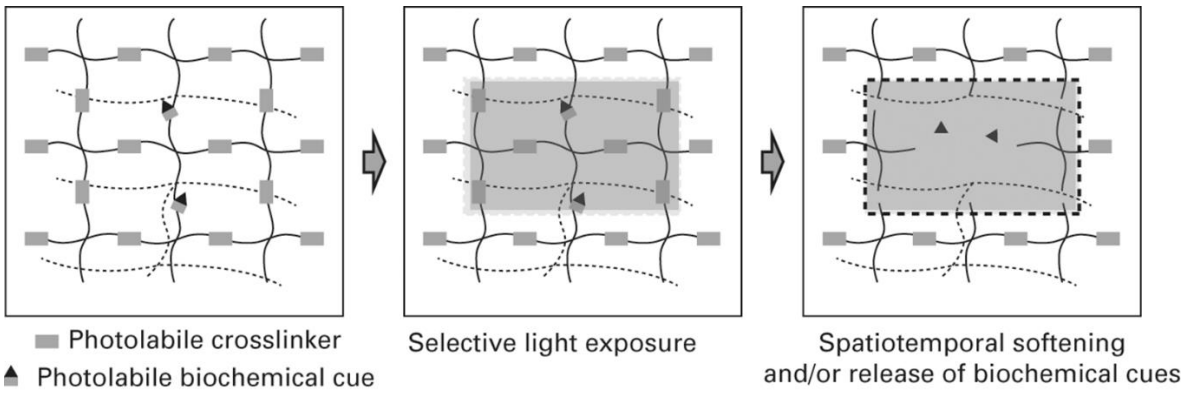

Figure 4.3: *An image depicting the selective photocleavage of cross-linking bonds in a hydrogel, resulting in the release of encapsulated materials. Image adapted from Guvendiren et al.*[12]

In addition to this, similar to click chemistry-based hydrogels, photoprotected hydrogels can be used to form smaller, patterned regions within the hydrogel structure itself. Through the caging of free functional groups within a hydrogel with PPGs, the functional groups can be uncaged selectively through the irradiation of the photoresponsive hydrogel through a photomask. This has been seen with agarose-based hydrogels which are photocaged with coumarin-based PPGs. The deprotection mechanism leaves the agarose gel functionalised with a thiol group in desired regions.[13]

There are many different chemical techniques for the formation of photoresponsive hydrogels. For strong 3D structures such as hydrogels, light induced reactions can allow for the formation of localised reactions to form high resolution patterns. These patterns can be modified to have tailored reactivities. Based on this, photoresponsive hydrogels have a multitude of potential uses in in a wide range of areas, ranging from tissue engineering, to drug delivery, to biosensing technologies.[14]

4.3 Internally Referenced Biosensors

Through the incorporation of internal references within a biosensing device, we create the ability to obtain accurate analyte detection rapidly by accounting for the effect of external factors. The simplest method of internal referencing is the implementation of a region where no detection is expected for ease of comparison.

Nucleic acid amplification tests such as PCR can contain a number of different control samples depending on the test and its purpose. The most commonly used referencing techniques for PCR are a positive control, which as expected contains the target analyte in order to produce a strong detection signal; and a no template control, in this instance the sample mixture contains all reagents excluding the target analyte.[15] A positive control is used to ensure the amplification technique is effective, whereas a no template control provides assurance that the reaction matrix is both analyte free and does not produce a false signal (Figure 4.4).[15]

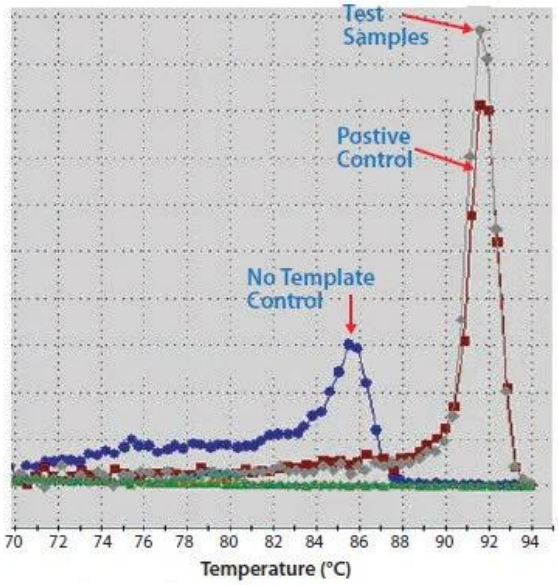

Figure 4.4: *An image displaying the signals observed following PCR tests which contain a positive and no template control sample, displaying differences to indicate the test is working correctly. Image obtained from Sigma Aldrich.*[16]

A positive control is possible in PCR as the samples are separate and self-contained, therefore the spiking of one area with target analyte cannot contaminate the samples (Figure 4.5); however, biosensors based on a single surface device, such as lateral flow and lab-on-a-chip devices do not have this capability. It is due to this that, for biosensors of this type, positive control biosensors are designed to be inert to the target analyte. This has been discussed previously with lateral flows containing a control line targeted to another analyte (Chapter 1.4.2), it is also a way for electrochemical biosensors to incorporate an internal reference. An example of this is one device developed by Moser *et al*, an electrochemical device with platinum sensing electrodes targeted to different analytes and a silver/silver chloride inert reference electrode.[17] In this instance the reference electrode is able to quantitate which signals are due to selective biosensing (which occur only at the sensing electrode) and which signals may be due to external effects (which occur at both electrodes).

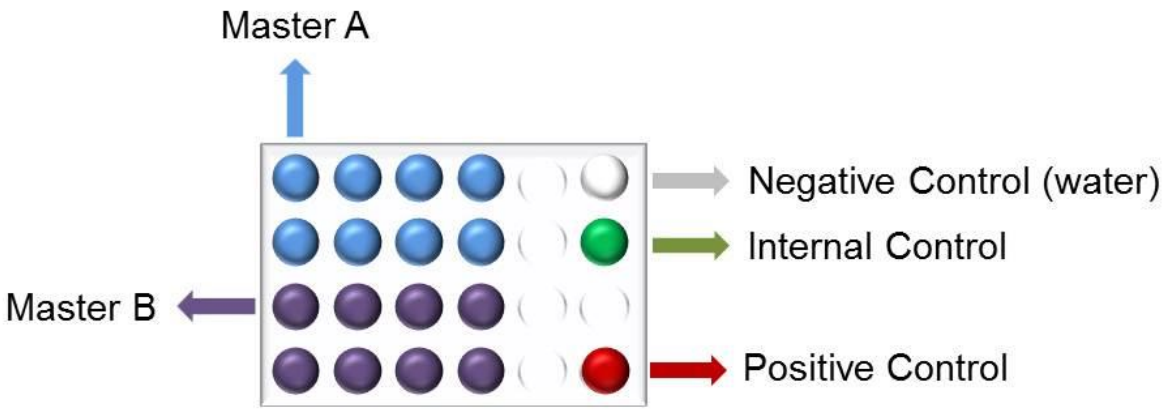

Figure 4.5: *An image depicting the presence of control samples within a PCR plate. Image used from Altona Diagnostics.*[18]

The use of a no template control within PCR allows for the normalisation of data, giving a more accurate representation of analyte detection. References to allow for data normalisation are also required in other techniques where external factors such as changes in

temperature can affect the signal received; this is a common problem among optical biosensors such as surface plasmon resonance (SPR). A simple method of creating a reference with SPR is to functionalise two regions of the chip differently, one which is inert and one with the ability to sense the target analyte (Figure 4.6).[19] The data collected from the inert region displays signals produced which are not specific to analyte detection, therefore this data can be used to normalise the detection results and give a more accurate representation of analyte sensing.

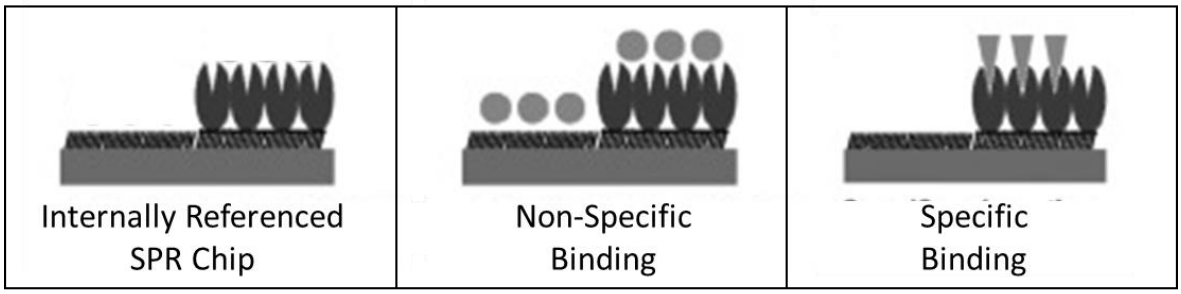

Figure 4.6: *An image displaying the formation of an internally referenced SPR biosensor based on forming regions for analyte detection. The regions can display whether signals are due to non-specific or specific binding. Image adapted from Nizamov et al.*[19]

4.4 Internally Referenced Waveguides

The biosensing capability of leaky waveguides (LWs), like SPR, is based on changes in refractive index (RI). Due to this, signals produced by LW biosensors are likewise susceptible to false or masked signals created by external stimuli, thus resulting in less accurate detection of analyte concentration in these quantitative biosensors.[20, 21] As previously discussed, the way to overcome this problem is to incorporate an internal reference into the LW device. Similar to the SPR example previously described, by comparing the data produced by a reference region to the sensing region, it is possible to eliminate temperature effects and other uncontrollable variables such as non-specific analyte binding from the final signal, therefore providing a more accurate representation of analyte concentration.

One approach to form an internal reference is to incorporate two channels, a sample channel and a reference channel, into the LW instrument.[22] One example of this is in work by Gupta *et al*, in which a two-channel flow cell is used, one for sensing and one for referencing. The biorecognition element streptavidin is not added to the reference channel, thus preventing the selective detection of immunoglobulin G (IgG).[23] As the reference channel does not contain the biorecognition element, any subsequent signal suggesting the detection of IgG can be deemed to be caused by non-specific binding, resulting in a more accurate representation of analyte detection. The accurate signal can then be obtained by taking the differential of the two regions, therefore subtracting non-specific signals from the sensing signal (Figure 4.7). This referencing method however does not take into account any non-specific binding caused directly by the biorecognition element itself. This means that only some, not all, of the uncontrollable variables are considered, therefore some non-specific binding may still be seen in the final signal.

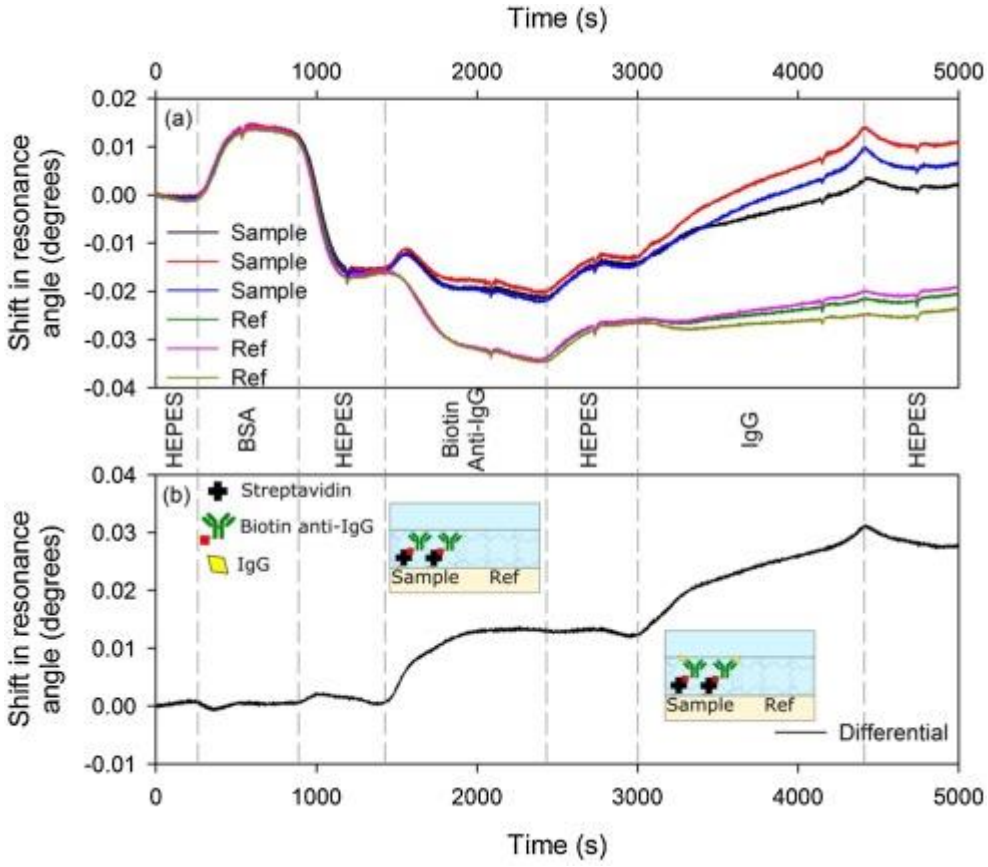

Figure 4.7: *Graphs depicting the signals obtained through using sensing and referencing channels on a LW device (top) to allow for the calculation of a differential signal (bottom) for accurate biosensing. Image obtained from Gupta et al.*[23]

Another internal referencing method which has been employed in LWs is the formation of stacked, or two layered, waveguides. The structure of stacked waveguides is designed to contain one layer functionalised with biorecognition elements, so as to act as a sensing region, while the other inert layer acts as a reference region.[24] In literature, a 3% (w/v) agarose hydrogel was used as a LW referencing layer, being topped with a 2% (w/v) functionalised agarose sensing hydrogel. The 2% agarose hydrogel was reacted with sodium periodate to oxidise the free alcohols into amine reactive carbonyl groups.[24] Due to this, covalent binding of biorecognition elements, and by extension target analytes, occurred only in the 2% agarose LW layer. Changes in signal in the 3% agarose layer represent non-specific

binding, and when subtracted from the sensing signal give a more accurate representation of analyte detection (Figure 4.8).[24] This method addresses the problems noted in having separate channels, in that the sensing and referencing regions are now exposed to the same chemistries, making them more accurate. Unfortunately, this method of self-referencing also has its drawbacks. To create layers of hydrogels, often the bottom layer needs to be dried. The most common methods of drying hydrogels are also problematic, for example, air drying is cost effective but time consuming, and heat drying costs more for the equipment but saves time. The major drawback here however is that often, when rehydrating, hydrogels dried in these ways will frequently crack, leading to waveguide visualisation problems, reduced porosity, and an inability to guide light.[25]

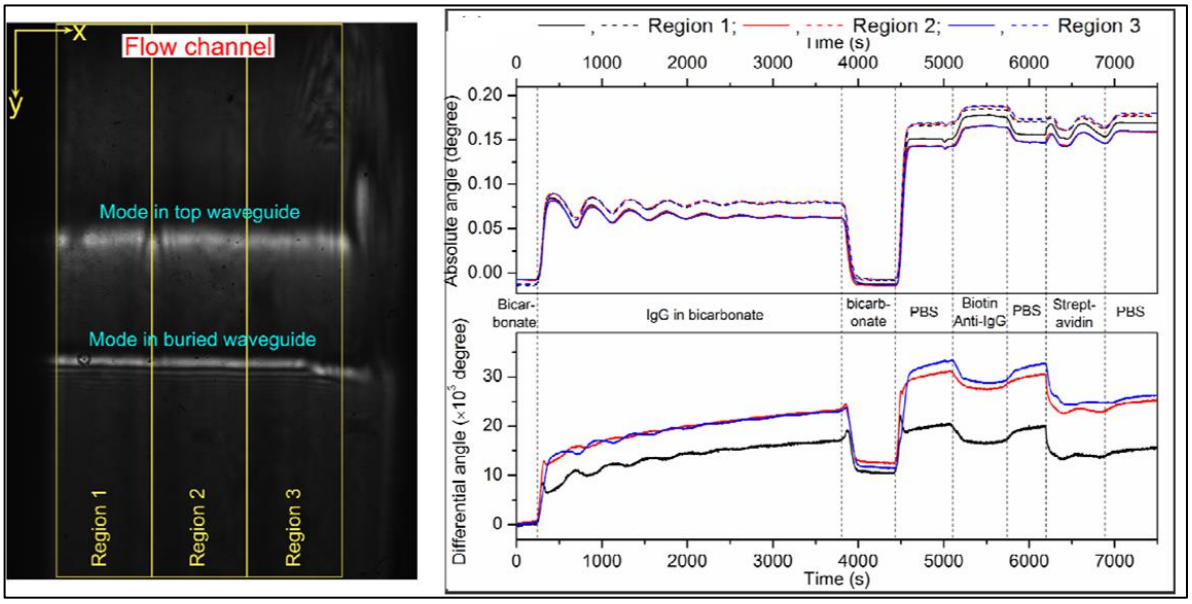

Figure 4.8: *An image depicting the output of a stacked LW device, showing modes relating to each layer (left) the signals obtained through using the device for biosensing (top right) and finally the differential signal observed between the sensing and referencing layers (bottom right). Image obtained from Gupta et al.* [24]

Due to the problems discussed with two-channel referencing and stacked waveguides, much research has been conducted into the use of photoresponsive hydrogels for LW

biosensing capabilities. As was discussed previously in Chapter 4.2, PPGs can be used to form highly controlled microstructures within 3D structures such as hydrogels. These microstructures can create arrays of protein reactive and inert regions within a hydrogel. When hydrogels functionalised with these moieties are implemented for LW devices, these arrays can form biosensing and referencing regions within the same device (Figure 4.9).[26] This has been noted in literature, LW devices have been created from chitosan films, which have been functionalised with a photocleavable biotin group. Following irradiation with UV-light, a pattern of sensing and referencing regions were created in the device, creating an internally referenced LW which does not need to be dried for formation.[21]

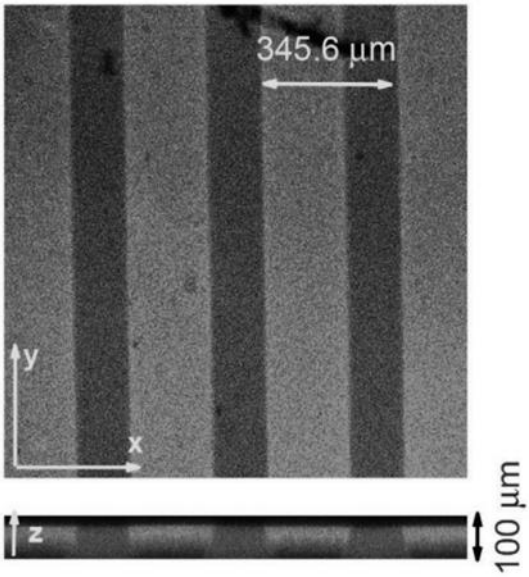

Figure 4.9: *An image displaying a photopatterned polyacrylamide hydrogel. Dark areas indicating photocaged regions, whereas the lighter areas show the photodeprotected free amines which were stained with fluorescein isothiocyanate. Image adapted from Pal et al.*[27]

As two-channel and stacked layer referencing techniques were found to have many drawbacks, photoresponsive hydrogels using PPGs are an ideal method of creating internal references within LW devices. Unfortunately, the photocleavable biotin reagent discussed in

literature is costly, which is not ideal for point of care (POC) testing. Based on this, within this thesis (Chapter 3.5.2) we have discussed the synthesis of a number of photocaged monomer groups (Figure 4.10); henceforth we will be discussing their suitability for the formation of photoresponsive hydrogels, and the ability of these hydrogels to form internally referenced LW devices.

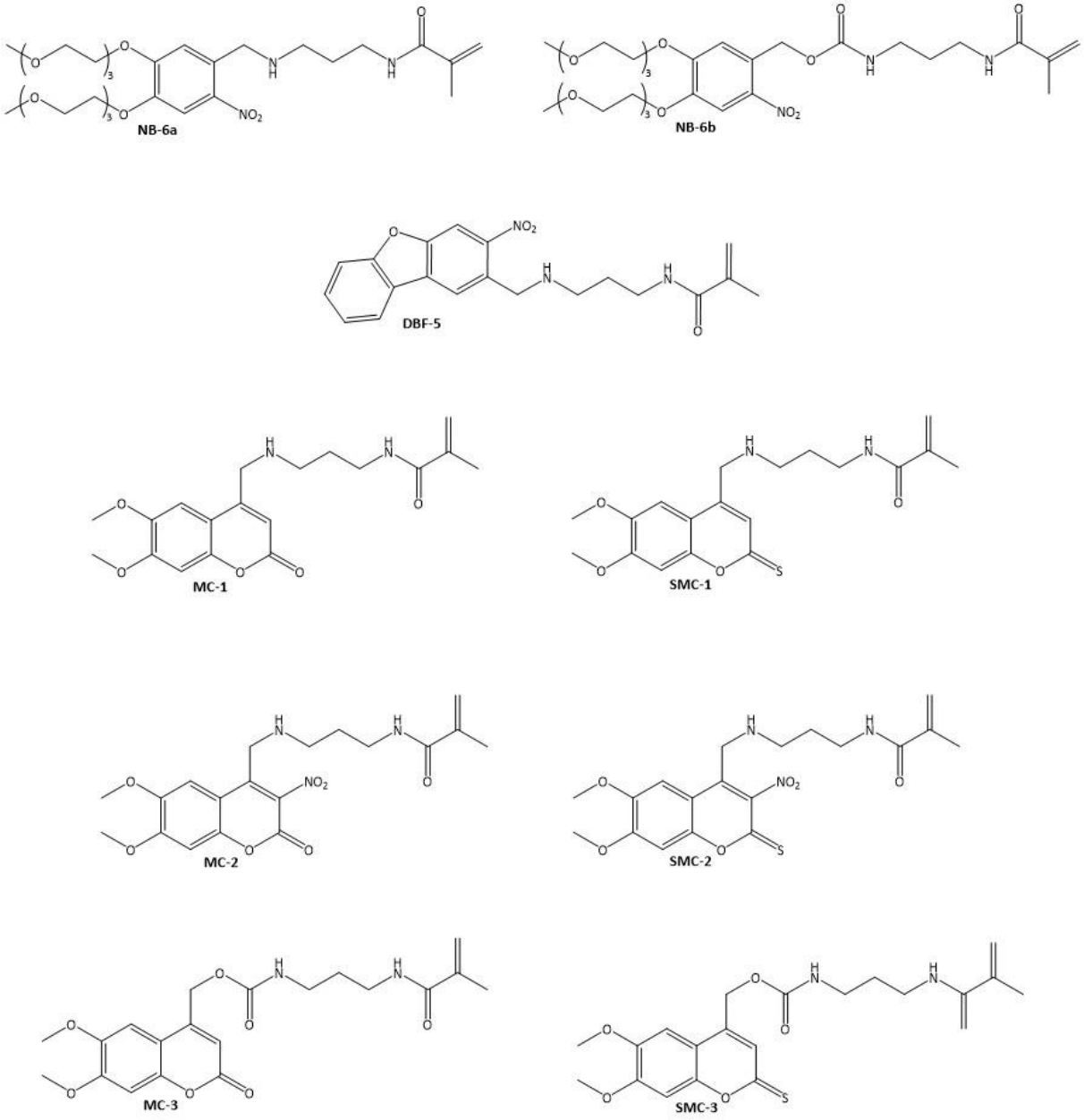

***Figure 4.10**: An image displaying the monomers synthesised in Chapter 3.5.2 which will be used throughout this chapter to form hydrogels.*

4.5 Project Aims

Within the group, we have previously shown the ability to use LW devices for the detection of biologically relevant analytes.[28] Throughout this work, the detection has been compared to a separate channel, which does not contain the all-important detection element. The purpose of this is to determine if a signal is due to detection element – analyte binding, or possibly unwanted interactions. While effective, this method is not perfect, a reference within the structure of the LW would be much more accurate. Therefore, the purpose of this work is to:

1. Determine the method of deprotection for PPGs.
2. To form and photopattern the LW devices to produce alternating arrays of biosensing and photocaged reference regions.
3. Test the refractive index sensitivity (RIS) and porosity of these LW devices.
4. Show the ability of the LW devices to provide an internal reference when performing as a biosensor.

4.6 Results and Discussion

4.6.1 Hydrogel Formation

In order to be used as internally referenced biosensors, the monomers must first be polymerised into hydrogels. In Chapter 3.5.2.1, the formation of **NVOC-APMA** was discussed, alongside the inability to incorporate enough monomer into the hydrogel matrix to form an effective biosensor. Due to this, all photocaged monomers were tested for their ability to form hydrogels prior to conducting any further studies.

Hydrogels were to be formed through free-radical polymerisation. To do this, acrylamide (AAm), photocaged *N*-(3-aminopropyl)methacrylamide (APMA) derivative, *N*-*N'*-methylenebis(acrylamide) (BAAm), a 10% ammonium persulfate (APS) solution, *N,N,N',N'*-tetraethylmethylenediamine (TEMED) and DI water, were combined in a pot.

To maintain the desired molar ratio of AAm to APMA derivative, initial mixtures tested were slight modifications of the composition used for AAm/APMA hydrogels in Chapter 3.5.1. On the basis of this, the exact masses and volumes for initial hydrogel formation are noted in Table 4.1.

While some compounds were observed to form hydrogels with this composition, **MC-1**, **SMC-1**, **MC-2** and **SMC-2**, for the rest, no gel formation was observed. Following this, as the monomer concentrations were already optimal for biosensor formation, studies were conducted to determine how initiator levels affected polymerisation. In an attempt to encourage hydrogel formation, levels of APS and TEMED were modified for each monomer, both exclusively and together. Despite many combinations of hydrogel mixture being tested for compounds **NB-6a**, **NB-6b**, **DBF-5**, **MC-3** and **SMC-3**, polymerisation into a hydrogel was not observed, likely due to the large structures of the PPGs.

Table 4.1: *A table depicting the volumes and masses of reagents used to create photocaged hydrogels.*

Gel Type	40 % AAm (µL)	APMA Derivative (mg)	BAAm (mg)	10% APS (µL)	TEMED (µL)	DI H_2O (µL)
AAm/APMA	35.2	1.97	1.53	25	2.5	376.55
AAm/**NB-6a**	35.2	6.63	1.53	25	2.5	376.55
AAm/**NB-6b**	35.2	7.12	1.53	25	2.5	376.55
AAm/**DBF-5**	35.2	4.05	1.53	25	2.5	376.55
AAm/**MC-1**	35.2	3.96	1.53	25	2.5	376.55
AAm/**SMC-1**	35.2	4.14	1.53	25	2.5	376.55
AAm/**MC-2**	35.2	4.46	1.53	25	2.5	376.55
AAm/**SMC-2**	35.2	4.64	1.53	25	2.5	376.55
AAm/**MC-3**	35.2	4.46	1.53	25	2.5	376.55
AAm/**SMC-3**	35.2	4.64	1.53	25	2.5	376.55

Unfortunately, despite trying many different ratios of the compounds for hydrogel mixtures, polymerisation failed to result in hydrogel formation for a number of photocaged monomers. Due to this, only 4 photocaged monomers were suitable for further testing, those being **MC-1**, **MC-2**, **SMC-1** and **SMC-2**.

4.6.2 Monomer Deprotection Studies

Following the synthesis and purification of photocaged APMA groups in Chapter 3.5.2, more information was required with regards to the monomers designed. One vital, yet unknown piece of information required, is the length of time required for deprotection. To determine this, studies were conducted on the monomers both in solution and once polymerised into a hydrogel. Another crucial factor is the optimum solvent for PPG cleavage. As observed by the PPG 4,5-dimethoxy-2-nitrobenzyl chloroformate (NVOC-Cl) (Figure 4.11), in some instances deprotections can require unique solvent conditions.

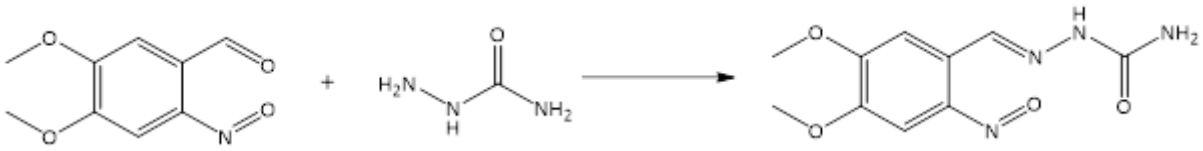

Figure 4.11: *An image displaying how semicarbazide hydrochloride is used to block the free aldehyde group produced following the deprotection of the PPG, NVOC-Cl. Image adapted from de Oliveira et al.*[29]

To aid in the determination of deprotection time periods and solutions, photocaged monomers were dissolved in a deprotection solution, which is selective for each monomer. Following the dissolution of monomers, they were exposed to 365 nm light, as per the absorbance studies conducted in Chapter 3.5.2, for 120 minutes. 1 mL aliquots of the solutions were taken at regular intervals and the ultraviolet-visible (UV-Vis) spectra were recorded. As the by-products of deprotection were expected to remain in solution and therefore provide a signal in the UV-Vis spectra, the absorbance spectra were never expected to replicate that of APMA upon complete deprotection. Due to this, the studies were instead looking for a plateau in the decrease of absorbance.

A plateau in absorbance is easier to discern when comparing absorbance at a fixed wavelength in contrast to comparing whole spectra; hence, in concordance with previous studies, the absorbance at 365 nm was monitored. Once an apparent plateau in absorbance was observed succeeding a period of decreasing absorbance, this was noted as the end point of the deprotection. The purpose of this study was to test if photodeprotection does occur prior to the more complex hydrogel studies, as photodeprotection in solution is expected to take longer than the corresponding hydrogel studies.

4.6.2.1 MC-1

Due to the chemically unreactive photocleavage product of **MC-1** (Scheme 4.1), deprotection studies were initially conducted in a solution of deionised (DI) water.

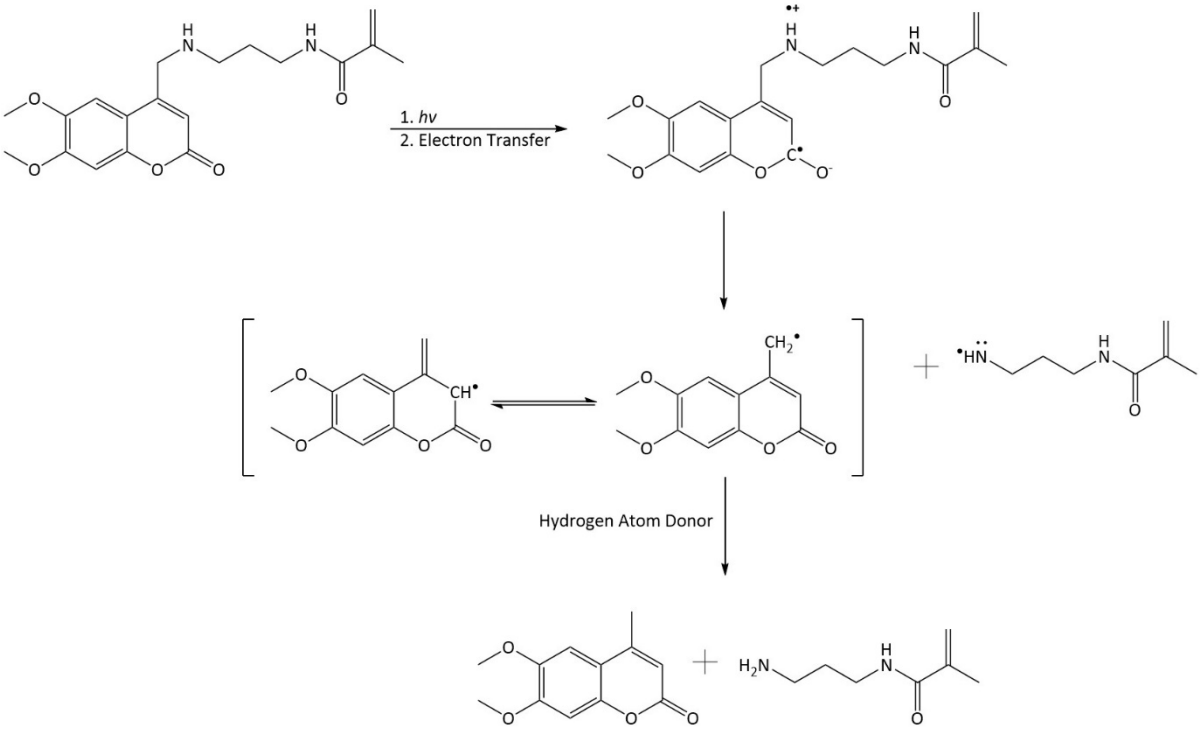

Scheme 4.1: *A reaction scheme depicting the mechanism of deprotection of compound* ***MC-1*** *and by extension, compound* ***SMC-1****. Image adapted from Klán et al.*[30]

Following the deprotection studies, a graph of absorbance at 365 nm was plotted against the time the aliquot was taken (Figure 4.12).

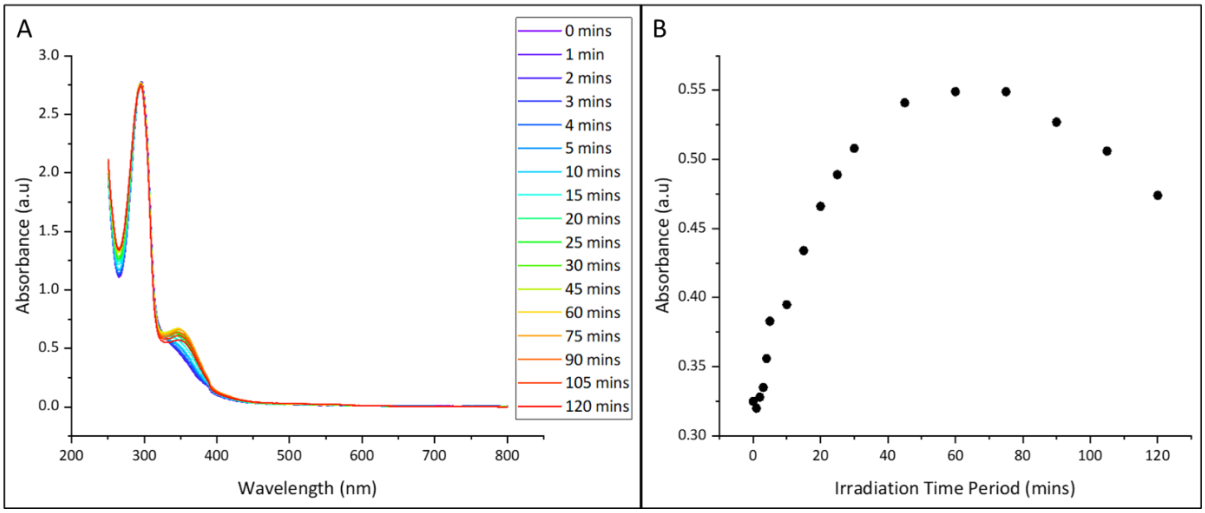

Figure 4.12: *Graphs depicting (A) the entire UV-Vis absorbance spectra of* ***MC-1*** *aliquots taken after various times of deprotection. (B) the absorbance at 365 nm of* ***MC-1*** *aliquots taken after various times of deprotection. Data is an average of 3 repeats of the study.*

Over time, absorbance of light has in fact increased, as shown more clearly by absorbance at 365 nm. Following 75 minutes of irradiation, the absorbance of the solution of light at 365 nm does begin to decrease. As can be seen in the deprotection mechanism (Scheme 4.1) a high energy radical intermediate is formed during photocleavage. It is possible that the formation of this intermediate is the cause of the increase in absorbance. It can be seen that after 2 hours, the absorbance of the compound had not yet reached a plateau. It was at this point that the study was terminated as this period of time was longer than that which was desired for PPG purposes. Due to these results, it was determined that deprotection is likely to be occurring, however DI water is not efficient at donating hydrogen atoms, which, as per Scheme 4.1, is a requirement for the reaction to proceed. The study was repeated (Figure 4.13), in place of DI water a hydrogen atom transfer (HAT) solution was used

as the deprotection solution, to provide the hydrogen atoms required for the deprotection mechanism. The HAT solution was comprised of 1-decanethiol in a minimal volume of THF, suspended in DI water.

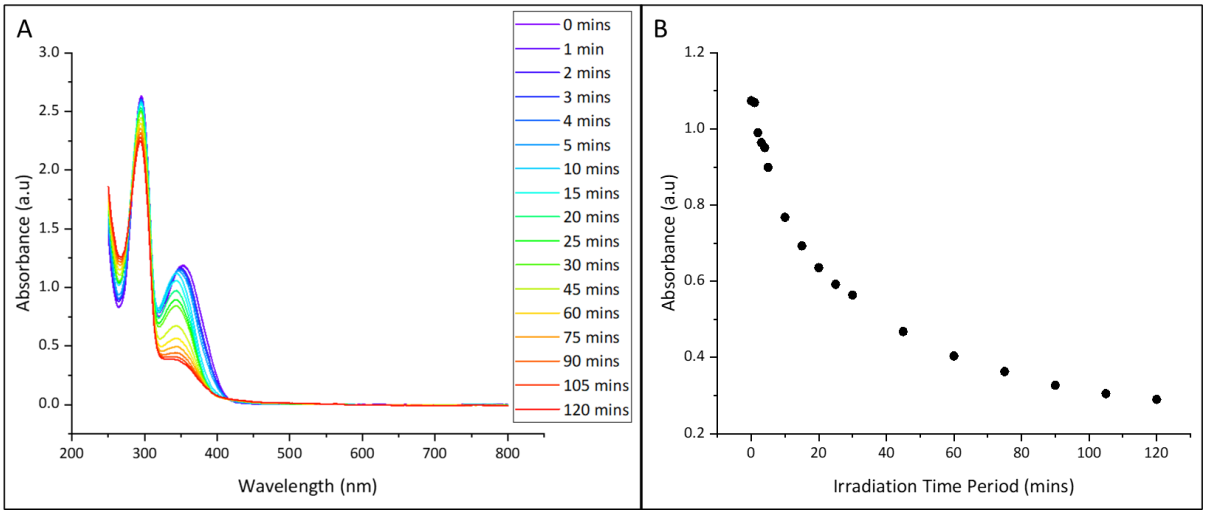

Figure 4.13: *Graphs depicting (A) the entire UV-Vis absorbance spectra of* ***MC-1*** *aliquots in a HAT solution taken after various times of deprotection. (B) the absorbance at 365 nm of* ***MC-1*** *aliquots in a HAT solution taken after various times of deprotection. Data is an average of 3 repeats of the study.*

The use of the HAT solution vastly improved the deprotection of **MC-1**. As can be observed clearly by the absorbance at 365 nm, deprotection occurs much more rapidly, so much so that it cannot be seen to enter the transition state through UV-Vis studies. Again, a plateau in absorbance was not reached by 120 minutes, however it appears that the absorbance was beginning to level off. As hydrogels are anticipated to complete deprotection faster, deprotection studies of hydrogels would be studies over the course of 90 minutes.

4.6.2.2 SMC-1

As the deprotection mechanism of **SMC-1** is identical to that of **MC-1**, deprotection studies were again conducted in a HAT solution (Figure 4.14).

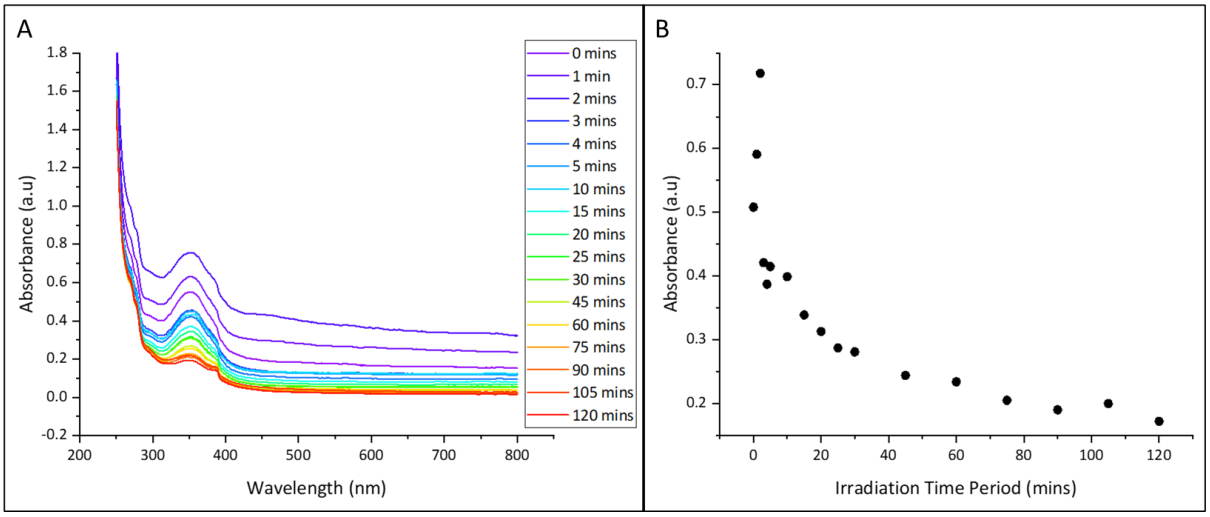

Figure 4.14: *Graphs depicting (A) the entire UV-Vis absorbance spectra of* ***SMC-1*** *aliquots in a HAT solution taken after various times of deprotection. (B) the absorbance at 365 nm of* ***SMC-1*** *aliquots in a HAT solution taken after various times of deprotection. Data is an average of 3 repeats of the study.*

Unlike compound **MC-1**, there is an increase in absorbance within the first few minutes of deprotection of **SMC-1**, this is again theoretically due to entering the high energy transition state. The decrease in absorbance is rapid until approximately 40 minutes into the study, at which it begins to slow down. The absorbance of the aliquots appears to be fairly consistent between 90 and 120 minutes with minor fluctuations. Based on this data, when conducting deprotection studies on hydrogel samples, the study would be terminated after 105 minutes.

4.6.2.3 MC-2

With the deprotection mechanism of *ortho*-nitrobenzyl PPGs in mind, compound **MC-2** was designed with a nitro group *ortho* to the leaving group. This was done in the hopes that the stabilising 5-membered ring would still form during deprotection thus improving deprotection (Scheme 4.2).

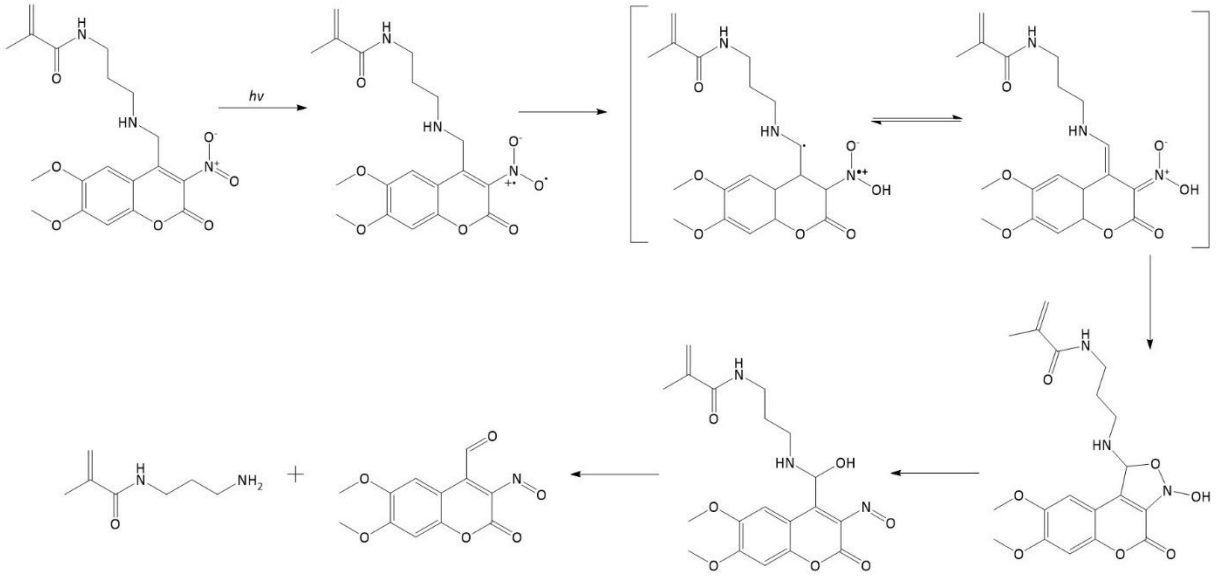

Scheme 4.2: *The theoretical deprotection mechanism of compound* ***MC-2****, and by extension* ***SMC-2****, based on the mechanism of deprotection of ortho-nitrobenzyl based PPGs. Image adapted from Pelliccioli et al.*[31]

As the theoretical deprotection product results in the formation of a free aldehyde functional group, the deprotection solution of choice for studies of **MC-2** (Figure 4.15) was a semicarbazide hydrochloride solution, as used in Chapter 3.5.1.2 alongside NVOC-Cl. The deprotection solution was created by dissolving molar equivalents of semicarbazide hydrochloride and sodium hydroxide in a 100 mM 4-(2-hydroxyethyl)-1-piperazineethanesulfonic acid (HEPES), pH 7.4 buffer solution. The purpose of the sodium hydroxide was to neutralise the hydrochloric acid salt, thus aid in maintaining a neutral pH.

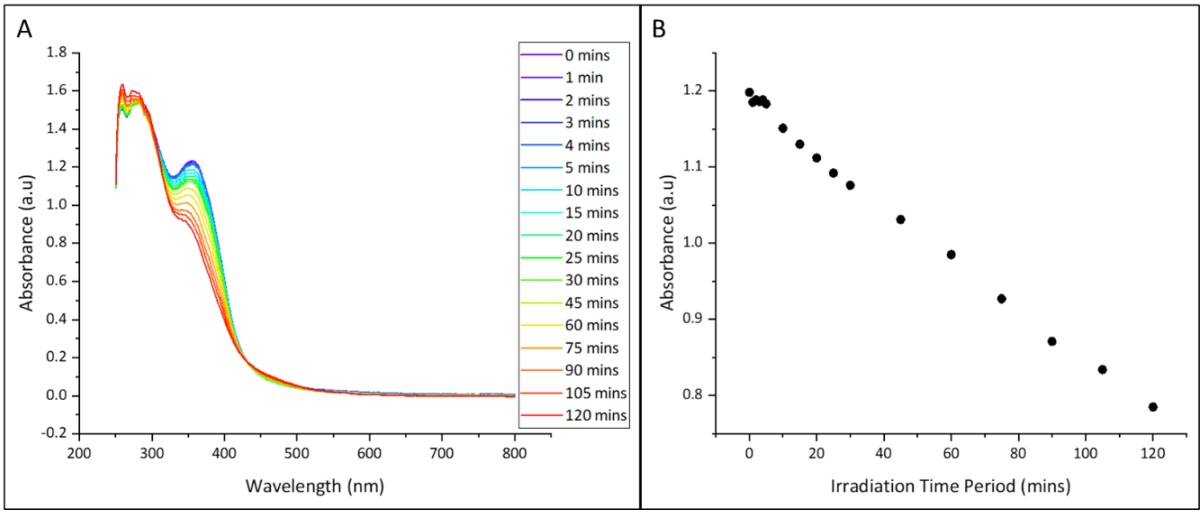

Figure 4.15: *Graphs depicting (A) the entire UV-Vis absorbance spectra of* ***MC-2*** *aliquots in a semicarbazide solution taken after various times of deprotection. (B) the absorbance at 365 nm of* ***MC-2*** *aliquots in a semicarbazide solution taken after various times of deprotection. Data is an average of 3 repeats of the study.*

The absorbance of **MC-2** at 365 nm shows a linear decrease with time, which was unexpected. Unfortunately, by 120 minutes, the absorbance had not reached a plateau. As deprotection may be slightly different in a hydrogel, and 120 minutes is the upper limit for deprotection time, hydrogel studies will be conducted, and terminated after 120 minutes.

4.6.2.4 SMC-2

As the deprotection mechanism of **SMC-2** is anticipated to be the same as that of **MC-2**, it was also studied in a semicarbazide hydrochloride solution (Figure 4.16).

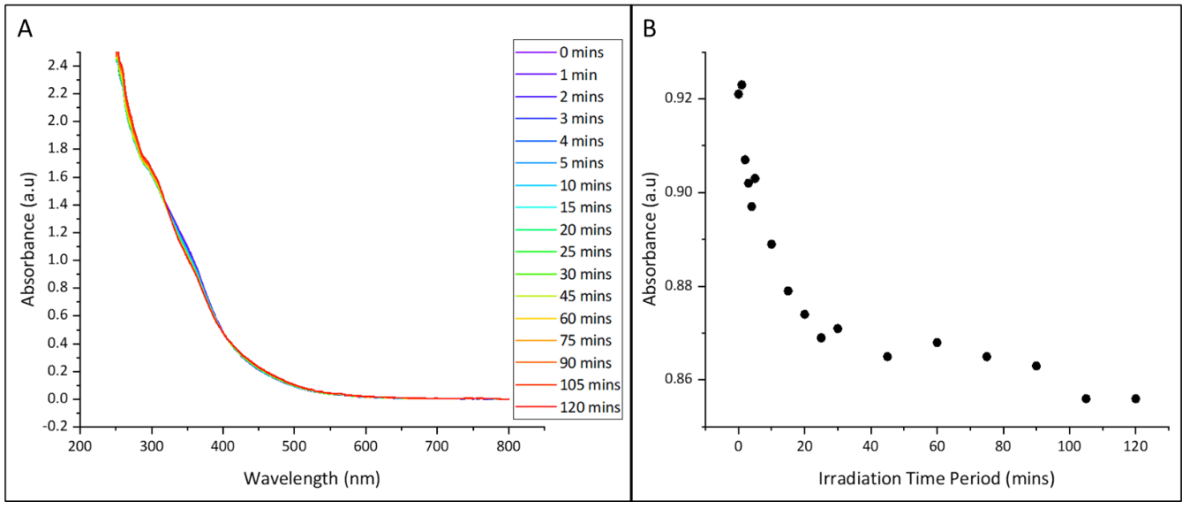

Figure 4.16: *Graphs depicting (A) the entire UV-Vis absorbance spectra of* ***SMC-2*** *aliquots in a semicarbazide solution taken after various times of deprotection. (B) the absorbance at 365 nm of* ***SMC-2*** *aliquots in a semicarbazide solution taken after various times of deprotection. Data is an average of 3 repeats of the study.*

While not as uniform as previous monomers, **SMC-2** does appear to undergo deprotection. The decrease in absorbance of light at 365 nm is great for the initial 30 minutes. From 45 minutes onwards, the decrease is not as uniform as was hoped however, as these are only preliminary studies, this is acceptable. Further research is required to investigate the deprotection more fully for more reliable data. The absorbance of 365 nm light does appear to plateau by 105 minutes; unfortunately, this cannot be said with 100% accuracy. Based on the data collected, hydrogel deprotection studies for **SMC-2** will be concluded within 105 minutes.

4.6.3 The Formation of Internally Referenced Waveguides

Studies of the PPG photolysis in hydrogels are imperative. This is due to the photocaged monomers behaving differently when polymerised. Not only that, but unlike solution studies where by-products remain contained in the solution, the deprotection

products can be washed out of the hydrogel structure. This results in a more accurate representation of bound PPG remaining in the hydrogel.

For these studies, 100 µm thick hydrogel films were formed by cleaning a glass substrate with decon 90, DI water and ethanol. The glass slide was then functionalised with chloro(dimethylvinyl)silane (CDMVS) and placed into a custom-made plastic mould. The hydrogel mixture, composed of AAm, photocaged APMA derivative, BAAm, 10% APS solution, TEMED and DI water, is combined in a pot; the exact masses and volumes for these compounds are noted in Table 4.1. This solution (200 µL) is then injected into the mould using a syringe, onto the functionalised glass slide. The centre of the mould contains a 100 µm thick plastic spacer which controls the thickness of the hydrogel formed. The solution is then left to polymerise before dismantling to obtain the hydrogel covered glass substrate.

Following the formation of 100 µm thick hydrogel films, hydrogel deprotection studies for each PPG were conducted. To do this, the 100 µm thick hydrogel films were immobilised in a glass petri dish. To this, a deprotection solution was added, the solution being specific to each monomer. The hydrogel film was then irradiated with 365 nm light, followed by a wash with water before the analysis of multiple regions of the film by UV-Vis. The hydrogel was then returned to the deprotection solution prior to irradiation for the next time period.

Regions of the hydrogel analysed by UV-Vis spectroscopy were kept consistent between irradiation periods. A graph of the average absorbance against cumulative irradiation time period was then plotted.

4.6.3.1 AAm/MC-1

The deprotection solution of choice for an AAm/**MC-1** co-polymer hydrogel was a HAT solution (Figure 4.17).

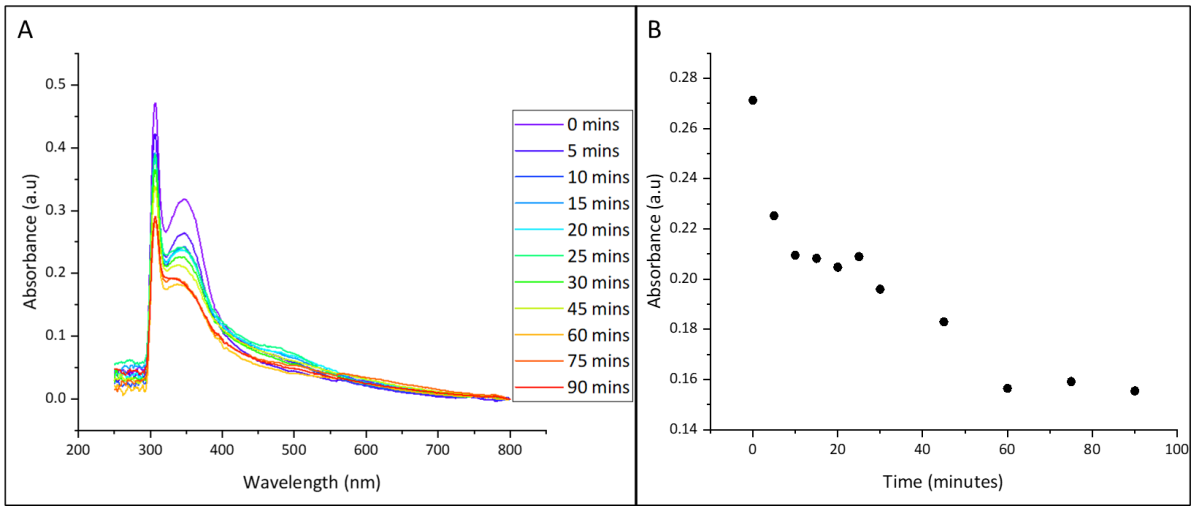

Figure 4.17: *Graphs depicting (A) the entire UV-Vis absorbance spectra of an AAm/**MC-1** hydrogel in a HAT solution taken after various times of deprotection. (B) the absorbance at 365 nm of an AAm/**MC-1** hydrogel in a HAT solution taken after various times of deprotection. Data is an average of 3 repeats of the study.*

Through observing the absorbance of the hydrogel at 365 nm, while not a perfect pattern, the general trend is a decrease in absorbance. Once 60 minutes of cumulative irradiation is reached, the absorbance appears to plateau as values fluctuate around an absorbance of 0.16 arbitrary units (a.u). It is due to this that 60 minutes is taken to be the end point of deprotection of AAm/**MC-1** co-polymer hydrogels.

4.6.3.2 AAm/SMC-1

Deprotection studies of AAm/**SMC-1** co-polymer hydrogels (Figure 4.18) were, as with AAm/**MC-1**, performed in a HAT solution to aid in deprotection.

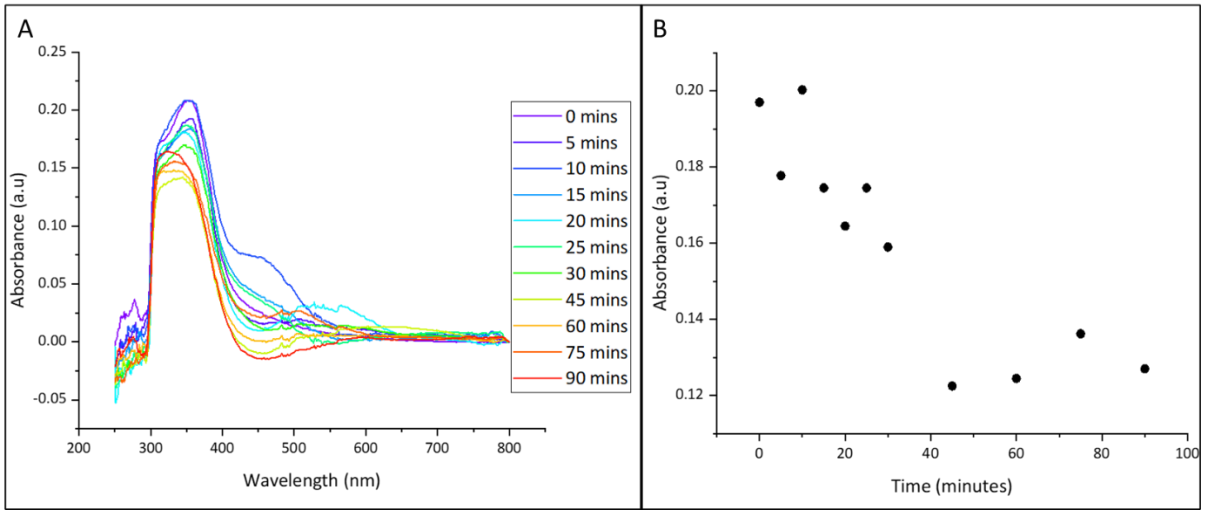

Figure 4.18: *Graphs depicting (A) the entire UV-Vis absorbance spectra of an AAm/**SMC-1** hydrogel in a HAT solution taken after various times of deprotection. (B) the absorbance at 365 nm of an AAm/**SMC-1** hydrogel in a HAT solution taken after various times of deprotection. Data is an average of 3 repeats of the study.*

While the deprotection spectra are not as uniform as would have been liked, a clear decrease in absorbance of light at 365 nm can be observed for the initial 45 minutes. Following this point, while the data is not a plateau as would have been desirable, the absorbance appears to cease decreasing. Unfortunately, values after this point vary from one another. This is likely due to large levels of diffraction caused by the hydrogel structure.

4.6.3.3 AAm/MC-2

The solution used for hydrogel deprotection studies using an AAm/**MC-2** co-polymer hydrogel (Figure 4.19) was a semicarbazide solution.

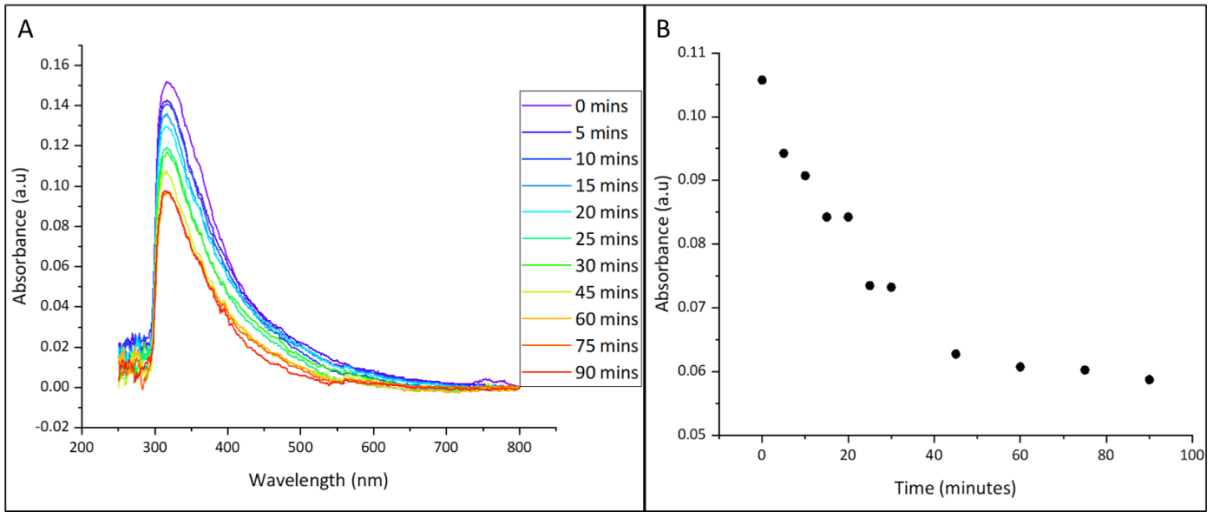

Figure 4.19: *Graphs depicting (A) the entire UV-Vis absorbance spectra of an AAm/**MC-2** hydrogel in a semicarbazide solution taken after various times of deprotection. (B) the absorbance at 365 nm of an AAm/**MC-2** hydrogel in a semicarbazide solution taken after various times of deprotection. Data is an average of 3 repeats of the study.*

While the solution deprotection studies suggested that this study would require 120 minutes to reach completion (Chapter 4.6.2.3), it was observed that by 90 minutes a plateau had been reached already. Based on the absorbance of 365 nm light, the end point of the reaction was at approximately 60 minutes.

4.6.3.4 AAm/SMC-2

When determining the end point for the deprotection of AAm/**SMC-2** co-polymer hydrogels, studies were completed in a semicarbazide hydrochloride solution (Figure 4.20).

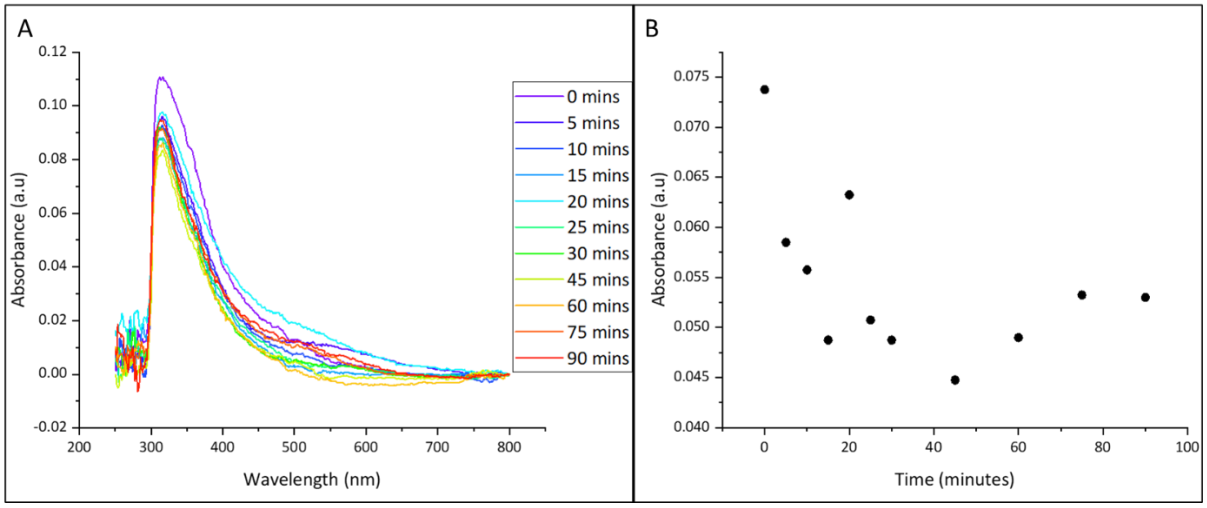

Figure 4.20: *Graphs depicting (A) the entire UV-Vis absorbance spectra of an AAm/**SMC-2** hydrogel in a semicarbazide solution taken after various times of deprotection. (B) the absorbance at 365 nm of an AAm/**SMC-2** hydrogel in a semicarbazide solution taken after various times of deprotection. Data is an average of 3 repeats of the study.*

Unfortunately, data collected in these studies does not appear to follow the expected trend. There is much variance in the plot points, likely due to imperfections in the hydrogel structure scattering light unusually. As there is a general downwards trend in absorbance of light at 365 nm until 45 minutes, this was taken to be the end point of the reaction. It is not known if this is the true end point as absorbance then increases again, however it is the lowest absorbance value and correlates with that obtained for an AAm/**MC-2** hydrogel which is a very similar structure.

4.6.4 Refractive Index Sensitivity Testing

Earlier in this thesis, in Chapter 3.5.1.1, we calculated the RIS of an AAm/APMA leaky waveguide device (Equation 4.1); meaning we tested how sensitive the resonance angle of this LW device is to changes in the refractive index (RI) of a sample. As RI index is given the

arbitrary unit of refractive index units (RIU), the RIS of these devices was determined to be 130.928 ± 2.392° RIU^{-1}.

$$\boldsymbol{RIS = \frac{\Delta\theta_R}{RI}}$$

Equation 4.1: *An equation displaying the relationship between RIS, $\Delta\vartheta_R$ and the RI of a solution.*

To test the RIS of photocaged co-monomer hydrogels, first LW devices must be formed. CDMVS functionalised glass substrates were prepared as described in Chapter 4.6.3. In this instance, as a plastic spacer could not be found of approximately 1 µm thickness, a spacer was formed from a hydrophobic glass slide functionalised with spacer beads. To create this, the glass slide was again cleaned, then functionalised with trimethoxy(trifluoropropyl)silane (TMTFS). The spacer was prepared by depositing a solution of 1.1 µm latex bead solution (1 µL) at 8 equal distances around the edge of the TMTFS functionalised glass slide. The hydrogel mixture (50 µL), as described in Table 4.1, was sandwiched between the CDMVS and TMTFS functionalised glass slides, which were compressed together using a 500 g weight. This resulted in the formation of ≈ 1.1 µm thick photocaged co-monomer hydrogel films.

Following the production of LW devices, to test for RIS a calibration curve was first made, using solutions of known RI and measuring the response. The calibration curve consisted of glycerol solutions equal to 0.125%, 0.25%, 0.5%, 1% and 2% (v/v) in a 100 mM HEPES, pH 7.4 buffer solution. Glycerol was the compound of choice as it is of a similar structure to the PEG chains that were used later, it is inert to the hydrogel film, and it is a small compound that should be able to penetrate the hydrogel film completely. Prior to for RIS

testing, the RI of these solutions was measured in triplicate. A baseline signal was created with buffer solution, following that, each solution was then added to the leaky waveguide device sequentially, then finally washed out back to the baseline with HEPES buffer solution.

Through creating a graph of the average $\Delta\theta_R$ caused by each RI, we obtained the calibration curve (Figure 4.21). Based on Equation 4.1, we see that the gradient of this graph is equal to the RIS, thus making the calculation of this characteristic straightforward. This was conducted for all 4 of the AAm/photocaged co-monomer hydrogels prior to deprotection.

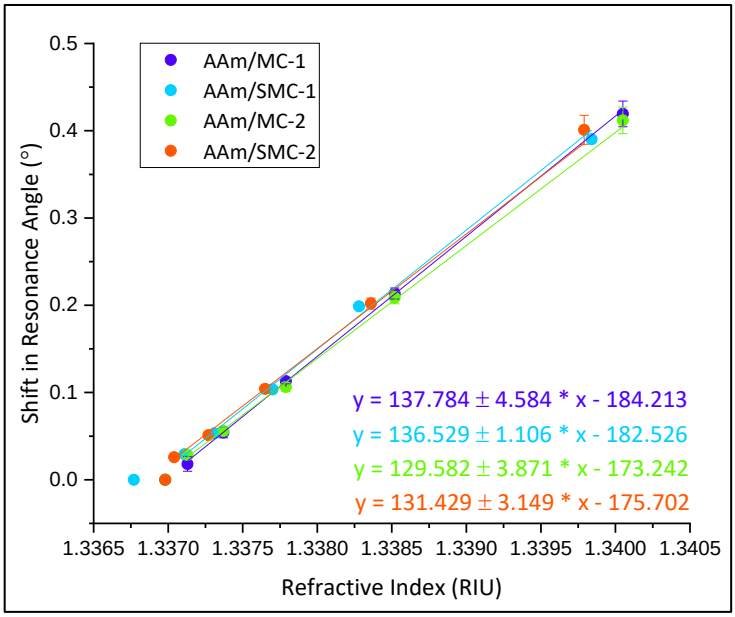

Figure 4.21: *A graph depicting the calibration curves of LW devices formed using photocaged AAm/**MC-1** (purple), AAm/**SMC-1** (turquoise), AAm/**MC-2** (green) and AAm/**SMC-2** (orange) co-monomer hydrogels. Data is an average of 3 repeats of each study.*

The graph above displays the RIS of AAm/photocaged co-monomer LW devices. These are all prior to deprotection. LW devices formed using the monomers maintained RIS values similar to that of AAm/APMA, listed in Table 4.2 for ease of comparison. Prior to deprotection, AAm/**MC-2** and AAm/**SMC-2** LW devices were very similar to AAm/APMA LW devices in terms of RIS and error between devices. LW devices made using the hydrogel AAm/**MC-1** had an

increased RIS in comparison to AAm/APMA, however, the higher error associated with different devices suggests that results are less consistent across different LW devices made of the same gel. On the other hand, whilst LW devices formed using AAm/**SMC-1** hydrogels also displayed an increased RIS when compared to that of AAm/APMA, the error associated with different devices was lower.

For the formation of internally referenced LW devices using these AAm/photocaged co-monomer hydrogels, the RIS of the photodeprotected hydrogel is also important to note. To create photodeprotected LW devices, thin films were formed as described for the photocaged hydrogel tests. Following this, the LW devices were submerged in either a HAT solution or a semicarbazide solution depending on the nature of the photocaged monomer. While immersed in solution, the hydrogel films were exposed to 365 nm for the time period determined in Chapter 4.6.3. Following this period, the LW devices were washed with water, before finally being tested for RIS (Figure 4.22).

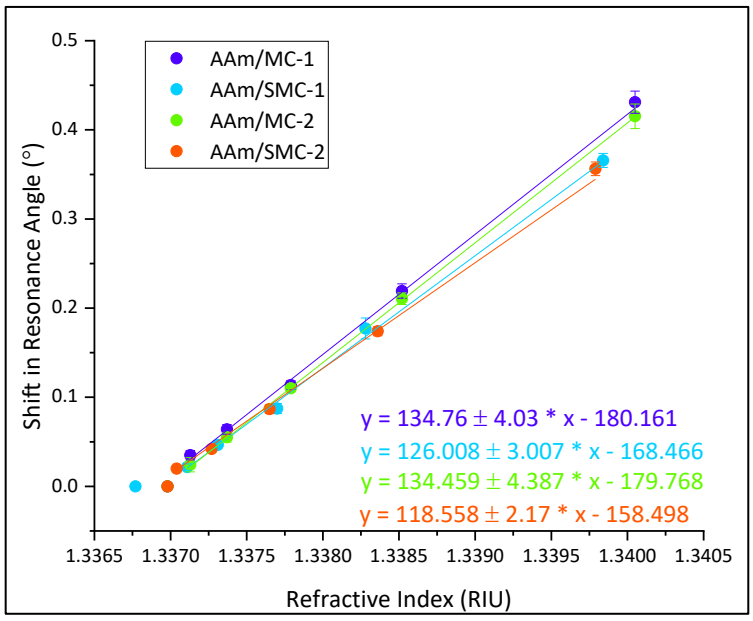

Figure 4.22: *A graph depicting the calibration curves of LW devices formed using photodeprotected AAm/**MC-1** (purple), AAm/**SMC-1** (turquoise), AAm/**MC-2** (green) and AAm/**SMC-2** (orange) co-monomer hydrogels. Data is an average of 3 repeats of each study.*

The graph above displays the RIS of AAm/photocaged co-monomer LW devices following photodeprotection. To allow for the simple comparison of RIS pre- and post-photodeprotection, all values are listed below in Table 4.2.

Table 4.2: *A table listing the RIS values and errors for AAm/photocaged co-monomer LW devices before and after photodeprotection compared to that of AAm/APMA LW devices. Data is an average of 3 repeats of each study.*

Gel Type	RIS Before Irradiation (° RIU^{-1})	Standard Deviation	RIS After Irradiation (° RIU^{-1})	Standard Deviation
AAm/APMA	130.928	± 2.392	130.928	± 2.392
AAm/**MC-1**	137.784	± 4.584	134.760	± 4.030
AAm/**SMC-1**	136.529	± 1.106	126.008	± 3.007
AAm/**MC-2**	129.582	± 3.871	134.459	± 4.387
AAm/**SMC-2**	131.429	± 3.149	118.558	± 2.170

Through Table 4.2 the effect photodeprotection has on RIS is clear to see. With the exception of AAm/**MC-2**, photodeprotection results in a small decrease in RIS of the LW devices. Also, for LW devices formed using AAm/**SMC-1** and AAm/**MC-2**, photodeprotection results in larger variation between devices, as observed by the increased standard deviation values.

Ultimately, the RIS of all devices, prior to or following photodeprotection, are similar to that of AAm/APMA hydrogels, with the exception of AAm/**SMC-2** which is slightly lower than expected. This data suggests that there will be minimal difference in RIS across the sensing and referencing regions of internally referenced LW devices, thus similar signals are expected for non-specific signals.

4.6.5 Leaky Waveguide Porosity Testing

Biomolecules such as proteins are often large compounds, as such, to be able to detect these elements within the structure of the hydrogel-based LW device, the hydrogel must be porous. As was discussed earlier (Chapter 2.5.5) traditional methods of establishing pore size are not suitable for these materials, therefore, in order to test for porosity, we use the RIS value determined previously (Chapter 4.6.4). Through the rearranging of the line of best fit obtained from RIS testing graphs, we can calculate the $\Delta\theta_R$ expected if the LW device were to be 100% porous to the molecules being tested, in this instance polyethylene glycol (PEG) chains. To do this the RI of the PEG solution is multiplied by the RIS of the LW device, followed by the addition of the intercept value (Equation 4.2).

$$\boldsymbol{\Delta\theta_{R\,(theoretical)} = (RIS \times RI) + c}$$

Equation 4.2: *An equation displaying how we can rearrange the straight line equation given from RIS testing graphs to achieve the calculation of a theoretical $\Delta\vartheta_R$ ($\Delta\vartheta_{R(theoretical)}$) caused by 100% permeation of a solution of (RI) into a LW device of (RIS) where © is equal to the intercept on the RIS graph.*

To test porosity, 1% (w/v) solutions of PEG chains, of molecular weights equal to 10 kDa, 100 kDa and 300 kDa were used. Multiple chain sizes were used to establish how the porosity of the film changes with compound size. As the average mass of proteins within the human body weight approximately 46 kDa, this range should be applicable for most relevant human analytes.[32] Below we see the trace given to us from the input of these solutions and their subsequent washing out of the AAm/photocaged co-monomer LW device (Figure 4.23).

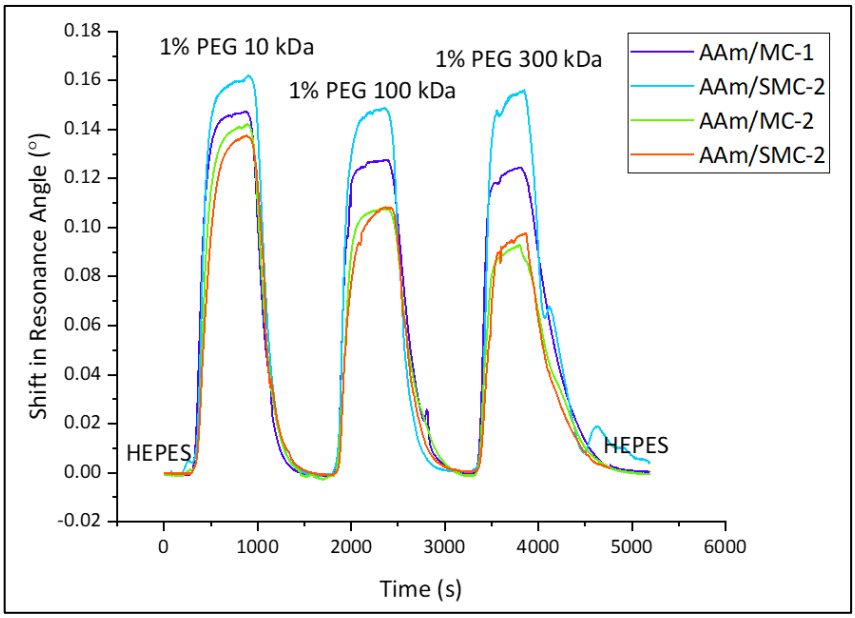

Figure 4.23: *A graph depicting the PEG porosity traces of LW devices formed using photocaged AAm/**MC-1** (purple), AAm/**SMC-1** (turquoise), AAm/**MC-2** (green) and AAm/**SMC-2** (orange) co-monomer hydrogels. Data is an average of 3 repeats of each study.*

Through comparing the average $\Delta\theta_R$ at the height of each signal, to the expected values that were calculated using Equation 4.2, the porosity of the LW device with regards to different sized compounds can be calculated as a percentage. These values for the LW device prior to photodeprotection have been listen in Table 4.3. Through looking at the table below, we can determine that the AAm/**SMC-1** LW device is the most porous to large molecular weight compounds, whereas AAm/**SMC-2** has the lowest porosity before photodeprotection. AAm/**MC-1** appears to be reasonably consistent in porosity across compounds of all sizes. In Chapter 3.5.1.1, we determined the porosity of a plain AAm/APMA LW device (Table 3.1), AAm/**MC-2** appears to be the most similar in terms of porosity to the non-photocaged LW device.

Table 4.3: *A table listing the refractive index of 1% PEG solutions used for porosity studies, the theoretical $\Delta\vartheta_R$, the obtained $\Delta\vartheta_R$, and the porosity of the film as a percentage of these values where the theoretical signal indicates 100% porous when tested on all 4 of the developed AAm/photocaged co-monomer LW devices. Data is an average of 3 repeats of each study.*

LW Device	Solution	Refractive Index (RIU)	Theoretical $\Delta\theta_R$ (°)	Actual $\Delta\theta_R$ (°)	Porosity (%)
AAm/**MC-1**	1% PEG 10 kDa	1.33825	0.17644	0.10599	60.07
	1% PEG 100 kDa	1.33822	0.17230	0.12671	73.54
	1% PEG 300 kDa	1.33827	0.17919	0.12269	68.47
AAm/**SMC-1**	1% PEG 10 kDa	1.33815	0.17028	0.15997	93.95
	1% PEG 100 kDa	1.33820	0.17711	0.14715	83.08
	1% PEG 300 kDa	1.33822	0.17984	0.15268	84.90
AAm/**MC-2**	1% PEG 10 kDa	1.33825	0.17111	0.14016	81.91
	1% PEG 100 kDa	1.33822	0.16722	0.10689	63.92
	1% PEG 300 kDa	1.33827	0.17370	0.09026	51.96
AAm/**SMC-2**	1% PEG 10 kDa	1.33825	0.18286	0.13563	74.17
	1% PEG 100 kDa	1.33822	0.17892	0.10622	59.37
	1% PEG 300 kDa	1.33827	0.18549	0.09497	51.20

Subsequently, the porosity of the films post-photodeprotection also had to be determined. LW devices were photodeprotected prior to repeating the porosity test as described in Chapter 4.6.4. The purpose of this was to test what effect, if any, the PPGs had on the porosity of LW devices. Below we see the trace given to us from the PEG porosity testing of photodeprotected AAm/photocaged co-monomer LW devices (Figure 4.24).

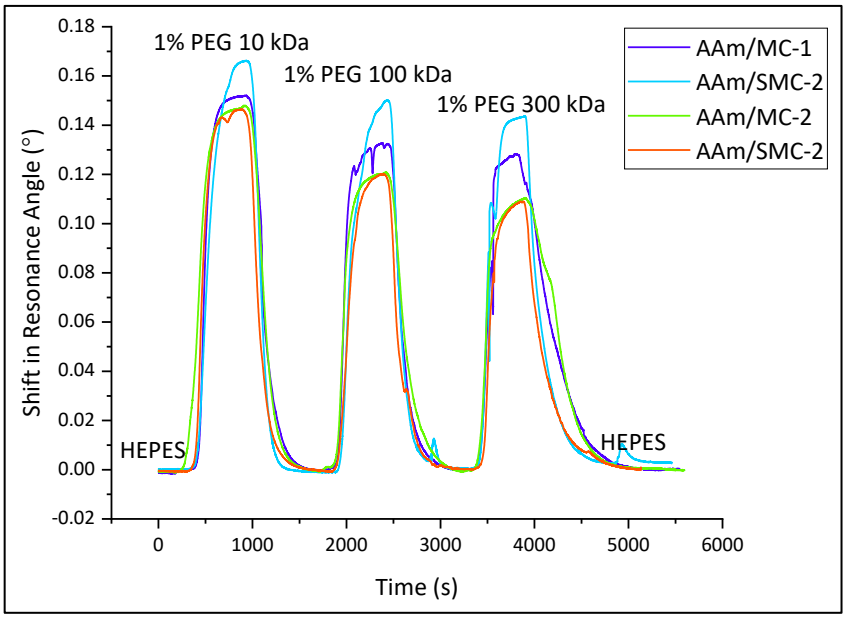

Figure 4.24: *A graph depicting the PEG porosity traces of LW devices formed using photodeprotected AAm/**MC-1** (purple), AAm/**SMC-1** (turquoise), AAm/**MC-2** (green) and AAm/**SMC-2** (orange) co-monomer hydrogels. Data is an average of 3 repeats of each study.*

As with the results prior to photodeprotection, values for $\Delta\theta_{R(Theoretical)}$ and $\Delta\theta_R$ are discussed below in Table 4.4 for the AAm/photocaged co-monomer hydrogels following photodeprotection; this allowed for the porosity of the LW device with regards to different sized compounds to be calculated as a percentage. The $\Delta\theta_R$ obtained for the porosity of AAm/**SMC-1** to a solution of 1% PEG 10 kDa exceeded expectations, resulting in an impossible percentage of over 100%. As discussed in Chapter 4.6.4, the RIS of this hydrogel decreased greatly following photodeprotection, this new data suggests that may not be the case, and further studies are required to ensure that the RIS calculated is accurate. It appears that the RIS determined for this hydrogel may be lower than it should be.

Table 4.4: *A table listing the refractive index of 1% PEG solutions used for porosity studies, the theoretical $\Delta\vartheta_R$, the obtained $\Delta\vartheta_R$, and the porosity of the film as a percentage of these values where the theoretical signal indicates 100% porous when tested on all 4 of the developed AAm/photocaged co-monomer LW devices following photodeprotection. Data is an average of 3 repeats of each study.*

LW Device	Solution	Refractive Index (RIU)	Theoretical $\Delta\theta_R$ (°)	Actual $\Delta\theta_R$ (°)	Porosity (%)
AAm/**MC-1**	1% PEG 10 kDa	1.33825	0.18157	0.15130	83.33
	1% PEG 100 kDa	1.33822	0.17753	0.12994	73.19
	1% PEG 300 kDa	1.33827	0.18427	0.12640	68.60
AAm/**SMC-1**	1% PEG 10 kDa	1.33815	0.15161	0.16526	109.01
	1% PEG 100 kDa	1.33820	0.15791	0.14774	93.57
	1% PEG 300 kDa	1.33822	0.16043	0.14171	88.33
AAm/**MC-2**	1% PEG 10 kDa	1.33825	0.17176	0.14644	85.26
	1% PEG 100 kDa	1.33822	0.16772	0.11871	70.78
	1% PEG 300 kDa	1.33827	0.17445	0.10848	62.18
AAm/**SMC-2**	1% PEG 10 kDa	1.33825	0.16224	0.14475	89.22
	1% PEG 100 kDa	1.33822	0.15869	0.11870	74.80
	1% PEG 300 kDa	1.33827	0.16462	0.10671	64.82

Through comparing the percentages calculated in Table 4.3 to those presented in Table 4.4, we can see that the LW devices are more porous to molecules of all sizes following deprotection. This suggests that the PPGs are blocking the pores slightly, meaning that large proteins may not enter the referencing regions of internally referenced LW devices as efficiently as the sensing regions.

4.6.6 The Development of Internally Referenced Biosensors

Throughout this work it has been determined that the RIS of AAm/photocaged co-monomer based LW devices are equal to or higher than the previously used chitosan-based LW devices, which had a RIS of 124.515 ± 11.911° RIU^{-1}. Not only this, but these devices are porous to large molecular weight compounds. Based on this data, the AAm/photocaged co-monomer LW devices began development into internally referenced biosensors.

To create internally referenced biosensors using AAm/photocaged co-monomer based LW devices, the first step is to photodeprotect a pattern of sensing and referencing regions. To do this, a 1 µm thick film was formed as described in Chapter 4.6.4, immobilised in a glass petri dish and immersed in the corresponding deprotection solution. The LW device was then irradiated over a photomask (Figure 4.25) for a predetermined period of time ranging from 45 minutes to 1 hour. The photomask allowed light to penetrate and selectively deprotect half of the film whilst leaving half untouched.

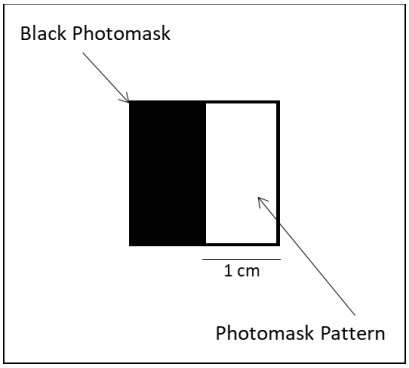

Figure 4.25: *An image depicting the photomask used for the formation of internally referenced biosensors, the black half blocks light, preventing photodeprotection, whilst light penetrates through the clear (white) half, selectively deprotecting half of the LW device.*

Initially, the circular flow cell used in Chapter 2.5 was used, however due to issues with the flow cell channel not filling completely, a new single-channel Y shaped flow cell was

developed and used. Unfortunately, due to the thin flow cell channel, it was difficult to ensure that both the photocaged and photodeprotected regions of the LW device were covered. It is due to this that these preliminary studies eventually settled on the use of a two-channel flow cell. The flow cell was orientated to allow for one channel to cover the sensing region whilst the other covered the referencing region. Solutions were added to the LW device through the flow cell channels for the immobilisation of proteins into the structure of the LW device (Scheme 4.3).

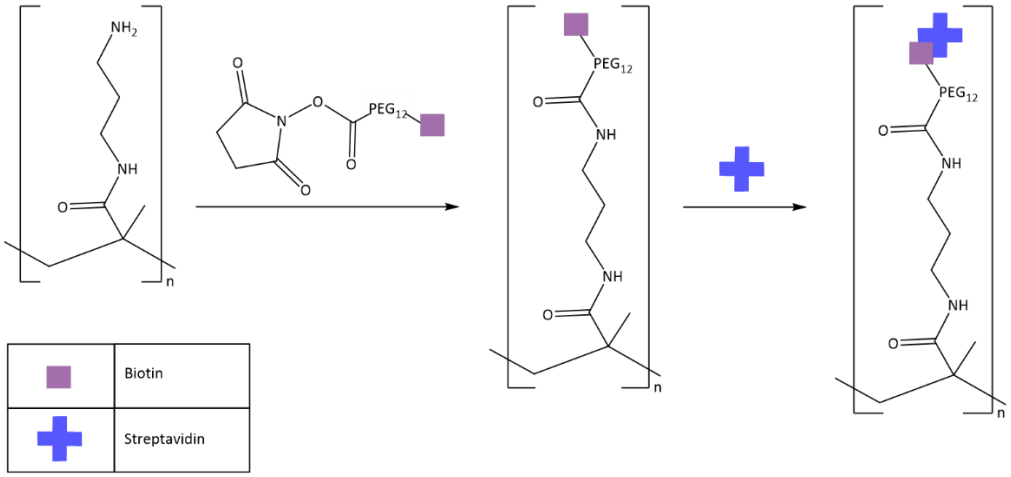

Scheme 4.3: *A reaction scheme displaying the immobilisation chemistry used to functionalise the LW devices with streptavidin.*

The initial step in the formation of an internally referenced LW device is based on *N*-hydroxysuccinimide (*NHS*) ester chemistry; this ester is highly reactive with primary amines, in the presence of which a substitution reaction occurs, releasing the *NHS* moiety.[33] This highly reactive chemical group was exploited to functionalise the LW device with a biotin terminal. Through the addition of *NHS*-PEG_{12}-biotin dissolved in 100 mM HEPES, pH 7.4 buffer solution to the flow cell channels, only the regions of the LW device containing free primary amines were labelled with biotin functional groups. Due to the strong binding affinity between

streptavidin and biotin, this provided an ideal surface for the immobilisation of streptavidin.[34] Previous work included the immobilisation of streptavidin into a LW device through the use of glutaraldehyde (Chapter 2.5.6); a new linking agent was used in this instance as the *NHS* ester is more specific with reactivity, more selective to the primary amine that would only be present in photodeprotected regions of the film.

Once the LW device was functionalised with streptavidin the study was completed, as the purpose here was simply to determine if proteins can be immobilised with high levels of spatial control within a LW device. Due to the 4 possible binding sites for biotin within a single streptavidin molecule, a streptavidin functionalised LW device opens up the possibility of immobilising a biorecognition element through the use of a biotinylated antibody, as described in Chapter 2.5.6.[35]

The binding events were measured in real time, with each step separated by buffer washes; the purpose of the buffer washes was to remove unbound analytes from the gel matrix. Through taking measurements following washing with buffer, a more accurate representation of covalently immobilised compounds is achieved as the RI of the sample is returned to the zero conditions, thus any changes must be caused by the permanent change of RI in the LW devices. Then, to determine if the proposed sensing and referencing regions had a difference in terms of permanent change, which would indicate selective binding, a differential result was calculated. The signals obtained in the referencing region were subtracted from those produced in the sensing region, the resulting differential signal theoretically being indicative of selective analyte immobilisation.

4.6.6.1 AAm/MC-1

Following the exposure of half of an AAm/**MC-1** based LW device to 365 nm light in a HAT solution for 60 minutes, the above immobilisation chemistry was performed. Below the data collected, in degrees, is plotted, alongside the differential results (Figure 4.26)

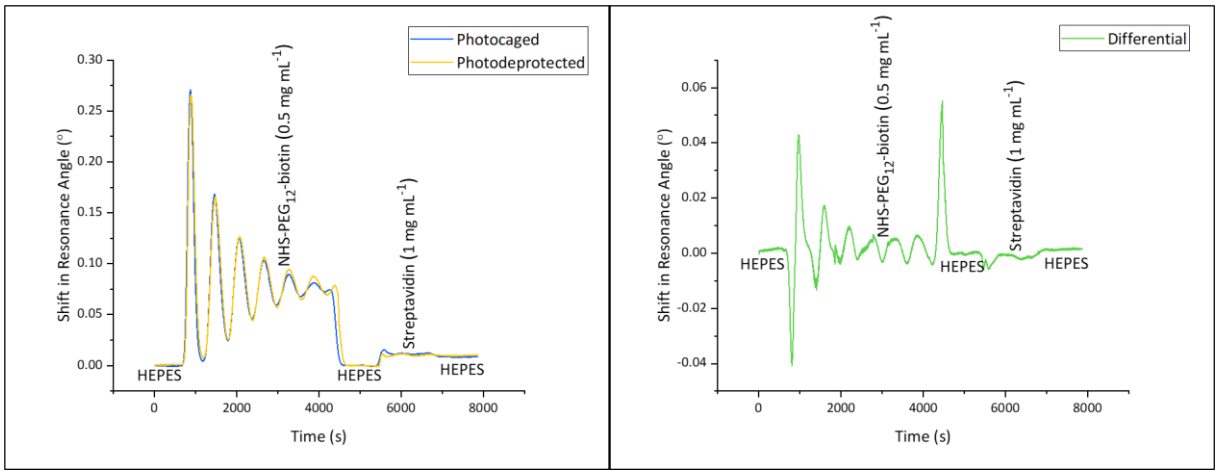

Figure 4.26: *Graphs displaying the data collected when testing for the formation of internally referenced LW devices using an AAm/**MC-1** co-monomer hydrogel (left), and the differential of this data to determine if the internal reference was effective (right). Data is an average of 2 repeats of the study.*

Based on the differential data collected, a recirculating solution of *NHS*-PEG$_{12}$-biotin had minimal effect on the resonance angle, resulting in a $\Delta\theta_R$ equal to 0.0000223°, a negligible value. This was not promising when determining if photodeprotection was successful. Following this, streptavidin caused a $\Delta\theta_R$ that was 0.0014° larger in the sensing region than that of the referencing region. While this may appear to be significant, due to the differences in RIS, it cannot be stated with absolute certainty; therefore, by rearranging Equation 4.1, we can determine the overall change in RI of the hydrogel (Table 4.5). This will give mathematical proof of a difference between the sensing and referencing regions.

Table 4.5: *A table displaying the RIS and $\Delta\vartheta_R$ of the referencing and sensing regions of an AAm/**MC-1** based internally referenced LW device, displaying the final RI of the hydrogel which has been calculated. Data is an average of 2 repeats of the study.*

Region	RIS ($^\circ$ RIU^{-1})	Streptavidin $\Delta\theta_R$ ($^\circ$)	Δ RI from Baseline (RIU)
Referencing	137.784	0.00847	+ 0.00006
Sensing	134.760	0.00987	+ 0.00007

The RI of the hydrogel had increased by an extra 0.00001 RIU in the sensing region when compared to the referencing region. While this may appear to be a small value, changes in RI are often small values, the difference between air and glass being only 0.5 RIU.[36,37] Therefore, this change is indicative of low level binding within the sensing region which did not occur in the referencing region.

4.6.6.2 AAm/SMC-1

Following the half film deprotection of an AAm/**SMC-1** based LW device by light of 365 nm in a HAT solution for 45 minutes the immobilisation of streptavidin was conducted. Below the data collected, in degrees, is plotted, alongside the differential results (Figure 4.27).

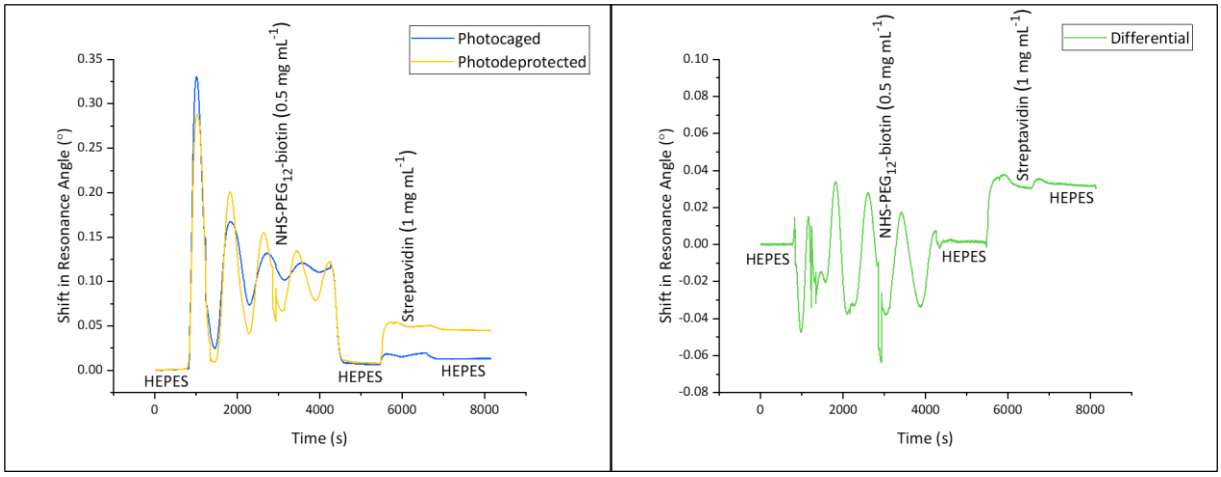

Figure 4.27: *Graphs displaying the data collected when testing for the formation of internally referenced LW devices using an AAm/**SMC-1** co-monomer hydrogel (left), and the differential of this data to determine if the internal reference was effective (right). Data is an average of 2 repeats of the study.*

In this instance, *NHS*-PEG$_{12}$-biotin caused a $\Delta\theta_R$ equal to 0.001539°, this signal suggests that deprotection was effective in releasing free primary amines. The immobilisation of streptavidin resulted in a signal that was 0.03234° larger in the sensing region than in the referencing region. This is a large difference in signal which is indicative of a well-formed internally referenced biosensor; however, to ensure the difference is not caused by differences in RIS between the two regions, the final change in RI of the hydrogel was calculated (Table 4.6).

Table 4.6: *A table displaying the RIS and $\Delta\vartheta_R$ of the referencing and sensing regions of an AAm/**SMC-1** based internally referenced LW device, displaying the final RI of the hydrogel which has been calculated. Data is an average of 2 repeats of the study.*

Region	RIS (° RIU^{-1})	Streptavidin $\Delta\theta_R$ (°)	Δ RI from Baseline (RIU)
Referencing	136.592	0.0131	+ 0.00010
Sensing	126.008	0.0454	+ 0.00036

The sensing region of the AAm/**SMC-1** internally referenced LW device had a change in refractive index which was 0.00026 RIU greater than that of the referencing region. This is indicative of selective PPG photodeprotection and streptavidin immobilisation within the referencing regions, thus making this monomer effective for the formation of internally referenced LW devices.

4.6.6.3 AAm/MC-2

The functionalisation of an AAm/**MC-2** based LW device with streptavidin was performed following the photopatterning. To photopattern the hydrogel the film was immersed in a semicarbazide solution while half of the film was exposed to light of 365 nm for 60 minutes. Below the data collected, in degrees, is plotted, alongside the differential results (Figure 4.28).

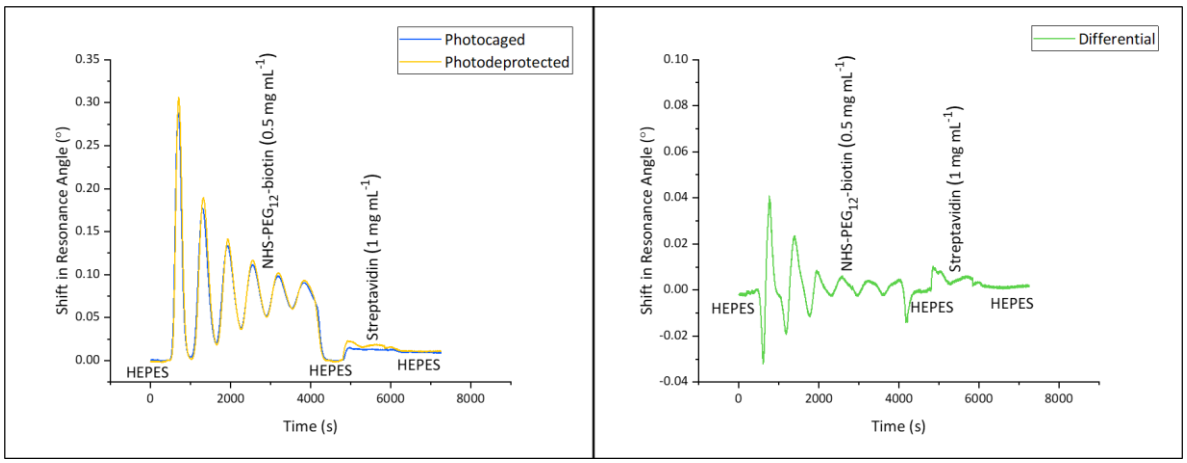

Figure 4.28: *Graphs displaying the data collected when testing for the formation of internally referenced LW devices using an AAm/**MC-2** co-monomer hydrogel (left), and the differential of this data to determine if the internal reference was effective (right). Data is an average of 2 repeats of the study.*

As with the AAm/**MC-1** LW device, minimal difference in response for *NHS*-PEG_{12}-biotin was observed for AAm/**MC-2**, with a difference of -0.00043° between the two regions. The response observed for streptavidin was also lower than expected with a difference of 0.001152°. It is hoped that due to differences in RIS between the two regions, this correlates to a significant change in RIU of the hydrogel. To determine if this is the case, the values were calculated and plotted below in Table 4.7.

Table 4.7: *A table displaying the RIS and $\Delta\vartheta_R$ of the referencing and sensing regions of an AAm/**MC-2** based internally referenced LW device, displaying the final RI of the hydrogel which has been calculated. Data is an average of 2 repeats of the study.*

Region	RIS ($° RIU^{-1}$)	Streptavidin $\Delta\theta_R$ (°)	Δ RI from Baseline (RIU)
Referencing	129.582	0.00981	0.000076
Sensing	134.459	0.01100	0.000082

Despite the absolute values of $\Delta\theta_R$ between sensing and referencing regions in LW devices formed from AAm/**MC-1** co-monomer hydrogels being similar to those of AAm/**MC-2**, the latter forms the more efficient internally referenced waveguides. The refractive index of the AAm/**MC-2** LW device in the sensing regions increased by 0.00006 RIU in comparison to the referencing region; this is larger than the 0.00001 RIU observed in hydrogels formed using the monomer **MC-1**.

4.6.6.4 AAm/SMC-2

An AAm/**SMC-2** based LW device was exposed to 365 nm light over a photomask to allow irradiation of half of the film in a semicarbazide solution for 45 minutes to promote

photodeprotection. Following this, streptavidin was immobilised into the structure of the hydrogel film. Below the data collected, in degrees, is plotted, alongside the differential results (Figure 4.29).

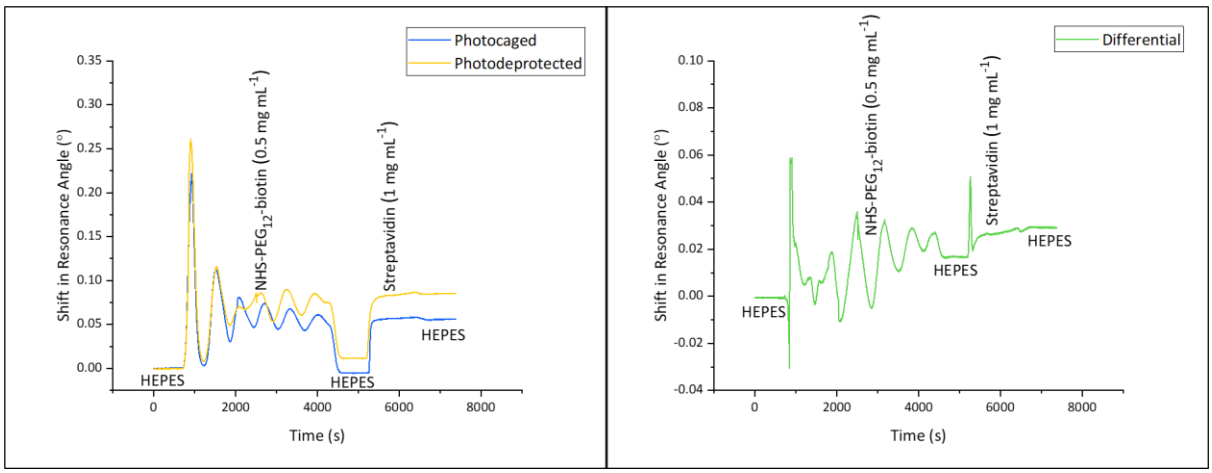

Figure 4.29: *Graphs displaying the data collected when testing for the formation of internally referenced LW devices using an AAm/**SMC-2** co-monomer hydrogel (left), and the differential of this data to determine if the internal reference was effective (right). Data is an average of 2 repeats of the study.*

Due to the unreliable nature of the deprotection data collected using thick AAm/**SMC-2** co-monomer hydrogels, it was uncertain if 45 minutes would be a long enough deprotection time period. It was determined that photodeprotection was effective, as *NHS*-PEG_{12}-biotin caused a $\Delta\theta_R$ that was 0.016762° larger in the sensing region than the referencing region. Following this, the signal with regards to the immobilisation of streptavidin was 0.029218° greater in the sensing region. These values indicate the formation of an effective internally referenced biosensor. For verification, to ensure the different RIS values of the two regions was not a factor in this, the final change in RI of the hydrogel regions was calculated. The values are listed below in Table 4.8.

Table 4.8: *A table displaying the RIS and $\Delta\vartheta_R$ of the referencing and sensing regions of an AAm/**SMC-1** based internally referenced LW device, displaying the final RI of the hydrogel which has been calculated. Data is an average of 2 repeats of the study.*

Region	RIS ($^\circ$ RIU^{-1})	Streptavidin $\Delta\theta_R$ ($^\circ$)	Δ RI from Baseline (RIU)
Referencing	131.429	0.0559	+ 0.00043
Sensing	118.558	0.0851	+ 0.00072

The difference between RIS of the sensing and referencing regions within an AAm/**SMC-2** internally referenced LW device was of some concern; this disparity could cause results to appear more significant than they are. That was not the case. Following the immobilisation of streptavidin, the RI of the sensing region had increased by 0.00029 RIU in comparison to that of the referencing region. This is the largest increase throughout all 4 of the LW devices formed. This would indicate that AAm/**SMC-2** hydrogels were the most effective for forming internally referenced LW devices in this work.

4.7 Conclusion

Throughout this work, photocaged monomers previously synthesised have been tested for their ability to polymerise into hydrogels. The photocaged monomers which were able to form hydrogels were tested for their ability to photodeprotect; conditions for photodeprotection were optimised. This culminated in studies into the time taken for photodeprotection to occur when using a 365 nm light source.

It was determined that LW devices are able to form using the photocaged monomers **MC-1**, **SMC-1**, **MC-2** and **SMC-2** as co-monomers with AAm and with a BAAm cross-linking agent. Studies have shown that the LW devices formed of these AAm/photocaged co-monomer hydrogels are highly porous to large molecular weight compounds and have a RIS comparable to LW devices used in literature.

Of the four hydrogels formed, differences were observed between the sensing and referencing regions for all LW devices; this means that all of the hydrogels were suitable for the formation of internally referenced biosensors.

Internally referenced LW devices formed using an AAm/**MC-1** co-monomer hydrogel were the least efficient at internal referencing. These devices had the smallest difference in change in RI between the sensing and referencing regions. Following this, LW devices formed of the AAm/**MC-2** co-monomer hydrogel were the next least effective.

LW devices formed using AAm/**SMC-1** and AAm/**SMC-2** hydrogels were the most efficient at forming internally referenced biosensors. These two LW devices had the greatest change in RI in the sensing region in comparison to the referencing region.

This work has determined that four of the monomers developed in Chapter 3.5.2 are suitable for the formation of internally referenced LW biosensors. Differences in signals

between the sensing and referencing regions across LW devices formed with all four monomers indicate the selective immobilisation of compounds within the sensing regions, while non-specific binding events occur across the entirety of the hydrogel structure. The differential of these two signals provides an accurate representation of the desired immobilisation.

4.8 Future Work

Following the development of these photocaged hydrogels, and their development as LW biosensors, the next step will be to further improve their sensing abilities. Possible methods to achieve this are the use of more water-soluble HAT molecules, which are difficult to find; the use of lower wavelengths of light for deprotections; the formation of more highly water-soluble compounds; or the formation of higher wavelength absorbing compounds as was discussed in Chapter 3.5.2.11. Following this, to continue to functionalisation of the LW devices with biorecognition elements would be the final step to the formation of internally referenced LWs. Following this, the longevity of the LW devices would need to be studied, along with the optimal storage conditions, to allow for production prior to use for POC testing.

Once optimised on the bulky, traditional benchtop laboratory-based instrument, the logical first step to take is to develop these further to be fit for POC testing; to do this, testing on the portable 3D printed instrument described in Chapter 2.5.3 would be conducted. Another plan for this work, would be to form a hydrogel using two of the monomers which absorb at different wavelengths, or deprotect under different solvent conditions, such as combining MC-1 and SMC-2. Through the use of two different PPGs, two different biorecognition agents could be immobilised into the structure of the waveguide device through successive reactions and deprotections. This would enable the formation of multiplexed biosensors, detecting two, or possibly more, different analytes simultaneously.

LW devices however, are not the limit for these hydrogel films. The spatiotemporal control of photodeprotection enables many uses for hydrogels made with these photocaged monomers. The original plan for this project was to conclude with the development of

photonic crystals, however, the COVID-19 pandemic caused the project to undergo significant modifications.

4.9 References

1 K. M. Koczula and A. Gallotta, *Essays Biochem.*, 2016, **60**, 111–120.
2 G. V. Raj, J. G. Moreno and L. G. Gomella, *Cancer*, 1998, **82**, 1419–1442.
3 H. Krüger, M. Asido, J. Wachtveitl, R. Tampé and R. Wieneke, *Commun. Mater.*, 2022, **3**, 9.
4 S. Matsumoto, S. Yamaguchi, A. Wada, T. Matsui, M. Ikeda and I. Hamachi, *Chem. Commun.*, 2008, 1545.
5 C. G. Bochet, *Tetrahedron Lett.*, 2000, **41**, 6341–6346.
6 X. Li, Y. Gao, Y. Kuang and B. Xu, *Chem. Commun.*, 2010, **46**, 5364.
7 J. Karcher, S. Kirchner, A.-L. Leistner, C. Hald, P. Geng, T. Bantle, P. Gödtel, J. Pfeifer and Z. L. Pianowski, *RSC Adv.*, 2021, **11**, 8546–8551.
8 I. Tomatsu, K. Peng and A. Kros, *Adv. Drug Deliv. Rev.*, 2011, **63**, 1257–1266.
9 C. D. McNitt, H. Cheng, S. Ullrich, V. V. Popik and M. Bjerknes, *J. Am. Chem. Soc.*, 2017, **139**, 14029–14032.
10 S. Waichman, C. You, O. Beutel, M. Bhagawati and J. Piehler, *Anal. Chem.*, 2011, **83**, 501–508.
11 D. R. Griffin and A. M. Kasko, *J. Am. Chem. Soc.*, 2012, **134**, 13103–13107.
12 M. Guvendiren and J. A. Burdick, in *Integrative Mechanobiology*, eds. Y. Sun, D.-H. Kim and C. A. Simmons, Cambridge University Press, 1st edn., 2015, pp. 90–109.
13 J. H. Wosnick and M. S. Shoichet, *Chem. Mater.*, 2008, **20**, 55–60.
14 Y. Sun, D. Nan, H. Jin and X. Qu, *Polym. Test.*, 2020, **81**, 106283.
15 S. A. Stromgren, 2019, 43, FDA - https://www.fda.gov/media/121751/download?attachment, (accessed 23 October 2022).
16 RT-PCR / RT-qPCR Troubleshooting, https://www.sigmaaldrich.com/GB/en/technical-documents/technical-article/genomics/pcr/troubleshooting, (accessed 20 October 2022).
17 I. Moser, *Biosens. Bioelectron.*, 2002, **17**, 297–302.
18 Kit Components of RealStar® PCR Kits (RUO/CE) - altona Diagnostics, https://www.altona-diagnostics.com/en/kit-components-of-realstar-pcr-kits-ruo-ce.html, (accessed 20 October 2022).
19 S. Nizamov, V. Scherbahn and V. M. Mirsky, *Sens. Actuators B Chem.*, 2015, **207**, 740–747.
20 L. Qiao, M. R. Benzigar, J. A. Subramony, N. H. Lovell and G. Liu, *ACS Appl. Mater. Interfaces*, 2020, **12**, 34337–34361.
21 A. K. Pal, N. J. Goddard, H. J. Dixon and R. Gupta, *Biosensors*, 2020, **10**, 134.
22 P. K. Yuen, N. H. Fontaine, M. A. Quesada, P. Mazumder, R. Bergman and E. J. Mozdy, *Lab. Chip*, 2005, **5**, 959.
23 N. J. Goddard and R. Gupta, *Sens. Actuators B Chem.*, 2020, **309**, 127776.
24 R. Gupta and N. J. Goddard, Freiburg, Germany, 2013, pp. 1490–1492.
25 G. D. Heda, *BioTechniques*, 2020, btn-2020-0117.
26 R. Gupta, S. El Sayed and N. J. Goddard, *RSC Adv.*, 2021, **11**, 40197–40204.
27 A. K. Pal, E. Labella, N. J. Goddard and R. Gupta, *Macromol. Chem. Phys.*, 2019, **220**, 1900228.
28 R. Gupta and N. J. Goddard, *The Analyst*, 2021, **146**, 4964–4971.
29 A. V. B. de Oliveira, V. Kartnaller, C. Costa Neto and J. Cajaiba, *ACS Omega*, 2019, **4**, 13530–13537.
30 P. Klán, T. Šolomek, C. G. Bochet, A. Blanc, R. Givens, M. Rubina, V. Popik, A. Kostikov and J. Wirz, *Chem. Rev.*, 2013, **113**, 119–191.
31 A. P. Pelliccioli and J. Wirz, *Photochem. Photobiol. Sci.*, 2002, **1**, 441–458.
32 T. Maier, A. Schmidt, M. Güell, S. Kühner, A. Gavin, R. Aebersold and L. Serrano, *Mol. Syst. Biol.*, 2011, **7**, 511.
33 Amine-Reactive Crosslinker Chemistry - UK, https://www.thermofisher.com/uk/en/home/life-science/protein-biology/protein-biology-learning-center/protein-biology-resource-library/pierce-protein-methods/amine-reactive-crosslinker-chemistry.html, (accessed 26 October 2022).
34 C. E. Chivers, A. L. Koner, E. D. Lowe and M. Howarth, *Biochem. J.*, 2011, **435**, 55–63.

35 Avidin-Biotin Interaction - UK, https://www.thermofisher.com/uk/en/home/life-science/protein-biology/protein-biology-learning-center/protein-biology-resource-library/pierce-protein-methods/avidin-biotin-interaction.html, (accessed 30 September 2022).
36 D. Y. Smith and W. Karstens, *J. Phys. Conf. Ser.*, 2010, **249**, 012034.
37 Refractive index - Light and sound - reflection and refraction - GCSE Physics (Single Science) Revision - Other, https://www.bbc.co.uk/bitesize/guides/zchyj6f/revision/4, (accessed 4 October 2022).

Chapter 5 – Conclusion and Future Work

5.1 Conclusion

In conclusion, the purpose of this thesis was to study hydrogels leading to the production of an optical biosensor suitable for point of care (POC) testing.

To begin this process, studies were conducted to determine the sensitivity of chitosan-based dye doped leaky waveguide (DDLW) devices, formed by an updated procedure to that previously observed in the literature. In this case, due to inconsistencies with chitosan samples, caused by the nature of their extraction, a method was adapted for the purification of chitosan for increased uniformity across DDLW devices (Chapter 2.5.1). These DDLW devices were then tested for their refractive index sensitivity (RIS) and porosity on a traditional benchtop laboratory-based waveguide instrument Following this, the experiments were repeated on a portable sized, lightweight three-dimensional (3D) printed instrument. In Chapters 2.5.4 and 2.5.5 data from the 3D printed instrument was compared to that obtained from the traditional benchtop laboratory-based instrument to ensure the newer device was akin to those already in use. Once this was determined to be the case, the DDLW devices were then tested for their ability to detect relevant target analytes on the 3D printed instrument (Chapter 2.5.6). While the traditional benchtop laboratory-based instrument allowed for the use of a two-channel flow cell to enable a referencing region of the DDLW device, the structure of the 3D printed instrument did not permit this. It is due to this that research into other methods of internal referencing within leaky waveguide (LW) devices was required.

Two other major methods of internal referencing were discussed, the use of referencing and biosensing layers to form a stacked LW device, or the formation of referencing and biosensing regions within a single LW device; we opted to continue research into the latter.

Research into photoresponsive hydrogels was the starting point for the formation of internally referenced LWs. Due to the high spatio-temporal control of photochemical reactions, these were determined to be the ideal method for the modification of hydrogels to incorporate regions of protein-reactive and protein-inert functional groups. Of the research into photoresponsive hydrogels, the use of photolabile protecting groups (PPGs) was highly studied, and determined to be the most applicable for the development of microstructures within hydrogels.

Initially, in an attempt to form photoresponsive hydrogels, the photocaging of a synthetic acrylamide (AAm)/*N*-3-aminopropyl methacrylamide (APMA) co-polymer hydrogel was attempted. The commercial photocaging agent, 4,5-dimethoxynitrobenzyl chloroformate (NVOC-Cl) is a water reactive compound, therefore in Chapter 3.5.1.1 studies were conducted to determine the effect of polar organic solvents on AAm/APMA LW devices. Dimethylsulfoxide (DMSO) was the only solvent found to not be detrimental to the hydrogel structure, however, further studies (Chapter 3.5.1.3) determined that an unwanted reaction was occurring between DMSO and NVOC-Cl. This led to the photocaging of APMA with NVOC-Cl prior to polymerisation to form the photocaged monomer, **NVOC-APMA**. The formation of **NVOC-APMA** was successful, however the compound was not water soluble (Chapter 3.5.2.1). It had previously been suggested that for efficient sensing, APMA should be present as 4% the total monomer weight. In order to dissolve **NVOC-APMA** with the reagents for hydrogel formation, a solution of DMSO and water was required. Even with this combined solution, the levels of **NVOC-APMA** present in the hydrogel were limited to 0.2% of the total monomer weight. It was therefore determined in Chapter 3.5.2.1 that this method was not sufficient for the formation of internally referenced LW devices.

The research into PPGs which is discussed in Chapter 3.3 showed much interest in two structures for amine protection, that of the *O*-nitrobenzyl protecting group, and coumarin derived compounds, thus these are the structures that provided the basis of PPGs developed in this work. In Chapter 3.5.2, three photocaged groups were developed based on the structure of NVOC-Cl; the first two were designed with polyethylene glycol chains at positions 3 and 4 to increase water solubility in comparison to the methoxy version. The difference between these two compounds being that one was photocaged *via* an amine bond (**NB-6a**), whereas the other was photocaged *via* a carbamate bond (**NB-6b**). The third compound was designed by incorporating an *O*-nitrobenzyl group on dibenzofuran (**DBF-5**), as dibenzofuran is a more conjugated system than benzene, this group was developed in an attempt to red-shift the absorbance spectra.

In addition to *O*-nitrobenzyl based structures, Chapter 3.5.2 also delves into the development of 6 PPG's based on the coumarin structure. A dimethoxycoumarin photocaged APMA compound was caged *via* both amine (Chapter 3.5.2.5) and carbamate (Chapter 3.5.2.7) bonds, resulting in the formation of compounds **MC-1** and **MC-3**. The absorbance spectra of these compounds indicated absorbance at low wavelengths, prompting the modification of the coumarin groups to contain a thiocarbonyl group at position 2 rather than a carbonyl, leading to the development of compounds **SMC-1** in Chapter 3.5.2.8 and **SMC-3** in Chapter 3.5.2.10. Finally, in an attempt to combine both of the PPG structures, Chapters 3.5.2.6 and 3.5.2.9 discuss the modification of the dimethoxycoumarin derivatives to incorporate a nitro functionality at position 3, thus creating a structure similar to that of the *O*-nitrobenzyl PPGs, forming compounds **MC-2** and **SMC-2**. This led to the development of 9 different photocaged APMA monomers for future studies. As observed in Chapter 3.5.2.11 synthesis into

dimethylaminocoumarin derivatives was also started, resulting in the formation of the precursor coumarin **AC**, however time constraints did not permit the completion of this. The photochemical properties of compound **AC** were compared to those of the dimethoxy analogue, **MC**; the data suggests that the presence of the amine at position 7 had the intended effect of red-shifting the absorbance maxima.

Following the formation of 9 photocaged APMA monomers, Chapter 4.6.1 discusses the optimisation of hydrogel formation using these compounds. It was discovered at this point that only the compounds **MC-1**, **MC-2**, **SMC-1** and **SMC-2** were able to form hydrogels when employed as co-monomers. Due to this, further studies were centred on these four photocaged monomers. Once gel optimisation was conducted, Chapter 4.6.2 delved into studies of the PPG deprotections at 365 nm both in monomer format as a solution, and in the polymerised form as a hydrogel. Due to the complex deprotection mechanisms of **MC-1** and **SMC-1**, Chapters 4.6.2.1 and 4.6.2.2 respectively show that water alone as a solvent was not an adequate environment for deprotection to take place, a hydrogen atom donor was required. The disulfide bond formation between two 1-decanethiol molecules releases two hydrogen atoms, thus this compound was used as the hydrogen atom transfer (HAT) compound. The deprotection of **MC-1** and **SMC-1** was significantly improved in the presence of a HAT compound.

Throughout Chapter 4.6.3 LW devices were formed using the four photocaged APMA compounds as co-monomers with AAm and in tested for refractive index sensitivity (RIS) in Chapter 4.6.4 and porosity to various sized molecules in Chapter 4.6.5. Following the compounds being determined to be suitable for LW device formation, throughout Chapter 4.6.6 the LWs were irradiated to contain half photocaged (referencing) and half deprotected

(biosensing) regions. In protein immobilisation studies, compounds **MC-1** (Chapter 4.6.6.1) and **MC-2** (Chapter 4.6.6.3) were shown to have minimal difference between the sensing and referencing regions, likely due to minimal deprotection occurring, therefore a low concentration of protein reactive immobilising functional groups. A more noticeable difference was observed with compounds **SMC-1** (Chapter 4.6.6.2) and **SMC-2** (Chapter 4.6.6.4).

As determined in Chapter 3.5.2, compounds **MC-1** and **MC-2** had much lower extinction coefficients at 365 nm in comparison to **SMC-1** and **SMC-2**; it appears that this may be a determining factor in the formation of internally referenced biosensors through the use of PPGs. Compounds with a higher extinction coefficient at the deprotection wavelength can absorb light more efficiently, thus improving the level of photodeprotection. However, the data collected suggests that this is not the only important factor within the formation of sensing and referencing regions. Whilst compounds **MC-1** and **SMC-1** have higher extinction coefficients at 365 nm than their nitrated analogues (**MC-2** and **SMC-2**), the nitrated PPGs were the better internally referenced LW devices. This is likely due to the improved deprotection method, caused by the nitro functional group, leading to increased deprotection kinetics. Thus, there are many factors to consider in the production of PPGs for the formation of internally referenced LW devices.

To summarise, throughout this thesis, a small, 3D printed instrument has been established to provide LW results comparable to that of the bulky traditional counterpart. Due to the inability to use a two-channel flow cell to introduce an internal reference, studies into the incorporation of internally referenced LW devices has been conducted. Ultimately, four PPGs have currently been synthesised and found to be suitable for this purpose, displaying

the ability to contain localised regions of protein reactivity. These photoresponsive hydrogel-based LW devices require further testing on the 3D printed instrument in the future.

5.2 Future Work

To progress this thesis further, development into amino-coumarin based PPGs would be the starting point. Once these PPGs are synthesised and developed into working internally referenced LW devices, a pathway to potentially forming multiplexed biosensors opens up due to the anticipated large difference in absorbance wavelengths between methoxy-coumarin PPGs and amino-coumarin PPGs.

Patterning currently occurs across the surface of a thin hydrogel for the formation of LW biosensors, in the future, once the photopatterning technique has been further improved, patterning horizontally into the structure of a thick hydrogel film would be studied. Through photopatterning horizontally into the structure of a thick hydrogel film, alternating layers of different refractive indices would be formed; this structure would provide the basis for a Bragg reflector, and the biosensing wound dressing. The hydrogel would be immobilised onto a substrate as current hydrogel based wound dressings already are, allowing wound fluids to be introduced directly from the source into the biosensor.

Before any of that can become a reality however, the biosensor has currently been proven to have the capability for biosensing through the immobilisation of biorecognition elements. Following this, the sensors would have to be used to detect possible biomarkers, for example IgG, before having the concentration decreased to determine the limit of detection for the biosensor. This would have to be completed for every clinically relevant biomarker to be tested, for example C-reactive protein. Following this, it would have to be

determined whether the limit of detection is capable of detecting the concentrations of analytes expected to be found in wound fluids.

Chapter 6 - Experimental

6.1 Techniques

6.1.1 Introduction

The purpose of this chapter is to discuss the theory of some recurring techniques throughout this work. Initially we will be discussing in depth the optical sensing technique known as leaky waveguides (LWs). LWs were used both for the characterisation of hydrogels and for biosensing applications. This was performed through testing changes in the refractive index (RI) of the hydrogel-based LW device to determine if the hydrogel was porous to large molecules, and also by showing the permanent shift in RI that indicates the covalent immobilisation of proteins. Following this some techniques used for the analysis of synthetic compounds will be introduced such as ultraviolet-visible (UV-Vis) spectroscopy and mass spectrometry (MS). These were used to determine the identity of synthesised products, not only that but UV-Vis spectroscopy was also used to follow reaction changes. In addition to these techniques, high performance liquid chromatography (HPLC) will be discussed in relation to the purification of compounds.

6.1.2 Waveguides

6.1.2.1 The Theory of Optics

The study of optics is defined as the area of physics in which the properties of light and its interactions are studied.[1] This is a vast area of study, of which only a few concepts will be discussed for this work. It is through the study of optics, that the speed of light in a vacuum was determined to be equal to 2.998×10^8 m s^{-1}, a constant value, denoted as *c*, which is important in many calculations in the field of optics.[2]

One of the most important optical properties of a material is the refractive index, which is defined as the speed of light in a chosen medium as a fraction of the value in a vacuum (Equation 6.1).[3,4] As refractive index is a ratio of two velocities, it is technically a unitless value, however occasionally it is assigned the arbitrary units of 'refractive index units' (RIU).[5]

$$n = \frac{c}{v}$$

Equation 6.1: *An equation displaying the calculation of refractive index (n) using the speed of light in a vacuum (c) compared to the speed of light in the new medium (v).*[4]

As RI and the speed of light in a medium are indirectly proportional, it stands to reason that when light travels between two media of different RIs, the speed at which the light travels changes; for example, when light travels from a material of high RI to a lower RI, the velocity of light will increase. This change in speed causes the light to bend or refract.[6] As displayed in Figure 6.1, when light travels into a medium of higher RI, it bends towards the normal, meaning towards a line intersecting the media at 90°. [7]

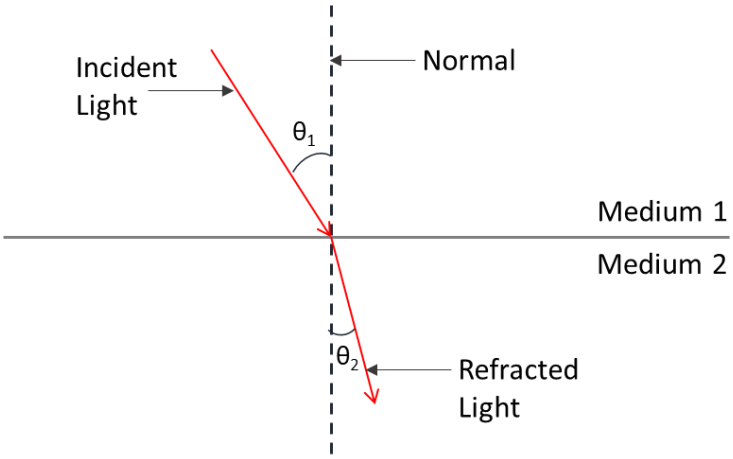

Figure 6.1: *An image depicting the bending of light as it travels from a medium of low RI (1) into a medium of high RI (2). Image adapted from Wong et al.*[8]

The reverse is true for light travelling from a material of high RI to a material of low RI, therefore in this case the light bends away from the normal. The extent to which light bends is dependent upon the angle of incidence, the angle at which light interacts with the interface.[9] When the angle of incidence is equal to or greater than the critical angle, light is refracted away from the normal to such an extent as to re-enter the high RI material, this is known as total internal reflection (TIR).[9,10] The critical angle (ϑ_c) is the angle at which TIR occurs and is dependent on the RI of the two materials, and can be calculated using Equation 6.2.

$$\theta_C = sin - 1\left(\frac{n_2}{n_1}\right)$$

Equation 6.2: *An equation showing the calculation of the critical angle (ϑ_C) for total internal reflection based on the refractive indices of two materials (n_1 and n_2).[11]*

Despite the total reflection of light under these conditions, a small amount of electromagnetic energy, known as an evanescent wave, extends into the low RI material (Figure 6.2).[12] This evanescent wave decays exponentially with distance, however at the interface, the energy is sufficient enough to excite responsive materials such as fluorescent compounds and metals.[12,13]

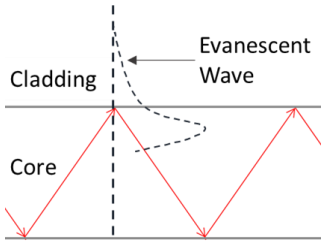

Figure 6.2: *An image depicting the decaying evanescent wave formed at the interface of two materials when TIR occurs. Image adapted from Zhao et al.[14]*

6.1.2.2 Optical Planar Waveguides

Waveguides operate through the confinement of light within a material through reflection.[15] These planar devices are comprised of three separate layers, the substrate, the waveguide material, and the sample.[16] Within an optical planar waveguide, TIR confines the light at both the substrate/waveguide and the waveguide/sample interfaces. As discussed in Chapter 6.1.1, for TIR to occur, light must be travelling from one medium of high RI to a medium of lower RI.[9,10] Due to this, the waveguide material layer of the planar optical waveguide device must be made of a material with a higher RI than that of both the substrate and the sample (Figure 6.3).

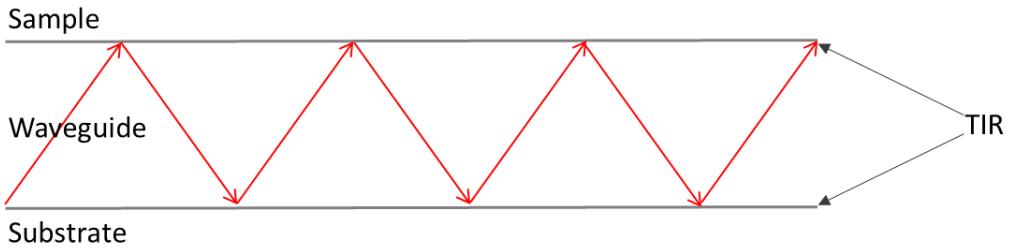

Figure 6.3: *An image depicting the setup of a conventional planar optical waveguide device, with a high RI waveguide material sandwiched between a substrate, usually glass, and sample, most commonly water-based, to allow for the confinement of light via TIR at both interfaces. Image adapted from Li et al.*[17]

As the sample is often an aqueous solution, the RI of this is commonly in the region of 1.3 RIU, so to exceed this value with a waveguide material is simple.[18] The difficulty comes in creating a waveguide of a material with a higher RI than that of the substrate, of which glass is the most widely used material, and has a RI of 1.5 RIU.[19]

In order to create waveguide devices with a RI higher than that of 1.5 RIU, often materials such as titanium dioxide are used.[20] To maintain such a high RI, these materials are known to be highly non-porous; due to the lack of porosity of the material, when using these

devices as biosensors, analyte detection occurs only at the surface of the device. It is because of this, that surface imperfections highly impact the usability of planar optical waveguide devices. If these devices could be made of a more porous material, sensing could occur throughout the entire device instead of merely at the surface; this would increase the sensing capability of waveguide devices and also reduce the dependency on uniform surfaces.

6.1.2.3 Leaky Waveguides

Research into the development of LW devices was conducted to aid in the improvement of waveguide biosensing techniques, as these can overcome many of the issues seen with planar optical waveguide devices. The setup of LWs is identical to that of optical planar waveguides, but whereas optical planar waveguides operate solely through TIR, LWs work through a combination of TIR and Fresnel reflection.[17] As with optical planar waveguides, the RI of the waveguide material is greater than that of the sample, thus TIR occurs at the waveguide/sample interface. The difference, however, is that in this instance, the waveguide material is of a lower RI than that of the substrate; due to this Fresnel reflection occurs at this interface (Figure 6.4).[21] As Fresnel reflection is the partial transmission of light into one medium, with partial reflection back into the original, some light is lost when sensing, hence the name LWs.[22]

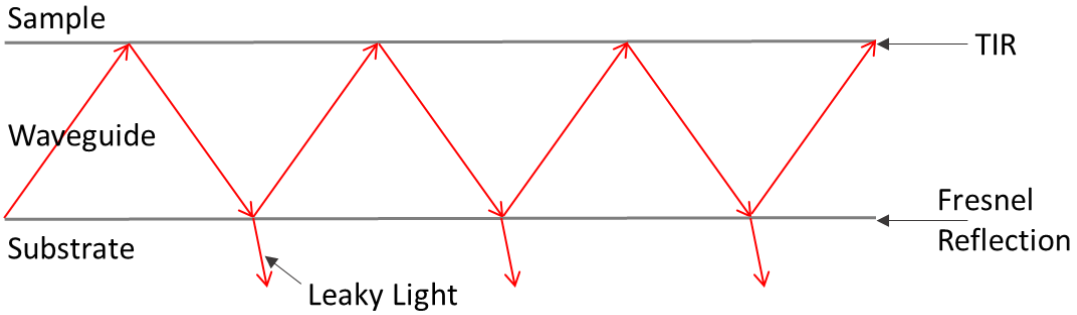

Figure 6.4: *An image depicting the configuration of a LW device, a substrate, topped with a waveguide material, topped with sample. TIR occurs at the waveguide-sample interface whereas Fresnel reflection is observed at the substrate-waveguide interface. Image adapted from Gupta et al.*[22]

The advantage to this method of light confinement within a LW device, is that the waveguide material is no longer required to have a RI that is higher than that of glass. This provides a much greater range of materials for waveguide production, whilst enabling the coupling of light into the LW structure.

6.1.2.4 Detection

The setup of LW biosensors includes a light source, a glass prism, the substrate, the LW device, the sample, and a camera (Figure 6.5).[23] The glass prism couples light into the LW device, light is then confined in the LW device between the sample and the substrate, before being detected by the camera. This angle of confinement is known as the resonance angle. The camera then captures real time images of the light.

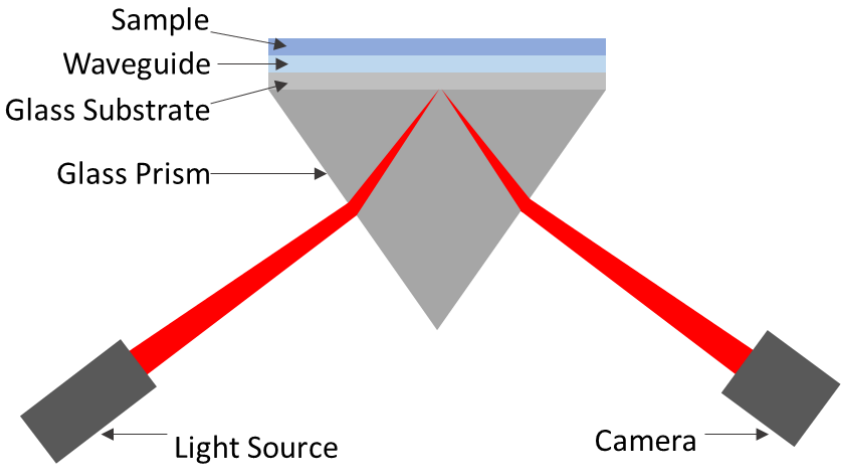

Figure 6.5: *An image depicting the setup of a LW instrument with a light source, a glass prism which couples light into a glass slide-supported LW device, which is then covered by a sample solution. Image adapted from Alamrani et al.*[24]

As light is reflected within the LW device, a dip in light transmission is observed on the camera. Depending on multiple factors such as the thickness and the material of the LW device, multiple resonance angles may be observed, these are known as modes of reflection. As the RI of the waveguide material or the sample changes, so does the resonance angle. This change in resonance angle causes a shift in position of the dip in transmission as observed by the camera. This change in resonance angle is the observed signal, and is directly proportional to the shift in RI, resulting in a quantitative biosensor.

6.1.2.5 Analysis

As was stated in Chapter 6.1.2.4, the resonance angle, henceforth known as the mode, is detected by the camera as a dip in light transmission. A made-for-purpose computer program, RMv8, was specially designed to track the position of modes in terms of camera pixels. The output image collected, as shown in Figure 6.6, displays the thin dip in reflectivity

representing a mode, from the resonance angle, and the large dip in reflectivity at the top of the film, from TIR.

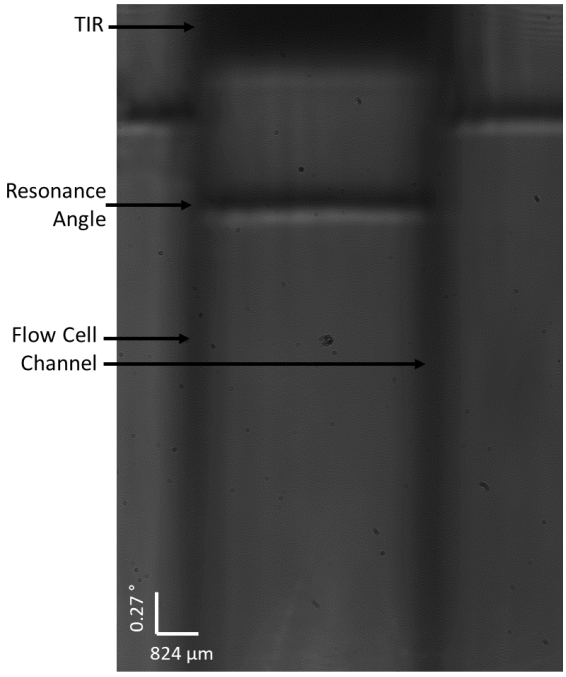

Figure 6.6: *An image displaying the output image as produced by the camera, showing the resonance angle and TIR of the hydrogel film, along with visualisation of the flow cell boundary lines.*

The LW device with buffer was normalised to be 0 pixels, then, as sample solutions of different RIs are introduced to the LW device, the resonance angle and thus position of the mode shifts. For solutions in which there is no permanent change to the LW device, the position of the mode returns to 0 pixels upon the reintroduction of the starting buffer solution. Immobilisation of compounds within the structure of the LW device is determined by the permanent change in position of the mode when buffer solution is reintroduced to the device.

As pixels moved are unique to each camera resolution, these results must then be modified into a more universal measurement. The following equation, (Equation 6.3) describes how the shift in pixels is converted from pixels to radians, following this, the result is then converted into the more commonly used unit of degrees.

$$Shift\ in\ Radians = \ Shift\ in\ Pixels\ \times ATAN\left(\frac{Pixel\ Size}{Distance\ from\ Camera\ to\ Prism}\right)$$

Equation 6.3: *An equation showing how the shift in pixels detected by the camera is used to calculate the shift in radians using the pixel size and distance between the camera and prism.*

6.1.3 Ultraviolet-Visible Spectroscopy

UV-Vis spectroscopy is an optical technique which, as mentioned in Chapter 6.1.2, is reliant upon the interactions of substances with light.[25] While some optical techniques are reliant on light scattering, as observed with dynamic light scattering spectroscopy, others utilise light absorbance, as is the case with UV-Vis spectroscopy.[26]

The premise behind UV-Vis spectroscopy is that when light ranging from 100 – 800 nm interacts with a compound, electrons absorb energy from the photons. The wavelength of light absorbed is dependent on the energy required to excite electrons, as shown in Equation 6.4.[27]

$$E = \frac{hc}{\lambda}$$

Equation 6.4: *An equation showing how the energy of a photon (E) is related to the wavelength of light (λ) in combination with Planck's constant (h) and the speed of light (c), both of which are constant values.*[28]

When light is absorbed by an electron in the ground state, the electron is then excited to a higher energy orbital; however, this only occurs when the photonic energy perfectly matches the energy gap between the ground and an excited state.[27,29] Numerous electron transitions are possible, as shown in Figure 6.7.

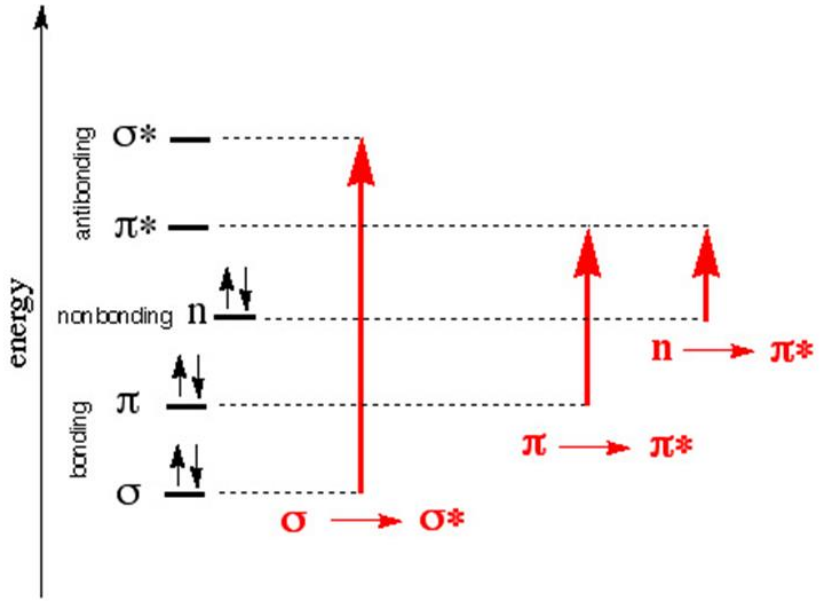

Figure 6.7: *An image displaying the hypothetical energy transitions that occur and give rise to observable signals within UV-Vis spectroscopy. Image adapted from chem.ucla.edu.*[30]

As light of specific wavelengths is absorbed by the compound, the rest is transmitted through the sample to the detector, and through the use of Equation 6.5, the absorbance of light is calculated from the initial intensity of light compared to the detected intensity.[31] This absorbance is calculated for every wavelength specified in the instrument parameters, thus producing a spectra of wavelength vs absorbance. As absorbance is determined through being a ratio of light, it is therefore a unitless parameter, however, it is often given the arbitrary units of absorbance (Abs) or absorbance units (a.u.).

$$A = log_{10}\left(\frac{I_0}{I}\right)$$

Equation 6.5: *An equation showing how absorbance (A) is calculated based on the original intensity of the wavelength of light (I_0) compared to the detected intensity of light (I).*[31]

According to the Beer-Lambert Law, absorbance is directly correlated with the concentration of a sample (Equation 6.6); due to this, and the simplicity of the technique, UV-Vis absorbance spectroscopy is often used to monitor reactions.[32]

$$A = \varepsilon l c$$

Equation 6.6: *The Beer-Lambert Law, depicting the relationship between absorbance (A), molar extinction coefficient (ε), the path length of light (l) and finally the concentration of the solution (c).*[32]

The molar extinction coefficient (ε) is a measure of how efficient the compound is at absorbing light and can vary depending on the solvent used.[33] The ε is typically measured at the major absorption wavelength (λ_{max}), however, can be measured at any desired wavelength. Based on the equation above, the ε can easily be calculated, by plotting a graph of concentration vs absorbance, the gradient of the graph is equal to the ε multiplied by the path length (l).

UV-Vis is a highly versatile analytical technique. Throughout these studies it will be used for the monitoring of reaction development, and for the characterisation of compounds.

6.1.4 High Performance Liquid Chromatography

Chromatography is a separation technique often used for the purification of synthetic products.[34] Separation is achieved based on the characteristics of a sample, whether that be hydrophobicity, particle size, or as is more commonly seen, polarity.[35]

Column chromatography is a standard purification technique within organic synthesis.[36] Using gravity to ensure sample passes through the column, mixtures are separated based on their interactions with the silica column and the solvent system, however,

occasionally, this method is not suitable.[37] In instances where a mixture is comprised of compounds with similar characteristics, column chromatography may not deliver the required separation resolution for compound purification. Another problem with column chromatography is that identification of the correct sample can only occur following collection.[38]

HPLC relies on the same fundamental characteristics as column chromatography, however instead of relying on gravity, the system uses a pressurising pump to separate the mixture.[39] In normal phase HPLC a polar silica column is used as the stationary phase, and the sample is introduced in a non-polar mobile phase. More polar compounds will interact more favourably with the stationary phase, thus taking longer to elute than the non-polar compounds which prefer the mobile phase, and therefore elute more quickly.[40]

Both of these techniques are useful for the purification of organic synthetic products, however, due to interactions with silica, polar solvents cannot be used for more polar compounds.[41] Reversed-phase chromatography solves this problem by using a non-polar stationary phase, often silica functionalised with long alkyl chains which are compatible with polar solvents.[42] Not only does reversed-phase HPLC (RP-HPLC) allow for the better separation of polar compounds, it also allows for purification with lower retention times than if normal phase were attempted; this is because due to the reversal of polarities with the stationary and mobile phases, polar compounds elute faster while non-polar compounds are slowed down by interactions with the stationary phase.[43]

HPLC and by extension RP-HPLC possess another advantage over the standard column chromatographic technique. As was explained earlier, in column chromatography, compound identification can only occur following purification, this is not the case with HPLC.[44] HPLC

systems can be fitted with analytical devices, such as UV-Vis spectrophotometers, refractometers, fluorescence spectrophotometers and MS instruments.[45] The combination of these analytical techniques with the HPLC allows for the identification of fractions prior to collection.

Within this work, RP-HPLC was used for the purification of the water soluble photocaged monomers, using UV-Vis detection to determine the correct fractions.

6.2 Materials and Methods

6.2.1 Commercially Available Materials and Instrumentation

Reagents and solvents used within this thesis were purchased from commercial suppliers and used without further purification, unless otherwise stated. Glass slides were cleaned in a PS-20 Digital ultrasonic Jakansonic cleaner. All pH values were obtained using a Hanna Instruments HI 2210 pH meter. Refractive index of solutions were collected using a Bellingham and Stanley RFM970-T Refractometer. Melting points were collected in open glass capillary tubes using a Stuart SMP10 melting point apparatus. Infrared (IR) spectroscopy was performed on dry samples with a Varian 660-IR FT-IR spectrometer. ^{1}H and ^{13}C nuclear magnetic resonance (NMR) spectra were obtained on Brüker AVIII400 spectrometers. Chemical shifts (δ) are given in ppm and are relative to the residual solvent peak. Data was acquired using Brüker Topspin v3.2 and analysed with MestReNova v10.0.2-15465. Mass spectrometry data was collected using a Waters Xevo G2-XS mass spectrometer.

6.2.2 Flow Cells

The circular flow cell (Figure 6.8) was made by taking a 3 mm thick polymethylmethacrylate slide and using computer numerical control (CNC) machining to create a 0.2 mm deep circular cavity that was 18 mm in diameter and surrounded by a 0.75 mm deep and 1 mm wide groove for the mounting of an O-ring. This cavity then has two holes plugged with bootlace ferrules, one to act as an inlet for the peristaltic pump and the other an outlet.

The two-channel flow cell (Figure 6.8) was made by taking a 3 mm thick polymethylmethacrylate slide of and using CNC machining to create two 0.2 mm deep c-

shaped cavities that were 18 mm in length and 3 mm in diameter and surrounded by a 0.75 mm deep and 1 mm wide groove for the mounting of an O-ring. There was a gap of 0.2 mm between each channel. The cavities then have two holes each, one at either end plugged with bootlace ferrules, one to act as an inlet for the peristaltic pump and the other an outlet.

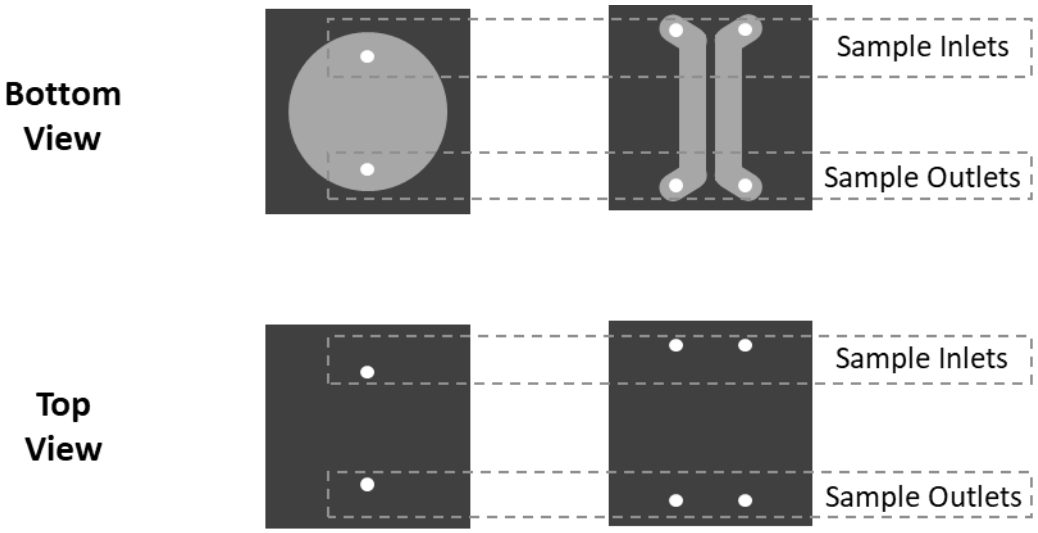

Figure 6.8: *An image displaying the two different types of flow cell used, a circular flow cell and a two-channel flow cell.*

6.2.3 3D-Printed Waveguide Instrument

The three-dimensional (3D) printed portable waveguide instrument was designed and constructed for this experiment. The structure was built from multiple 3D printed components as described by *Goddard et al*. The light source used was a 650 nm point source light emitting diode (LED), model MTPS8065WC (Marktech Optoelectronics Inc, Latham, NY, USA). Using a plastic aspheric lens (Knight Optical, Maidstone, UK) the light was collimated, before being polarised in the transverse electric (TE) plane with a plastic polariser (32WL100, Comar Optics, Cambridge, UK) then finally using a 25 mm focal length cylindrical lens (25 YQ 25, Comar Optics, Cambridge, UK) the light was focused into a wedge beam. This wedge beam is coupled

into the waveguide device through a BK7 equilateral prism (Optotronics Inc, Mead, CO, USA). The light coupled out of the waveguide was reflected by a rotatable λ/4 front surface mirror, model 40 MX 25 (Comar Optics Ltd, Cambridge, UK) onto a 10 Mpixel USB2 camera, model UI-1492-LE (IDS Imaging, Obersulm, Germany). The instrument is then connected via USB to a standard desktop computer which is used to control motors within the 3D printed instrument to modify the positions of the camera and mirror. The computer also runs a software written for this work which captures images from the camera at regular intervals then uses the average intensity of light reflected per pixel to create an image which displays the resonance angle of light within the waveguide. Waveguide devices are supported on a glass substrate, which are then placed on the BK7 prism with refractive index matching oil. A custom-made flow cell was then mounted on top of the waveguide device and held in place with a fixture. Samples were then exposed to the waveguide device by being pumped with a peristaltic pump (Minipuls 3, Gilson, Bedfordshire, UK) through the flow cell.

6.2.4 Traditional Benchtop Laboratory-Based Waveguide Instrument

All traditional benchtop laboratory-based instruments were built up manually. The light source used was a point source LED, described in Table 6.1. Using an aspheric lens (Knight Optical, Maidstone, UK) the light was collimated, before being polarised in the TE plane with a plastic polariser (32WL100, Comar Optics, Cambridge, UK) then finally using a cylindrical lens (25 YQ 25, Comar Optics, Cambridge, UK) the light was focused into a wedge beam. This wedge beam is coupled into the waveguide device through a BK7 equilateral prism (Qioptic Photonics, Denbighshire, UK). The light coupled out of the waveguide was directed onto a camera, which is then connected via USB to a standard desktop computer for power. The

positions of the camera and LED can be manipulated manually or *via* the computer. The computer also runs a software written for this work which captures images from the camera at regular intervals then uses the average intensity of light reflected per pixel to create an image which displays the resonance angle of light within the waveguide. Waveguide devices are supported on a glass substrate, which are then placed on the BK7 prism with refractive index matching oil. A custom-made flow cell was then mounted on top of the waveguide device and held in place with a fixture. Samples were then exposed to the waveguide device by being pumped with a peristaltic pump (Minipuls 3, Gilson, Bedfordshire, UK) through the flow cell. Instrument A was used for studies in Chapter 2 whereas instrument B was used to complete the studies described in Chapter 4.

Table 6.1: *A table displaying the different components of the two different traditional benchtop laboratory-based waveguide instruments used throughout this thesis.*

Benchtop Instrument	LED Light Source	Camera	Water Bath
A	650 nm LED	10 Mpixel Pixelink (Gloucester, Canada)	Grant Instruments LT ecocool 100 recirculating water bath
B	640 nm LED (TL-6, iC-Haus)	20 Mpixel (MER-2000-19U3M-L, Daheng Imaging, Beijing, China)	N/A

6.2.5 UV Irradiation Source

The ultraviolet (UV) irradiation source (Figure 6.9) consisted of a 365 nm LED, which passed through a 25 mm diameter planoconvex lens to form a collimated beam in a black box. The light source was cooled by a fan to prevent over-heating.

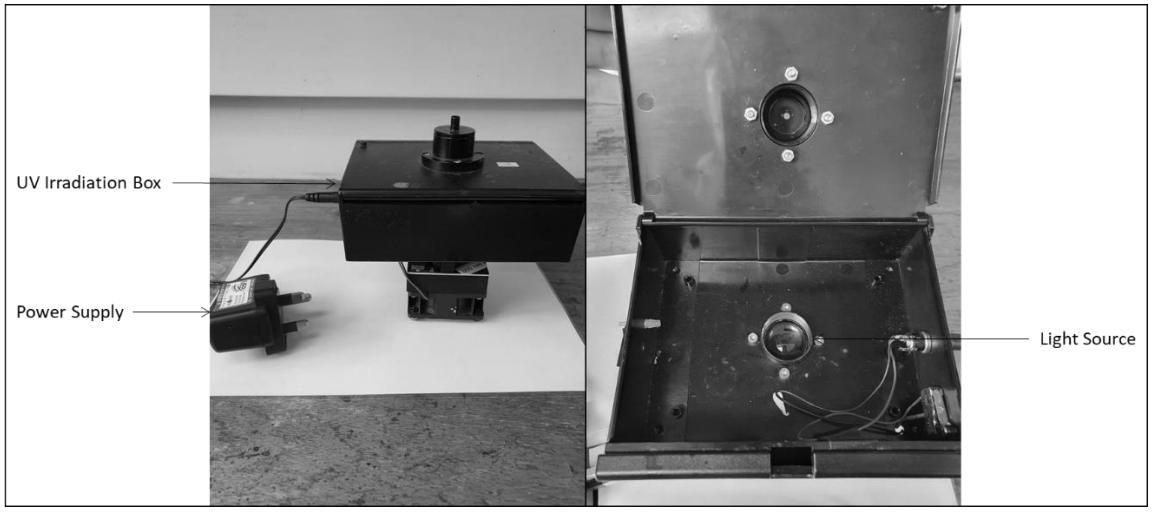

Figure 6.9: *An image displaying the UV irradiation source used throughout these studies, the external structure (left) and the inside (right).*

6.3 Chapter 3 Experimental

6.3.1 Glass Slide Cleaning

Glass microscope slides (7.5 cm × 2.5 cm × 0.15 cm) were cut using a diamond-tipped scribe to be ≈2.5 cm × 2.5 cm × 0.15 cm. They were then cleaned by sonicating for 30 minutes each in decon 90, then deionised (DI) water, and finally in absolute ethanol for a combined total of 90 minutes.

6.3.2 Preparation of a 100 mM HEPES pH 7.4 Buffer Solution

In a glass beaker (500 mL) dissolve 4-(2-hydroxyethyl)-1-piperazineethanesulfonic acid (HEPES) (11.915 g, 50 mmol) in DI water (≈ 400 mL). 1 M sodium hydroxide was added dropwise to the solution until a pH of 7.4 was measured by the pH meter. Following this, the solution was transferred to a volumetric flask (500 mL) and DI water added until the volume was equal to 500 mL.

6.3.3 Spin coating Chitosan Waveguide Films

The crude chitosan (M.W. 100 kDa to 300 kDa) was purified prior to use. To do this chitosan (2.5 g) was dissolved in 0.1 M acetic acid (250 mL) and left to stir at room temperature overnight. This solution was then filtered through a 5 µm syringe filter membrane. 1 M sodium hydroxide was added until an off-white precipitate no longer formed. The precipitate was centrifuged (40 mL at a time) for 10 minutes each at 4.4 rpm using an Eppendorf Centrifuge 5702. The precipitate was then further purified for 5 days through dialysis with DI water using a 10,000 kDa dialysis membrane. The chitosan was then re-dissolved in methanol, which was then evaporated under reduced pressure. Finally, the chitosan was washed with DI water, and

then freeze dried for 24 hours to obtain a dry product. This resulted in a 60% yield of chitosan. The purified chitosan appeared to be whiter in colour, the structure more closely resembled that of flakes rather than a powder.

The purified chitosan (0.1 g) was dissolved in 0.1 M acetic acid (10 mL) and left to stir for 16 hours. This solution (100 µL) was spin coated onto the surface of cleaned glass slides at 900 rpm with an acceleration of 100 rpm s^{-1} for 30 s using a Laurell WS-650MZ-23NPPB spin coater. The slides were then incubated at 25 °C for 3 minutes. A 0.03% glutaraldehyde solution was prepared by taking 25% glutaraldehyde (25 µL) and diluting to 20 mL using 100 mM HEPES pH 7.4 buffer solution. The slides were then submerged in this 0.03% glutaraldehyde solution for 10 minutes to allow the glutaraldehyde to form cross-links between the chitosan polymer chains. After 10 minutes the slides were removed from the glutaraldehyde solution and washed gently with a HEPES buffer solution. Finally, to allow for the optical imaging of the chitosan films, they were stained with a 0.1 mM solution of reactive blue 4 (RB4) dye (10 mL), formed by dissolving RB4 (6.374 mg, 0.01 mmol) in 100 mM HEPES pH 7.4 buffer solution (100 mL). The slides were then stored in 100 mM HEPES pH 7.4 buffer solution out of direct light until use.

6.3.4 Glycerol Sensitivity Testing

To make the glycerol solutions, glycerol (1 mL) was dissolved in 100 mM HEPES pH 7.4 buffer solution (9 mL) to create a 10% (v/v) solution. Serial dilutions were then performed with 100 mM HEPES pH 7.4 buffer solution to create solutions with concentrations equal to 0.125%, 0.25%, 0.5%, 1% and 2% (v/v). The refractive indices of these solutions were measured in triplicate before use.

For the refractive index sensitivity testing using any waveguide instrument, 100 mM HEPES pH 7.4 buffer solution was run through the flow cell to create a baseline. The glycerol solutions were then introduced to the flow cell sequentially until the signal plateaued at its peak, increasing concentration with time. The signal was then returned to the baseline, again using 100 mM HEPES pH 7.4 buffer solution.

To obtain a glycerol trace, data collected was converted from shift in pixels to shift in resonance angle ($\Delta\theta_R$) through the use of Equation 6.3. The $\Delta\theta_R$ was plotted in a graph against time using Origin.

In order to obtain a glycerol calibration curve, the average $\Delta\theta_R$ at the peak of each glycerol solution was plotted in a graph against the refractive index of the solution using Origin.

6.3.5 Polyethylene Glycol Porosity Testing

1% (w/v) solutions of polyethylene glycol (PEG)-10 kDa, PEG-100 kDa and PEG-300 kDa were created by dissolving PEG (0.1 g) in 100 mM HEPES pH 7.4 buffer solution (10 mL) for each of the different chain lengths. The refractive indices of these solutions were then measured before use.

For the porosity testing using any waveguide instrument, 100 mM HEPES pH 7.4 buffer solution was run through the flow cell to create a baseline. The 1% PEG-10 kDa solution was then introduced to the flow cell until the signal plateaued. The PEG-10 kDa was then washed out of the pores with 100 mM HEPES pH 7.4 buffer until the signal reached the baseline. This procedure was repeated with PEG-100 kDa and PEG-300 kDa.

To obtain a PEG trace, data collected was converted from shift in pixels to shift in resonance angle ($\Delta\theta_R$) through the use of Equation 6.3. The $\Delta\theta_R$ was plotted in a graph against time using Origin.

6.3.6 IgG Protein Detection with a 3D Printed Instrument

Using a single-channel flow cell, a peristaltic pump was used to introduce a 100 mM HEPES pH 7.4 buffer solution to the chitosan leaky waveguide (LW) device through the flow cell until the signal presented a steady baseline. A solution of 25% glutaraldehyde (240 µL) dissolved in 100 mM HEPES pH 7.4 (29.76 mL) was then run through the channel for 30 minutes. Following this, the flow cell channel was washed with 100 mM pH 7.4 HEPES until the signal was stable. In the next step, a 0.5 mg mL^{-1} solution of streptavidin in 100 mM HEPES pH 7.4 was added until the signal plateaued and was subsequently washed with 100 mM HEPES pH 7.4 until the signal stabilised. This wash was followed by the introduction of a 5 mg mL^{-1} solution of bovine serum albumin for 2 hours, after which the channel was washed with buffer. The next solution to be introduced was a 0.4% (v/v) solution of biotin anti-immunoglobulin G, which was allowed to flow through the channel until the signal plateaued before again being washed with 100 mM HEPES pH 7.4. The final analyte to be introduced to the waveguide was a 0.1 mg mL^{-1} solution of immunoglobulin G in 100 mM HEPES pH 7.4, this was left to run until the signal plateaued. The last step was to wash the channel with 100 mM HEPES pH 7.4 buffer solution until the signal had stabilised, creating a new baseline.

To obtain a protein immobilisation trace, data collected was converted from shift in pixels to shift in resonance angle ($\Delta\theta_R$) through the use of Equation 6.3. The $\Delta\theta_R$ was plotted in a graph against time using Origin.

6.4 Chapter 4 Experimental

6.4.1 Ultraviolet-Visible Spectroscopy

Ultraviolet-visible (UV-Vis) absorbance data was collected using a benchtop Jenway 6715 UV/Vis Spectrophotometer, data was then collected and transformed into graphs using Origin.

6.4.1.1 Photoresponsive Hydrogel Confirmation

UV-Vis studies measured wavelengths ranging from 350 to 800 nm. The baseline was collected with a clean glass microscope slide connected to the side of the cuvette holder. Samples were oriented on the side of the cuvette holder, in the direction that light penetrates the glass slide substrate, followed by the hydrogel, before reaching the detector.

6.4.1.2 Solutions

When using a plastic cuvette, UV-Vis studies measured wavelengths ranging from 340 to 800 nm. The baseline was collected with the solvent in a 1 cm × 1 cm 1 mL plastic cuvette.

When using a quartz cuvette, UV-Vis studies measured wavelengths ranging from 200 to 800 nm. The baseline was collected with the solvent in a 1 cm × 1 cm 1 mL quartz cuvette.

6.4.1.3 Hydrogel Deprotection Studies

UV-Vis studies measured wavelengths ranging from 200 to 800 nm. The baseline was collected with a clean glass microscope slide connected to the side of the cuvette holder.

Samples were oriented on the side of the cuvette holder, in the direction that light penetrates the glass slide substrate, followed by the hydrogel, before reaching the detector.

6.4.2 Forming Acrylamide Co-Monomer Hydrogels

To create the gel solution, nitrogen gas was bubbled through DI water (30 mL) for 30 minutes to remove oxygen air bubbles and to degas the water. DI water, 40% acrylamide (AAm) solution, *N*-(3-aminopropyl)methacrylamide hydrochloride (APMA) derivative, *N,N*-methylenebisacrylamide (BAAm), 10% ammonium persulfate (APS) solution and *N,N,N',N'*-tetraethylmethylenediamine (TEMED) were mixed together in different ratios, as displayed in Table 6.2.

***Table 6.2**: A table depicting the volumes and or masses of reagents used in the formation of hydrogels.*

Gel Type	40 % AAm (µL)	APMA Derivative (mg)	BAAm (mg)	10% APS (µL)	TEMED (µL)	DI H_2O (µL)
AAm/APMA	35.2	1.97	1.53	25	2.5	376.55
NVOC-APMA	38.5	0.82	0.67	15	7.5	1000.00

Hydrogels formed using NVOC-APMA also contained dimethylsulfoxide (DMSO) (182.5 µL) as an additive to increase the solubility of NVOC-APMA.

6.4.2.1 Hydrophilic Functionalisation of Glass Slides

Glass microscope slides were prepared and cleaned as described in Chapter 6.3.1. Glass petri dishes were functionalised with hexamethyldisilazane (HMDS) (50 µL) in toluene

(4.95 mL) for 10 minutes. Following this, the solution was disposed of, and the petri dishes washed with toluene before leaving to air dry. Then toluene (4.99 mL) and chloro(dimethyl)vinylsilane (CDMVS) (10 µL) were added to the petri dish. Cleaned glass slides were submerged in this solution for 30 minutes. The functionalised slides were then washed with toluene and allowed to air dry.

6.4.2.2 Hydrophobic Functionalisation of Glass Slides

Glass microscope slides were prepared and cleaned as described in Chapter 6.3.1. Glass petri dishes were functionalised with HMDS (50 µL) in toluene (4.95 mL) for 10 minutes. Following this, the solution was disposed of, and the petri dishes washed with toluene before leaving to air dry. Then toluene (4.95 mL) and trimethoxy(3,3,3-trifluoropropyl)silane (TMTFS) (50 µL) were added to the petri dish. Cleaned glass slides were submerged in this solution for 30 minutes. The functionalised slides were then washed with toluene and allowed to air dry. Once dry, these slides then had 0.005% 1.1 µm latex bead solution (1 µL) spotted at 8 points around the edge of the sides at equal distances (Figure 6.10). The addition of this solution resulted in the formation of the 1.1 µm spacer.

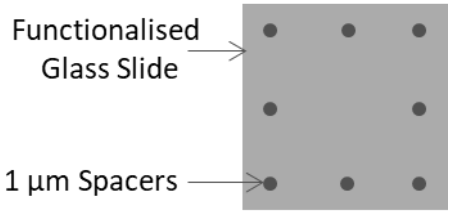

Figure 6.10: *An image displaying the distribution of 1.1 µm latex bead solution on the surface of a functionalised glass slide.*

6.4.2.3 Casting 1 µm Thick Acrylamide Co-Monomer Waveguide Films

To create a 1 µm thick film, the gel mixture of choice (50 µL) was aliquoted onto the centre of a CDMVS treated glass slide. A TMTFS treated glass slide was then placed on top of the solution and secured in place with a 500 g weight. The solutions were left to polymerise for 36 hours, following which the slides were immersed in DI water for 20 minutes before being separated. Occasionally this method led to surface imperfections on the slides. The LW films were then stored in 100 mM HEPES pH 7.4 buffer solution, prepared as described in Chapter 6.3.2, until use.

6.4.2.4 Casting 100 µm Thick Acrylamide Co-Monomer Waveguide Films

To create a 100 µm thick film, a 100 µm thick plastic spacer was sealed with silicon oil to the surface of a CDMVS-treated slide. This setup was then encompassed by two custom made plastic holders, that were screwed together as tightly as possible. Following this the hydrogel mixture of choice (500 µL) was injected from a syringe through a hole in the surface plastic to coat the slide underneath (Figure 6.11). Once gelation had occurred, the setup was dismantled, and the slide was stored in 100 mM HEPES pH 7.4 buffer solution.

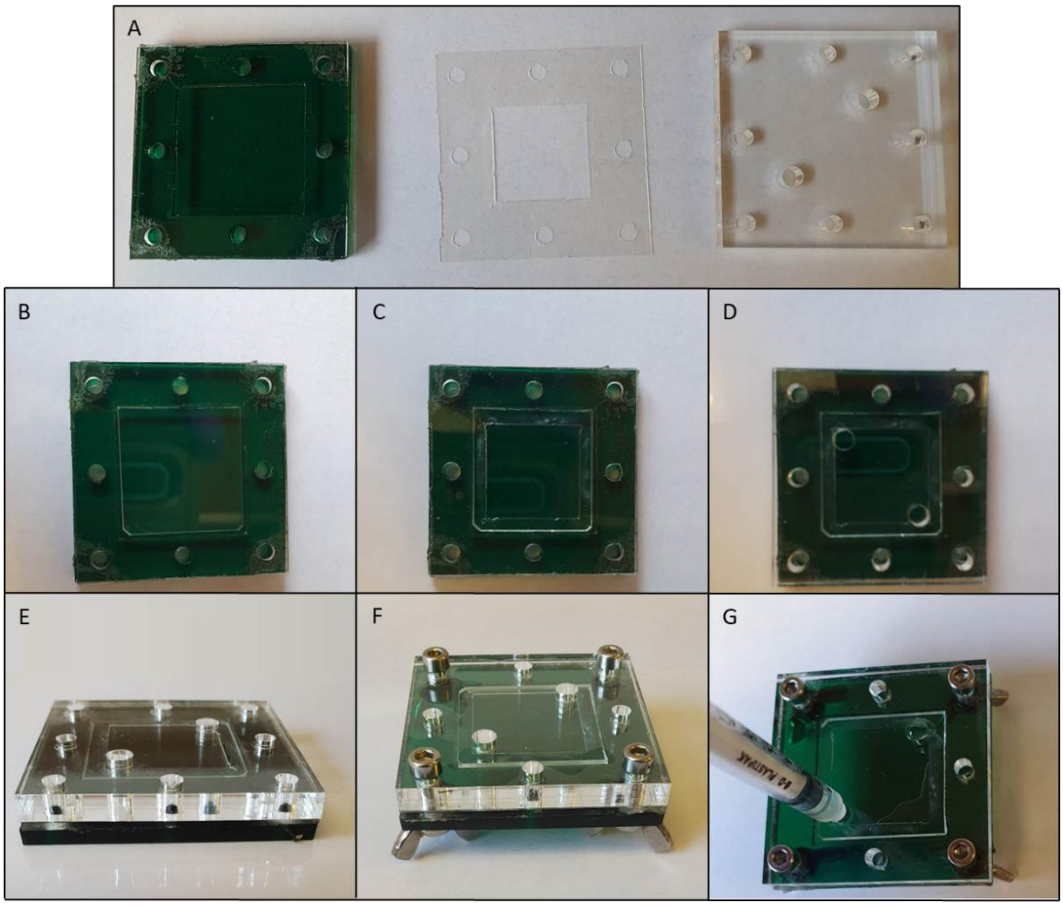

Figure 6.11: *Images displaying the setup for 100 µm thick hydrogel film formation. (A) the two parts of the custom-made plastic holder with plastic spacer in the middle. (B) the positioning of a glass substrate in the plastic holder. (C) the sealing of the spacer onto the glass substrate with silicon oil. (D) the addition of the top of the plastic holder. CAN a side view of the glass slide in the 100 µm spacer. (F) the screws which hold the spacer together. (G) the injection of polymer solution onto the surface of the glass substrate.*

6.4.3 LW Solvent Exchange Studies

The 1 µm thick AAm/APMA LW device was tested for refractive index sensitivity and porosity prior to use as described in Chapters 6.3.4 and 6.3.5 respectively. Following this, the film was submerged in DI water. After 90 minutes the solution was changed to be 90% DI water and 10% organic solvent, solvents of choice were methanol, 1,4-dioxane or DMSO. Every 90 minutes thereafter the solution decreased in DI water by 10% and increased in organic solvent by 10% until it was 100% organic solvent. Following this the reverse procedure

was used to return the environment to being 100% DI water. Finally, the functionality of the LW device was tested again using glycerol and PEG solutions *via* the same processes used earlier to determine if the organic solvent had an impact on the LW properties.

6.4.4 Photocaging of Hydrogels

The photocaging was conducted on 100 µm thick AAm/APMA hydrogel films. An AAm/APMA hydrogel film underwent a solvent exchange into DMSO. Once the hydrogel was in 100% DMSO, 4,5-dimethoxy-2-nitrobenzyl chloroformate (NVOC-Cl) and triethylamine were added to the solvent. This was then left to react for overnight at room temperature. Following this the photocaged hydrogel film was exchanged back into DI water. UV-Vis spectra were collected of the hydrogel films immediately following the reaction, then again following the transfer into DI water. UV-Vis studies are described in more detail in Chapter 0.

UV-Vis studies measured wavelengths ranging from 350 to 800 nm. The baseline was collected with a clean glass microscope slide connected to the side of the cuvette holder. Samples were oriented again on the cuvette holder, in the direction that light penetrates the glass slide substrate, followed by the hydrogel, before reaching the detector.

Semicarbazide hydrochloride (250 mg, 2.24 mmol) was dissolved in 100 mM HEPES pH 7.4 buffer solution (20 mL) with 1 M sodium hydroxide (2.24 mL) to create a semicarbazide deprotection solution. The hydrogel films were then placed in a glass petri dish and immersed in the semicarbazide solution for 1 hour. The hydrogels were then irradiated with 365 nm light for 40 minutes in the UV irradiation box (Chapter 6.2.5). The hydrogels were then washed with fresh 100 mM HEPES pH 7.4 buffer solution every 30 minutes for 6 hours.

To stain the deprotected regions for visualisation, they were tagged with fluorescein isothiocyanate. To do this they were submerged in a solution of fluorescein isothiocyanate (0.5 mg) in 100 mM HEPES pH 7.4 buffer solution (5 mL) for 40 minutes. Following this the hydrogels were again washed with fresh 100 mM HEPES pH 7.4 buffer solution every 30 minutes for 6 hours.

6.4.5 NVOC-APMA Hydrogel Studies

6.4.5.1 Synthesis of 4,5-dimethoxy-2-nitrobenzyl (3-methacrylamidopropyl)carbamate (NVOC-APMA)

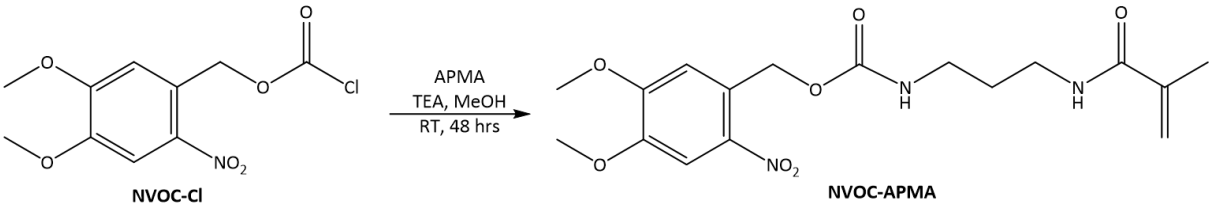

Scheme 6.1: *A reaction scheme showing the formation of* ***NVOC-APMA*** *from NVOC-Cl and APMA in methanol with the presence of triethylamine.*

A round bottom flask was charged with anhydrous methanol (30 mL), to this APMA (1.25 g, 7 mmol) was added. NVOC-Cl (1.8 g, 6.5 mmol) was dissolved in anhydrous methanol (40 mL) before being added to the aforementioned solution. Triethylamine (2.5 mL, 18 mmol) was added to the reaction mixture, then it was left to react at room temperature for 48 hours with magnetic stirring. The compound was concentrated under reduced pressure. The product was resuspended in dichloromethane (30 mL) and washed with DI water (3 × 10 mL). The dichloromethane solution was dried with anhydrous sodium sulfate. The solution was gravity filtered and the final compound was concentrated under reduced pressure to yield **NVOC-**

APMA (Scheme 6.1) as a yellow powder (1.652 g, 4.261 mmol, 65.6%) which was used without further purification.

M.P. 112 – 118 °C. **IR neat (cm^{-1}):** 3497*w* (N-H), 3343*m* (N-H), 2937*w* (N-H), 1693*s* (C=O), 1649*w* (C=C), 1609*m* (C=O), 1583*w* (C=C, arom.), 1512*s* (N-O), 1462*m* (C-H), 1428*m* (C=C, arom.), 1375*m* (C-H), 1327*m* (N-O), 1269*s* (C-O), 1215*s* (C=O), 1162*s* (C-O), 1143*m* (C-N), 1062*s* (C-N), 1037*s* (C-N), 984m (=C-H), 929*w* (=C-H), 871m (C-H, arom.). **^{1}H NMR** (400 MHz, DMSO) δ 7.70 (s, 1H), 7.19 (s, 1H), 5.63 (s, 1H), 5.33 (s, 2H), 5.31 (s, 1H), 3.90 (s, 3H), 3.88 (s, 3H), 3.13 (q, *J* = 6.7 Hz, 2 H), 3.03 (q, *J* = 6.6 Hz, 2H), 1.85 (s, 3H), 1.60 (p, *J* = 6.9 Hz, 2H). **^{13}C NMR** (101 MHz, DMSO) δ 167.91, 156.15, 148.17, 140.46, 139.80, 134.65, 128.33, 119.31, 111.07, 62.76, 56.66, 38.58, 36.96, 29.90, 19.10. **MS (ESI) *m/z*** calculated for $C_{17}H_{23}N_3O_7$: 381.385, found: $[M + Na]^+$ 404.14.

6.4.5.2 NVOC-APMA Photopatterning

The NVOC-APMA hydrogel was formed in a sample vial according to Chapter 6.4.2. Following this, the hydrogel was submerged in a semicarbazide deprotection solution, as described in Chapter 6.4.4, for 1 hour. Once the hydrogel was saturated with deprotecting solution, it was exposed to 365 nm light through a photomask for a further 40 minutes in the UV irradiation box (Chapter 6.2.5) The hydrogel was then washed with fresh 100 mM HEPES pH 7.4 buffer solution every 30 minutes for 6 hours.

To stain the deprotected regions for visualisation (Figure 6.12), they were tagged with a solution of fluorescein isothiocyanate (0.5 mg) in 100 mM HEPES pH 7.4 buffer solution (5 mL) for 40 minutes. Following this the hydrogels were again washed with fresh 100 mM HEPES pH 7.4 buffer solution every 30 minutes for 6 hours.

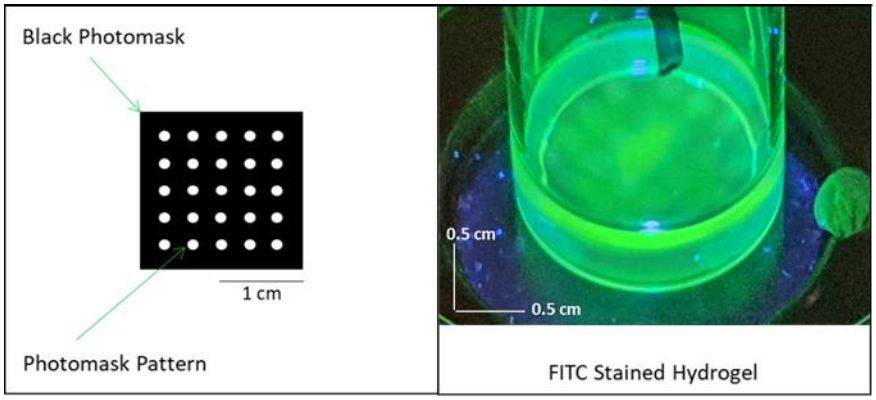

Figure 6.12: *An image depicting the photomask used (left) and the resulting photopatterned hydrogel in which the deprotected areas are stained with FITC (right).*

6.4.6 *N*-(3-((4,5-bis(2-(2-(2-methoxyethoxy)ethoxy)ethoxy)-2-nitrobenzyl)amino)propyl) methacrylamide (NB-6a)

6.4.6.1 Synthesis of 2-(2-(2-methoxyethoxy)ethoxy)ethyl-4-methylbenzenesulfonate (NB-1)

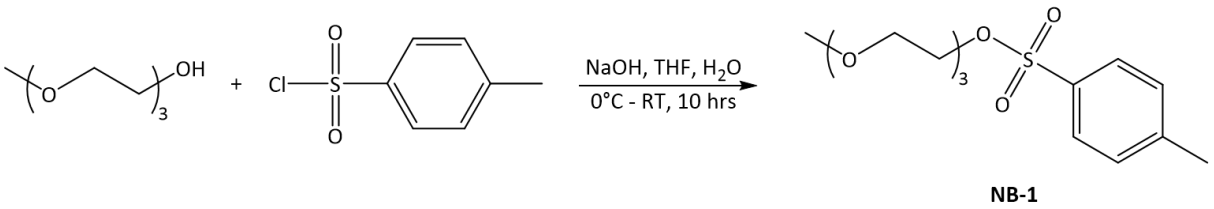

Scheme 6.2*: A reaction scheme depicting the protecting of the primary alcohol in triethylene glycol monomethyl ether with p-toluenesulfonyl chloride in tetrahydrofuran and DI water, initiated by sodium hydroxide to form* ***NB-1****.*

To a round bottom flask, sodium hydroxide (2.575 g, 64.4 mmol) in DI water (4 mL) was added. To this, triethylene glycol monomethyl ether (8.21 g, 50 mmol) in tetrahydrofuran (4 mL) was added and the resultant solution cooled to 0 °C. Following this, *p*-toluenesulfonyl chloride (9.53 g, 53.5 mmol) in tetrahydrofuran (16 mL) was added to the solution over a period of 30 minutes. Following this, the reaction mixture was left to stir for 10 hours while

being left to reach room temperature. To quench the reaction, DI water (20 mL) was added, and the resulting solution was acidified with sulfuric acid (3 mL). The product was extracted with dichloromethane (2 × 20 mL), this solution in turn was washed with DI water (3 × 20 mL) and dried with anhydrous sodium sulfate. The solution was gravity filtered and the final solution was concentrated under reduced pressure to yield **NB-1** (Scheme 6.2) as a colourless liquid (13 g, 40.832 mmol, 81.7%) which was used without further purification.

IR neat (cm^{-1}): 2876*m* (br., C-H), 1598*w* (C=C, arom.), 1452*m* (C-H), 1353*s* (S=O), 1292*w* (C-O), 1247*w* (C-O), 1189*m* (S=O), 1175*s* (S=O), 1096*s* (C-O), 1017*m* (C-O), 917*s* (C=C, arom.), 816*m* (C-H, arom.). **^{1}H NMR** (400 MHz, $CDCl_3$) δ 7.65 (t, 2H), 7.22 (t, *J* = 8.1 Hz, 2H), 4.03 (t, *J* = 10.5 Hz, 2H), 3.64 – 3.32 (m, 10H), 3.20 (s, 3H), 2.29 (s, 3H). **^{13}C NMR** (101 MHz, $CDCl_3$) δ 144.58, 132.66, 129.60, 127.61, 70.17, 69.10, 68.29, 58.62, 21.28. **MS (ESI) *m/z*** calculated for $C_{14}H_{22}O_6S$: 318.38, found: $[M + NH_4]^+$ 336.15.

6.4.6.2 Synthesis of 3,4-bis(2-(2-(2-methoxyethoxy)ethoxy)ethoxy) benzaldehyde (NB-2)

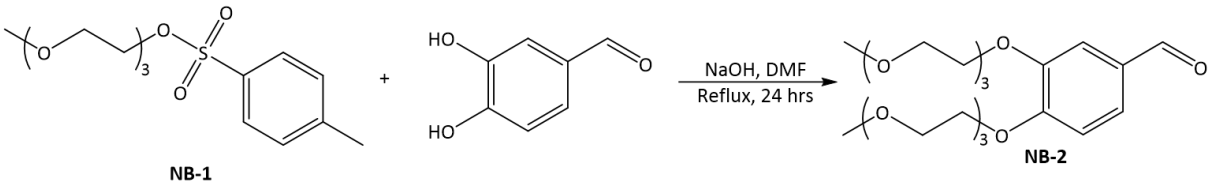

***Scheme 6.3**: A reaction scheme displaying the sodium hydroxide and heat initiated ether formation between **NB-1** and 3,4-dihydroxybenzaldehyde in N,N-dimethylformamide.*

To a round bottom flask, 3,4-dihydroxybenzaldehyde (2.5 g, 18 mmol), **NB-1** (12.74 g, 40 mmol) and sodium hydroxide (3.2 g, 80 mmol) were added to *N,N*-dimethylformamide (25 mL) and stirred at 90 °C for 16 hours. Following this period, the solution was left to cool to

room temperature, before being extracted with dichloromethane (2 × 15 mL). The dichloromethane solution was washed with a saturated sodium bicarbonate solution (3 × 10 mL), DI water (3 × 10 mL) and brine (10 mL) and was then dried with anhydrous sodium sulfate. The solution was gravity filtered and the final compound was concentrated under reduced pressure to yield **NB-2** (Scheme 6.3) as an orange oil (6.845 g, 15.9 mmol, 88.3%).

IR neat (cm^{-1}): 2873*m* (br., C-H), 1735*w* (C=O), 1684*s* (C=O), 1595*m* (C=C, arom.), 1584*m* (C=C, arom.), 1508*m* (C=C, arom.), 1452*w* (C-H), 1435*m* (C=C, arom.), 1396*w* (C-H), 1351*w* (C-H), 1265*s* (C-O), 1240*s* (C-O), 1199*w* (C-O), 1168*m* (C-O), 1100*s* (C-O), 1046*s* (C-O). 942*m*, 850*m* (C-H, arom.), 811*m* (C-H, arom.). **^{1}H NMR** (400 MHz, $CDCl_3$) δ 9.72 (s, 1H), 7.34 (d, *J* = 8.1 Hz, 2H), 6.92 (t, *J* = 8.7 Hz, 1H), 4.22 – 4.07 (m, 4H), 3.89 – 3.76 (m, 4H), 3.71 – 3.41 (m, 16H), 3.26 (s, 6H). **^{13}C NMR** (101 MHz, $CDCl_3$) δ 190.58, 170.80, 154.12, 148.93, 130.00, 126.37, 112.34, 111.73, 71.68, 70.66, 70.29, 69.18, 68.47, 60.07, 58.74, 20.78, 13.98. **MS (ESI) *m/z*** calculated for $C_{21}H_{34}O_9$: 430.49, found: $[M + NH_4]^+$ 448.26.

6.4.6.3 Synthesis of 4,5-bis(2-(2-(2-methoxyethoxy)ethoxy)ethoxy)-2-nitrobenzaldehyde (NB-3)

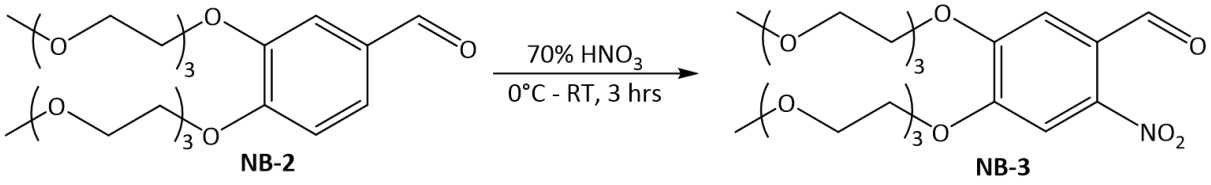

***Scheme 6.4**: A reaction scheme displaying the nitration of **NB-2** in the presence of nitric acid to form **NB-3**.*

To a round bottom flask nitric acid (70%, 10 mL) was added and cooled to 0 °C. To this, **NB-2** (0.861 g, 2 mmol) was added, the mixture was stirred and allowed to reach room

temperature for 3 hours. Following this, the reaction mixture was diluted with DI water (20 mL) and extracted with dichloromethane (20 mL). The dichloromethane layer was washed with DI water (3 × 10 mL), and brine (2 × 10 mL), before being dried with anhydrous sodium sulfate. The solution was gravity filtered and the final compound was concentrated under reduced pressure to yield **NB-3** (Scheme 6.4) as an orange oil (0.815 g, 1.713 mmol. 85.7%).

IR neat (cm^{-1}): 2876*m* (C-H), 1735*w* (C=O), 1688*m* (C=O), 1600*w* (C=C, arom.), 1571*m* (C=C), arom.), 1516*s* (N-O), 1452*m* (C-H, arom.), 1400*w* (C-H), 1334*s* (C-N), 1279*s* (C-O), 1243*s* (C-O), 1221*s* (C-O), 1200*m* (C-O), 1098*s* (C-O), 1060*s* (C-O), 948*m*, 850*s* (C-H, arom.), 802*m* (C-H, arom.). **^{1}H NMR** (400 MHz, $CDCl_3$) δ 10.35 (s, 1H), 7.64 (s, 1H), 7.38 (s, 1H), 4.30 – 4.23 (m, 5H), 3.72 – 3.67 (m, 7H), 3.63 – 3.57 (m, 15H), 3.31 (s, 6H). **^{13}C NMR** (101 MHz, $CDCl_3$) δ 187.77, 171.23, 154.50, 143.79, 125.59, 111.48, 109.22, 71.03, 70.73, 69.55, 60.45, 59.06, 21.10, 14.25. **MS (ESI) *m/z*** calculated for $C_{21}H_{33}NO_{11}$: 475.49, found: $[M + NH_4]^+$ 493.24.

6.4.6.4 Synthesis of (4,5-bis(2-(2-(2-methoxyethoxy)ethoxy)ethoxy)-2-nitrophenyl)methanol (NB-4)

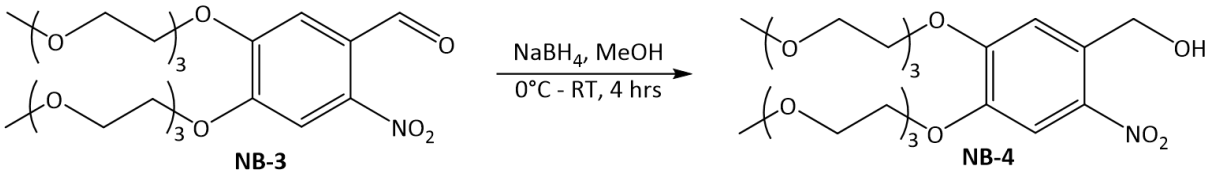

Scheme 6.5*: A reaction scheme showing the reduction of **NB-3** with sodium borohydride in methanol to form **NB-4**.*

To a round bottom flask a solution of **NB-3** (0.951 g, 2 mmol) in methanol (10 mL) was added. To this sodium borohydride (0.114 g, 3 mmol) was slowly added. This mixture was left to stir at room temperature for 4 hours. Following this the reaction mixture was concentrated

under reduced pressure. To the residue, DI water (20 mL) and dichloromethane (20 mL) were added. The dichloromethane layer was washed with DI water (2 × 10 mL) and brine (2 × 10 mL), before being dried with anhydrous sodium sulfate. The solution was gravity filtered and the final compound was concentrated under reduced pressure to yield **NB-4.** The crude product was purified by flash chromatography, with a solvent system of 9:1 dichloromethane:methanol. The desired fractions were collected and combined and concentrated under reduced pressure to yield pure **NB-4** (Scheme 6.5) as a red oil (0.757 g, 1.586 mmol, 79.3%).

IR neat (cm^{-1}): 2878*m* (br., C-H), 1514*m* (N-O), 1452*w* (C-H), 1351*m* (N-O), 1276*s* (C-H), 1243*w* (C-O), 1190*m* (C-O), 1177*m* (C-O), 1102*s* (C-O), 1056*s* (C-O), 990*w*, 924*m* (C-H, arom.), 850*m* (C-H, arom.), 806*m* (C-H, arom.). **^{1}H NMR** (400 MHz, DMSO) δ 7.67 (s, 1H), 7.31 (s, 1H), 4.91 (d, *J* = 2.7 Hz, 1H), 4.20 – 4.13 (m, 2H), 3.90 – 3.81 (m, 5H), 3.74 – 3.66 (m, 4H), 3.65 – 3.58 (m, 10H), 3.54 – 3.46 (m, 5H), 3.32 (d, *J* = 3.6 Hz, 6H). **^{13}C NMR** (101 MHz, $CDCl_3$) δ 171.22, 153.86, 147.03, 139.13, 133.77, 127.97, 112.06, 71.89, 70.68, 70.55, 70.45, 69.65, 62.10, 60.42, 59.02, 21.06, 14.21. **MS (ESI) *m/z*** calculated for $C_{21}H_{35}NO_{11}$: 477.506, found: $[M + NH_3]^+$ 495.29

6.4.6.5 1-(chloromethyl)-4,5-bis(2-(2-(2-methoxyethoxy)ethoxy)ethoxy)-2-nitrobenzene (NB-5a)

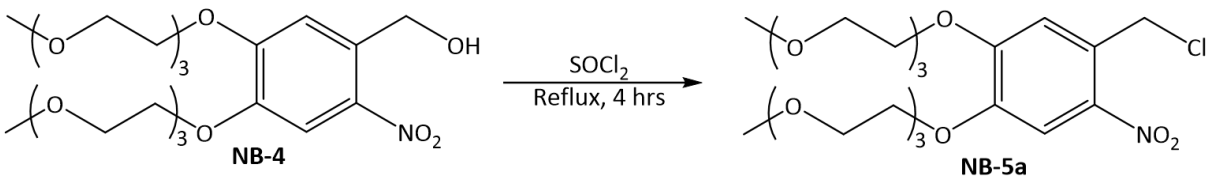

***Scheme 6.6**: A reaction scheme depicting the chlorination of **NB-4** with thionyl chloride while heating to form **NB-5a**.*

A round bottom flask was charged with thionyl chloride (15 mL). To this, **NB-4** (0.955 g, 2 mmol) was slowly added. The round bottom flask was connected to a reflux condenser and heated to reflux for 4 hours. Thionyl chloride and the sulfur dioxide by-product were removed *via* evaporation under reduced pressure to yield the product **NB-5a** (Scheme 6.6) as a red oil, which was used immediately without further purification.

6.4.6.6 N-(3-((4,5-bis(2-(2-(2-methoxyethoxy)ethoxy)ethoxy)-2-nitrobenzyl)amino)propyl)methacrylamide (NB-6a)

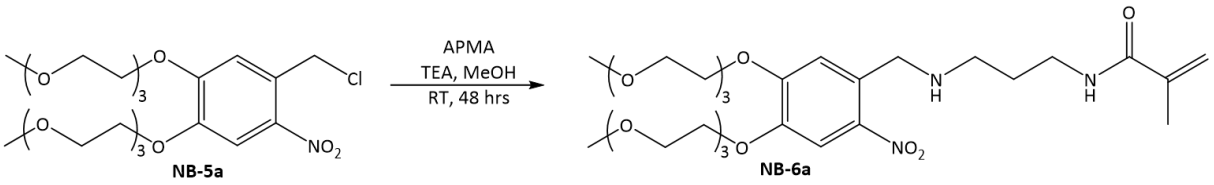

***Scheme 6.7**: A reaction scheme showing the formation of **NB-6a** from **NB-5a** and APMA in methanol with the presence of triethylamine.*

NB-5a (0.992 g, 2 mmol) was used without further purification and dissolved in methanol (20 mL) in a round bottom flask. To this solution, APMA (0.39 g, 2.2 mmol) was added, followed by the slow addition of triethylamine (1 mL, 7.17 mmol). This reaction mixture was allowed to stir at room temperature overnight. Following this, the solvent and remaining base were evaporated under reduced pressure, before recrystallising the crude product in tetrahydrofuran. The salt impurities were removed *via* filtration under vacuum prior to concentration under reduced pressure to give **NB-6a** (0.825 g, 1.371 mmol, 68.6%). The crude compound was then purified by reversed-phase high performance liquid chromatography (RP-

HPLC) under the conditions displayed below (Table 6.3) to yield the final product **NB-6a** (Scheme 6.7) as a red oil (54.5%).

***Table 6.3**: A table showing the times when changes in solvent concentration occurred in the RP-HPLC purification of **NB-6a**.*

Time (mins)	HPLC Water (%)	Methanol (%)
0	65	35
30	0	100
35	0	100
35.1	65	35
40	65	35

λmax(H_2O)/nm 365 (ε/dm^3 mol^{-1} cm^{-1} 2845.53). **IR neat (cm^{-1}):** 2875*m* (br., C-H), 1736*w* (C=O), 1677*w* (C=C, arom.), 1596*w* (N-H), 1512*m* (N-O), 1452*m* (C=C, arom.), 1339*m* (N-O), 1288*s* (C-O), 1244*m* (C-O), 1197*m* (C-O) 1177*s* (C-O), 1098*s* (C-N), 1050*s* (C-N), 923*m* (=C-H), 850*m* (C-H, arom.), 818*m* (=C-H). **^{1}H NMR** (400 MHz, $CDCl_3$) δ 7.72 (s, 0H), 7.53 (s, 1H), 7.20 (s, 1H), 5.64 (s, 1H), 5.22 (d, *J* = 1.7 Hz, 1H), 4.17 – 4.13 (m, 4H), 3.87 – 3.78 (m, 6H), 3.69 – 3.65 (m, 7H), 3.49 – 3.45 (m, 9H), 3.29 (s, 8H), 3.22 (s, 2H), 2.77 (t, *J* = 6.3 Hz, 1H), 1.89 – 1.84 (m, 3H), 1.68 – 1.58 (m, 1H). **^{13}C NMR** (101 MHz, DMSO) δ 168.58, 152.55, 148.11, 140.97, 139.78, 128.04, 111.19, 110.51, 100.05, 70.58, 69.42, 69.23, 69.18, 68.82, 58.93, 54.85, 39.50, 37.84, 30.66, 18.60. **MS (ESI) *m/z*** calculated for $C_{28}H_{47}N_3O_{11}$: 601.694, found: $[M + H]^+$ 602.33.

6.4.7 Synthesis of 4,5-bis(2-(2-(2-methoxyethoxy)ethoxy)ethoxy)-2-nitrobenzyl (3-acrylamidopropyl)carbamate (NB-6b)

6.4.7.1 Synthesis of 4,5-bis(2-(2-(2-methoxyethoxy)ethoxy)ethoxy)-2-nitrobenzyl carbonochloridate (NB-5b)

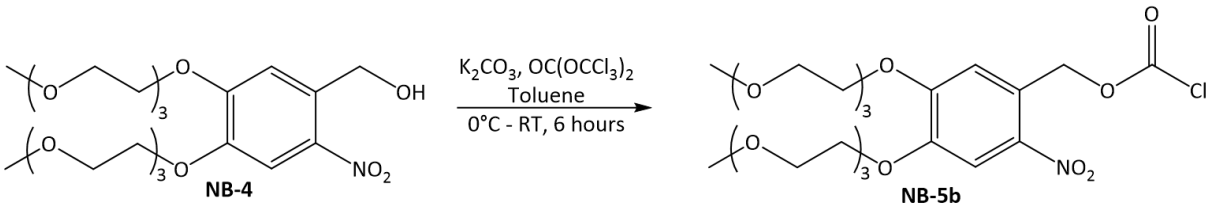

***Scheme 6.8**: A reaction scheme displaying the formation of a chloroformate group using **NB-4** and triphosgene in the presence of potassium carbonate and toluene.*

Dried potassium carbonate (2.49 g, 18 mmol) was added to a round bottom flask and cooled to 0 °C in an ice bath. To this a solution of triphosgene (1.19 g, 4 mmol) in toluene (10 mL) was added and left to stir for 30 minutes. Following this a solution of **NB-4** (0.955 g, 2 mmol) in toluene (10 mL) was added to the round bottom flask and stirred at room temperature for 5 hours. To this solution chloroform (10 mL) was added, the mixture was filtered and concentrated under reduced pressure to yield the final product **NB-5b** (Scheme 6.8) as a red oil, which was used immediately without further purification.

6.4.7.2 Synthesis of 4,5-bis(2-(2-(2-methoxyethoxy)ethoxy)ethoxy)-2-nitrobenzyl (2-acrylamidopropyl)carbamate (NB-6b)

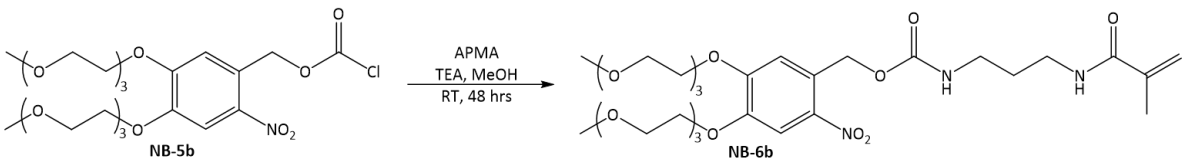

***Scheme 6.9**: A reaction scheme showing the formation of **NB-6b** from **NB-5b** and APMA in methanol with the presence of triethylamine.*

NB-5b was used immediately as collected from the previous step. A solution of APMA (0.39 g, 2.2 mmol) and triethylamine (1 mL, 7.17 mmol) in methanol (20 mL) was added to a round bottom flask. **NB-5b** (1.29 g, 2 mmol) was added dropwise to the aforementioned solution, this reaction mixture was stirred at room temperature overnight. Following this, the solution was concentrated under reduced pressure. The reagents were recrystallised in tetrahydrofuran. Insoluble salts were collected *via* vacuum filtration prior to concentration under reduced pressure to yield crude **NB-6b** (0.924 g, 1.431 mmol, 71.6%). The crude compound was then purified by RP-HPLC under the conditions displayed below (Table 6.4) to yield the final product **NB-6b** (Scheme 6.9) as a red oil (48%).

***Table 6.4**: A table showing the times when changes in solvent concentration occurred in the RP-HPLC purification of **NB-6b**.*

Time (mins)	HPLC Water (%)	Methanol (%)
0	65	35
30	0	100
35	0	100
35.1	65	35
40	65	35

λmax(H_2O)/nm 365 (ε/dm^3 mol^{-1} cm^{-1} 3781.68). **IR neat (cm^{-1}):** 3319*m* (N-H), 2977*m* (N-H), 1692*s* (C=O), 1656*m* (C=O), 1601*s* (N-H), 1532*m* (N-O), 1475*m* (C-H), 1449*s* (C=C, arom.), 1434*s* (C=C, arom.), 1393*m* (C-H), 1348*m* (N-O), 1324*m* (C=O), 1303*m* (C-O), 1246*m* (C-H), 1191*s* (C-O), 1118*m* (C-N), 1102*m* (C-N), 1088*m* (C-O), 1021*m* (C-O), 934*m* (=C-H), 908*m* (=C-

H), 894*m* (=C-H), 841*s* (C-H, arom.), 814*m* (C-H, arom.). **^{1}H NMR** (400 MHz, DMSO) δ 8.11 (d, *J* = 2.1 Hz, 0H), 8.09 (d, *J* = 2.1 Hz, 0H), 7.73 (s, 1H), 7.42 (s, 1H), 6.87 (d, *J* = 0.8 Hz, 1H), 5.75 – 5.62 (m, 1H), 5.38 – 5.27 (m, 1H), 4.83 (s, 2H), 4.31 – 4.17 (m, 4H), 3.79 (dt, *J* = 14.1, 1.5 Hz, 3H), 3.52 – 3.50 (m, 16H), 3.24 (s, 4H), 3.22 (s, 6H), 3.06 (s, 0H), 2.18 (s, 2H), 1.88 – 1.84 (m, 3H). **^{13}C NMR** (101 MHz, DMSO) δ 153.58, 151.94, 146.71, 139.67, 134.78, 128.50, 126.63, 125.37, 116.32, 111.50, 110.37, 71.74, 70.49, 70.25, 70.06, 69.27, 69.04, 60.55, 58.49, 45.85, 34.84, 21.49, 19.10.

6.4.8 Synthesis of *N*-(3-(((3-nitrodibenzo[*b,d*]furan-2-yl)methyl)amino)propyl) methacrylamide (DBF-5)

6.4.8.1 Synthesis of dibenzo[b,d]furan-2-carbaldehyde (DBF-1)

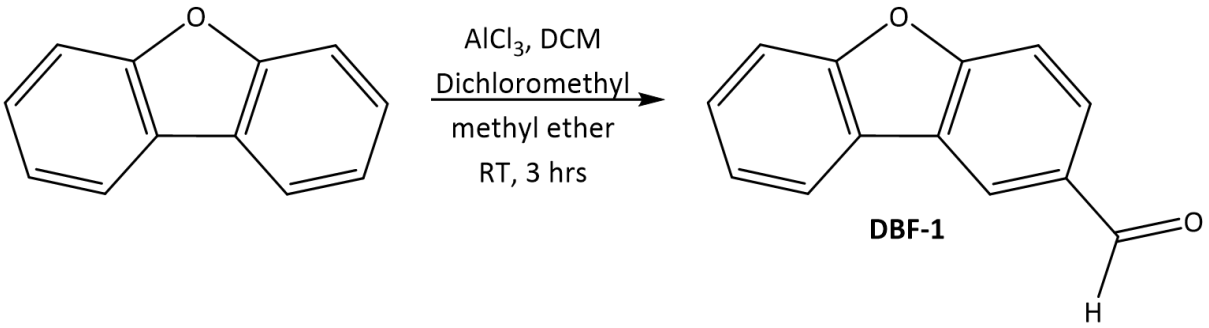

***Scheme 6.10**: A reaction scheme showing the Rieche Formylation of DBF through the addition of aluminium chloride and dichloromethyl methyl ether in dichloromethane.*

In a round bottom flask, dibenzofuran (2.5 g, 14.864 mmol) was dissolved in dichloromethane (50 mL). To this, ground aluminium chloride (3 g, 22.5 mmol) was slowly added followed by dichloromethyl methyl ether (2.015 mL, 22.3 mmol) and stirred vigorously for 5 minutes. This was left to stir at room temperature for 3 hours. Following this, 1 M hydrochloric acid (50 mL) was then added and proceeded to stir at room temperature for 10

minutes. The organic phase was collected in a separating funnel, then the aqueous phase was washed with dichloromethane (50 mL). The organic layers were washed with DI H_2O (50 mL), saturated sodium hydrogen carbonate solution (30 mL) and brine (30 mL) before being dried over anhydrous sodium sulfate. This solution was then gravity filtered before being evaporated to dryness under reduced pressure to yield the crude product. This was purified by flash chromatography, with a solvent system of 94:6 hexane:ethyl acetate. The desired fractions were collected and combined, before concentration under reduced pressure to yield pure **DBF-1** (Scheme 6.10) as a yellow powder (2.425 g, 12.36 mmol, 83.2%).

M.P. 78 – 81 °C. **IR neat (cm^{-1}):** 3048*m* (C-H, arom.), 1940*w* (C=C, arom.), 1896*w* (C=C, arom.), 1867*w* (C=C, arom.), 1823*w* (C=C, arom.), 1783*w* (C=C, arom.), 1691*s* (C=O), 1596*m* (C=C, arom.), 1587*m* (C=C, arom.), 1472*m* (C-H), 1444*s* (C=C, arom.), 1347*m* (C-H), 1322*m*, 1308*m* (C=O), 1283*m* (C-O), 1241*m* (C-O), 1191*s*, 1153*s*, 1114*m*, 1100*s*, 1021*m*, 998*m* (C-H, arom.), 927*m* (C-H, arom.), 908*w* (C-H, arom.), 865*m* (C-H, arom.), 848*s* (C-H, arom.), 840*s* (C-H, arom.). **^{1}H NMR** (400 MHz, $CDCl_3$) δ 10.12 (s, 1H) 8.49 (d, *J* = 1.6 Hz, 1H), 8.02 (d, *J* = 1.8 Hz, 1H), 8.00 (d, *J* = 1.9 Hz, 1 H), 7.56 (s, 1H), 7.45 (d, *J* = 1.3 Hz, 1H), 7.43 (t, *J* = 1.4 Hz, 1H), 7.34 (d, *J* = 1.0 Hz, 1H). **^{13}C NMR** (101 MHz, $CDCl_3$) δ 191.45, 123.05, 122.69, 121.12, 120.66, 112.35, 112.07, 111.68. **MS (ESI) *m/z*** calculated for $C_{13}H_8O_2$: 196.205, found: $[M + H]^+$ 197.06.

6.4.8.2 Synthesis of 3-nitrodibenzo[b,d]furan-2-carbaldehyde (DBF-2)

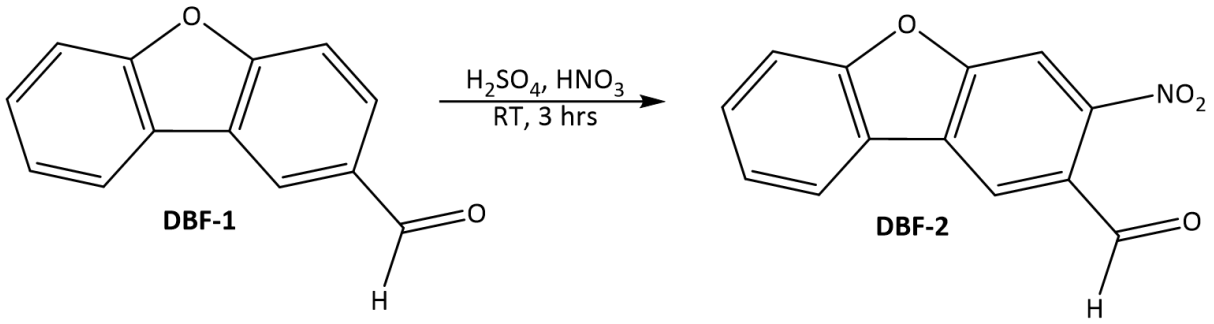

Scheme 6.11*: A reaction scheme displaying the nitration of* ***DBF-1*** *in the presence of nitric acid and sulfuric acid to form* ***DBF-2****.*

To a round bottom flask nitric acid (70%, 10 mL) and sulfuric acid (10 mL) were added and cooled to 0 °C. To this, **DBF-1** (1.96 g, 10 mmol) was added, the mixture was stirred and allowed to reach room temperature for 3 hours. Following this, the reaction mixture was diluted with DI water (50 mL) and extracted with ethyl acetate (50 mL). The ethyl acetate layer was washed with DI water (3 × 30 mL), and brine (2 × 30 mL), before being dried with anhydrous sodium sulfate. The solution was gravity filtered and the final solution was concentrated under reduced pressure to yield crude **DBF-2.** The crude product was purified by flash chromatography, with a solvent system of 9:1 hexane:ethyl acetate. The desired fractions were collected and combined and concentrated under reduced pressure to yield pure **DBF-2** (Scheme 6.11) as an orange powder (1.95 g, 8.067 mmol, 80.7%).

M.P. 138 – 142 °C. **IR neat (cm^{-1}):** 3096*w* (C-H, arom.), 1691*s* (C=O), 1654*w* (C=C, arom.), 1632*w* (C=C, arom.), 1594*w* (C=C, arom.), 1520*s* (N-O), 1469*m* (C=C, arom.), 1420*w* (C-H), 1341*s* (N-O), 1247*m* (C-O), 1197*s* (C-O), 1118*m*, 1063*m*, 1021*m*, 969*w* (C-H, arom.), 879*m* (C-H, arom.), 820*s* (C-H, arom.). **^{1}H NMR** (400 MHz, DMSO) δ 10.13 (s, 1H), 8.78 (d, *J* = 10.1 Hz, 1H), 8.67 (s, 1H), 8.11 (s, 1H), 7.80 (d, *J* = 3.1 Hz, 1H), 7.48 (s, 1H). **^{13}C NMR** (101 MHz, DMSO)

δ 192.63, 156.64, 132.58, 130.23, 129.78, 129.07, 128.87, 124.33, 124.12, 123.98, 122.28, 112.95, 112.46. **MS (ESI) *m/z*** calculated for $C_{13}H_7NO_4$: 241.202, found: $[M + H]^+$ 242.05.

6.4.8.3 Synthesis of (3-nitrodibenzo[b,d]furan-2-yl)methanol (DBF-3)

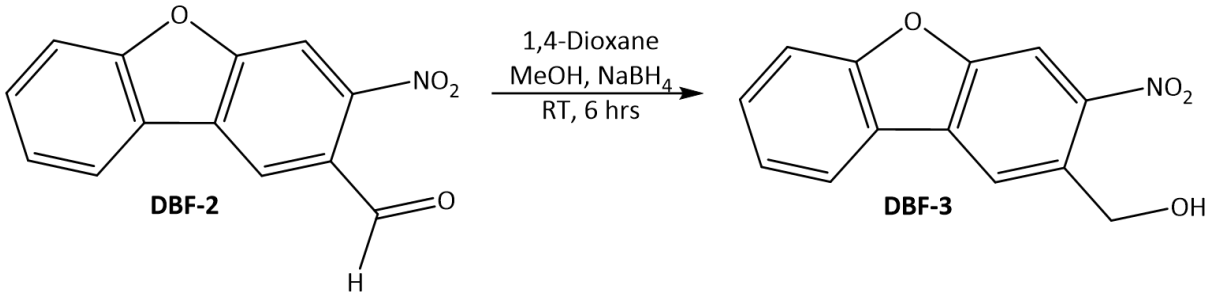

***Scheme 6.12**: A reaction scheme showing the reduction of **DBF-2** with sodium borohydride in methanol and 1,4-dioxane to form **DBF-3**.*

To a round bottom flask a solution of **DBF-2** (2.41 g, 10 mmol) in methanol (25 mL) and 1,4-dioxane (25 mL) was added. The reaction mixture was then cooled to 0 °C, to allow for the slow addition of sodium borohydride (0.57 g, 15 mmol). The reaction then proceeded to stir at room temperature for 6 hours. Following this the reaction mixture was concentrated under reduced pressure, before being recrystallised and hot filtered in dichloromethane (30 mL). The solution was then dried with anhydrous sodium sulfate, filtered then concentrated under reduced pressure to yield impure **DBF-3**. This product was purified by flash chromatography, with a solvent system of 9:1 hexane:ethyl acetate. The desired fractions were collected and combined and concentrated under reduced pressure to yield pure **DBF-3** (Scheme 6.12) as an orange powder (1.756 g, 7.22 mmol, 72.2 %).

IR neat (cm^{-1}): 3367*m* (br., O-H), 3101*m* (C-H, arom.), 1690*w* (C=O), 1632*m* (C=C, arom.), 1604*m* (C=C, arom.), 1521*s* (N-O), 1480*s* (C=C, arom.), 1458*s* (C=C, arom.), 1422*m* (C-

H), 1339*s* (N-O), 1249*s* (C-O), 1232*s* (C-O), 1199*s*, 1120*s*, 1062*s* (C-O), 1018*s*, 930*m* (C-H, arom.), 892*s* (C-H, arom.), 875*s* (C-H, arom.), 846*s* (C-H, arom.), 820*s* (C-H, arom.). **^{1}H NMR** (400 MHz, DMSO) δ 8.76 (d, *J* = 11.0 Hz, 1H), 8.68 (s, 1H), 8.24 (s, 1H), 8.16 (d, *J* = 6.5 Hz, 1H), 7.67 (s, 1H), 7.53 (s, 1H), 5.77 (s, 1H), 5.56 (s, 1H), 2.09 (s, 0H). **^{13}C NMR** (101 MHz, DMSO) δ 156.28, 133.86, 128.18, 126.64, 124.09, 123.66, 123.56, 121.80, 119.80, 112.14, 111.71, 103.17, 53.05. **MS (ESI) *m/z*** calculated for $C_{13}H_9NO_4$: 243.218, found: $[M + CAN]^+$ 284.29.

6.4.8.4 Synthesis of 2-(chloromethyl)-3-nitrodibenzo[b,d]furan (DBF-4)

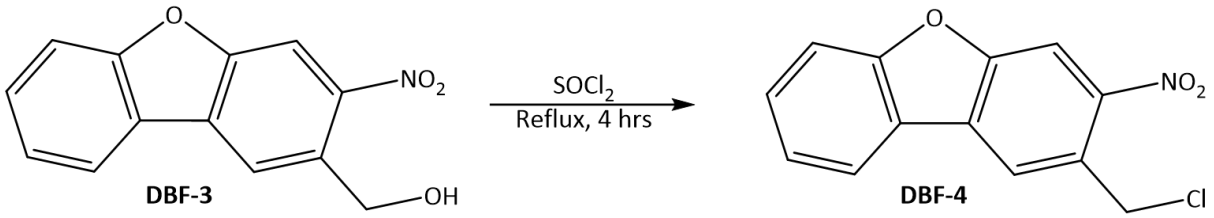

***Scheme 6.13**: A reaction scheme depicting the chlorination of **DBF-3** with thionyl chloride while heating to form **DBF-4**.*

A round bottom flask was charged with thionyl chloride (20 mL). To this, **DBF-3** (2.432 g, 10 mmol) was slowly added. The round bottom flask was connected to a reflux condenser and heated to reflux for 4 hours. Thionyl chloride and the sulfur dioxide by-product were removed *via* evaporation under reduced pressure to yield the product **DBF-4** (Scheme 6.13) as a red oil which was used immediately without further purification.

6.4.8.5 Synthesis of N-(3-(((3-nitrodibenzo[b,d]furan-2-yl)methyl)amino)propyl)methacrylamide (DBF-5)

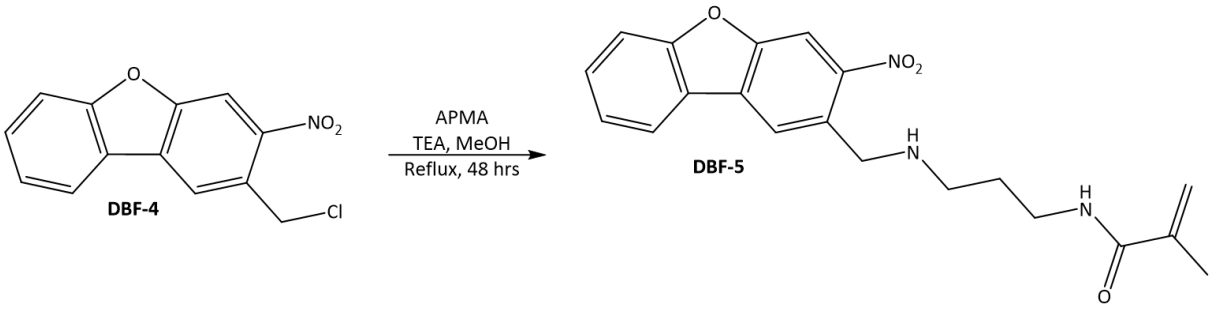

***Scheme 6.14**: A reaction scheme showing the formation of **DBF-5** from **DBF-4** and APMA in methanol with the presence of triethylamine.*

DBF-4 was used unpurified immediately from the previous step. A solution of APMA (1.97 g, 11 mmol) and triethylamine (5 mL, 35.85 mmol) in methanol (50 mL) was added to a round bottom flask. **DBF-4** was added dropwise to the aforementioned solution, this reaction mixture was stirred at room temperature for 48 hours. Following this, the solution was concentrated under reduced pressure. The reagents were recrystallised in tetrahydrofuran, insoluble salts were removed via vacuum filtration prior to concentration under reduced pressure. This yielded the final product **DBF-5** (Scheme 6.14) as a dark red oil (1.575 g, 4.286 mmol, 42.9%) however further purification is required.

Λmax(H_2O)/nm (ε/dm^3 mol^{-1} cm^{-1} 266.80). **IR neat (cm^{-1}):** 3330*w* (N-H), 2876*m* (N-H), 1717*w* (C=O), 1660*w* (C=C, arom.), 1616*m* (C=C), 1580*w* (N-H), 1518*s* (N-O), 1452*m* (C=C, arom.), 1351*m* (N-O), 1338*m* (C-H), 1275*s* (C-O), 1190*s* (C=O), 1177*s* (C=O), 1101*s* (C-N), 1061*s* (C-N), 991*w* (=C-H), 926*m* (=C-H), 850*w* (C-H, arom.), 806*m* (C-H, arom.). **^{1}H NMR** (400 MHz, DMSO) δ 8.19 (t, *J* = 5.9 Hz, 1H), 8.11 – 7.88 (m, 5H), 5.69 (t, *J* = 1.2 Hz, 1H), 5.35 (d, *J* = 1.5 Hz, 1H), 3.18 (q, *J* = 6.4 Hz, 3H), 2.77 (q, *J* = 7.8, 7.0 Hz, 2H), 1.86 (d, *J* = 1.3 Hz, 3H), 1.78 – 1.70 (m,

3H), 1.20 (t, *J* = 7.3 Hz, 1H). **^{13}C NMR** (101 MHz, DMSO) δ 167.80, 158.92, 152.05, 148.19, 141.46, 140.51, 130.57, 128.08, 127.03, 119.23, 112.71, 111.49, 110.42, 108.71, 99.81, 58.47, 54.60, 36.80, 30.62, 19.08. **MS (ESI) *m/z*** calculated for $C_{20}H_{21}N_3O_4$: 367.405, found: $[M]^+$ 367.15.

6.4.9 Synthesis of *N*-3-(((6,7-dimethoxy-2-oxo-2*H*-chromen-4-yl)methyl)amino)propyl) methacrylamide (MC-1)

6.4.9.1 Synthesis of 4-(chloromethyl)-6,7-dimethoxy-2H-chromen-2-one (MC)

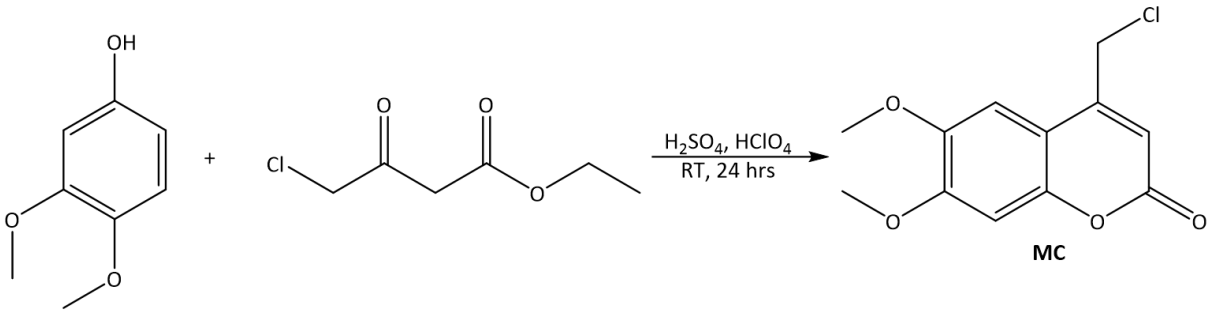

***Scheme 6.15**: A reaction scheme showing the Pechmann Condensation reaction between 3,4-dimethoxyphenol and ethyl 4-chloroacetoacetate in the presence of sulfuric acid and perchloric acid to form **MC**.*

To an Erlenmeyer flask, 3,4-dimethoxyphenol (0.308 g, 2 mmol) and ethyl 4-chloroacetoacetate (0.54 mL, 4 mmol) were added. To the reaction vessel, a mixture of perchloric acid (2 mL) and sulfuric acid (2 mL) was added dropwise. The reaction mixture was then left to stir at room temperature for 24 hours. Following this period, the reaction mixture was poured into ice water (100 mL) to allow for precipitation of the product. The crude product was then collected *via* vacuum filtration. This was then purified by recrystallisation in a minimal amount of hot methanol. The methanol solution was then left to cool to room

temperature and the solvent removed under vacuum filtration to yield **MC** (Scheme 6.15) as a yellow powder (0.45 g, 1.767 mmol, 88.4%). **M.P**. 196 – 199 °C (from methanol).

Λmax(DCM)/nm 365 (ε/dm^3 mol^{-1} cm^{-1} 5931.94). **IR neat (cm^{-1}):** 3067*w* (C-H, arom.), 3013*w* (=C-H), 2945*w* (C-H), 1710*s* (C=O), 1615*m* (C=C), 1558*s* (C=C, arom.), 1522*s* (C=C, arom.), 1465*m* (C-H), 1451*m* (C=C, arom.), 1441*m* (C=C, arom.), 1425*s* (C=C, arom.), 1386*s* (C-H), 1284*s* (C=O), 1278*s* (C=O), 1241*s* (C-O), 1222*s* (C-O), 1206*s* (C-O), 1197*m* (C-O), 1170*m*, 1161*m*, 1151*s*, 1057*s*, 1037*m*, 1004*s* (=C-H), 955*m*, 910*m*, 872*s* (C-H, arom.), 854*s* (C-H, arom.). **^{1}H NMR** (400 MHz, DMSO) δ 7.26 (s, 1H), 7.12, (s, 1H), 6.50 (t, *J* = 1.0 Hz, 1H), 5.05 (d, *J* = 0.9 Hz, 2H), 3.86 (d, *J* = 11.3 Hz, 6H). **^{13}C NMR** (101 MHz, DMSO) δ 160.71, 153.28, 151.41, 149.77, 146.27, 112.42, 109.82, 106.52, 100.86, 56.70, 56.60, 42.05. **MS (ESI) *m/z*** calculated for $C_{12}H_{11}ClO_4$: 254.67, found: $[M + H]^+$ 255.96.

6.4.9.2 Synthesis of N-(3-(((6,7-dimethoxy-2-oxo-2H-chromen-4-yl)methyl)amino)propyl) methacrylamide (MC-1)

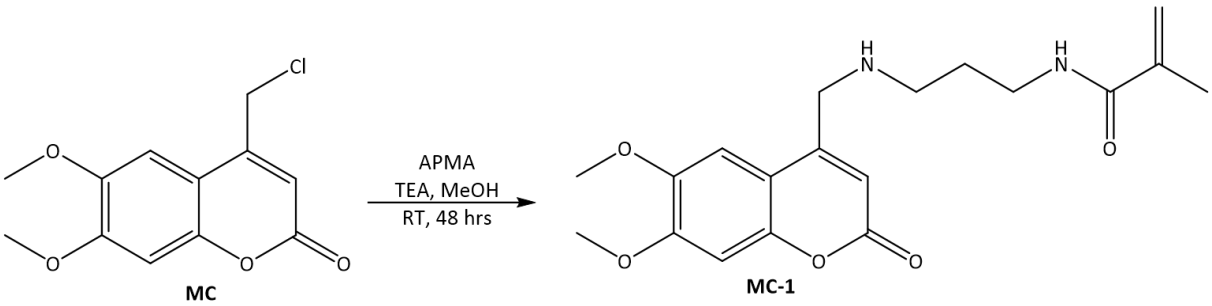

***Scheme 6.16**: A reaction scheme showing the formation of **MC-1** from **MC** and APMA in methanol with the presence of triethylamine.*

MC (0.509 g, 2 mmol) was dissolved in hot methanol (20 mL). To the reaction vessel APMA (0.39 g, 2.2 mmol) and triethylamine (1 mL, 7.17 mmol) were added. The reaction

mixture was heated to reflux with magnetic stirring for 48 hours. The reaction mixture was then cooled to room temperature and filtered under vacuum, before being concentrated under reduced pressure. Following this, the mixture was recrystallised and hot filtered in tetrahydrofuran (50 mL). This solution was then concentrated under reduced pressure to yield the crude final product **MC-1** (0.71 g, 1.969 mmol, 98.4%). This was then purified by RP-HPLC under the conditions displayed below (Table 6.5) to yield **MC-1** (Scheme 6.16) as a viscous brown oil (72.6%).

Table 6.5*: A table showing the times when changes in solvent concentration occurred in the RP-HPLC purification of* ***MC-1****.*

Time (mins)	HPLC Water (%)	Methanol (%)
0	65	35
30	0	100
35	0	100
35.1	65	35
40	65	35

λmax(H_2O)/nm 365 (ε/dm^3 mol^{-1} cm^{-1} 44.72). **IR neat (cm^{-1}):** 3357*w* (N-H), 2936*w* (N-H), 2835*w* (N-H), 2251*w*, 1683*s* (C=O), 1661*m* (C=C), 1620*m* (N-H), 1536*m* (C=C, arom.), 1498*s* (C=C, arom.), 1455*s* (C=C. arom.), 1419*m* (C-H), 1353*m* (C-H), 1313*m* (C-O), 1254*m* (C-O), 1221*m* (C-O), 1207*s* (C=O), 1188*s* (C=O), 1170*m* (C-N), 1153*m* (C-N), 1093*m* (C-N), 1028*m*, 980*m* (=C-H), 912*s* (C-H, arom.), 828*m* (C-H, arom.). **^{1}H NMR** (400 MHz, $CDCl_3$) δ 7.09 (t, *J* = 6.3 Hz, 1H), 6.74 (d, *J* = 0.9 Hz, 1H), 6.45 (s, 1H), 6.05 (d, *J* = 7.0 Hz, 1H), 5.84 – 5.76 (m, 1H), 3.84 (d, *J* = 3.9 Hz, 6H), 3.60 (ddd, *J* = 13.4, 7.5, 5.3 Hz, 2H), 3.45 – 3.25 (m, 2H), 3.14 (ddt, *J* = 11.2,

7.2, 5.3 Hz, 1H), 2.93 (dd, *J* = 17.4, 9.3 Hz, 1H), 1.99 – 1.96 (m, 3H), 1.85 (dddd, *J* = 14.1, 12.2, 7.0, 3.5 Hz, 2H). **^{13}C NMR** (101 MHz, $CDCl_3$) δ 174.25, 168.19, 151.30, 150.48, 144.64, 139.74, 119.79, 118.38, 108.18, 96.67, 95.49, 56.88, 56.15, 53.48, 38.55, 37.00, 35.63, 27.43, 18.51. **MS (ESI) *m/z*** calculated for $C_{19}H_{24}N_2O_5$: 360.41, found: $[M + H]^+$ 361.18.

6.4.10 Synthesis of *N*-(3-(((6,7-dimethoxy-3-nitro-2-oxo-2*H*-chromen-4-yl)methyl)amino)propyl)methacrylamide (MC-2)

6.4.10.1 Synthesis of 4-(chloromethyl)-6,7-dimethoxy-3-nitro-2H-chromen-2-one (MC-2a)

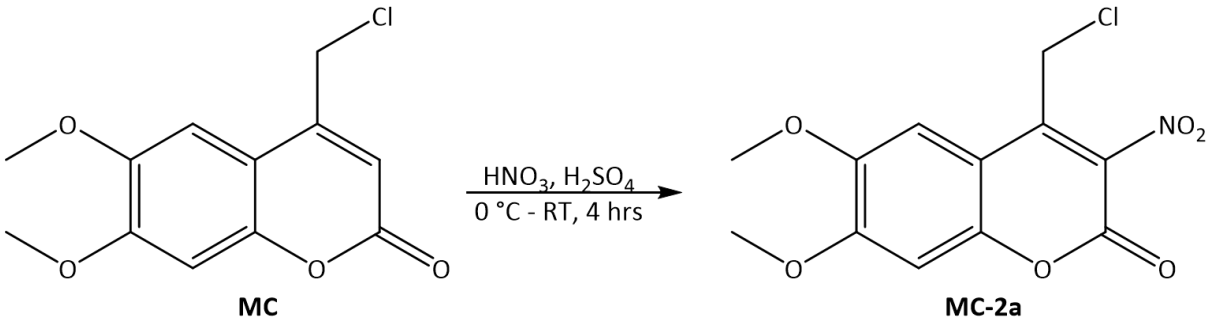

MC **MC-2a**

***Scheme 6.17**: A reaction scheme displaying the nitration of **MC** in the presence of nitric acid and sulfuric acid to form **MC-2a**.*

To a round bottom flask, nitric acid (70%, 5 mL) and sulfuric acid (5 mL) were added and cooled to 0 °C. Following this, **MC** (0.509 g, 2 mmol) was slowly added to the round bottom flask while stirring. This reaction mixture was left to stir at room temperature for 4 hours. Following this, the reaction was diluted with DI water (20 mL), before extracting the product with ethyl acetate (2 × 20 mL). The organic solution was washed with DI water (2 × 15 mL) and concentrated sodium hydrogen carbonate solution (2 × 15 mL) before being dried over anhydrous sodium sulfate. The resultant solution was filtered then concentrated under

reduced pressure to yield the final product, **MC-2a** (Scheme 6.17) as a red powder (0.56 g, 1.86 mmol, 93%) which required no further purification.

IR neat (cm^{-1}): 3048*w* (C-H, arom.), 2945*w* (C-H), 1721*s* (C=O), 1607*m* (C=C), 1553*m* (C=C, arom.), 1531*s* (N-O), 1517*s* (C=C, arom.), 1466*s* (C-H), 1445*m*, 1425*s*, 1382*s* (N-O), 1275*s* (C=O), 1261*s* (C=O), 1243*s* (C-O), 1208*s* (C-O), 1165*s* (C-O), 1074*m* (C-O), 1038*s* (C-N), 1028*m*, 999*s* (=C-H), 966*m*, 890*m* (C-H, arom.), 836*m* (C-H, arom.), 823*m*. **^{1}H NMR** (400 MHz, $CDCl_3$) δ 7.12 (s, 1H), 6.91, (s, 1H), 4.64 (s, 2H), 4.00 (d, *J* = 9.4 Hz, 6H). **^{13}C NMR** (101 MHz, $CDCl_3$) δ 155.49, 149.86, 147.69, 141.85, 107.55, 105.79, 100.38, 56.82, 56.59, 35.10. **MS (ESI)** ***m/z*** calculated for $C_{12}H_{10}ClNO_6$: 299.66, found: $[M + H]^+$ 300.03.

6.4.10.2 Synthesis of N-(3-(((6,7-dimethoxy-3-nitro-2-oxo-2H-chromen-4-yl)methyl)amino)propyl)methacrylamide (MC-2)

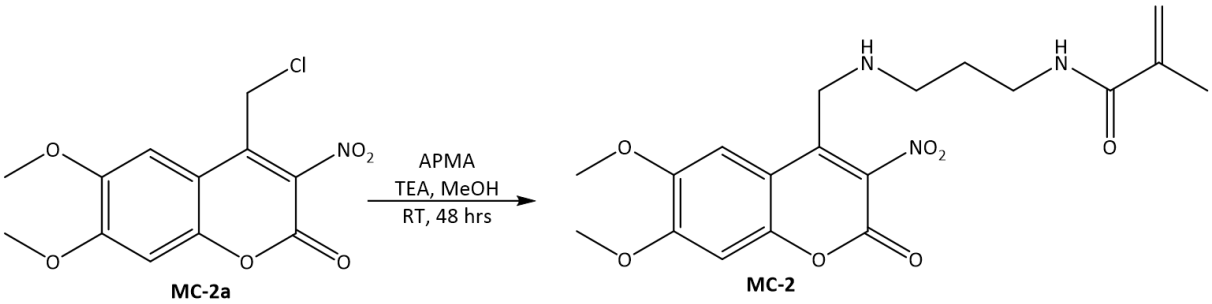

Scheme 6.18*: A reaction scheme showing the formation of* ***MC-2*** *from* ***MC-2a*** *and APMA in methanol with the presence of triethylamine.*

MC-2a (0.599 g, 2 mmol) was dissolved in methanol (25 mL). To the reaction vessel APMA (0.39 g, 2.2 mmol) and triethylamine (1 mL, 7.17 mmol) were added. The reaction mixture proceeded to react at room temperature magnetic stirring for 48 hours. Solvent and triethylamine were evaporated under reduced pressure prior to resuspending the remaining

compounds in tetrahydrofuran. The reaction mixture was then filtered under vacuum, before being concentrated under reduced pressure to yield crude **MC-2** as an orange, oily solid (0.676 g, 1.67 mmol, 83.3%) Following this, the compound was purified via RP-HPLC under the conditions displayed below (Table 6.6) to yield the final product, **MC-2** (Scheme 6.18) as a dark red oil (62.8%).

***Table 6.6**: A table showing the times when changes in solvent concentration occurred in the RP-HPLC purification of **MC-2**.*

Time (mins)	HPLC Water (%)	Methanol (%)
0	85	15
30	85	70
30.1	0	100
35	0	100
35.1	85	15
40	85	15

λmax(H_2O)/nm 365 (ε/dm^3 mol^{-1} cm^{-1} 34.98). **IR neat (cm^{-1}):** 3319*w* (N-H), 2979*m* (N-H), 2954*m* (N-H), 1696*m* (C=O) 1653*s* (C=O), 1614*s* (N-H), 1533*s* (N-O), 1452*s* (C=C, arom.), 1374*s* (N-O), 1316*s* (C-O), 1221*s* (C-O), 1036*m* (C-N), 931*m* (=C-H), 836*m* (C-H, arom.). **^{1}H NMR** (400 MHz, DMSO) δ 8.74 (t, *J* = 6.3 Hz, 1H), 8.07 – 7.72 (m, 1H), 5.59 (s, 1H), 5.26 (t, *J* = 1.6 Hz, 1H), 4.10 (s, 2H), 3.81 – 3.69 (m, 2H), 3.10 (d, *J* = 7.1 Hz, 8H), 1.79 (s, 3H), 1.54 (p, *J* = 6.7 Hz, 1H), 1.20 – 1.11 (m, 1H). **MS (ESI) *m/z*** calculated for $C_{19}H_{23}N_3O_7$: 405.41, found: $[M]^+$ 405.05.

6.4.11 Synthesis of (6,7-dimethoxy-2-oxo-2*H*-chromen-4-yl)methyl (3-methacrylamidopropyl)carbamate (MC-3)

6.4.11.1 Synthesis of 4-(hydroxymethyl)-6,7-dimethoxy-2H-chromen-2-one (MC-3a)

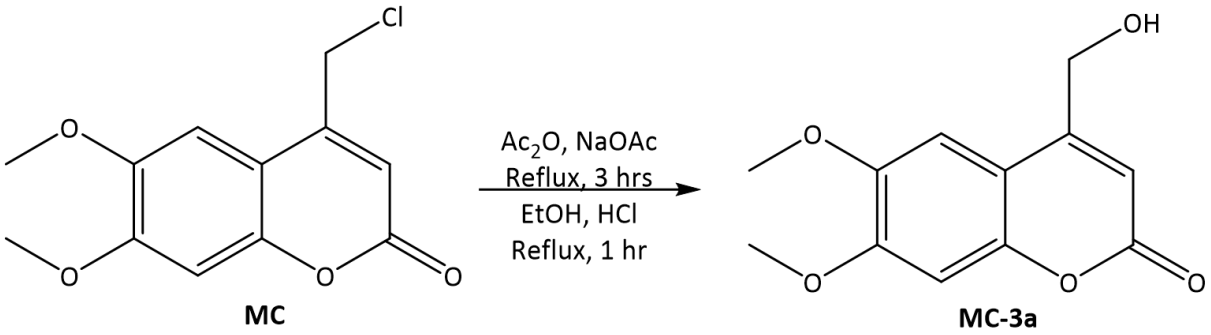

***Scheme 6.19**: A reaction mechanism displaying the two-step hydroxylation of **MC** to form **MC-3a** initially through ester formation with acetic anhydride and sodium acetate, followed by ester cleavage with ethanol and hydrochloric acid.*

To a round bottom flask, acetic anhydride (10 mL) and sodium acetate (1.64 g, 20 mmol) were added. To this solution, compound **MC** (0.509, 2 mmol) was added. The reaction mixture was heated to reflux for 3 hours, before being cooled to room temperature. Subsequently, the intermediate was precipitated over ice, and collected under vacuum filtration. The intermediate was then dissolved in a mixture of absolute ethanol (25 mL) and hydrochloric acid (25 mL) before being heated to reflux for 1 hour. Once cooled, the addition of ice water resulted in precipitation of the product. The product was collected under vacuum filtration and required no further purification. **MC-3a** (Scheme 6.19) was collected as a yellow powder (0.336 g, 1.42 mmol, 71%).

IR neat (cm^{-1}): 3587*m* (O-H), 3383*m* (O-H), 1714*s* (C=O), 1659*m* (C=C), 1612*s* (C=C, arom.), 1556*s* (C=C, arom.), 1522*s* (C=C, arom.), 1468*m* (C=C, arom.), 1455*s* (C=C, arom.), 1421*s*, 1385*s* (C-H), 1284*s* (C=O), 1273*s* (C=O), 1238*s* (C-O), 1220*s* (C-O), 1202*s* (C-O), 1182*m*

(C-O), 1165*s* (C-O), 1146*s*, 1056*s* (C-O), 1035*s*, 998*s* (=C-H), 946*m*, 904*m*, 878*m* (C-H, arom.), 865*s* (C-H, arom.), 846*s*, 824*s*. **^{1}H NMR** (400 MHz, $CDCl_3$) δ 7.02 (s, 1H), 6.88, (s, 1H), 6.42 (s, 1H), 4.63 (d, *J* = 0.9 Hz, 2H), 3.96 (d, *J* = 3.7 Hz, 6H). **^{13}C NMR** (101 MHz, $CDCl_3$) δ 160.91, 153.16, 150.03, 149.37, 146.38, 113.07, 109.79, 104.70, 100.36, 56.49, 56.43, 41.64. **MS (ESI)** ***m/z*** calculated for $C_{12}H_{12}O_5$: 236.22, found: $[M]^+$ 235.08.

6.4.11.2 Synthesis of (6,7-dimethoxy-2-oxo-2H-chromen-4-yl)methyl (4-nitrophenyl) carbonate (MC-3b)

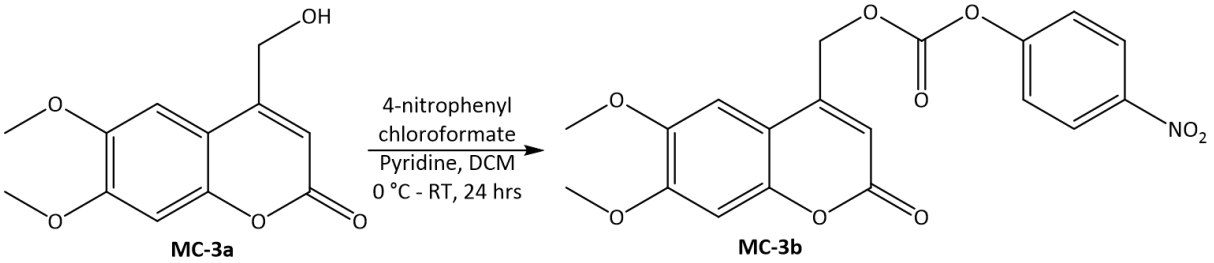

Scheme 6.20*: A reaction scheme depicting the formation of* ***MC-3b*** *from the pyridine catalysed reaction of* ***MC-3a*** *with 4-nitrophenyl chloroformate in dichloromethane.*

A reaction vessel was charged with dichloromethane (20 mL) then cooled to 0 °C. **MC-3a** (0.472 g, 2 mmol) was dissolved in the solvent, before 4-nitrophenyl chloroformate (0.403 g, 2 mmol) and pyridine (0.2 mL, 2.47 mmol) were slowly added. This mixture was allowed to reach room temperature, at which it proceeded to react for 24 hours. Following this, the reaction was quenched with excess dichloromethane. This organic solution was washed with DI water (2 × 20 mL) before being dried over anhydrous sodium sulfate and filtered. The solution was then concentrated to dryness under reduced pressure, co-evaporating with toluene to aid in pyridine removal. This led to the collection of the final product **MC-3b**

(Scheme 6.20) as a yellow powder, which was used immediately without purification for the next reaction.

6.4.11.3 Synthesis of (6,7-dimethoxy-2-oxo-2H-chromen-4-yl)methyl (3-methacrylamidopropyl)carbamate (MC-3)

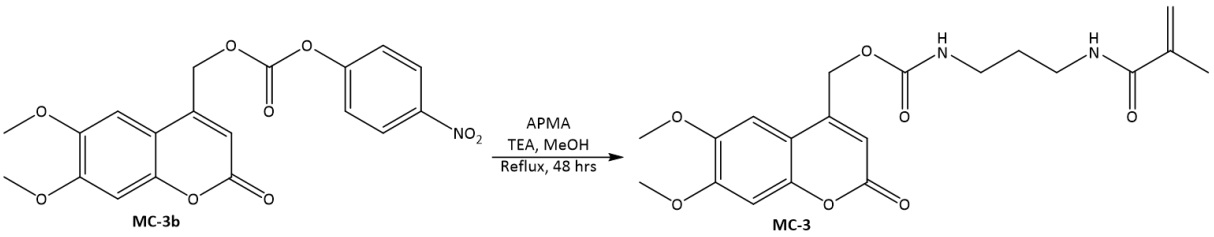

***Scheme 6.21**: A reaction scheme showing the formation of **MC-3** from **MC-3b** and APMA in methanol with the presence of triethylamine.*

MC-3b was dissolved in hot methanol (30 mL). To the reaction vessel APMA (0.39 g, 2.2 mmol) and triethylamine (1 mL, 7.17 mmol) were added. The reaction mixture was heated to reflux with magnetic stirring for 48 hours. The reaction mixture was then cooled to room temperature and filtered under vacuum, before being concentrated under reduced pressure. Following this, the mixture was recrystallised and hot filtered in tetrahydrofuran (50 mL). This solution was then concentrated under reduced pressure to yield the crude final product, **MC-3** as a hygroscopic yellow powder (0.674 g, 1.67 mmol, 83.3%). This was then purified by RP-HPLC under the conditions displayed below (Table 6.7) to yield **MC-3** (Scheme 6.21) as a yellow oil (43.7%).

***Table 6.7**: A table showing the times when changes in solvent concentration occurred in the RP-HPLC purification of **MC-3**.*

Time (mins)	HPLC Water (%)	Methanol (%)
0	65	35
30	0	100
35	0	100
35.1	65	35
40	65	35

λmax(H_2O)/nm 365 (ε/dm^3 mol^{-1} cm^{-1} 1746.13). **IR neat (cm^{-1}):** 3083*m* (N-H), 1767*m* (C=O), 1724*m* (C=O), 1616*m* (N-H), 1592*m* (N-H), 1558*m* (C=C, arom.), 1523*s* (C=C, arom.), 1490*m*(C=C, arom.), 1468*m* (C-H), 1454*m* (C=C, arom.), 1423*m* (C-H), 1385*m* (C-H), 1349*m* (C-H), 1336*m* (C-H), 1239*s* (C-O), 1191*s* (C=O), 1160*s* (C-O), 1107*m* (C-N), 1056*s* (C-O), 1002*s* (=C-H), 953*m* (=C-H), 909*m* (=C-H), 894*m*, 855*s* (C-H, arom.), 840*s* (C-H, arom.). **^{1}H NMR** (400 MHz, D_2O) δ 8.06 (D, *j* = 9.3 Hz), 6.83 (d, *J* = 2.2 Hz), 6.81 (d, *J* = 2.2 Hz), 5.57 (dd, *J* = 13.3, 1.0 Hz), 5.33 (dd, *J* = 13.3, 1.5 Hz), 4.75 (s), 3.86 (d, *J* = 6.4 Hz), 3.25 (t, *J* = 6.8 Hz), 2.11 (s), 1.76 (d). **MS (ESI) *m/z*** calculated for $C_{12}H_{11}O_4^-$: 219.22, found: [M] 220.06. **MS (ESI) *m/z*** calculated for $C_7H_{13}N_2O^-$: 141.11, found: $[M]^-$ 139.01.

6.4.12 Synthesis of *N*-(3-(((6,7-dimethoxy-2-thioxo-2*H*-chromen-4-yl)methyl)amino)propylmethacrylamide (SMC-1)

6.4.12.1 Synthesis of 4-(chloromethyl)-6,7-dimethoxy-2H-chromene-2-thione (SMC)

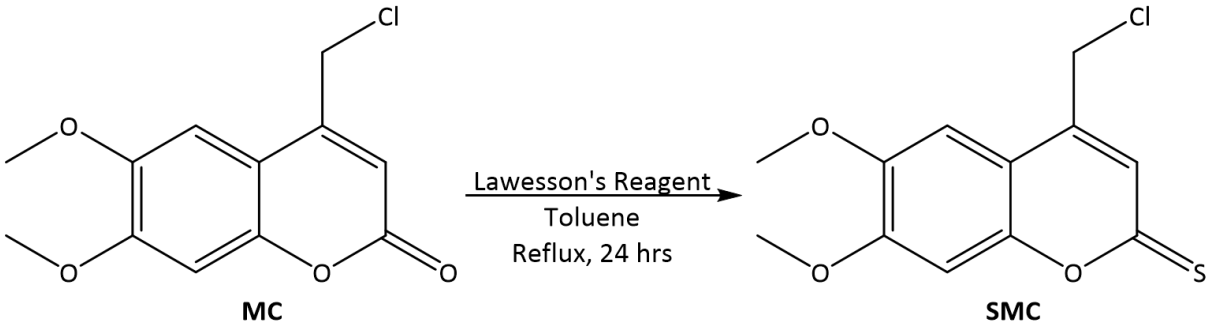

MC **SMC**

Scheme 6.22*: A reaction scheme displaying the formation of a thiocarbonyl group through heating* ***MC*** *in the presence of Lawesson's reagent in toluene to form* ***SMC****.*

A round bottom flask was charged with anhydrous toluene (20 mL), before the addition of compound **MC** (0.509 g, 2 mmol). To this solution, Lawesson's reagent (0.65 g, 1.6 mmol) was added slowly. This reaction mixture was heated to reflux and proceeded to react for 24 hours. Following this period, the solution was hot gravity filtered. The filtrate was then concentrated to dryness under reduced pressure to yield the crude product. This was then purified by recrystallisation in methanol, with the filtrate being collected and evaporated under reduced pressure to yield final product, **SMC** (Scheme 6.22) as a pungent green powder (0.479 g, 1.77 mmol, 88.5%).

IR neat (cm^{-1}): 3068*w* (C-H, arom.), 3013*w* (=C-H), 2945*w*, 2858*w* (C-H), 1713*s* (C=C, arom.), 1615*m* (C=C), 1558*s* (C=C, arom.), 1523*s* (C=C, arom.), 1465*s* (C-H), 1451*s* (C=C, arom.), 1441*m* (C=C, arom.), 1426*s* (C=C, arom.), 1386*s* (C-H), 1285*s* (C-O), 1241*s* (C-H), 1222*s* (C-O), 1206*s* (C-O), 1197*m*, 1170*s* (C-O), 1161*s* (C-O), 1151*s* (C-O), 1057*s* (C=S), 1037*s*, 1004*s* (=C-H), 955*s*, 910*s*, 872*s* (C-H, arom.), 854*s* (C-H, arom). **^{1}H NMR** (400 MHz, $CDCl_3$) δ 7.02 (s, 1H), 6.87

(s, 1H), 6.43 (d, *J* = 1.0 Hz, 1H), 4.64 (d, *J* = 0.8 Hz, 2H), 3.96 (d, *J* = 2.7 Hz, 6H). **^{13}C NMR** (101 MHz, $CDCl_3$) δ 191.31, 152.20, 149.01, 148.25, 145.36, 112.46, 108.81, 105.20, 103.95, 55.55, 55.39. **MS (ESI) *m/z*** calculated for $C_{12}H_{11}ClO_3S$: 270.73, found: $[M]^+$ 268.02.

6.4.12.2 Synthesis of N-(3-(((6,7-dimethoxy-2-thioxo-2H-chromen-4-yl)methyl)amino)propylmethacrylamide (SMC-1)

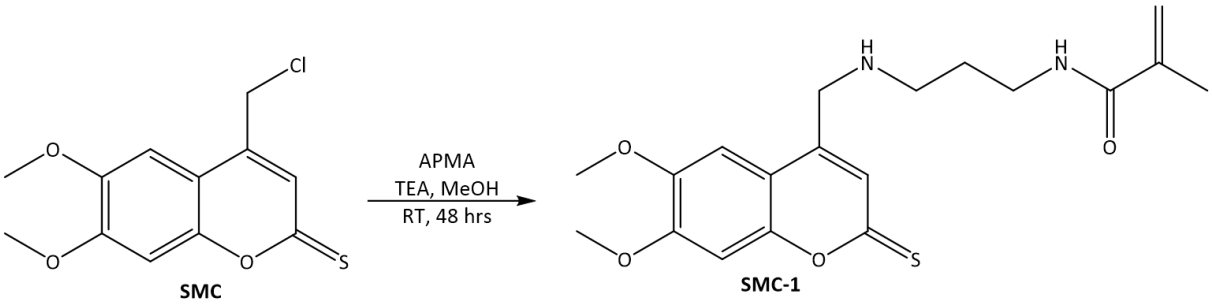

***Scheme 6.23**: A reaction scheme showing the formation of **SMC-1** from **SMC** and APMA in methanol with the presence of triethylamine.*

SMC (0.542 g, 2 mmol) was dissolved in anhydrous methanol (25 mL). To the reaction vessel APMA (0.39 g, 2.2 mmol) and triethylamine (1 mL, 7.17 mmol) were added. The reaction mixture was reacted at room temperature with magnetic stirring for 48 hours. Triethylamine and methanol were evaporated under reduced pressure. Following this, the mixture was recrystallised in tetrahydrofuran (50 mL) and filtered to remove impurities. This solution was then concentrated under reduced pressure to yield the crude final product, **SMC-1** as a dark red viscous compound (0.68 g, 1.806 mmol, 90.3%). This was then purified by RP-HPLC under the conditions displayed below (Table 6.8) to yield pure **SMC-1** (Scheme 6.23) as a red oil (61%).

***Table 6.8**: A table showing the times when changes in solvent concentration occurred in the RP-HPLC purification of **SMC-1**.*

Time (mins)	HPLC Water (%)	Methanol (%)
0	60	40
30	0	100
35	0	100
35.1	60	40
40	60	40

λmax(H_2O)/nm 365 (ε/dm^3 mol^{-1} cm^{-1} 1461.45). **IR neat (cm^{-1}):** 3390*m* (N-H), 1731*m* (C=O), 1634*m* (N-H), 1551*s* (C=C, arom.), 1518*m* (C=C, arom.), 1424*m*, 1384*m* (C-H), 1329*s* (S=O), 1282*s* C-H(), 1233*s* (C-O), 1207*s* (C=O), 1161*s* (C-N), 1044*s* (C-N), 1008*s* (=C-H), 827*m* (C-H, arom.). **^{1}H NMR** (400 MHz, $CDCl_3$) δ 7.83 (s, 0H), 7.23 (s, 1H), 6.75 (s, 1H), 6.15 (s, 1H), 5.74 (s, 1H), 5.38 (dd, *J* = 1.7, 1.1 Hz, 1H), 3.97 – 9.92 (m, 6H), 3.86 (d, *J* = 6.2 Hz, 4H), 3.46 (q, *J* = 6.3, 2H), 1.95 (s, 1H), 1.28 – 1.21 (m, 0H). **^{13}C NMR** (101 MHz, $CDCl_3$) δ 192.94, 169.82, 161.59, 154.88, 153.38, 150.36, 146.24, 139.10, 120.83, 108.92, 108.32, 106.59, 99.97, 56.43, 56.34, 41.81, 36.54, 28.16, 18.61. **MS (ESI) *m/z*** calculated for $C_{19}H_{24}N_2O_4S$: 376.47, found: $[M]^+$ 374.07.

6.4.13 Synthesis of *N*-(3-(((6,7-dimethoxy-3-nitro-2-thioxo-2*H*-chromen-4-yl)methyl)amino)propyl)methacrylamide (SMC-2)

6.4.13.1 Synthesis of 4-(chloromethyl)-6,7-dimethoxy-3-nitro-2H-chromene-2-thione (SMC-2a)

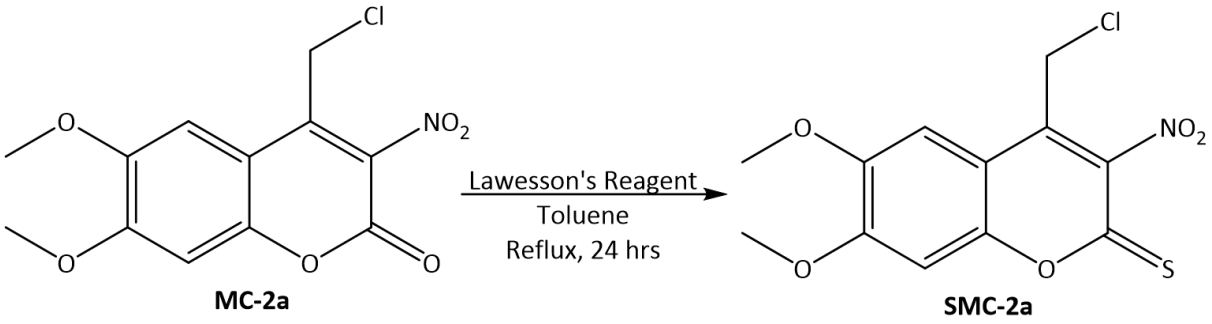

MC-2a **SMC-2a**

Scheme 6.24*: A reaction scheme displaying the formation of a thiocarbonyl group through heating* ***MC-2a*** *in the presence of Lawesson's reagent in toluene to form* ***SMC-2a****.*

A round bottom flask was charged with anhydrous toluene (20 mL), before the addition of compound **MC-2a** (0.599 g, 2 mmol). To this solution, Lawesson's reagent (0.65 g, 1.6 mmol) was added slowly. This reaction mixture was heated to reflux and proceeded to react for 24 hours. Following this period, the solution was hot gravity filtered. The filtrate was then concentrated to dryness under reduced pressure to yield the final product, compound **SMC-2a** (Scheme 6.24) as a dark red powder (0.546 g, 1.73 mmol, 86.5%).

IR neat (cm^{-1}): 3026*w* (=C-H), 1746*s* (C=C, arom.), 1602*m* (C=C), 1546*s* (N-O), 1495*m* (C=C, arom.), 1452*m* (C-H), 1416*m* (C-H), 1375*s* (N-O), 1330*m* (C-H), 1286*m* (C-O), 1245*m* (C-O), 1205*s* (C-N), 1158*s* (C=S), 1111*m*, 1082*m*, 1039*s* (C-O), 1012*s* (C-O), 973*m*, 930*m*, 891*m*, 832*s* (C-H, arom), 811*m* (C-H, arom.). **^{1}H NMR** (400 MHz, DMSO) δ 7.59 (dd, *J* = 12.8, 8.7 Hz, 1H), 6.97 (dd, *J* = 8.8, 3.0 Hz, 1H), 3.73 (s, 2H), 3.13 (s, 3H). **^{13}C NMR** (101 MHz, DMSO) δ 162.11,

132.93, 132.82, 124.81, 122.92, 114.27, 114.12, 62.32, 61.33, 55.62, 53.64, 49.03. **MS (ESI) *m/z*** calculated for $C_{12}H_{10}ClNO_5S$: 315.72, found: $[M + CH3OH + H]^+$ 351.1.

6.4.13.2 Synthesis of N-(3-(((6,7-dimethoxy-3-nitro-2-thioxo-2H-chromen-4-yl)methyl)amino)propyl)methacrylamide (SMC-2)

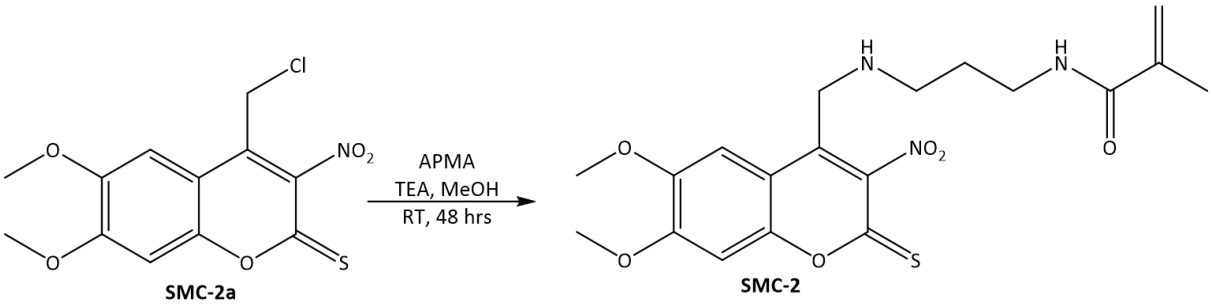

***Scheme 6.25**: A reaction scheme showing the formation of **SMC-2** from **SMC-2a** and APMA in methanol with the presence of triethylamine.*

SMC-2a (0.631 g, 2 mmol) was dissolved in anhydrous methanol (25 mL). To the reaction vessel APMA (0.39 g, 2.2 mmol) and triethylamine (1 mL, 7.17 mmol) were added. The reaction mixture was reacted at room temperature with magnetic stirring for 48 hours. The reaction mixture was concentrated under reduced pressure. Following this, the mixture was recrystallised and hot filtered in tetrahydrofuran (50 mL). This solution was then concentrated under reduced pressure to yield the crude final product, **SMC-2** (Scheme 6.25) as a dark red hygroscopic solid (91.5 g, 1.83 mmol, 91.5%). This was then purified by RP-HPLC under the conditions displayed below (Table 6.9) to yield pure **SMC-2** as a red oil (67%).

***Table 6.9**: A table showing the times when changes in solvent concentration occurred in the RP-HPLC purification of **SMC-2**.*

Time (mins)	HPLC Water (%)	Methanol (%)
0	65	35
30	0	100
35	0	100
35.1	65	35
40	65	35

λmax(H_2O)/nm 365 (ε/dm^3 mol^{-1} cm^{-1} 538.92). **IR neat (cm^{-1}):** 3379*m* (N-H), 2949*m* (C-H), 1741*m* (C=C, arom.), 1652*m* (C=O), 1597*s* (N-H), 1569*m* (C=C, arom.), 1535*s* (N-O), 1503*s* (C=C, arom.), 1453*s* (C=C, arom.), 1376*m* (N-O), 1298*m* (C-O), 1258*s* (C-H), 1228*s* (C-O), 1204*s* (C-O), 1177*s* (C-N), 1136*m* (C-N), 1120*s* (C-O), 1023*s* (C=S), 932*m* (=C-H), 833*s* (C-H, arom.), 807*s* (C-H, arom.). **^{1}H NMR** (400 MHz, DMSO) δ 7.71 (dd, *J* = 12.8, 8.8 Hz, 1H), 7.12 (dd, *J* = 8.8, 3.5 Hz, 1H), 5.65 (s, 1H), 5.32 (d, *J* = 1.6 Hz, 1H), 3.96 – 3.68 (m, 6H), 3.17 (s, 1H), 2.51 (p, *J* = 1.8 Hz, 4H), 2.08 (d, *J* = 3.5 Hz, 1H), 1.85 (d, *J* = 3.2 Hz, 2H). **MS (ESI) *m/z*** calculated for $C_{19}H_{25}N_3O_6S$: 421.47, found: $[M]^+$ 421.1.

6.4.14 Synthesis of (6,7-dimethoxy-2-thioxo-2*H*-chromen-4-yl)methyl (3-methacrylamidopropyl)carbamate (SMC-3)

6.4.14.1 Synthesis of 4-(hydroxymethyl)-6,7-dimethoxy-2H-chromene-2-thione (SMC-3a)

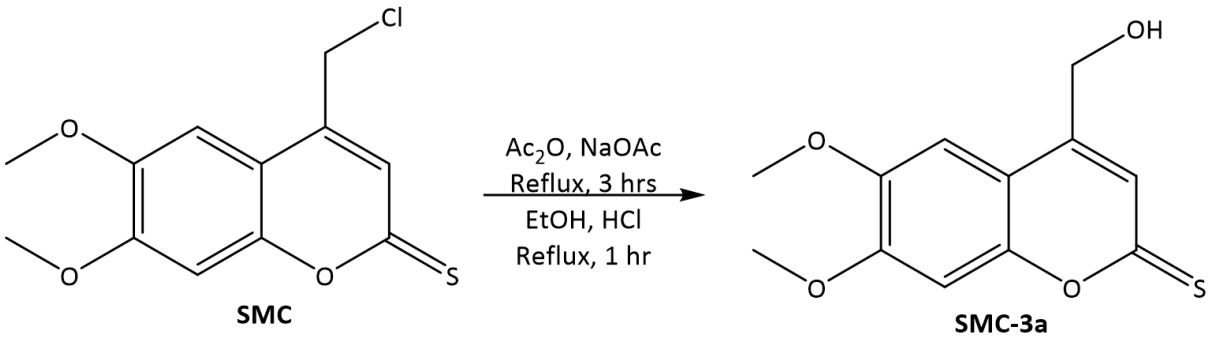

***Scheme 6.26**: A reaction mechanism displaying the two-step hydroxylation of **SMC** to form **SMC-3a** initially through ester formation with acetic anhydride and sodium acetate, followed by ester cleavage with ethanol and hydrochloric acid.*

To a round bottom flask, acetic anhydride (10 mL) and sodium acetate (1.64 g, 20 mmol) were added. To this solution, compound **SMC** (0.542, 2 mmol) was added. The reaction mixture was heated to reflux for 3 hours, before being cooled to room temperature and quenched with DI water (40 mL). Subsequently, the intermediate was extracted with ethyl acetate (2 × 25 mL) and concentrated under reduced pressure The intermediate was then dissolved in a mixture of absolute ethanol (25 mL) and hydrochloric acid (25 mL) before being heated to reflux for 1 hour. Once cooled, the addition of ice water resulted in precipitation of the starting reagent. Product was extracted from the aqueous solution using ethyl acetate (2 × 25 mL). Concentration under reduced pressure yielded the product **SMC-3a** (Scheme 6.26) as an orange powder (0.43 g, 1.7 mmol, 85%).

IR neat (cm^{-1}): 3456*w* (O-H), 2924*w* (C-H), 2852*w* (C-H), 1696*s* (C=C, arom.), 1614*s* (C=C), 1559*s* (C=C, arom.), 1515*s* (C=C, arom.), 1463*s* (C-H), 1451*s* (C-H), 1418*s* (C-H), 1382*s* (C-H), 1277*s* (C-O), 1233*s* (C-O), 1201*s* (C-O), 1153*s* (C=S), 1096*s*, 1051*s* (C-O), 1032*s*, 998*s* (=C-H), 960*m*, 932*s* (C-H, arom.), 847*s* (C-H, arom.). **^{1}H NMR** (400 MHz, $CDCl_3$) δ 7.02 (s, 1H), 6.88 (s, 1H), 6.42 (s, 1H), 4.63 (d, *J* = 0.9 Hz, 2H), 3.96 (d, *J* = 2.8 Hz, 6H). **^{13}C NMR** (101 MHz, $CDCl_3$) δ 160.61, 153.21, 150.02, 149.34, 146.39, 113.46, 109.83, 104.92, 100.49, 56.57, 56.42, 50.88. **MS (ESI) *m/z*** calculated for $C_{12}H_{12}O_4S$: 252.28, found: $[M]^+$ 252.06

6.4.14.2 Synthesis of (6,7-dimethoxy-2-thioxo-2H-chromen-4-yl)methyl (3-methacrylamidopropyl)carbamate (SMC-3b)

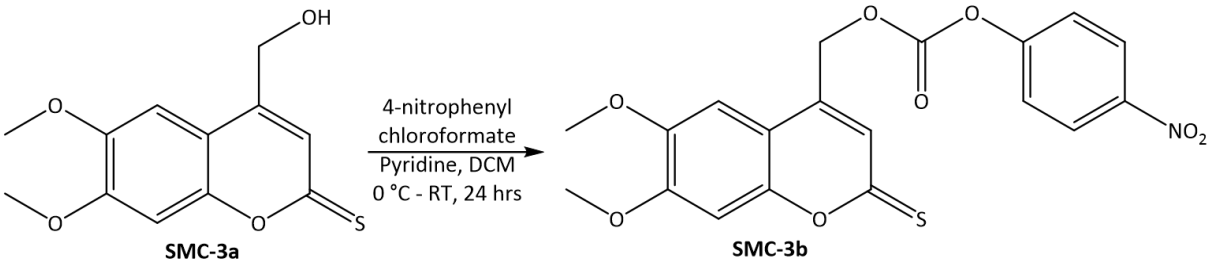

***Scheme 6.27**: A reaction scheme depicting the formation of **SMC-3b** from the pyridine catalysed reaction of **SMC-3a** with 4-nitrophenyl chloroformate in dichloromethane.*

A reaction vessel was charged with dichloromethane (20 mL) then cooled to 0 °C. **SMC-3a** (0.505 g, 2 mmol) was dissolved in the solvent, before 4-nitrophenyl chloroformate (0.403 g, 2 mmol) and pyridine (0.2 mL, 2.47 mmol) were slowly added. This mixture was allowed to reach room temperature, at which it proceeded to react for 24 hours. Following this, the reaction was quenched with excess dichloromethane. This organic solution was washed with DI water (2 × 20 mL) before being dried over anhydrous sodium sulfate. The solution was then

filtered and concentrated to dryness under reduced pressure to obtain the final product **SMC-3b** (Scheme 6.27) as a red powder, which was used straight away for the next reaction**.**

6.4.14.3 Synthesis of (6,7-dimethoxy-2-thioxo-2H-chromen-4-yl)methyl (3-methacrylamidopropyl)carbamate (SMC-3)

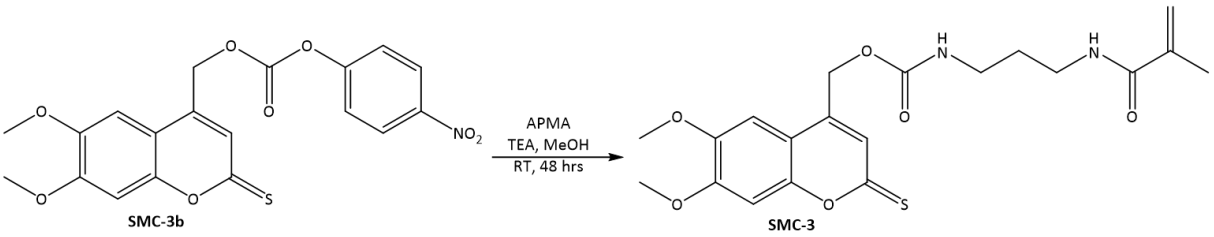

Scheme 6.28: *A reaction scheme showing the formation of* ***SMC-3*** *from* ***SMC-3b*** *and APMA in methanol with the presence of triethylamine.*

SMC-3b (0.84 g, 2 mmol) was dissolved in methanol (25 mL). To the reaction vessel APMA (0.39 g, 2.2 mmol) and triethylamine (1 mL, 7.17 mmol) were added. The reaction mixture was reacted at room temperature with magnetic stirring for 24 hours. The reaction mixture was then concentrated under reduced pressure to remove triethylamine and methanol. Following this, the mixture was recrystallised in tetrahydrofuran (50 mL) and filtered under vacuum to remove salt impurities. This solution was then concentrated under reduced pressure to yield the crude final product, **SMC-3** (Scheme 6.28) as a red oil (0.68 g, 1.61 mmol, 80.5%). This was then purified by RP-HPLC under the conditions displayed below (Table 6.10) to yield **SMC-3** as an orange oil (45%).

***Table 6.10**: A table showing the times when changes in solvent concentration occurred in the RP-HPLC purification of **SMC-3**.*

Time (mins)	HPLC Water (%)	Methanol (%)
0	65	35
30	0	100
35	0	100
35.1	65	35
40	65	35

λmax(H_2O)/nm 365 (ε/dm^3 mol^{-1} cm^{-1} 799.1). **IR neat (cm^{-1}):** 3083*w* (N-H), 3024*w* (C-H), 1767*m* (C=O), 1724*m* (C=C, arom.), 1616*m* (C=C), 1592*m* (C=C, arom.), 1558*w* (C=C, arom.), 1523*m* (C=C, arom.), 1490*m* (C-H), 1467*m* (C-H), 1454*m* (C-H), 1423*m*, 1385*m* (C-H), 1349*m*, 1336*m*, 1284*s* (C-O), 1239*s* (C=O), 1222*s* (C=O), 1191*s* (C=S), 1160*s* (C-N), 1107*m* (C-N), 1056*s* (C-O), 1037*m*, 1002*s* (=C-H), 953*m* (=C-H), 909*m* (=C-H), 895*m* (C-H, arom.), 855*s* (C-H, arom.), 840*s* (C-H, arom.). **^{1}H NMR** (400 MHz, $CDCl_3$) δ 8.07 (d, *J* = 8.5 Hz), 6.85 (d, *J* = 8.4 Hz), 6.09 (s), 5.6 (d, *J* = 1 Hz), 5.36 (d, *J* = 0.8 Hz), 3.79 (d), 3.09 (m), 1.82 (m). **MS (ESI) *m/z*** calculated for $C_{12}H_{11}O_3S^-$: 235.28, found: [M] 236.02. **MS (ESI) *m/z*** calculated for $C_7H_{13}N_2O^-$: 141.11, found: $[M]^-$ 139.01.

6.4.15 Synthesis of 4-(chloromethyl)-7-(dimethylamino)-2H-chromen-2-one (AC)

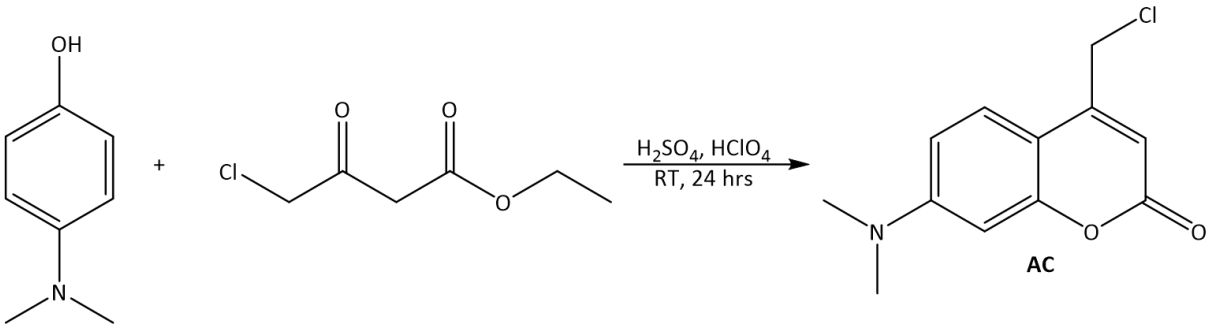

Scheme 6.29: *A reaction scheme showing the synthesis of* ***AC*** *from 4-dimethylaminophenol and ethyl 4-chloroacetoacetate in the presence of sulfuric acid and perchloric acid.*

To an Erlenmeyer flask, 4-dimethlyaminophenol (0.274 g, 2 mmol) and ethyl 4-chloroacetoacetate (0.54 mL, 4 mmol) were added. To the reaction vessel, a mixture of perchloric acid (2 mL) and sulfuric acid (2 mL) was added dropwise. The reaction mixture was then left to stir at room temperature for 24 hours. Following this period, the reaction mixture was poured into ice water (100 mL) and sodium hydroxide (2 g) was added. The product was then extracted from the aqueous solution using dichloromethane (3 ×30 mL). Evaporation under reduced pressure was used to remove the solvent. **AC** (Scheme 6.29) was then dissolved in a minimal amount of diethyl ether and hot filtered to remove remaining 4-dimethylaminophenol. The diethyl ether solution was then left to cool to room temperature, dried over anhydrous sodium sulfate, filtered and the solvent removed under reduced pressure to yield **AC** (Scheme 6.29) as a pink oil (0.338 g, 1.43 mmol, 71.5%). Analysis showed ethyl 4-chloroacetoacetate impurities.

λmax(DCM)/nm 365 (ε/dm^3 mol^{-1} cm^{-1} 1193.66). **IR neat (cm^{-1}):** 2924*w* (C-H), 2801*w* (C-H), 1612*s* (C=O), 1575*s* (C=C, arom.), 1505*s* (C=C, arom.), 1441*s* (C-H), 1351*s* (C-N), 1234*s* (C-O), 1168*s* (C=O), 1150*s* (C=O), 1129*s* (C-N), 1061*s* (C-N), 999*s* (=C-H), 975*s*, 885*m* (C-H,

arom.), 821*s* (C-H, arom.). **^{1}H NMR** (400 MHz, $CDCl_3$) δ 7.05 (t, *J* = 8.4 Hz, 1H), 6.34 – 6.29 (m, 1H), 6.22 (dd, *J* = 7.4, 2.0 Hz, 2H), 4.20 (s, 2H), 2.87 (s, 7H). **^{13}C NMR** (101 MHz, $CDCl_3$) δ 176.30, 160.91, 159.05, 152.99, 113.29, 104.53, 43.14, 40.92.

6.4.16 Purification of Photocaged Monomers

Analytical high performance liquid chromatography (HPLC) data was collected on a Shimadzu Prominence Modular HPLC using a Kinetex 5µ C18 100A 250 × 4.60 mm column. The system comprised of a Shimadzu SIL-20AC autosampler, Shimadzu LC-20AD pump, Shimadzu CTO-20AC column oven, with a Shimadzu SPD-20A UV-Vis detector. The column oven was maintained at 35 °C, 20 µL of sample was injected per sample with a flow rate of 1 mL min^{-1}. Run times for each monomer are listed in their respective chapters. The UV-Vis detectors were set to follow wavelengths of 210 nm and 254 nm.

Preparative RP-HPLC was conducted on an Agilent Technologies 1260 Infinity LC System using a Kinetex 5µ C18 100A, AXIA New Column 250 × 21.1 mm column.for the purification of photocaged monomers. Sample (10 mg) dissolved in 50 % methanol (10 mL) was injected into the column with a flow rate of 10 mL min^{-1}. Run times varied per sample and are listed in the corresponding monomer synthesis chapters along with solvent gradient events. Samples were monitored following the UV-Vis absorbance at 210 and 254 nm.

Collected fractions for each photocaged monomer were combined and evaporated to dryness under reduced pressure.

6.5 Chapter 5 Experimental

6.5.1 Functionalisation of Glass Slides

To create a stronger bond between glass slides and the hydrogels, they were functionalised as described in Chapter 6.4.2.1.

To form 1.1 µm spacer slides for thin film formation, the procedure described in Chapter 6.4.2.2 was followed.

6.5.2 Casting AAm/APMA derivative Co-Monomer Hydrogel Films

Nitrogen gas was bubbled through DI water (30 mL) for 30 minutes to remove oxygen air bubbles and to degas the water. DI water, 40% AAm solution, APMA derivative, BAAm, 10% APS solution and TEMED were mixed together in different ratios, shown in Table 6.11.

***Table 6.11**: A table depicting the volumes and masses of reagents used to create photocaged hydrogels.*

Gel Type	**40 % AAm (µL)**	**APMA Derivative (mg)**	**BAAm (mg)**	**10% APS (µL)**	**TEMED (µL)**	**DI H_2O (µL)**
AAm/MC-1	35.2	3.96	1.53	25	2.5	376.55
AAm/MC-2	35.2	4.46	1.53	25	2.5	376.55
AAm/SMC-1	35.2	4.14	1.53	25	2.5	376.55
AAm/SMC-2	35.2	4.64	1.53	25	2.5	376.55

To create 100 µm thick hydrogel films for deprotection studies the procedure discussed in Chapter 6.4.2.4 was followed for each monomer.

1 µm thick photocaged hydrogel-based LW devices were formed *via* the method described in Chapter 6.4.2.3.

6.5.3 Preparation of Photodeprotection Solutions

HEPES (11.915 g, 50 mmol) was dissolved in DI water (≈ 400 mL). 1 M sodium hydroxide was added dropwise to the solution until a pH of 7.4 was measured by the pH meter. Following this, the solution was transferred to a volumetric flask (500 mL) and DI water added until the volume was equal to 500 mL.

For a hydrogen atom transfer (HAT) solution, 1-decanethiol (100 µL) was dissolved in tetrahydrofuran (100 µL). This was then diluted with a 100 mM HEPES pH 7.4 buffer solution (4.8 mL) to a total volume of 5 mL.

To create a scavenger for *O*-nitrobenzyl derived PPGs, semicarbazide hydrochloride (250 mg, 2.24 mmol) was dissolved in 100 mM HEPES pH 7.4 buffer solution (20 mL). The hydrochloric acid salt was neutralised with 1 M sodium hydroxide (2.24 mL).

6.5.4 Deprotection Studies of Photocaged Monomers

The photocaged APMA monomers were dissolved in a solution corresponding to their particular structure (Table 6.12). Following this, the solution was irradiated with UV light of 365 nm for 120 minutes. Initially, aliquots (1 mL) were taken for UV-Vis spectroscopy in a 1 cm quartz cuvette every 60 seconds until 5 minutes was reached, following this aliquots were taken every 5 minutes until 30 minutes was reached, then finally every 30 minutes for the remainder of the time. The UV-Vis blank was the corresponding deprotection solution. The parameters were to analyse from 200 to 800 nm.

***Table 6.12**: A table depicting the solutions used to aid in deprotection and which photocaging group they are used for.*

Deprotection Solution	**Caged Groups**
DI H_2O	MC-1
100 mM HEPES, pH 7.4	MC-1, MC-3, SMC-3
HAT in 100 mM HEPES, pH 7.4	MC-1, SMC-1
Semicarbazide	NB-6a, NB-6b, DBF-5, MC-2, SMC-2

6.5.5 Deprotection Studies of Photoresponsive Hydrogels

Following hydrogel formation with the photocaged APMA monomers, AAm/APMA hydrogels were studied for photodeprotection. 100 µm thick hydrogel films were produced as discussed previously in Chapter 6.5.2 and submerged into the corresponding solution (Table 6.12). Studies were only conducted on MC-1, MC-2, SMC-1, and SMC-2 due to these monomers being the only ones able to form hydrogels. Following this, the hydrogel was irradiated with UV light of 365 nm in a UV irradiation box.

A clean glass microscope slide was used as the blank for UV-Vis spectra, with studies ranging from wavelength 200 nm to 800 nm. Initially, films were irradiated for 5 minutes in the deprotection solution, followed by the washing of the film in DI water for 30 minutes. The UV-Vis spectra of the film was obtained, prior to a 30 minute submersion in deprotection solution for 30 minutes prior to the next irradiation session. Once the films were deprotected for a cumulative 30 minute period, the irradiation time periods were increased from 5 minutes to 15 minutes, until the end of the study.

6.5.6 Photopatterning of Photoresponsive Hydrogels

Once deprotection studies were conducted, irradiation time periods were determined. Following hydrogel formation with the photocaged APMA monomers, AAm/APMA hydrogels were immersed in their corresponding solution (Table 6.12). Where deprotections were studied on glass slide supported hydrogels, the glass slides were immobilised in a petri dish prior to the addition of photodeprotection solution to prevent movement of the slide affecting the photopattern. Hydrogels were then placed over the desired photomask and irradiated with 365 nm light for a pre-determined period of time (Table 6.13). The hydrogels were then washed with fresh 100 mM HEPES pH 7.4 buffer solution every 30 minutes for 6 hours.

***Table 6.13**: A table depicting the photocaged monomers and their solvent, with the length of time in which they were irradiated with light for.*

Photocaged Monomer	Deprotection Solution	Deprotection Time (mins)
MC-1	HAT in DI H_2O	75
SMC-1	HAT in DI H_2O	60
MC-2	Semicarbazide	75
SMC-2	Semicarbazide	60

6.5.7 LW Functionality Testing

The refractive index sensitivity of AAm/APMA derivative based LW devices was determined using the method described in Chapter 6.3.4.

Porosity of the LW devices in relation to PEG groups of a variety of sizes was established based on the method described in Chapter 6.3.5.

6.5.8 Streptavidin Immobilisation

Using a flow cell, either a single or 2-channel, on waveguide instrument B, a peristaltic pump was used to introduce a 100 mM pH 7.4 HEPES buffer solution to the AAm/APMA derivative co-monomer LW device through the flow cell channel or channels until the signal presented a steady baseline. A solution of N-hydroxysuccinimide (*NHS*)-PEG_{12}-biotin (0.25 mg) dissolved in 100 mM pH 7.4 HEPES (500 µL) was recirculated through the flow cell for 1 hour. This was subsequently washed with 100 mM pH 7.4 HEPES until the signal was stable. Following this, a 1 mg mL^{-1} solution of streptavidin in 100 mM pH 7.4 HEPES (500 µL) was recirculated through the channel for 20 minutes. Finally, the channel was again washed with 100 mM pH 7.4 HEPES until the signal stabilised.

To obtain a protein immobilisation trace, data collected was converted from shift in pixels to shift in resonance angle ($\Delta\theta_R$) through the use of Equation 6.3. The $\Delta\theta_R$ was plotted in a graph against time using Origin.

6.6 References

1 *McGraw-Hill encyclopedia of science & technology: an international reference work in twenty volumes including an index*, McGraw-Hill, New York, NY, 10. ed. ff., 2007.
2 CODATA Value: speed of light in vacuum, https://physics.nist.gov/cgi-bin/cuu/Value?c, (accessed 15 September 2022).
3 S. Singh, *Phys. Scr.*, 2002, **65**, 167–180.
4 Refractive index, https://spark.iop.org/refractive-index, (accessed 15 September 2022).
5 M. Gómez-Castaño, J. L. Garcia-Pomar, L. A. Pérez, S. Shanmugathasan, S. Ravaine and A. Mihi, *Adv. Opt. Mater.*, 2020, **8**, 2000865.
6 Refraction of light, https://www.sciencelearn.org.nz/resources/49-refraction-of-light, (accessed 26 September 2022).
7 Refraction of waves - Reflection and refraction - AQA - GCSE Physics (Single Science) Revision - AQA, https://www.bbc.co.uk/bitesize/guides/zw42ng8/revision/2, (accessed 26 September 2022).
8 W. Long, T. Wu, S. Cai, X. Liang, J. Jiao and M. Xu, *IEEE Access*, 2019, **7**, 57805–57819.
9 Optical fibres - Refraction of light - National 5 Physics Revision, https://www.bbc.co.uk/bitesize/guides/z3jbh39/revision/2, (accessed 26 September 2022).
10 S. Zhu, A. W. Yu, D. Hawley and R. Roy, *Am. J. Phys.*, 1986, **54**, 601–607.
11 *Dielectric Phenomena in Solids*, Elsevier, 2004.
12 D. Axelrod, T. Burghardt P. and N. Thompson L., *Annu. Rev. Biophys. Bioeng.*, 1984, **13**, 247–268.
13 C. M. Miyazaki, F. M. Shimizu and M. Ferreira, in *Nanocharacterization Techniques*, Elsevier, 2017, pp. 183–200.
14 Z. Zhao, M. Lanzarini-Lopes, E. Westerhoff, X. Long, H. Rho, Y. Bi, L. Ling and P. Westerhoff, *Environ. Sci. Nano*, 2021, **8**, 2441–2452.
15 A. West, .
16 P. Kozma, F. Kehl, E. Ehrentreich-Förster, C. Stamm and F. F. Bier, *Biosens. Bioelectron.*, 2014, **58**, 287–307.
17 B. Li and H. Ju, *BioChip J.*, 2013, **7**, 295–318.
18 K. Lee, J. Kunjappu, S. Jockusch, N. J. Turro, T. Widerschpan, J. Zhou, B. W. Smith, P. Zimmerman and W. Conley, in *Advances in Resist Technology and Processing XXII*, SPIE, 2005, vol. 5753, pp. 537–553.
19 Refractive index - Light and sound - reflection and refraction - GCSE Physics (Single Science) Revision - Other, https://www.bbc.co.uk/bitesize/guides/zchyj6f/revision/4, (accessed 4 October 2022).
20 H.-Y. Li, W.-C. Hsu, K.-C. Liu, Y.-L. Chen, L.-K. Chau, S. Hsieh and W.-H. Hsieh, *Sens. Actuators B Chem.*, 2015, **206**, 371–380.
21 R. Ulrich and W. Prettl, *Appl. Phys.*, 1973, **1**, 55–68.
22 R. Gupta and N. J. Goddard, *Sens. Actuators B Chem.*, 2020, **322**, 128628.
23 R. Gupta and N. J. Goddard, *The Analyst*, 2013, **138**, 1803.
24 N. A. Alamrani, G. M. Greenway, N. Pamme, N. J. Goddard and R. Gupta, *The Analyst*, 2019, **144**, 6048–6054.
25 UV-visible absorption spectra, https://www.chemguide.co.uk/analysis/uvvisible/theory.html, (accessed 6 October 2022).
26 J. Stetefeld, S. A. McKenna and T. R. Patel, *Biophys. Rev.*, 2016, **8**, 409–427.
27 J. W. Robinson, E. S. Frame and G. M. Frame II, *Undergraduate Instrumental Analysis, Seventh Edition*, CRC Press, Hoboken, 7th edn., 2014.
28 G. Wypych, *Handbook of solvents*, ChemTec Publishing, Toronto, 2nd edition., 2014.
29 I. Fleming and D. Williams, *Spectroscopic methods in organic chemistry*, Springer, Cham, Switzerland, Seventh edition., 2019.
30 UV-VIS theory, http://www.chem.ucla.edu/~bacher/UV-vis/uv_vis_tetracyclone.html.html, (accessed 28 September 2022).
31 absorption spectra - the Beer-Lambert Law, https://www.chemguide.co.uk/analysis/uvvisible/beerlambert.html, (accessed 6 October 2022).
32 Beer's Law, https://spie.org/publications/fg08_p65_beers_law?SSO=1, (accessed 6 October 2022).
33 What is a molar extinction coefficient? | AAT Bioquest, https://www.aatbio.com/resources/faq-frequently-asked-questions/What-is-a-molar-extinction-coefficient, (accessed 6 October 2022).
34 C. F. Poole, in *Encyclopedia of Separation Science*, Elsevier, 2000, pp. 40–64.

35 O. Coskun, *North. Clin. Istanb.*, , DOI:10.14744/nci.2016.32757.
36 R. P. Sinha and D.-P. Häder, Eds., *Natural bioactive compounds: technological advancements*, Academic Press, Amsterdam, 2020.
37 Column Chromatography, https://www.orgchemboulder.com/Technique/Procedures/Columnchrom/Columnchrom.shtml, (accessed 10 October 2022).
38 P. J. Worsfold, A. Townshend and C. F. Poole, *Encyclopedia of analytical science*, Elsevier, S.l., 2010.
39 high performance liquid chromatography - hplc, https://www.chemguide.co.uk/analysis/chromatography/hplc.html, (accessed 10 October 2022).
40 W. T. Cooper, in *Encyclopedia of Analytical Chemistry*, ed. R. A. Meyers, John Wiley & Sons, Ltd, Chichester, UK, 2006, p. a5913.
41 D. Roy, S. Liu, B. L. Woods, A. R. Siler, J. T. Fourkas, J. D. Weeks and R. A. Walker, *J. Phys. Chem. C*, 2013, **117**, 27052–27061.
42 M.-I. Aguilar, in *HPLC of Peptides and Proteins*, Humana Press, New Jersey, 2003, vol. 251, pp. 9–22.
43 P. Žuvela, M. Skoczylas, J. Jay Liu, T. Bączek, R. Kaliszan, M. W. Wong and B. Buszewski, *Chem. Rev.*, 2019, **119**, 3674–3729.
44 M. Akkbik, Z. B. Assim and F. B. Ahmad, *Int. J. Anal. Chem.*, 2011, **2011**, 858153.
45 Liquid Chromatography | SHIMADZU EUROPA, https://www.shimadzu.co.uk/liquid-chromatography?gclid=EAIaIQobChMI0oKNlNTV-gIV-IFQBh13cABwEAAYAyAAEgL98PD_BwE, (accessed 10 October 2022).

Chapter 7 - Appendices

7.1 Chapter 4

7.1.1 H NMR of NVOC-Cl in DMSO at 12 Hours

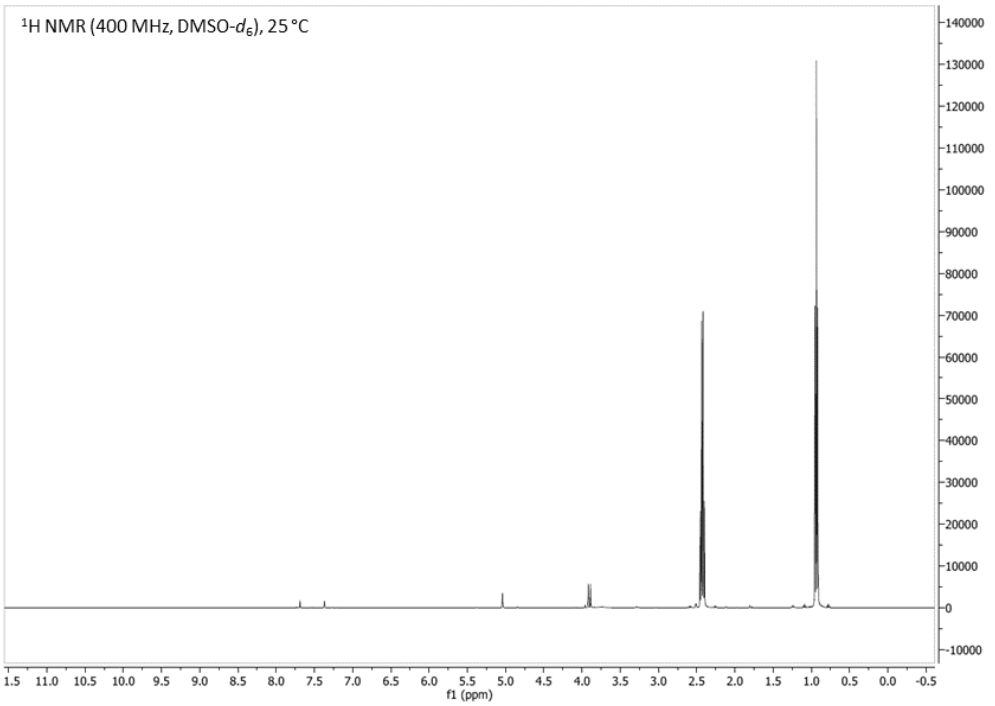

7.1.2 H NMR of NVOC-Cl in DMSO at 24 Hours

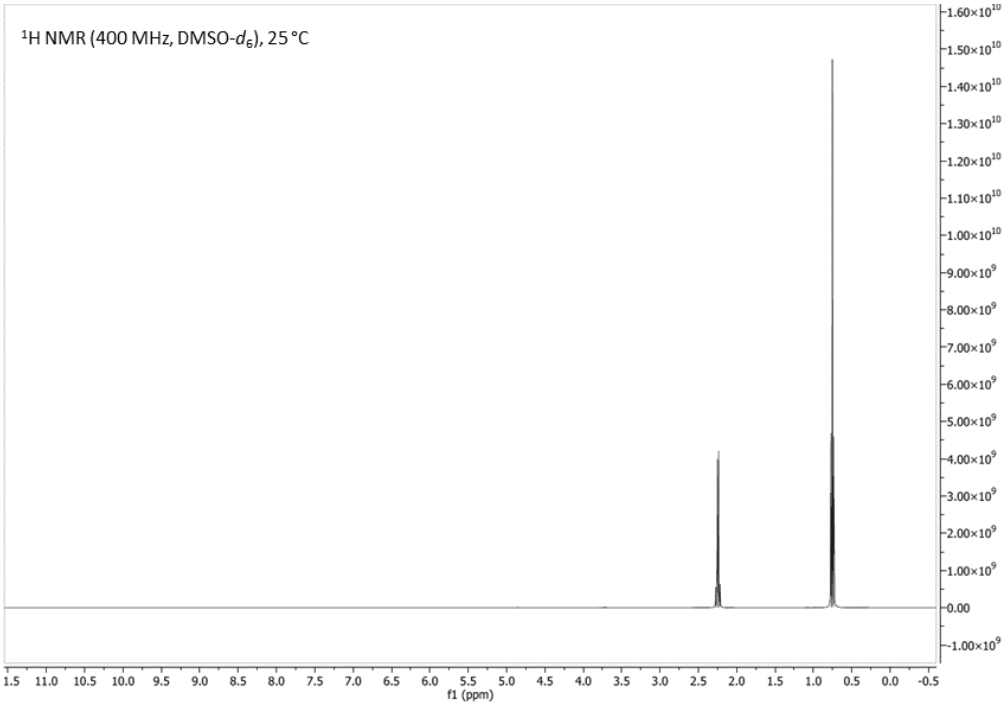

7.1.3 H NMR of NVOC-Cl in DMSO at 48 Hours

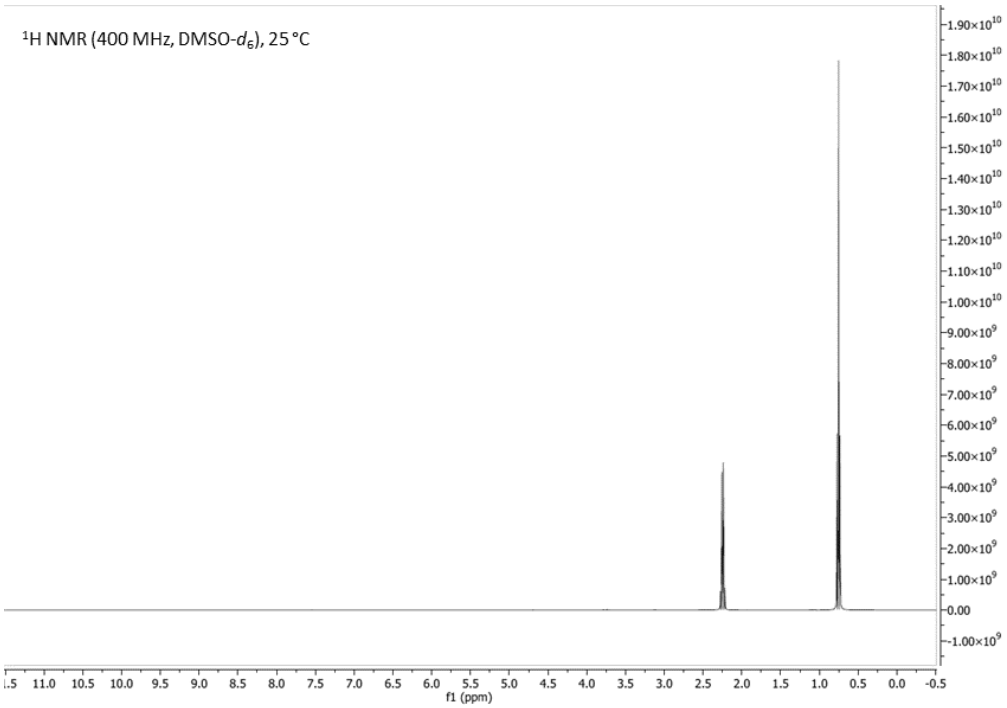

7.1.4 H NMR of Compound MC

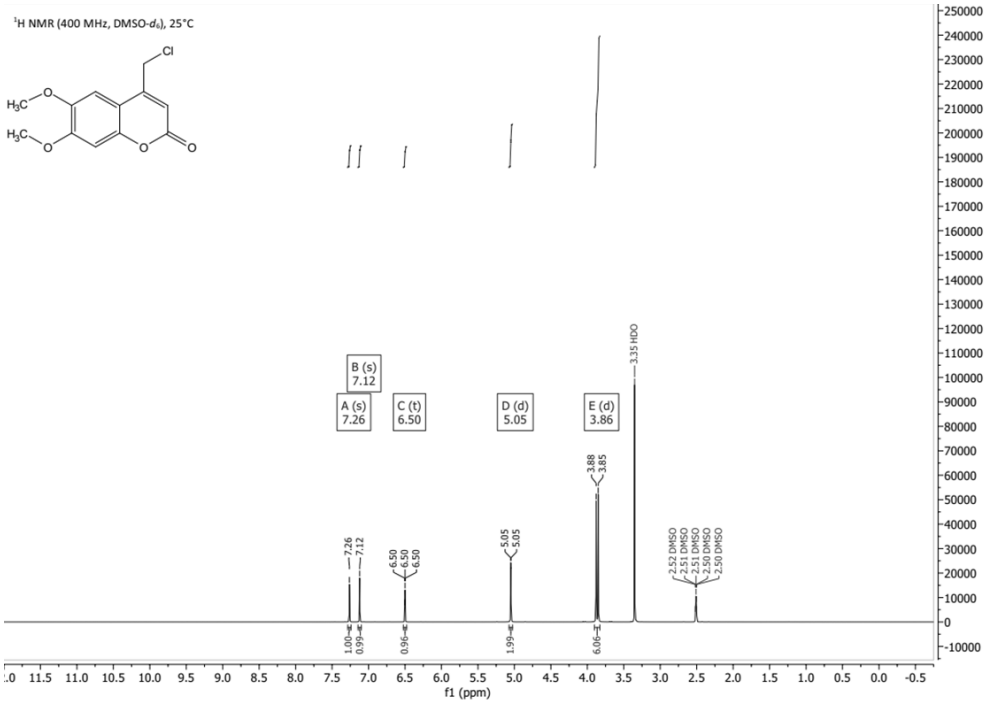

7.1.5 H NMR of Compound MC-2a

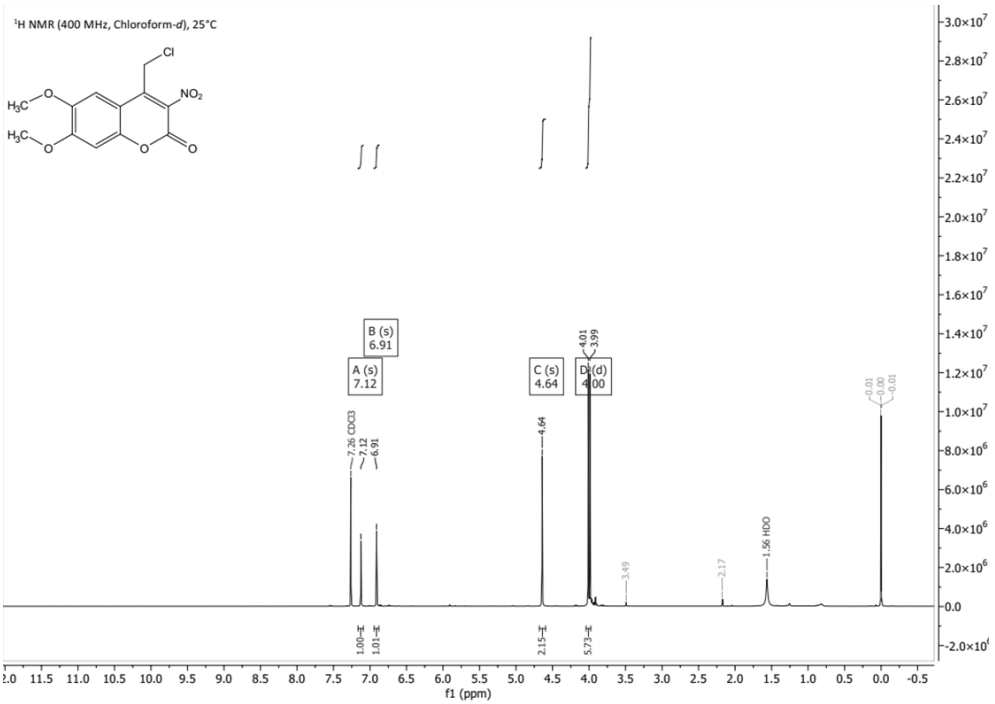

7.1.6 UV-Vis Absorbance Spectrum of Compound MC in DCM at Varying Concentrations

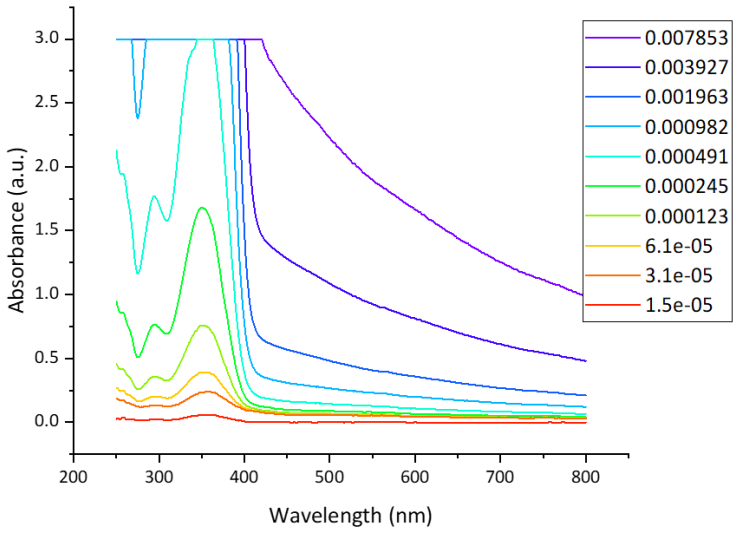

7.1.7 UV-Vis Absorbance Spectrum of Compound AC in DCM at Varying Concentrations

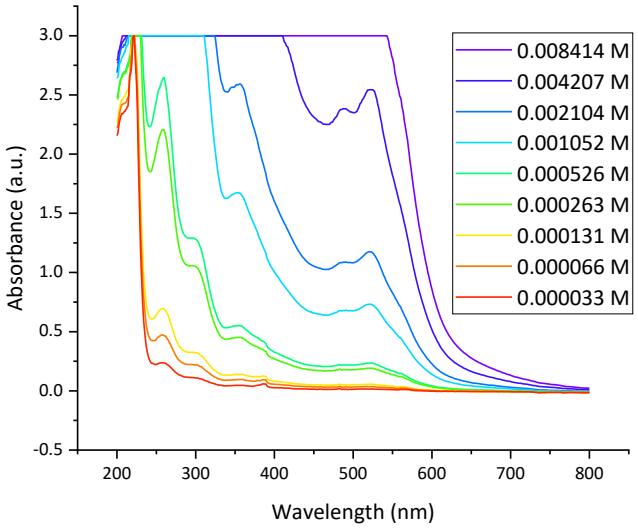

7.2 Chapter 5

7.2.1 Glycerol Trace for Photocaged AAm/MC-1 LW Devices

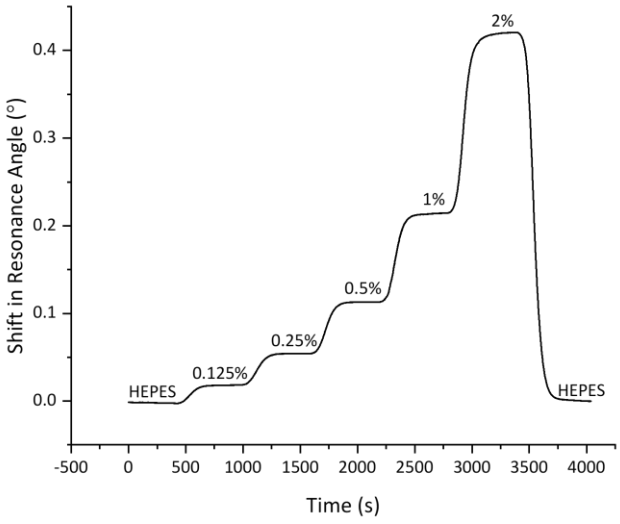

7.2.2 Glycerol Trace for Photocaged AAm/SMC-1 LW Devices

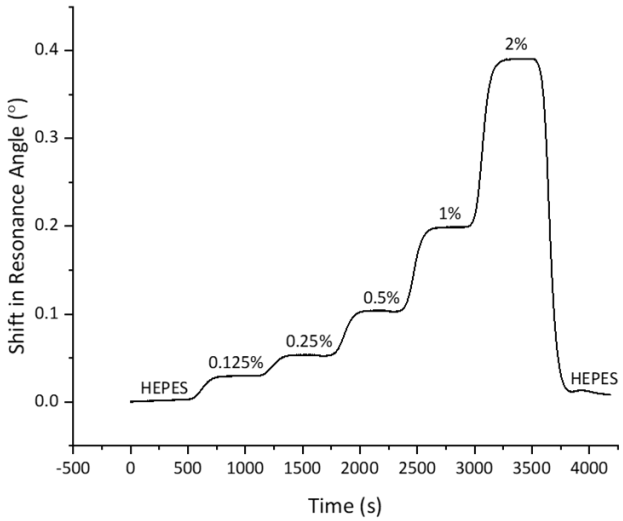

7.2.3 Glycerol Trace for Photocaged AAm/MC-2 LW Devices

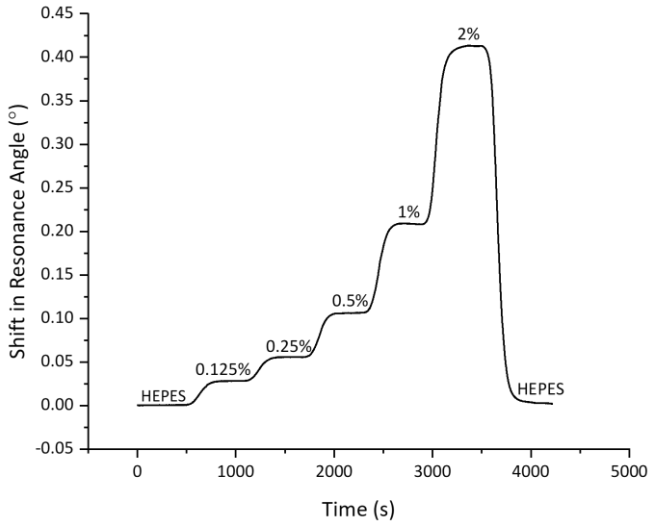

7.2.4 Glycerol Trace for Photocaged AAm/SMC-2 LW Devices

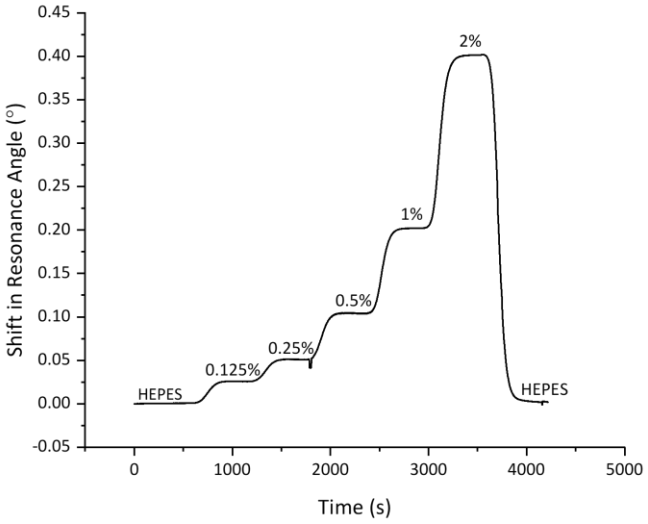

7.2.5 Glycerol Trace for Photodeprotected AAm/MC-1 LW Devices

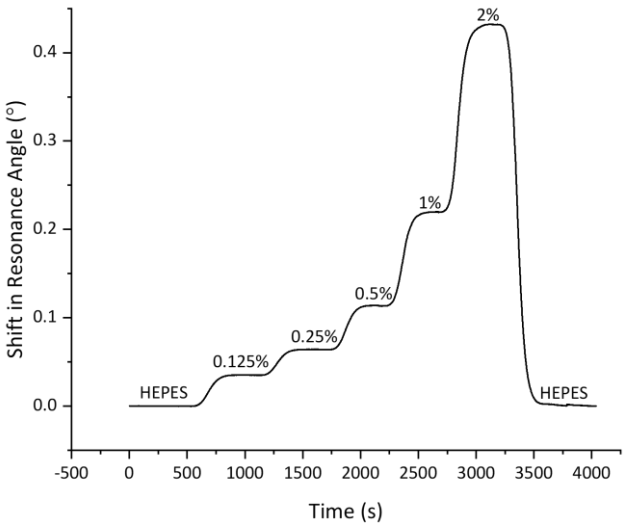

7.2.6 Glycerol Trace for Photodeprotected AAm/SMC-1 LW Devices

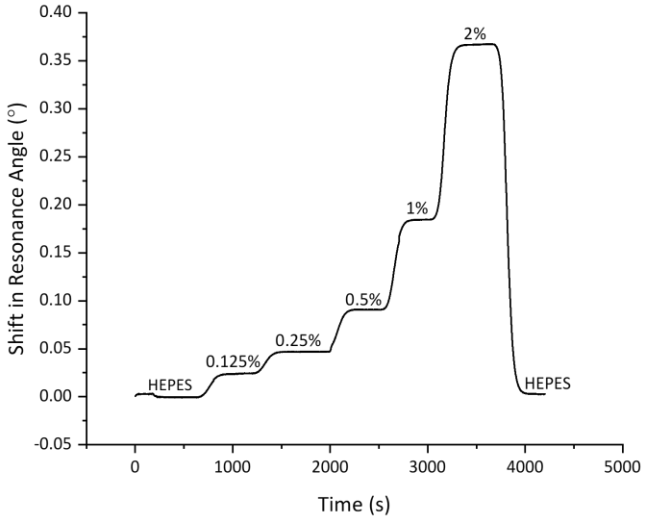

7.2.7 Glycerol Trace for Photodeprotected AAm/MC-2 LW Devices

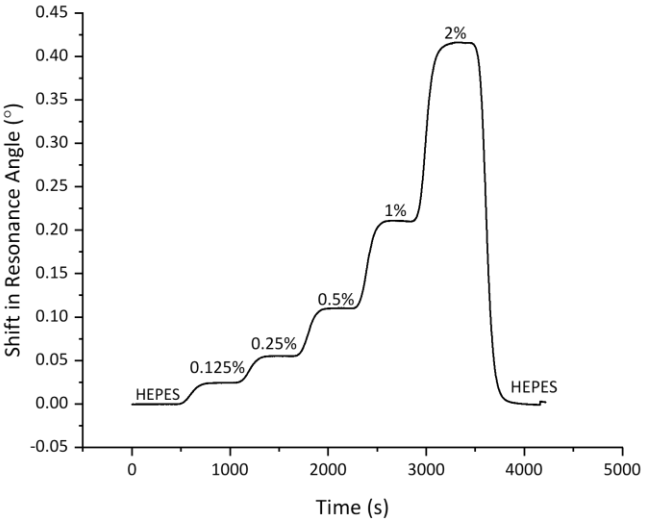

7.2.8 Glycerol Trace for Photodeprotected AAm/SMC-2 LW Devices

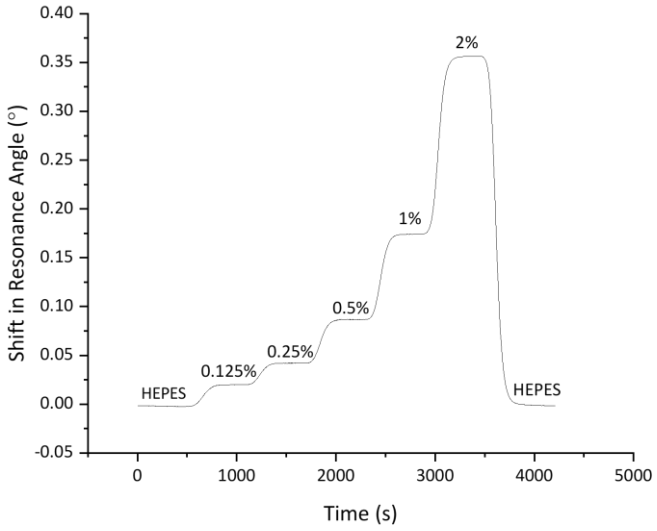

7.3 Presentations of Work in this Thesis

Work in this thesis, most specifically the work in Chapter 3.5.1: Photocaging of Hydrogels was presented to the School of Chemistry at the University of Birmingham in the form of a poster presentation at the June 2020 Postgraduate Symposium.

Work in this thesis, most specifically the work in Chapter 3.5.2: Photocaging of Monomers was presented to the School of Chemistry at the University of Birmingham in the form of an oral presentation at the June 2021 Postgraduate Symposium.

7.4 Publications of Work in this Thesis

Work in this thesis, most specifically the work in Chapter 2.5 was published in the journal IEEE Transactions on Instrumentation and Measurement in 2020, under the title of 3D Printed Instrumentation for Point-of-Use Leaky Waveguide (LW) Biochemical Sensor by N.J. Goddard, H. Dixon, N. Toole and R. Gupta. DOI: 10.1109/TIM.2020.2969036.